Magnetisation Dynamics of Nanostructured Spintronic Devices

Submitted by Christopher John Durrant to the University of Exeter as a thesis for the degree of Doctor of Philosophy in Physics in October 2016.

I certify that all material in this thesis which is not my own work has been identified and that no material has previously been submitted and approved for the award of a degree by this or any other University.

.....

Christopher John Durrant

Abstract

In this thesis investigations of the static and dynamic properties of magnetic thin films and thin magnetic multilayers with spintronic properties are presented. A selective area chemical vapour deposition technique has been used to fabricate continuous and patterned epitaxial CrO_2 thin films grown on (100)-oriented TiO_2 substrates. Precessional magnetization dynamics were stimulated both electrically and optically, and probed by means of time-resolved Kerr microscopy (TRSKM) and vector network analyser ferromagnetic resonance (VNA-FMR) techniques. The dependence of the precession frequency and the effective damping parameter upon the static applied magnetic field were investigated. All films exhibited a large in-plane uniaxial anisotropy. The effective damping parameter was found to exhibit strong field dependence in the vicinity of the hard axis saturation field. However, continuous and patterned films were found to generally possess similar dynamic properties, confirming the suitability of the deposition technique for fabrication of future spintronic devices. Ta/CoFeB/MgO trilayers with perpendicular magnetic anisotropy were fabricated by magnetron sputtering and patterned into Hall bars by photolithography. Scanning Kerr microscopy (SKM) was combined with electrical transport measurements to gain insight into the underlying mechanisms of current-induced spin-orbit torque (SOT) switching within such devices. Switching was found to be a stochastic, domain wall driven process, the speed of which is strongly dependent on the switching current. Kerr imaging shows domain nucleation at one edge of the device which modelling reveals is likely assisted by the out-of-plane component of the Oersted field. Further domain growth, leading to magnetisation reversal, may still be dominated by spin torques, but the Oersted field provides an additional mechanism by which to control the switching process. Pulsed current TRMOKE experiments were performed on both Ta/CoFeB/MgO trilayers patterned into large Hall bars, and on patterned Ta/CoFeB/MgO trilayers formed upon planar waveguides. Magnetisation dynamics in these structures were found to be complex and to have strong dependence on bias field direction, bias field polarity, pulsed current direction, current density and device size. Two components of the dynamic response were observed in Hall bars, a fast oscillatory component and a slow unipolar deflection. A strong spatial dependence of the dynamic response was observed for patterned CoFeB/MgO devices formed upon planar waveguides with a particularly large in-plane rotation observed at the edges of a square element. These studies highlight the complexity of the SOTs generated by the spin Hall and Rashba effects. Spin pumping within Ta/Ag/Co_2MnGe(5

nm)/Ag(6 nm)/$Ni_{81}Fe_{19}$(0-5 nm)/Ag/Ta large area spin valve structures was studied by vector network analyser ferromagnetic resonance (VNA-FMR), and element-specific phase-resolved x-ray ferromagnetic resonance (XFMR). Spin current absorption as a function of $Ni_{81}Fe_{19}$ sink layer thickness was explored indirectly by VNA-FMR as a modification of the Co_2MnGe source layer damping. XFMR was used to directly detect the motion of the sink layer magnetization at the source layer resonance. The bipolar form of the sink layer signal clearly indicates the action of spin transfer torque (STT) resulting from spin pumping, while comparison with a macrospin model allows the real part of the spin mixing conductance to be directly determined. The dependence of the source layer damping upon the sink layer thickness was observed to be different to previous studies, due to both spin current absorption in the outer Ta layers, and superparamagnetic relaxation in sink layers with thickness less than or equal to 0.6 nm. The XFMR measurements show that the absorption of spin current within the sink layer continues to increase up to the largest sink layer thickness of 5 nm, presumably due to improving interface quality.

To my family.

Acknowledgements

My first thanks must go to my supervisor Professor Rob Hicken for giving me the opportunity to study for a PhD. Rob has provided unwavering support and encouragement throughout my studies alongside invaluable expertise and insight. I am especially grateful for his patience and willingness to explain concepts from first principles, always ensuring clarity in the more challenging elements of my studies, also for his thoroughness and attention to detail which consistently challenged me to improve my scientific writing. Thanks must also go to the University of Exeter for the award of the scholarship which enabled me to pursue this PhD.

I wish to acknowledge the members of the Magnetic Materials group at Exeter University who made this an enjoyable and stimulating group to work in. Dr Paul Keatley consistently provided invaluable experience and technical expertise, and made downtime at conferences particularly enjoyable. Dr Leigh Shelford for his technical expertise and patience. Dr Volodymyr Kruglyak and Dr Feodor Ogrin for their insightful questions during group meetings. Tom Loughran for always challenging and amusing me with interesting ideas, and especially for helping me through the darker PhD times when nothing seemed to work. Rob Valkass for his friendship and unerringly precise knowledge of coding and legislation. Dr Wei Yu for his technical help during the early stages of my PhD, and for becoming a dedicated 'gym buddy'. I would also like to thank Nick Bukin, Dr Haider Mohamad, Reem Alsaigh and Timothy Spicer for both their contributions to this work and friendly attitude. Many members of the wider physics community at Exeter University have also made direct or indirect contributions to this work. Including the workshop staff, who must be acknowledged for their ability to turn even the most vague and ill conceived idea or scrappy sketch into a reality. All of the lecturers and professors who ignited my passion for research, with particular thanks going to professor Roy Sambles and Alistair Hibbins who supervised my MPhys project.

I would like to thank Professor Gang Xiao and his research group at Brown University, who provided the facilities for the growth of CrO_2 and Ta/CoFeB/MgO. This was supported by the Nanoelectronics Research Initiative (NRI) through the Institute for Nanoelectronics Discovery and Exploration (INDEX), and by the National Science Foundation through Grant No. DMR-1307056. I wish to specifically thank the members of Professor Xiao's group, Michael Jokubaitus, Shu-tong Wang, Wenzhe Chen and Qiang Hao, for their direct assistance in the work presented in this thesis, and also

for their friendly and welcoming attitude during my extended stays in an unfamiliar country.

Finally I wish to thank those who did not make direct contributions to this work, but without whom I would not have made it through the last four years. My parents Kate and Graham have always given me love and support throughout whatever I chose to pursue. They taught me the value of working hard for what I wished to achieve, and this thesis is a result of the dedication and sacrifices they made for me throughout my life. My brother Rich for being my oldest friend and confidant, and for always being ready with a beer or a surfboard when I needed a break. My grandparents and wider family for their help, support and understanding. I wish to thank all of my friends who have helped me along the way, especially those who have never hesitated to make the long trek to see me. Finally I wish to thank my dedicated and loving partner Charli, for her almost saintlike patience during the final few months of write up, and for always providing just what I needed to help me through, whether that was support, advice, distraction, lasagne, or just a smile.

Contents

List of Publications

1. C. J. Durrant, L. R. Shelford, R. A. J. Valkass, A. I Figueroa, A. A. Baker, L. Duffy, G. van der Lann, P. Shafer, E. Arenholz, C. Klewe, S. A. Cavill, J. R. Childress, J. A. Katine and R. J. Hicken *Spin pumping and spin transfer torque in Ta/Ag/Co_2MnGe (5 nm)/Ag (6 nm)/$Ni_{81}Fe_{19}$ (0 - 5 nm)/Ag/Ta spin valve structures*, Submitted to Phys. Rev. B. (2016)

2. C. J. Durrant, Qiang Hao, Gang Xiao and R. J. Hicken. *Scanning Kerr microscopy study of current-induced switching in Ta/CoFeB/MgO films with perpendicular magnetic anisotropy.* Phys. Rev. B. **93**(1) 014414 (2016).

3. C. J. Durrant, M. Jokubaitis, W. Yu, H. Mohamad, L. R. Shelford, P. S. Keatley, Gang Xiao and R. J. Hicken. *Ferromagnetic resonance of patterned chromium dioxide thin films grown by selective area chemical vapour deposition* J. Appl. Phys. **117**(17) 17B707 (2015).

4. C. J. Durrant, B. Tremain (joint authorship), I. E. Carter, A. P. Hibbins and J. R. Sambles *The Effect of Rotational Disorder on the Microwave Transmission of Checkerboard Metal Square Arrays*, Sci. Rep. **5** 16608 (2015).

5. P. S. Keatley, C. J. Durrant, S. J. Berry, E. Sirotkin, A. P. Hibbens and R. J. Hicken. *Ferrite-filled cavities for compact planar resonators*, Appl. Phys. Lett. **104**(2) 022405 (2014).

List of Figures

List of Tables

Declaration

The contributions to the work presented in this thesis by my colleagues is outlined below. This entire work was supervised by Prof. R. J. Hicken so he will not be acknowledged specifically as his contributions permeate the entire thesis. A general acknowledgement must be given to the workshop staff at the University of Exeter who made contributions to the development and maintenance of experiments and assisted in the fabrication of bespoke equipment. A general acknowledgement must also be given to Dr Paul Keatley for upkeep of the time-resolved scanning Kerr microscopy experiment (TRSKM) used extensively in this thesis.

Chapter 2 *Background* This chapter covers the background theory relevant to this thesis and has been compiled by myself. The content is not a result of my own work, and the relevant authors and texts are acknowledged throughout the chapter.

Chapter 3 *Fabrication Techniques* The theory of the fabrication techniques has not been developed in this thesis, and is referenced to the relevant authors in this chapter. The sputter deposition systems and chemical vapour deposition systems at Brown University were developed by members of Prof. Gang Xiao's group with contributions in recent years from from Michael Jokubaitus, Dr Qiang Hao, Wenzhe Chen and Shutong Wang. Photolithography and annealing systems are maintained and developed by multiple groups including Prof. Gang Xiao's at Brown University. Clean room processes at the University of Exeter such as wire-bonding were maintained and overseen by Mark Heath.

Chapter 4 *Experimental Techniques* The theory of the experimental techniques has not been developed in this thesis, and is referenced to the relevant authors in this chapter. The vibrating sample magnetometer was set up at Brown University by Michael Jokubaitus and Dr Qiang Hao under the supervision of Prof. Gang Xiao. X-ray reflectivity and X-ray diffraction experiments are maintained by a number of groups at Brown University. Time-resolved experiments have been developed at the University of Exeter by Prof. R. J. Hicken, Dr Jing Wu, Dr Ralph Wilks, Dr Anjan Barman, Dr Volodymyr Kruglyak, Dr Paul Keatley, Dr Leigh Shelford and Dr Wei Yu before my arrival in the group. Data acquisition software was written by Prof. R. J. Hicken, Dr Ralph Wilks, Dr Anjan Barman, Tom Loughran and Tim Spicer. The vector network analyser ferromagnetic resonance (VNA-FMR) experiment and software was developed by myself and Dr Leigh Shelford with the supervision of Prof. R. J. Hicken at the University of Exeter .

Chapter 5 *Ferromagnetic Resonance of CrO_2 Thin Films Patterned by Selective Area Chemical Vapour Deposition* The samples studied in this chapter were fabricated by myself and Michael Jokubaitus under the supervision of Prof. Gang Xiao at Brown University. Structural and magnetic sample characterisation was performed by myself with assistance from Michael Jokubaitus at Brown University. Optical sample characterisation was performed by myself with assistance from Tom Loughran at Exeter University. VNA-FMR experiments were conducted by myself. TRSKM measurements were conducted by myself with assistance from Dr Wei Yu. Time-resolved optical pump-probe measurements were performed by Dr Leigh Shelford and Dr Haider Mohamad and interpretation of these results was conducted by myself.

Chapter 6 *Current Induced Switching in Ta/CoFeB/MgO Films With Perpendicular Magnetic Anisotropy* The samples studied in this chapter were fabricated by Wenzhe Chen under the supervision of Prof. Gang Xiao at Brown University. Structural and magnetic sample characterisation was performed by Wenzhe Chen. Optical sample characterisation was performed by myself at Exeter University. The combined Hall resistance and MOKE experiment was designed and built by myself, the data acquisition software was written by myself with assistance from Tom Loughran and Rob Valkass. Modelling was designed and conducted by myself.

Chapter 7 *Time-Resolved Scanning Kerr Microscope Studies of Spin Orbit Torque Induced Magnetisation Dynamics in Ta/CoFeB/MgO Hall Bars* The samples studied in this chapter were fabricated by Wenzhe Chen under the supervision of Prof. Gang Xiao at Brown University. Structural and magnetic sample characterisation was performed by Wenzhe Chen. Optical sample characterisation and TRSKM experiments were performed by myself at Exeter University.

Chapter 8 *Time-Resolved Scanning Kerr Microscope Studies of Spin Orbit Torque Induced Magnetisation Dynamics in Patterned Ta/CoFeB/MgO Ultra Thin Films* The samples studied in this chapter were designed by myself and fabricated by myself and Wenzhe Chen, with assistance from Shu-tong Wang, under the supervision of Prof. Gang Xiao, at Brown University. Structural and magnetic sample characterisation was performed by myself and Wenzhe Chen at Brown University. Electrical and optical sample characterisation was performed by myself at the University of Exeter. TRSKM experiments were performed by myself with assistance from Tim Spicer at Exeter University.

Chapter 9 *Development of a Vector Network Analyser Ferromagnetic Resonance (VNA-FMR) Experiment* The vector network analyser ferromagnetic resonance (VNA-FMR) experiment and software was developed by myself and Dr Leigh Shelford under the supervision of Prof. R. J. Hicken at the University of Exeter. Data processing codes

were developed by myself and Dr Leigh Shelford.

Chapter 10 *Spin pumping and spin transfer torque in Ta/Ag/Co_2MnGe (5 nm)/Ag (6 nm)/$Ni_{81}Fe_{19}$ (0 - 5 nm)/Ag/Ta spin valve structures* The samples studied in this chapter were fabricated by J.R. Childress and J.A. Katine at Hitachi Global Storage Technologies, San Jose, California. VNA-FMR experiments were performed by myself and Dr Leigh Shelford. X-ray ferromagnetic resonance (XFMR) was performed at Beamlines I06 and I10 at the Diamond Light Source, Didcot, by Rob Valkass and Dr Leigh Shelford with assistance from A. I. Figueroa, A. A. Baker, L. Duffy and G. van der Lann. XFMR was also performed at Beamline 4.0.2 at the Advanced Light Source (ALS), Berkeley, by Rob Valkass with assistance from P. Shafer, E. Arenholz and C. Klewe. XFMR data analysis and modelling was conducted by myself.

Chapter 1

Introduction

Spintronics is a broad field that aims to control conduction electrons by means of their spin as well as their charge. Over the past decade spintronic devices have undergone a rise in prominence in the information technology industry, becoming widely used in hard disk drives. Essential to this rise was the "spin-valve", a trilayer structure consisting of two ferromagnetic (FM) layers sandwiching a non-magnetic (NM) spacer layer. A nonferromagnetic metallic spacer layer gives rise to the Giant Magnetoresistance (GMR) effect[1], in which it is possible to control the magnetoresistance of the spin-valve by controlling the relative orientation of the magnetisation vectors of the ferromagnetic layers. The spin valve can act as a sensor as it flies above a magnetic recording medium, sensing transitions between the bits as their stray field reverses. Although GMR spin valves and advanced magnetic media led to dramatic increases in areal storage density in hard disk drives, this technology was quickly superseded by spin-dependent tunnelling devices (known as magnetic tunnel junctions (MTJs)). In MTJs the metal spacer layer is replaced by an insulating barrier to exploit Tunneling Magnetoresistance (TMR)[2]), increasing the magnetoresistance of the spin-valve upwards of ten times at room temperature.

The discovery of spin-transfer torque (STT) has since led to the development of active spintronics, in which angular momentum of the conduction electrons is used to reorient the magnetisation of a ferromagnet. STTs are utilised in an emergent class of non-volatile memories (spin-transfer torque magnetic random access memory (STT-MRAM)) which store and read information electrically rather than by magnetic fields, and so do not require moving parts. Recording bits are encoded as the parallel and antiparallel alignment of ferromagnetic layers, which can be read out through the magnetoresistance. This is a key difference that enables integration of magnetic

devices with semiconductor chips. Such devices may fulfil the speed requirements of a computer's working memory, whilst having the inherent advantage that no energy is needed to retain information in magnetic states. Initially ferromagnetic electrodes were required to generate spin-polarised currents in STT devices. However, injection of a writing current through a tunnel barrier leads to problems with fatigue and electromigration. Recently there has been considerable interest in instead utilising spin-orbit (SO) torques, generated via the spin Hall effect (SHE) and the Rashba effect (RE). These spin-orbit torques (SOTs) arise from the spin-orbit (SO) interaction and offer an efficient means by which to control the state of a ferromagnet without current injection through the MTJ barrier and the efficacy of this approach has been demonstrated by fabricating MTJs on a heavy metal (HM) underlayer. Key questions in this emergent field include how the magnitude and direction of the SOTs torques depend on film composition and structure, as well as how they depend on the magnitude and duration of the currents which generate them.

This thesis explores the dynamic properties of a half-metallic material in which charge currents are already spin-polarised (chapter 5), details the generation of pure spin-currents by spin-pumping (chapter 10), and discusses current-induced STT magnetisation switching and SOTs (chapters 6, 7 and 8).

Chapter 2 outlines the principles of magnetism relevant to this thesis. The origins of the magnetic moment are discussed in terms of the spin and orbital contributions. Next the origins of ferromagnetism and the contributions to the free energy of a ferromagnetic material are discussed. The classical view of magnetic anisotropy and magnetic domains are introduced before discussion of the magnetic hysteresis loop. Next the response of magnetic materials to time varying external fields are explored introducing the concepts of magnetic precession and resonance. Finally the principles of electron transport and STTs are discussed with a focus on SOTs. This chapter provides general background while in each subsequent chapter the literature of immediate relevance is also reviewed.

Chapter 3 describes the fabrication techniques used to create the TiO_2/CrO_2 and Ta/CoFeB/MgO thin film devices used in this work. This chapter can be broadly broken down into design considerations, pre-treatment, growth techniques (including magnetron sputtering deposition and selective area chemical vapour deposition (CVD)), patterning techniques (including photolithography and ion-beam etching) and finally thermal annealing.

Chapter 4 describes several experimental techniques. The first section discusses the methods used to refine the fabrication procedure including Vibrating Sample

Magnetometery (VSM), which was principally used as a rapid means to analyse the magnetic anisotropy of films, alongside X-Ray Reflectivity (XRR) and X-Ray Diffraction (XRD) techniques which were used to analyse the films' structural properties. Next the two main experimental principles are discussed; the Magneto-Optical Kerr Effect (MOKE) and Ferromagnetic Resonance (FMR). The origins of the MOKE are described before discussion of the static (no time varying external field) MOKE measurement geometries and experiments. Then the dynamic (time varying external field) time-resolved Magneto-Optical Kerr Effect (TRMOKE) experiments are outlined. Finally this chapter gives a discussion of the Vector Network Analyser Ferromagnetic Resonance (VNA-FMR) theory and experiment.

In Chapter 5 electrically and optically stimulated precessional magnetisation dynamics in continuous and patterned epitaxial CrO_2 thin films grown on (100)-oriented TiO_2 substrates are explored by means of Kerr microscopy and VNA-FMR. Chromium dioxide is a highly attractive material for spintronic applications[3, 4], due to its near 100% spin polarization[5]. The realisation of CrO_2 based spintronic devises requires both the fabrication of high quality elements on a sub-micron scale, and a comprehensive understanding of their dynamical properties. Fabrication of patterned CrO_2 structures is however a complex task since CrO_2 readily decomposes to Cr_2O_3 when traditional post deposition patterning processes are used[6, 7, 8]. This study utilises selective area (CVD) of epitaxial CrO_2 onto rutile TiO_2 substrates through pre-patterned amorphous SiO_2 stencils so as to avoid decomposition and seeks to further understand the dynamic properties and assess whether they are affected by the patterning process.

In Chapter 6 Scanning Kerr Microscopy (SKM) was combined with electron transport measurements to gain insight into the underlying switching mechanisms of current-induced switching in Ta/CoFeB/MgO trilayer Hall bars with perpendicular magnetic anisotropy (PMA). Such devices are expected to play a key role in the next generation of current and electric field switched memory and logic devices for next generation high density magnetic random access memory (MRAM)[9]. Existing MRAM requires an external magnetic field, generated by a current, to induce switching during the read/write procedure. Recently there has been great interest in switching the memory bit directly by using spin transfer torques (STT) generated by charge currents[10, 11]. Conventional STT switching requires current to be injected directly through a tunnel barrier. However, recent studies have utilised the torques generated by spin Hall and Rashba effects to switch elements with an in plane current, leading to smaller write currents for equivalent thermal stability, and avoiding degradation associated with passing high current densities through a tunnel barrier[12]. It has been demonstrated

that the Ta/CoFeB/MgO sub-unit could fulfil the three criteria required for high performance MTJs for STT-MRAM, namely (TMR), low switching current, and high thermal stability for small device dimensions. Recently many studies have used electron transport measurements to infer information about the switching mechanics. This study combines electron transport with simultaneous SKM measurements to also gain information about the role of domain nucleation and propagation in current-induced switching. Many studies of similar structures do not discuss the presence of Oersted fields. Some studies[13, 14] do calculate the in-plane component of the Oersted field (B_x) and conclude that it does not have any significant effect upon the switching since B_x is about 1 order of magnitude smaller than the effective fields generated by spin-torquess[13] and this field often acts to oppose the spin-torques[15]. This study also models the out-of-plane component of the Oersted field and discusses the significant effect this may have on the switching process.

In Chapter 7 Time Resolved Scanning Kerr Microscopy was applied to Ta/CoFeB/MgO trilayer Hall bars to gain a deeper understanding of the underlying dynamic processes on the time-scales associated with MRAM. Intense efforts have recently been made to distinguish between STTs due to the SHE and RE. This is complicated since both effects have been shown to produce similar torques. The relative contributions of the torques have been shown to have a strong dependence on HM and FM thickness[16, 17] and are also influced by temperature[18] and capping layer thickness[19]. Whilst many recent studies have focused on the critical current densities (J_c) required for current induced switching, many have used DC currents, or very long (on the time-scales of MRAM) duration current pulses τ_p. It is not immediately obvious what the effect of reducing τ_p to sub ns time-scales will have on J_c for SOT switching, as τ_p is reduced is it likely that J_c will increase as switching transitions from a thermally activated process to an incoherent, then coherent rotation. The stroboscopic nature of TRSKM allowed the exploration of dynamic response of the magnetisation to very short < 1 ns pulses, whilst the spatial resolution of TRSKM allowed the investigation of the positional variance of the dynamic response, associated with incoherent or domain processes to be investigated.

In chapter 8 Ta/CoFeB/MgO trilayer devices specifically designed for high frequency excitation were fabricated and measured by TRSKM to further build on the work of chapter 7. In Ta/CoFeB/MgO structures there has been a wide variation of the J_c values across similar stack structures[20, 21, 15, 22, 18]. One key similarity is that these values are all smaller than the values predicted by the macrospin model. This variation may be due to differences in the switching regimes of coherent reversal, incoherent

reversal and domain nucleation and propagation. The switching regime is expected to have a strong dependence on device size[23, 24, 25] and τ_p[21]. In this study devices of different size and shape were fabricated and excited by current pulses with varying τ_p. The spatial variance of the dynamic device response was explored with different magnitudes, directions and polarities of the bias magnetic field.

In chapter 9 the development of a VNA-FMR experiment is discussed. VNA-FMR is a powerful technique which can be used to quickly measure magnetisation dynamics over a wide frequency and field range. However the speed and efficiency of this technique means that, typically, large data sets are generated. This chapter describes the difficulties and potential pitfalls in accurately analysing the data and demonstrates a robust automated processing algorithm to overcome systemic errors and experimental noise.

In chapter 10 spin pumping within Ta/Ag/Co_2MnGe(5 nm)/Ag(6 nm)/$Ni_{81}Fe_{19}$(0-5 nm)/Ag/Ta large area spin valve structures was studied by vector network analyser ferromagnetic resonance (VNA-FMR), and element-specific phase-resolved x-ray ferromagnetic resonance (XFMR). Pure spin currents can circumvent the constraints placed on traditional electronics and have the potential to allow low-power and high-bandwidth information transfer[26, 27]. Crucial to the development of smaller and more efficient devices is a strong understanding of the mechanisms by which spin currents can be generated and how these currents propagate through ultra-thin films. Often the detection of pure spin current is indirect, being achieved through measurement of effects induced by the spin current, such as spin-torque driven magnetic precession[28, 29] and the inverse spin Hall effect[30, 31, 32]. Only very recently have methods been devised to detect the local spin density by means of soft x-ray probes[33]. In this study the generation and propagation of spin current by precessional spin pumping in a spin valve comprising a ferromagnetic/normal/ferromagnetic (FM_1/NM/FM_2) metal hybrid structure is explored. The indirect (VNA-FMR) and direct (XFMR) spin-current observation methods are compared. The dynamic behaviour is modelled using coupled LLG equations which allows the real part of the spin mixing conductance $Re(g^{\uparrow\downarrow})$ to be calculated directly from the torque on the spin sink FM layer.

Finally in Chapter 11 a summary of the work in this thesis is presented along with a discussion of the open questions posed by these studies and a description of developments for future work.

Chapter 2

Background

2.1 Introduction

This chapter introduces the background concepts in magnetism required to understand this thesis. Typically a base understanding of classical physics is assumed. Whilst often the origins of the relevant phenomena are quantum mechanical in nature a fully exhaustive quantum mechanical treatment is not discussed, as the results presented in this thesis are assessed semi-classically. This chapter briefly discusses the origins of magnetism and emergent phenomena before discussing static and dynamic magnetic processes with a final focus on the generation of spin orbit torques and their usage in the manipulation of magnetic moments.

2.2 Magnetic Order

There are several contributions to the magnetic moment of an atom, this thesis deals primarily with phenomena which arise from with electron orbital angular momentum and the electron's intrinsic spin angular momentum, however it should be noted that the nuclear spin can also produce a magnetic moment. All magnetic phenomena result from one, or a combination of these contributions, depending on the electronic configuration of the material. Magnetic materials can be broadly classified by their magnetic order as diamagnetic, paramagnetic, ferromagnetic, antiferromagnetic or ferrimagnetic. In diamagnetic materials the sum of the orbital (l_i) and spin (s_i) moments is zero ($\sum l_i = 0$, $\sum s_i = 0$) and no magnetic moment is produced on macroscopic scale. On the application of an external field $\mathbf{H}$ the electron motion within the atom is altered such that a magnetic moment is induced in the direction opposite to $\mathbf{H}$. All other

magnetic phenomena are associated with atoms that possess a permanent magnetic moment. In paramagnetic materials each atom possesses a small magnetic moment but the orientation of the moments is random so the net magnetic moment moment on the macroscopic scale is zero. When an external field **H** is applied the moments tend to align along **H** and the magnetisation becomes non zero in the direction of the field. Paramagnetism, where present, is stronger than diamagnetism and produces magnetization proportional to the applied field in the limit of low **B** or high T. In ferromagnetic materials interaction between the permanent magnetic moments is strong enough to overcome thermal energy fluctuations causing an ordered magnetic state, with moments aligned in the same direction in the absence of an applied field. All the experiments presented in this thesis were performed on ferromagnetic materials and the origins of ferromagnetism are discussed further in section 2.6. A description of other magnetic orderings is beyond the scope of this thesis[34].

2.3 Diamagnetism

Diamagnetic materials create an induced magnetic field in a direction opposite to an externally applied field **H**. This is a property exhibited by all materials. The origins of diamagnetism can be described by a semi-classical model of magnetic moments as circulating electric charges. Whilst diamagnetism is exhibited by all materials the magnetic phenomena discussed in this thesis all arise as a result of materials whose atomic configuration gives rise to a permanent magnetic moment.

2.4 The Origin of the Magnetic Moment

The classic magnetic dipole can be thought of as consisting of a fictitious positive magnetic charge separated by some distance r from a fictitious negative charge. By definition the magnetic dipole moment **m** points from the negative to positive magnetic pole. Before the discovery of spin the origin of the magnetic moment was thought to arise solely from rotating electric charges as shown in figure 2.1.

The magnetic moment of a ring current I around the area S enclosed by the loop is given by $|\mathbf{m}| = \mu_o IS$. The magnetic moment of the ring current can then obtained by substituting the current $I = q(\omega/2\pi)$ and the area of the loop $S = r^2\pi$ obtaining

$$\mathbf{m} = \frac{q}{2} r^2 \boldsymbol{\omega}. \tag{2.1}$$

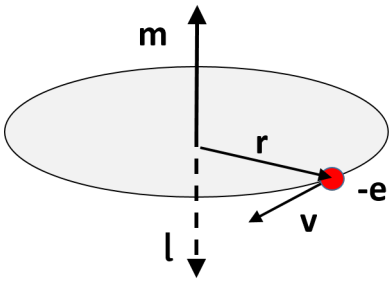

Figure 2.1: Definition of a magnetic moment **m** caused by an electron orbiting at a distance **r** with a tangential velocity **v**. The classical angular momentum **l** is also shown.

For an electron circulating with charge $q = -e$ the definition $\mathbf{v} = \boldsymbol{\omega} \times \mathbf{r}$ can be utilised to express the magnetic moment as

$$\mathbf{m} = -\frac{|e|}{2}(\mathbf{r} \times \mathbf{v}). \tag{2.2}$$

The moment is perpendicular to the orbit of the circulating charge (as shown in figure 2.1). Combing equation 2.2 with the expression for classical angular momentum $\mathbf{l} = m_e(\mathbf{r} \times \mathbf{v})$ an expression for **m** for an electron of mass m_e can be obtained in terms of **l** as

$$\mathbf{m} = -\frac{|e|}{2m_e}\mathbf{l}. \tag{2.3}$$

2.4.1 Orbital and Spin Magnetic Moments

The classical equation 2.3 can be converted to its quantum mechanical equivalent by replacing the classical angular momentum **l** with a quantum expectation value. In quantum mechanics the expectation value of **l** cannot be observed but the component along a single quantization axis (in this case we use z) can be. **l** can be replaced by the expectation value $\langle \mathbf{l}_z \rangle$, which for a single electron with wave function $|l, l_z, s, s_z\rangle$ is given by $\langle \mathbf{l}_z \rangle = \langle l, l_z, s, s_z | \mathbf{l}_z | l, l_z, s, s_z \rangle = \hbar l_z$. As $\hbar l_z$ is the eigenvalue of the operator $\mathbf{l}_z$, the quantum mechanical expression for the measured moment along z is therefore

$$\langle \mathbf{m}^z \rangle = -\frac{|e|}{2m_e}\hbar l_z. \tag{2.4}$$

Equation 2.4 describes the magnetic moment due to a circulating electron, also known as the orbital magnetic moment. This is used to define the so called *Bohr magneton*

$\mu_B = e\hbar/2m_e$. The orbital magnetic moment can then be written as

$$\langle \mathbf{m}_o^z \rangle = -\mu_B \langle \mathbf{l}_z \rangle, \tag{2.5}$$

where the orbital angular momentum is given by the expectation value of the angular momentum operator $\langle \mathbf{l}_z \rangle$.

In addition to the orbital angular momentum the electron also has an intrinsic, or spin, angular momentum with half integer spin quantum number $s = \hbar/2$, and observable projections $s_z = \pm\hbar/2$. The electron spin generates a full Bohr magneton with a spin of only $\hbar/2$, and so for the spin magnetic moment $\langle \mathbf{m}_s \rangle$ it is possible to write a similar general expression to equation 2.5 which has the form

$$\langle \mathbf{m}_s^z \rangle = -2\frac{\mu_B}{\hbar} \langle \mathbf{s}_z \rangle. \tag{2.6}$$

In practice the the spin actually generates a slightly larger moment, this small increase is known as the anomalous magnetic moment and is caused by the effect of fields of the moving electron itself. When writing the magnetisation in terms of the so-called g-factor (a dimensionless quality relating the moment of a particle to its angular momentum quantum number) as $\mathbf{m}_s = -g\mu_B \mathbf{s}/\hbar$ this small correction corresponds to $g = 2.002319$, whilst this is important in quantum electrodynamics the small correction is not important when discussing magnetism.

The total magnetic moment is given by the sum of the orbital and spin magnetic moments as

$$\langle \mathbf{m}_{tot}^z \rangle = -\frac{\mu_B}{\hbar}(2\langle \mathbf{s}_z \rangle + \langle \mathbf{l}_z \rangle) = -\frac{\mu_B}{\hbar}(g_s \langle \mathbf{s}_z \rangle + g_l \langle \mathbf{l}_z \rangle), \tag{2.7}$$

where a g-factor of $g_s = 2$ is associated with the spin moment and $g_l = 1$ is associated with the orbital moment.

2.4.2 Quenching of the Orbital Angular Momentum

In certain materials the magnetic moment of an atom can result from contributions from either orbital or spin angular momentum. In an isolated atom, an electron experiences a centrally symmetric potential. The plane of the classical electron orbit is fixed in space such that L_x, L_y and L_z are constant. Quantum mechanically L^2 and L_z are taken as the constants of motion in a central electric field. In a non-central electric field such as in a crystalline material, the plane of the electron orbit may drift and the angular

momentum components may no longer be constant and may average to zero. When L_z averages to zero the orbital angular momentum is said to be *quenched* and the magnetic moment of the atom is due to the spin angular momentum only.

2.5 Paramagnetism

Paramagnetic materials have a small but positive magnetic susceptibility $\chi > 0$. When an external field is applied to these materials they will develop a magnetisation vector in the same direction as the applied field. Paramagnets do not retain any magnetisation in the absence of an externally applied field because thermal fluctuations are large enough to randomise the spin orientations. Even in the presence of a field the induced magnetisation is considerably smaller than for ferromagnets and other high susceptibility materials as only a small fraction of the spins align with the field.

2.6 The Origins of Ferromagnetism

Ferromagnetic materials have a large magnetic susceptibility and a spontaneous net magnetisation. These effects arise due to a strong interaction between permanent atomic moments, leading to long range ordering in the absence of an external magnetic field. It was quickly realized that dipolar fields were too weak to align the magentisation against thermal agitation. Early attempts to describe this spontaneous alignment introduced an internal (Weiss) field[35] proportional to the magnetisation $\mathbf{B}_w \propto \lambda_w \mathbf{M}$, where λ_w is a constant. This internal field was postulated to be very large in ferromagents and to act to align the magentic moments at temperatures below the characteristic Curie temperature T_C. Above the Curie temperature thermal agitation of the magnetic moments becomes sufficient to overcome the internal field and randomise their alignment, destroying the spontaneous magnetisation. This property allows an estimation of the internal field[36], which for atoms with a moment μ_B the internal field is proportional to

$$\mu_B B_w \propto k_B T_C, \tag{2.8}$$

where k_B is Boltzmann's constant. For Iron $T_C \approx 1000$ K so this field would need to be of the order 10^7 Oe. Weiss could not explain the origins of such a strong field, however later developments in quantum mechanics provided an explanation in the form of the exchange interaction (section 2.7.1).

2.6.1 Band Theory of Ferromagnetism

The first theories of ferromagnetism were based on the Heisenberg model in which it is assumed electrons are localised at the atom. More modern theories consider mobile electrons or holes in unfilled bands, these provide a more realistic description. The Stoner model of ferromagentism[37, 36] treats the conduction electrons as a high density electron gas and Bloch-type wavefunctions[38] are used to treat their interaction with ion cores. Since ferromagnets belong to the Fe group these calculations were made for the electrons and holes of the 3*d* band. This model is based on three assumptions. First,

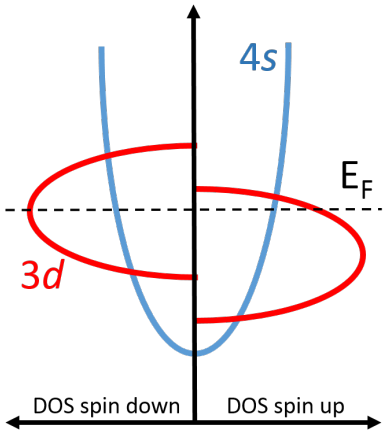

Figure 2.2: Representation of the density of states (DOS) for the 4*s* and 3*d* bands of a ferromagnetic metal showing the spin inbalance due to splitting of the *d* band by the exchange interaction.

the 3*d* band is parabolic around the Fermi level such that the density of states has the parabolic form $C(E)dE = KE^{1/2}dE$. Second, the exchange interaction between electrons can be described by a molecular field $\mathbf{B}_w \propto \lambda_w \mathbf{M}$ so that the energy of an electron with spin parallel or antiparallel to the magnetisation is $E_e = \pm\mu_B\lambda_w M$. Thirdly, the electrons or holes obey Fermi-Dirac statistics. Under these assumptions it is possible to numerically calculate the dependence of M on T[37, 39], which depends on the magnitude of the exchange forces compared to the Fermi energy. Critically this theory can predict values for the magnetic moment of an atom or ion that are a non-integer multiples of μ_B. A phenomena which had been observed experimentally, but previously could not be explained. The origin of the non-integer values of the magnetic moment is the exchange interaction (discussed in section 2.7.1), which causes a shift in the energy of the 3*d* band for electrons of one spin direction relative to that with opposite spin as shown in figure 2.2. If E_F lies within the 3*d* band, then the displacement will lead to

more electrons of the lower-energy spin direction and hence a spontaneous magnet moment in the ground state. This exchange splitting is negligible for the 4*s* electrons but significant for 3*d* electrons. In the case of Ni the sum of the 3*d* and 4*s* electrons is 10, there are approximately 9.4 electrons in the 3*d* band and 0.6 electrons in the 4*s* band[36] and so the saturation magnetisation of Ni is $M_s = 0.6N\mu_B$, where N is the total number of Ni atoms.

2.7 Ferromagnetic Free Energy Contributions

The ground state and dynamic magnetisation of a ferromagnet is determined by the interplay of the contributions to its total free energy. In the lowest energy equilibrium state the torque acting on the magnetisation is zero and the static magnetisation can be described by Brown's differential equation[40]

$$\mathbf{M} \times \mathbf{H}_{eff} = 0, \tag{2.9}$$

where $\mathbf{H}_{eff}$ is the total effective field and is the derivative of the free energy density W w.r.t. the magnetisation

$$\mathbf{H}_{eff} = -\frac{\delta W}{\delta M}. \tag{2.10}$$

The free energy $W = w_{so} + w_{ex} + w_{ze} + w_{ms} + w_0$ contains, in order, contributions from the spin orbit interaction (section 2.7.2), exchange interaction (section 2.7.1), Zeeman interaction (section 2.7.3), magnetostatic interaction (section 2.7.4) and finally a term representing all other contributions to the total free energy.

2.7.1 The Exchange Interaction

The Weiss field phenomenologically explains the spontaneous magnetisation within ferromagnetic materials. The origins of such a large internal field were shown by Heisenberg[41] to be the result of the quantum mechanical exchange interaction. The exchange interaction is the result of the Coulombic interaction energy[42] and the Pauli exclusion principle[43, 44]. A full mathematical quantum mechanical description of this interaction is beyond the scope of this thesis but can be found in reference [38] and the references therein.

The concept of direct exchange between electron spins is often explained using the Heitler-London[45] model of the hydrogen molecule. In this model the two hydrogen electrons exist in states described by their spatial coordinates $\mathbf{r}_i$ and spin state $\mathbf{s}_i$ and

so the total eigenfunction for a two-electron system is the product of the individual electron wavefunctions

$$\psi(\mathbf{a},\mathbf{b}) = \psi(\mathbf{r}_1,\mathbf{s}_1;\mathbf{r}_2,\mathbf{s}_2) = \psi_1(\mathbf{a})\psi_2(\mathbf{b}). \tag{2.11}$$

As the electrons are indistinguishable, this function must be equivalent to $\psi_2(\mathbf{a})\psi_1(\mathbf{b})$, when the electron position (a,b) has been exchanged. A solution must therefore be of the form

$$\psi(\mathbf{a},\mathbf{b}) = \frac{1}{\sqrt{2}}[\psi_1(\mathbf{a})\psi_2(\mathbf{b}) \pm \psi_2(\mathbf{a})\psi_1(\mathbf{b})], \tag{2.12}$$

where the plus symbol represents a symmetric wave function and the minus sign represents an antisymmetric wave function. Upon exchange of electrons symmetric functions remain unchanged ($\psi_{sym}(\mathbf{a},\mathbf{b}) = \psi_{sym}(\mathbf{b},\mathbf{a})$) however antisymmetric functions must change sign ($\psi_{as}(\mathbf{a},\mathbf{b}) = -\psi_{as}(\mathbf{b},\mathbf{a})$). In the case of electrons the total wave function must be antisymmetric to satisfy the Pauli exclusion principle, so upon the exchange of two electrons the sign of the total wave function must reverse. This can be achieved one of in two ways. Either the spatial part is symmetric and the spin part antisymmetric, known as the *singlet state*, or the spatial part is antisymmetric and the spin part symmetric, known as the *triplet state*. The electrostatic interaction Hamiltonian $\hat{H}_{12}$ for the two atoms within the H_2 molecule is given by

$$\hat{H}_{12} = \frac{e^2}{r_{ab}} + \frac{e^2}{r_{12}} + \frac{e^2}{r_{1b}} + \frac{e^2}{r_{2a}}, \tag{2.13}$$

where r_{ab} is the distance between nuclei, r_{12} is the distance between the electrons and r_{1b} and r_{2a} are the distances between a given nucleus and the electron of the other atom. By considering $\hat{H}_{12}$ as a perturbation of the two-electron system (as in [38]) the energies of the singlet E_s and triplet E_t states can be calculated as

$$E_s = A^2(K_{12} + J_{12}) \tag{2.14}$$

and

$$E_t = B^2(K_{12} - J_{12}), \tag{2.15}$$

where A and B are normalising factors, K_{12} is the average Coulombic interaction energy given by

$$K_{12} = \int \phi_a(r_1)^2 H_{12} \phi_b(r_2)^2 d^3r_1 d^3r_2, \tag{2.16}$$

and J_{12} is the exchange integral

$$J_{12} = \int \phi_a^*(r_1)\phi_b^*(r_2)H_{12}\phi_b(r_1)\phi_a(r_2)d^3r_1d^3r_2. \tag{2.17}$$

The system tends to the lowest energy state spin alignment which occurs when J_{12} is positive and corresponds to a net magnetic moment. In the H_2 molecule J_{12} is negative, so spins are antiparallel and there is no net magnetic moment. Qualitative analysis demonstrates that J_{12} is positive when interatomic spacing r_{ab} is large compared to the electron orbital radius[46] and is therefore most likely for d and f orbitals. It should be noted that only the case of *direct exchange*, the interaction between overlapping orbitals, has been considered here. In some ferromagnetic materials, such as the rare earth ferromagnets, the $4f$ electrons are strongly localised and do not overlap. In such cases a form of *indirect exchange* must exist whereby the interaction is mediated by some other means such as superexchange in some antiferromagnetic oxides or the conduction electrons in metals.

2.7.2 Spin-Orbit (SO) Interaction

The spin and orbital moments can interact via the spin-orbit (SO) interaction (or spin-orbit coupling). The SO interaction couples the spin-system to the lattice, allowing energy and angular momentum exchange. This interaction describes the coupling of the orbital angular momentum $\mathbf{l}$ to the spin angular momentum $\mathbf{s}$ which gives a new total angular momentum $\mathbf{j} = \mathbf{l} + \mathbf{s}$.

The SO interaction can be described in semi-classical terms (a quantum mechanical formulation of this interaction is beyond the scope of this thesis). Following the derivation in reference [47], the Bohr model assumes that an electron orbits the nucleus which is at rest in the laboratory frame. In this frame the equation of motion for the electron with rest mass m and charge e is

$$\frac{d}{dt}(m\mathbf{v}) = -\frac{Ze^2\mathbf{r}}{r^3}, \tag{2.18}$$

where $\mathbf{v}$ is the velocity of the electron, and Z is the charge of the nucleus. Equation 2.18 yields the well known result

$$mv^2 = -\frac{Ze^2}{r}, \tag{2.19}$$

from which the total energy of the system can be determined

$$U = \frac{mv^2}{2} - \frac{Ze^2}{r} = -\frac{Ze^2}{2r}. \tag{2.20}$$

The radius of the electron's orbit can be found by the addition of the second Bohr postulate to the classical treatment

$$r = \frac{n\hbar}{mv}, \tag{2.21}$$

where n is the principal quantum number. Combining equations 2.20 and 2.21 yields

$$U = -\frac{Ze^2}{2r_n}, \tag{2.22}$$

where $r_n = n^2 r_B$ and $r_B = \hbar^2/mZe^2$ is the Bohr radius. In the classical treatment of spin-orbit coupling, its contribution is considered as a perturbation to the energy in equation 2.22, with the radius of the electrons orbit fixed. Following this approach the energy of the spin-orbit coupling (U_{so}) can be expressed as the sum

$$U_{so} = U_P + U_T, \tag{2.23}$$

where U_P is the additional potential energy of the moment of the electron in an electromagnetic field and the term U_T, first found by Thomas, emerges due to the slow precession of the electron's spin (Thomas precession). In the electron rest frame the apparent circular motion of the nucleus induces a magnetic field

$$\mathbf{B} = \frac{\mathbf{E} \times \mathbf{v}}{c^2} = \frac{Ze}{c^2 r^3}(\mathbf{r} \times \mathbf{v}), \tag{2.24}$$

at the location of the electron, combining equations 2.18 and 2.23 yields

$$\mathbf{B} = -\frac{1}{ec}\left(\frac{d}{dt}(m\mathbf{v} \times \mathbf{v})\right). \tag{2.25}$$

With the magnetic moment of the electron ($\boldsymbol{\mu}$) expressed as

$$\boldsymbol{\mu} = \frac{ge}{2m}\mathbf{s} = \frac{e}{m}\mathbf{s}, \tag{2.26}$$

and g set equal to 2 then in the proper electron frame the additional potential energy is

equal to

$$U_P = -\boldsymbol{\mu} \cdot \mathbf{B}, \tag{2.27}$$

which causes the Larmor precession of the electron's magnetic moment. A derivation of U_T can be found in reference [47] and has close analogy to equation 2.27. The energy associated with the precession of the electron's spin is

$$U_T = \frac{\boldsymbol{\mu} \cdot \mathbf{B}}{2}. \tag{2.28}$$

The total energy of the spin-orbit coupling becomes

$$U_{so} = U_P + U_T = -\frac{\boldsymbol{\mu} \cdot \mathbf{B}}{2}. \tag{2.29}$$

The terms in equation 2.29 arise respectively from the electron's spin and orbital angular momentum and so

$$U_{so} \propto \mathbf{l}.\mathbf{s}. \tag{2.30}$$

The spin and hence $\mathbf{m}_s$ has two possible equilibrium orientations with respect to the effective field generated by $\mathbf{l}$, the parallel orientation is a lower energy state and the antiparallel is the higher energy state. The energy represented by equation 2.30 corresponds to the energy difference between the spin $\mathbf{s}$ oriented parallel or antiparallel states. If the orbital moment prefers to lie along a specific lattice direction then the energy represents the difference between the energetically favourable and energetically unfavourable spin directions and therefore corresponds to the magnetocrystalline anisotropy energy. In this way the spin-orbit interaction gives rise to the magnetocrystalline anisotropy in solids (section 2.8). It is generally believed that SO coupling varies as Z^4[48, 49], implying that SO coupling is most important in heavy elements, and related effects such as the spin Hall effect will be larger in heavy elements.

2.7.3 Zeeman Energy

The Zeeman energy is the potential energy associated with permanent atomic moments in an applied field and is given by

$$E_{ze} = -\int_V \mathbf{M}.\mathbf{H}_{ext} dV, \tag{2.31}$$

where $\mathbf{H}_{ext}$ is the external field and the integral is performed over the volume of the body. In order to minimise this energy ferromagnetic moments will align with the

external field, and the magnetisation will be maximised.

2.7.4 Magnetostatic Energy

There is a long range interaction energy associated with the interaction of atomic moments with the magnetostatic fields of other spontaneously magnetised regions of the material. This energy has the form

$$E_{ms} = -\frac{1}{2}\int_V \mathbf{H}_d.\mathbf{M}dV, \tag{2.32}$$

where $\mathbf{H}_d$ is the demagnetising field. The strength of the magnetostatic interaction is several orders of magnitude less than the exchange interaction (section 2.7.1), which is short range and isotropic, but acts at a far longer range and is also sensitive to the shape of the material. The competition of these short and long range interactions can cause preferential magnetisation alignment along a particular axis, and can also lead to the formation of magnetic domains.

2.8 Magnetic Anisotropy

Experimentally the magnetisation $\mathbf{M}$ tends to lie along one of several energetically favourable axes, known as easy axes, in a magnetic solid. Rotation of the magnetisation away from the easy axes requires energy and so the magnetic anisotropy is defined as the energy required to rotate the magnetisation to the hard direction. The magnetic anisotropy can be represented as an effective magnetic field $\mathbf{H}_{ani}$ which must be parallel to the easy axis but change sign when $\mathbf{M}$ changes sign. If $\mathbf{M}$ deviates from the easy axis $\mathbf{H}_{ani}$ induces a precession of $\mathbf{M}$ around the easy axis until the damping of the precession forces $\mathbf{M}$ back to the easy axis direction. For the simple case of uniaxial anisotropy the generating torque is equal to $\mathbf{M} \times \mathbf{H}_{ani} = MH_{ani}\sin\phi$ (where ϕ is the angle between $\mathbf{M}$ and $\mathbf{H}_{ani}$).

The easy axis direction is determined by competition between different types of anisotropy. In the following section three main types, magnetocrystalline anisotropy, shape anisotropy and surface anisotropy are discussed.

2.8.1 Dipole-Dipole Interaction

Magnetic dipole-dipole interaction refers to the direct interaction between two magnetic dipoles. This dipole-dipole interaction between magnetic moments $\mathbf{m}_s$ at different

atomic positions in the lattice is given, to first order, by the summation over all atomic dipoles $\mathbf{m}_i$ and $\mathbf{m}_j$ as

$$E_{dip-dip} = -\frac{1}{2\pi\mu_0}\sum_{i\neq j}\frac{1}{r_{ij}^3}\left[\mathbf{m}_i\cdot\mathbf{m}_j - 3\frac{(\mathbf{r}_{ij}\cdot\mathbf{m}_i)(\mathbf{r}_{ij}\cdot\mathbf{m}_j)}{r_{ij}^2}\right], \tag{2.33}$$

whose absolute values are equal to the spin moment $\mathbf{m}_s$, while $\mathbf{r}_{ij}$ is the vector between the two moments. The energy of the exchange interaction (section 2.7.1) is minimised when the atomic moments align parallel along the internuclear axis. In thin films the internuclear axis is typically preferentially oriented in-plane (although for some materials such as the Ta/CoFeB/MgO stacks in chapters 6, 7 and 8 careful engineering can produce thin films with a perpendicular magnetic anisotropy), and $E_{dip-dip}$ is smallest for an in-plane direction.

The preferential, or *easy* magnetisation axis of a sample is determined by a competition between different types of anisotropy including the magneto-crystalline, shape and surface anisotropies.

2.8.2 Shape Anisotropy

The shape anisotropy expresses the preference for the magnetisation to lie along a particular geometric axis of a magnetic sample. This anisotropy is mediated by the dipolar interaction and is long range and dependent on the shape of the sample. In the simple case of an ellipsoid (figure 2.3) both the magnetisation and demagnetising field are uniform and the demagnetising factors are directionally dependent constants. The demagnetising field is therefore different for different orientations of the magnetisation and the magnetostatic (or shape anisotropy) energy is only minimised when the magnetisation lies along the major axis of the ellipsoid.

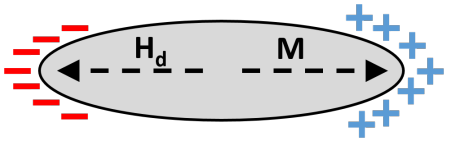

Figure 2.3: Surface charges on an ellipsoidal magnetic particle with a uniform magnetisation **M** in an external field **H**.

For thin films the shape anisotropy tends to dominate and the easy magnetisation axis tends to lie in-plane. For certain structures other forms of anisotropy can dominate, and the magnetisation can favour a crystallographic axis, as in the case of the TiO_2/CrO_2

films discussed in section 5, or even a perpendicular alignment, as in the case of the Ta/CoMnGe/MgO samples discussed in sections 6 and 8. These effects occur due to an increase in the contributions of magnetocrystalline and surface anisotropies.

2.8.3 Magnetocrystalline Anisotropy

A magnetocrystalline anisotropy is induced by an anisotropic crystal structure. The spin-orbit interaction induces a small orbital moment which couples the total (spin +orbital) moments of orbiting electrons to the crystal lattice. Electron orbits are therefore linked to the symmetry of the crystal lattice and the energy of the electron spin system depends on the direction of the magnetisation relative to the crystal axis. This leads to preferred magnetisation alignment along or between crystallographic axes and the magnetocrystalline anisotropy energy corresponds to the largest difference in the spin-orbit energy when the sample is magnetised along two different crystallographic directions. In practice, due to the complexity of electronic band structure calculations[50], an empirical constant K_u is used to describe the form of this anisotropy, which can be derived from ferromagnetic resonance (FMR) or magnetisation curve measurements. The magnetocrystalline anisotropy and magneto-elastic (or strain) anisotropy are often distinguished from each other, though both arise from the anisotropy of the atomic structure and bonding along with the spin-orbit interaction. As the spin moments are coupled to the lattice, if the lattice is changed by strain the distances between magnetic atoms is altered and hence the interaction energies are changed producing magneto-elastic anisotropy. Strain in thin films can be induced by specific growth conditions such as epitaxial growth on a crystal substrate as in the case of the TiO_2/CrO_2 films discussed in section 5, the small lattice mismatch between the TiO_2 and CrO_2 can induce a magneto-elastic anisotropy.

2.8.4 Surface Anisotropy

The behaviour of a magnetic material at its surface can be markedly different to that in the bulk due to the reduction in microscopic symmetry. Whilst the magnetic moment in a bulk film has interactions dominated by its nearest neighbours (in accordance with equation 2.33) at the surface the nearest neighbours may be another material, or if it is an external surface, not present at all. The exchange energy of a surface moment and its nearest neighbours therefore cannot be the same as in the bulk of the material. For sufficiently thin films the reduction of the 'bulk portion' of the film can make the surface anisotropy the dominant contribution (an effect which leads to

the perpendicular magnetic anisotropy (PMA) exhibited by the films in sections 6 and 8). Again due to the complexity of electronic band structure calculation an empirical surface anisotropy constant K_s is often introduced.

2.9 Magnetic Domains

A magnetic domain structure is specified if the vector field of magnetic polarisation $\mathbf{J}(\mathbf{r})$ is known, where $\mathbf{r}$ is the position vector of the sample and $\mathbf{M} = \mathbf{J}/\mu_0$. The magnetic polarisation is connected with the magnetic flux density $\mathbf{B}$ and the magnetic field $\mathbf{H}$ by the relation

$$\mathbf{B} = \mu_0\mathbf{H} + \mathbf{J}. \tag{2.34}$$

Maxwell's equation $\nabla\mathbf{B} = 0$ yields

$$\mu_0\nabla\mathbf{H} = -\nabla\mathbf{J} \tag{2.35}$$

which means that any divergence of $\mathbf{J}(\mathbf{r})$ creates a magnetic field. If no external field is present then $\mathbf{H}$ is just the stray field. As Maxwell's equations state $\mathbf{B}$ must be continuous, $\mathbf{H}$ must be discontinuous at surfaces with normal components of $\mathbf{M}$ (ends of finite samples). In a magnetic sample the magnetic north pole acts as a source and the south pole acts as a sink, and $\mathbf{H}$ points in the opposite direction *inside* the sample as in figure 2.4.

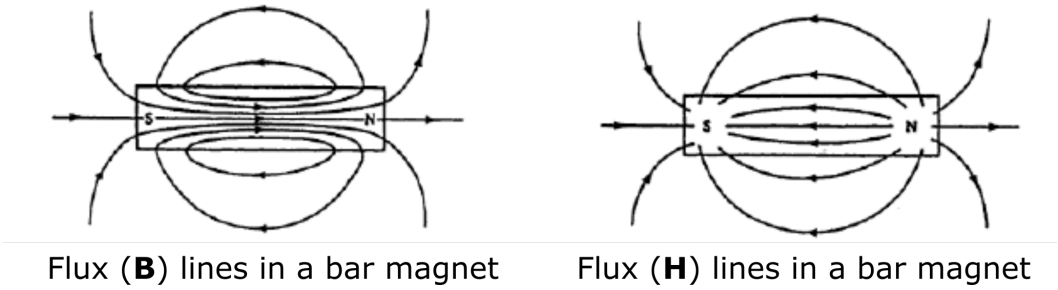

Figure 2.4: $\mathbf{B}$ and $\mathbf{H}$ in a bar magnet.

The flux closing path of least energy between north and south poles is through the sample and inside $\mathbf{H}$ opposes $\mathbf{B}$ and so the demagnetising field $\mathbf{H}_d$ opposes $\mathbf{M}$ that created the poles in the first place.

As discussed in section 2.7 the magnetic state of a ferromagnet is defined by competing energies. The formation of domains can minimise the energy of the system. At any

internal or external surface of a uniformly magnetised body, there is a discontinuous change in the component of **M** normal to the surface, this can be envisaged as a source of 'free poles'. These are magnetic (north or south) poles which are not compensated by

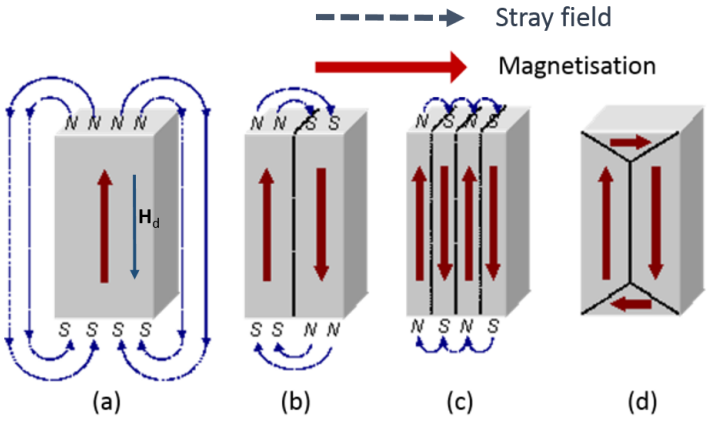

Figure 2.5: The break up of a single domain (a) structure into a two domain (b), four domain (c) and closure domain structure (d). Figure adapted from [51].

poles of the opposite kind in the immediate vicinity. Reduction of the stray field energy favours a change in the magnetisation such that the poles disappear. Considering a thin film in a single domain state, shown in figure 2.5.(a) the magnetostatic energy is large due to the presence of magnetic free poles generating a large stray magnetic field outside of the sample in which energy is stored. By breaking the magnetisation into two domains as shown in figure 2.5.(b) the magnetostatic energy has been reduced by half. However there is an anisotropy energy penalty associated with the formation of a domain (section 2.9.1). In general, increasing the number of domains reduces the magnetostatic energy between them by 1/N. The division into domains continues whilst the reduction in magnetostatic energy is greater than the energy penalty. Materials without a strong uniaxial anisotropy can form closure domain states (figure 2.5.(d)) where the magnetostatic energy is reduced to zero.

2.9.1 Domain walls

While the multi-domain state can minimise the magnetostatic energy, an abrupt change of the magnetisation is unfavourable as the positioning of two spins oriented in the opposite direction in each-other's proximity results in a large exchange energy penalty. Instead a transition region in which the magnetisation gradually changes is formed.

Whilst initially it may seem energetically favourable to have infinitely thick domain walls to minimise the exchange energy, however the magnetic anisotropy energy increases when spins are not orientated in the direction of the easy axis. This means the domain wall width δ is determined by the balance between the exchange energy and the magnetic anisotropy. The thickness of the wall $\delta \propto \sqrt{J/K_u}$ so a strong magnetocrys-

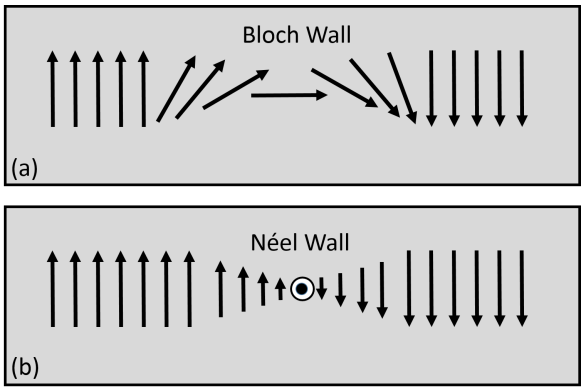

Figure 2.6: Examples of (a) Bloch and (b) Néel domain walls.

talline anisotropy (K_u) favours a narrow wall and a larger exchange integral interaction (J) favours a wider wall. There are generally two types of domain wall in thin films; Bloch walls (figure 2.6.(a)) where the magnetisation rotates out of the x-y plane and Néel walls (figure 2.6.(b)) in which the magnetisation rotates within the x-y plane from one domain to another.

2.10 The Hysteresis Loop

A great deal of information about the magnetic properties of a material can be learned by studying its hysteresis curve (or hysteresis loop); the relationship between the induced magnetic flux density **B** (defined as $\mathbf{B} = \mu_0(\mathbf{H} + \mathbf{M})$ in SI units and $\mathbf{B} = \mathbf{H} + 4\pi\mathbf{M}$ in CGS units, where **M** is the sample magnetisation) and **H** field Care must be taken to distinguish between M-H (where the M curve becomes a straight line with zero slope after saturation) and B-H hysteresis loops (which continue to increase)[52]. In this thesis hysteresis loops are typically measured by Kerr rotation which reflects **M**, so here we focus on the M-H curve.

A typical magnetisation curve (oa) and hysteresis loop (abcdefa) for a ferromagnetic material is shown in figure 2.7. For a sample which is initially demagnetised (i.e. the domains are configured so the net magnetisation is zero) the magnetisation will follow

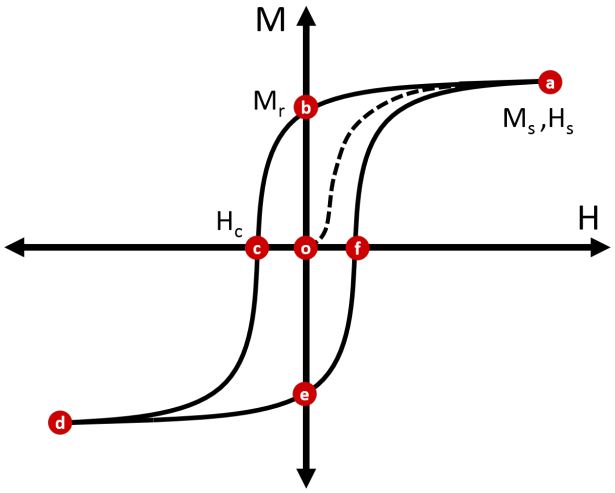

Figure 2.7: A typical magnetisation curve *oa* and hysteresis loop *abcdefa* for a ferromagnetic material.

the dashed line *oa*. As the applied field is increased there is an increased alignment of the domains to **H** until at the saturation field (H_s), domains are fully aligned with the field and the magnetisation is described as saturated (M_s) point *a* in figure 2.7. When the field is reduced the variation of the magnetisation may not follow the path *ao* due to irreversible magnetisation processes.

Typically the magnetisation will follow a curve like *ab*. At *b* when $\mathbf{H} = 0$ the sample can still posses a non-zero magnetisation known as remanent magnetisation M_r. When the field is reversed the magnetisation continuous to reduce until it reaches zero at *c*, which is known as the coercive field (H_c). As the field is further increased the sample becomes magnetised in the opposite direction until reaching -M_s relative to *a* at point *d*. When the field is reversed the magnetisation processes *abcd* are reversed along *defa*.

2.11 Magnetic Precession

The interactions discussed thus far largely describe the behaviour of a magnetic materials in the absence of a time varying external field or excitation. In the following sections the dynamic behaviour of magnetic materials in response to some possible external stimuli are discussed.

If a dipole of moment **m** is placed in a uniform film then the field exerts an equal and opposite torque $\boldsymbol{\tau}$ on each pole. The net force is therefore zero but the dipole

experiences a torque given by

$$\boldsymbol{\tau} = \mathbf{m} \times \mathbf{H}. \tag{2.36}$$

The action of a uniform field $\mathbf{H}$ is thus to tend to rotate the dipole until it is parallel to $\mathbf{H}$. This action arises as the dipole is assumed to be a rigid body, capable of only rotating about an axis. In order to discuss the dynamical behaviour of the dipole its origins must first be considered. If it is assumed the dipole moment $\mathbf{m}$ arises from the motion of an electron in circular orbit with radius r, charge e and period of rotation T then the moving electron can be considered essentially as a current flowing in a wire that coincides with the orbit. It is then possible to derive[36] an expression for $\mathbf{m}$ as

$$\mathbf{m} = \frac{e}{2m_e c}\mathbf{L}, \tag{2.37}$$

where m_e is the electrons mass and $\mathbf{L}$ its angular momentum. Historically the relationship between the $\mathbf{m}$ and $\mathbf{L}$ is written in terms of the gyromagnetic ratio γ, according to $\mathbf{m} = \gamma\mathbf{L}$ where

$$\gamma = qg\mu_0/2m_e. \tag{2.38}$$

The sign of γ depends on the charge q of the particle and so is negative in the case of an electron as $q = -e$. Since the γ is negative $\mathbf{m}$ and $\mathbf{L}$ are anti-parallel. Combining equations 2.36 and 2.37 together with Newtons law for angular momentum $d\mathbf{L}/dt = \boldsymbol{\tau}$ gives

$$\frac{d\mathbf{L}}{dt} = \boldsymbol{\tau} = \mathbf{m} \times \mathbf{H}. \tag{2.39}$$

The equation of motion of a magnetic moment $\mathbf{m}$ in a field $\mathbf{H}$ can be found by substituting $\mathbf{m} = \gamma\ \mathbf{L}$ into equation 2.39 as

$$\frac{d\mathbf{m}}{dt} = \gamma[\mathbf{m} \times \mathbf{H}]. \tag{2.40}$$

This equation represents the equation of motion of a vector $\mathbf{m}$ precessing with an angular frequency ω which is known as the Larmor precession frequency. This is an addition to the motion possessed by the electron before the field is applied. The Lamour precession frequency can be derived from the equation of motion. According to equation 2.39, the change $d\mathbf{m}$ of the magnetic moment is perpendicular to both $\mathbf{m}$ and $\mathbf{H}$. Therefore, $\mathbf{m}$ can only precess around $\mathbf{H}$. If $m_\perp$ is the component of $\mathbf{m}$ perpendicular to $\mathbf{H}$, then $d\mathbf{m} = m_\perp d\phi$ where $d\phi$ is the angle by which $\mathbf{m}$ precesses in the time interval dt. This yields $d\mathbf{m}/dt = \omega m_\perp$ and then from equation 2.40 $d\mathbf{m}/dt = \gamma m_\perp H$ and so $\omega = \gamma H$.

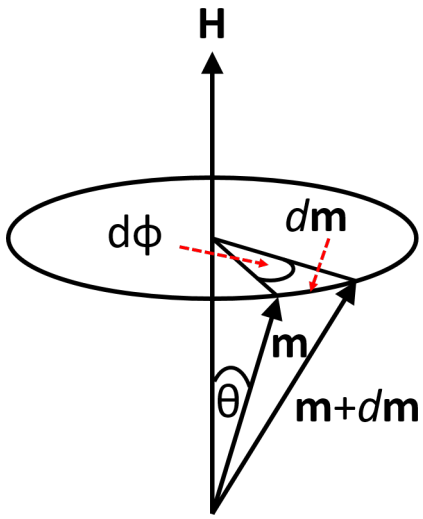

Figure 2.8: Magnetic moment **m** of an electron precessing about a field **H**

In this model the angle θ between **H** and **m** does not change during precession and hence the energy $E = -\mathbf{m}.\mathbf{H}$ is constant and not a minimum. This contradicts experimental evidence that tells us the magnetic moment eventually moves into the field direction. The precessional torque $\boldsymbol{\tau} = \mathbf{m} \times \mathbf{H}$ alone cannot accomplish this as it is perpendicular to **H**, so an additional damping torque $\boldsymbol{\tau}_d$ is introduced which is perpendicular to both **m** and $\boldsymbol{\tau}$ expressed as

$$\boldsymbol{\tau}_d = C\left[\mathbf{m} \times \frac{d\mathbf{m}}{dt}\right] \tag{2.41}$$

where C is a purely phenomenological constant of proportionality encompassing material specific dissipative phenomena. A realistic equation of motion for **m** is the *Landau-Lifshitz-Gilbert (LLG)* equation[53] typically written

$$\frac{d\mathbf{m}}{dt} = \gamma[\mathbf{m} \times \mathbf{H}_{eff}] + \frac{\alpha}{m}\left[\mathbf{m} \times \frac{d\mathbf{m}}{dt}\right] \tag{2.42}$$

where $\mathbf{H}_{eff}$ is the effective magnetic field including the external, demagnetisation, and the crystal anisotropy fields and α is a phenomenological constant, the so-called damping parameter including unspecified dissipitative phenomena (typically governed by spin-orbit interactions[54] in the $3d$ transition metals). The first term on the right hand side of equation 2.42 represents the undamped precession at a fixed θ of **m** about $\mathbf{H}_{eff}$.

The second term represents the damping introduced by Gilbert[53] and describes the change of **m** due to the damping torque $\boldsymbol{\tau}_d$. With this damping present the precession spirals down to a time independent magnetization along the field direction on a time scale of $1/\alpha\omega$.

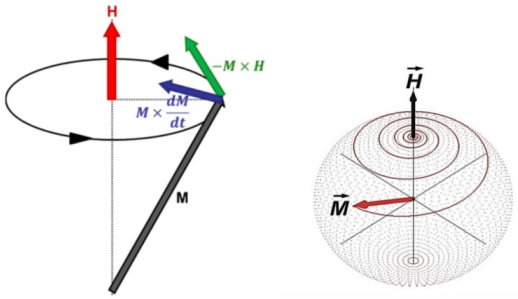

Figure 2.9: Precessional motion of the magnetic moment **m** with a positive damping parameter α showing **m** spirals into the direction of the field **H**. (Figure adapted from [55])

As shown in figure 2.9, during the damping the magnetisation spirals into the field direction. This process corresponds to a change in angular momentum which, according to the laws of conservation, must be transferred to another reservoir. Initially angular momentum may be transferred in the spin system itself by excitation of spin waves, but ultimately the angular momentum is transferred to the lattice. The LLG equation describes the motion of a moment **m** with a constant absolute value, so the endpoint moves in a sphere (figure 2.9). When this equation is applied to describe the magnetisation of **M** of a body it is implicitly assumed that $\mathbf{M} = \mathbf{m}/V$ where V is the volume containing **m** which remains constant. This 'macrospin approximation', in which the spins in the entire body are strongly coupled in parallel, may break down if the individual spins dephase over the time-scale of the excitation. In this case the magnitude of **m** changes with time and the LLG equation is no longer appropriate.

2.12 Magnetic Resonance

Magnetic resonance is a powerful tool which can be used to study the dynamics of a magnetic moment **m** in an external magnetic field **H**. In magnetic resonance experiments the damping described in section 2.11 is countered by the application of a time varying field such that the precession angle θ remains constant. Several different forms of magnetic resonance measurement exist including electron paramagnetic

resonance (EPR)[56], nuclear magnetic resonance (NMR)[57] and ferromagnetic resonance (FMR). The experiments conducted in this work focus only on FMR where the time varying field is of the order 10 GHz and the so the notation $\mathbf{h}_{rf}$ is used for this field. It should be noted that the dynamics described here only hold true for nanoscopic thin films. In bulk metals $\mathbf{h}_{rf}$ cannot penetrate due to the generation of eddy currents. Typical penetration or 'skin depths' of the magnetic field at Gigahertz frequencies are of the order 0.1-1 μm so for films with thickness small compared to the skin depth, here the macrospin approximation is valid and it is assumed the magnetization precesses as a whole around the sum of all fields.

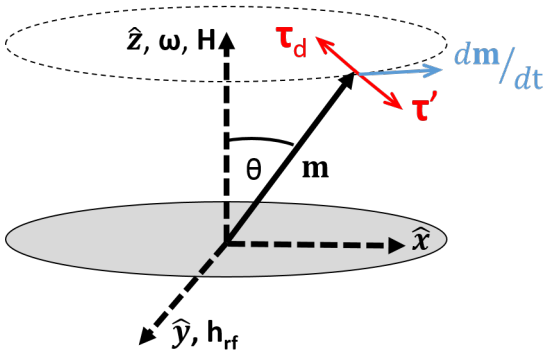

Figure 2.10: Fields and torques involved for a magnetic moment **m** undergoing magnetic resonance about a constant field **H** in the $\hat{\mathbf{z}}$ direction due to a time varying field $\mathbf{h}_{rf}$ in the $\hat{\mathbf{x}}$-$\hat{\mathbf{y}}$ plane.

The geometry for FMR is shown in figure 2.10. Here a constant magnetic field $\mathbf{H} \parallel \hat{\mathbf{z}}$ causes **m** to precess about $\hat{\mathbf{z}}$ with $d\mathbf{m}/dt$ parallel to the $\hat{\mathbf{x}}$-$\hat{\mathbf{y}}$ plane. As discussed, this precession generates a damping torque $\boldsymbol{\tau}_d$ which acts to decrease the precession angle θ and align **m** with **H**. When a second weaker field $\mathbf{h}_{rf} \perp \mathbf{m}$ is applied in the $\hat{\mathbf{x}}$-$\hat{\mathbf{y}}$ plane a second torque $\boldsymbol{\tau}'$ is generated which acts in the opposite direction to $\boldsymbol{\tau}_d$. The torque $\boldsymbol{\tau}'$ causes **m** to increase its angle θ with the $\hat{\mathbf{z}}$ axis, driving **m** away from **H**. The resonance condition consists of balancing the characteristic damping torque $\boldsymbol{\tau}_d$ with the torque generated by $\mathbf{h}_{rf}$, $\boldsymbol{\tau}'$, so that θ remains constant ($\theta \approx 1°$). This condition is met when the field $\mathbf{h}_{rf}$ and **m** rotate together about **H** at the Larmor frequency inducing a steady state precession.

In FMR measurements the width of the resonance is a measure of the damping of the precessional motion. In the simplified case of an electron in vacuum, no damping is present and the form of the dynamic susceptibility tends to a δ function. In solids the damping term broadens the δ function into a characteristic lineshape of finite width,

meaning that the FMR linewidth is proportional to the strength of the of damping (discussed further in section 4.6).

In this work $\mathbf{h}_{rf}$ was typically applied to samples by means of a waveguide as discussed further in section 4.7.1.

2.13 Electron Transport and Spin Currents

Many modern magnetic devices rely on transport of electrons and spins. An area of considerable interest in this field is the spin-dependent transport that arises during current flow within a ferromagnet (FM), current flow between a ferromagnet and non-magnetic metal (NM), and from the injection of a spin-polarised current into a ferromagnet.

In the case of current flow within a FM it is necessary to deal with both charge and spin. When discussing spin-polarised electron transport it is useful to distinguish several different lengths, the transport (momentum exchange) mean-free-path λ_t, the spin-flip length λ_{sf} and the spin-diffusion length l_{sf}. Qualitatively, electrons are pictured as moving ballistically between collisions, but making many collisions as they traverse a sample (diffusive transport). λ_t is the mean distance between collisions of all kinds (spin-conserving and spin-flipping). λ_{sf} is the mean distance between spin-flipping collisions (the distance in the direction of electron flow between spin-flip events). l_{sf} is the mean distance that electrons diffuse between spin flipping collisions (the straight line distance between spin-flip events)[58].

As a FM contains two species of particle, namely the majority and minority spin electrons, conductivity in such materials can be described in terms of two largely independent conduction channels. The probability of spin-flip scattering processes in metals is normally small compared to the probability of spin-conserving processes meaning there is no mixing of the majority and minority carriers and conduction occurs in parallel between the two spin channels[59]. This is a good approximation as λ_{sf} is typically about ten times larger than the (spin averaged) λ_t[60]).

In ferromagnets the band structure is generally exchange split (section 2.7.1) at the Fermi energy and, as scattering rates are proportional to the density of states, the scattering rate, and therefore conductivities are different for spin-up and spin-down electrons and can be defined as

$$\sigma_{FM}^{\uparrow} = \alpha_s \sigma_{FM} \text{ and } \sigma_{FM}^{\downarrow} = (1 - \alpha_s)\sigma_{FM}, \tag{2.43}$$

where here the dimensionless factor $0 \leq \alpha_s \leq 1$ accounts for the conduction asymmetry in the FM. A NM is described by $\alpha_s = 0.5$, for all other cases α_s describes a FM, and the special case $\alpha_s = 1$ corresponds to a *half metallic ferromagnet* in which only one spin state is present at the Fermi level. This is a principle in the important phenomenon of giant magnetoresistance (GMR)[38].

In understanding transport at a FM/NM interface it is useful to describe the spin imbalance in the FM in terms of the thermodynamic *chemical potential*. When no current flows perpendicular to the FM/NM interface the chemical potential across the interface will be constant across the interface as Fermi-levels of the two materials will have adjusted to the same value, i.e. the chemical potential μ_0 will be constant across the interface. The chemical potential for up spins ($\mu^{\uparrow}$) will be equal to the one for down spins ($\mu^{\downarrow}$), i.e. $\mu^{\uparrow} = \mu^{\downarrow}$, and $\mu_0 = (\mu^{\uparrow} + \mu^{\downarrow})/2$.

If a current of density j flows from FM to NM, if x is taken as the current flow direction perpendicular to the interface then

$$\frac{\partial \mu_0}{\partial x} = -\frac{e}{\sigma} j, \tag{2.44}$$

where $-e$ is the electron charge and σ the total conductivity determined by the conductivities of both the spin-up and spin-down electrons $\sigma = \sigma^{\uparrow} + \sigma^{\downarrow}$. Charge neutrality leads to $j = const.$ across the interface. Ignoring the existence of spins μ_0 is a straight line with a change in slope at the interface due to the change in σ between FM and N. However when the spin is considered this slope is modified. n accordance with equation 2.43 the FM has different conductivities for the spin-up and spin-down channels. The asymmetry of conduction for each spin channel leads to asymmetric currents. As transitions between the two spin channels are rare in NMs it takes time, or distance for the current in NM to reach spin equilibrium. This leads to a voltage drop at the interface known as the spin accumulation voltage V_{AS} which can be thought of as the jump in the spin averaged chemical potential at the FM-NM interface proportional to $\mu^{\uparrow} - \mu^{\downarrow}$ (full derivation in [38]), this is illustrated in figure 2.11.

This voltage decreases away from the interface, quantitatively this decrease can be calculated from the spin diffusion equation, a differential equation governing the currents in the two spin channels. A full derivation of this equation can be found in [38] and is obtained by investigating the dependence of the density of surplus spins $n^{\uparrow}(x,t) - n^{\downarrow}(x,t)$ produced by the current as a function of the distance x from the

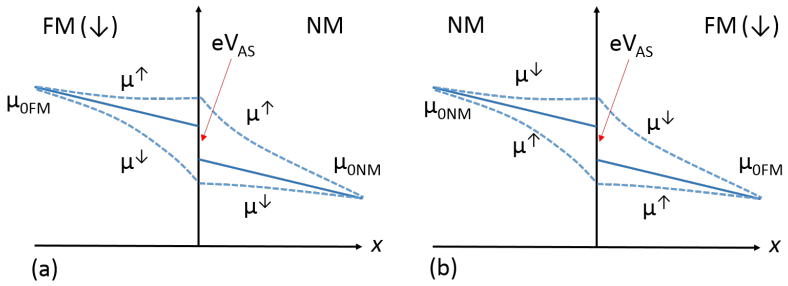

Figure 2.11: The majority ($\mu^{\uparrow}$) and minority ($\mu^{\downarrow}$) chemical potentials at a FM/NM interface with a constant current density flowing in the x direction, with $\alpha_s > 0.5$. The spin averaged chemical potentials are shown as μ_{0FM} for the FM and μ_{0NM} for the NM. The spin accumulation potential is given by $eV_{AS} = \mu_{0FM}(0) - \mu_{0NM}(0)$.

interface. The steady state solution is given by

$$\mu^{\uparrow} - \mu^{\downarrow} = [\mu^{\uparrow}(0) - \mu^{\downarrow}(0)]e^{-x/l_{sf}}, \tag{2.45}$$

where l_{sf} is given by

$$l_{sf} = \sqrt{\beta_D \tau_{se}}, \tag{2.46}$$

where τ_{se} is the characteristic equilibrium time and β_D is the diffusion constant (with dimension area/time) equal to $1/3\nu_f\lambda_t$ where ν_f is the Fermi velocity.

In NMs, τ_{se} is dominated by spin-dephasing processes due to spin-orbit coupling in Coulomb scattering processes[61] with atoms and so is related to the transverse relaxation time in magnetic resonance[62]. As an electron travels through a sample it will experience different effective magnetic fields and along any given axis this leads to spin randomization with equal spin up and down probabilities. In such processes the angular momentum is transferred to the lattice atoms and so scattering may be enhanced by heavier atoms with large spin-orbit interactions and also by the addition of paramagnetic impurities (which lead to additional exchange scattering).

2.13.1 Giant Magnetoresistance (GMR)

The potential drop at the interface between between FM and NM leads to a boundary resistance. This effect when properly combined at two FM/NM interfaces in a FM/NM/FM sandwich lead to an effect known as giant magnetoresistance (GMR)[1]. GMR structures are composed of thin alternating FM and NM conducting layers and the resistance of the structure is dependent on the alignment of the magnetisation of the

FM layers, relatively low for parallel (P) alignment and relatively high for antiparallel (AP) alignment. The resistance of the GMR structure can be controlled by reorienting the magnetisation direction (traditionally with an external field).

GMR structures are often classified according to whether the current flows parallel (current in plane CIP) or perpendicular (current perpendicular to plane CPP) to the interfaces between layers. The magnetisation $\mathbf{M}_1$ is typically fixed in one layer (by exchange bias) whilst the other (sensor) layer magnetisation $\mathbf{M}_2$ can switch between configurations parallel or antiparallel to $\mathbf{M}_1$.

The physical mechanism of the GMR for the CIP geometry was first proposed by Fert *et al*[1], and was based on the simple free electron picture. This starts from the premise that the majority and minority spin electrons are differently scattered as they pass through the FM layers. In the FM layers parallel configuration one of the spin directions will be weakly scattered for all for all FM layers and there will be shorting of the conduction by the corresponding channel. In the FM layers antiparrallel configuration electrons of both channels will be strongly scattered by every second magnetic layer and the short-circuit by one of the channels disappears, and the resistance is much higher. This simple picture assumes that the electrons average the scatterings occurring in different FM layers, this only holds true when the distance between the NM layer thickness $t_{NM} < \lambda_t$. For a more realistic picture one must take into account that the layers are not much thinner than λ_t, consider the physical origin of the spin dependent scattering and go beyond free electron models this is beyond the scope of this thesis but more realistic models can be found in references [63] and [64]. The free electron picture allows estimation of the GMR ratio as

$$GMR = \frac{R_{ap} - R_p}{R_p}, \tag{2.47}$$

where R_p and R_{ap} are the resistances of the parallel and anti-parallel states respectively.

Initially experiments on GMR were only performed in the CIP geometry, in more recent years experiments on GMR have been performed in the CPP geometry. The CPP geometry has several advantages, the GMR ratio is typically higher than in CIP but also subsists in much thicker layers. The physical mechanism for CPP-GMR is based on spin-accumulation at the FM/NM interface. In the simple picture of a single interface, no interface resistance and single polarity the incoming electron flux is predominantly carried by a single spin direction (spin-up in this description), where as the outgoing flux is carried equally by both spins. The consequence of this is an accumulation of spin at the interface which diffuses on both sides of the FM/NM interface to a distance of

the order of l_{sf}. The spin polarisation of the current decreases progressively as it goes through this spin-accumulation zone, similarly the current in the opposite direction, a similar mechanism polarises the current. In a multilayer structure there is an interplay between spin accumulation effects at successive interfaces. The spin accumulation in a NM layer is larger for the antiparallel configuration in which the easily injected spin direction is less easily extracted. The CPP-GMR is related to the difference between the spin accumulation in the parallel and antiparallel configurations. This theory of spin accumulation is described by the Valet-Fert model and can be found in reference [60].

The main application of GMR is magnetic field sensors which are used extensively to read hard disk drive data, and more recently GMR multilayers have been used as storage elements in magnetoresistive random-access memory (MRAM).

2.13.2 Tunnelling Magnetoresistance (TMR)

Tunnelling magnetoresistance (TMR) has now replaced GMR in the majority of hard disk drives and is also used in MRAM. TMR can be thought of as similar to spin-valve GMR, however in TMR the electrons travel across a thin insulator which replaces the NM spacer layer. Typically TMR achieves a larger magnetoresistance than GMR.

The tunnel barrier consists of two conducting electrodes separated by a thin dielectric layer. Due to the wave-like nature of electrons when the dielectric layer is sufficiently thin, from a few Å to a few nm, tunnelling of the electrons through the dielectric layer becomes possible. The resulting electrical conductance is determined by the evanescent state of the electron wave function within the tunnel barrier[65].

In a magnetic tunnel junction (MTJ) the two electrodes are FMs. As discussed the electrical current in a FM has two partial currents each with either spin-up or spin-down electrons. In a tunnelling process that conserves spin, the electron conductance (G) is dependent on the angle θ (of the magnetizations) between the two FMs and is given by

$$G(\theta) = \frac{1}{2}(G_p + G_{ap}) + \frac{1}{2}(G_p - G_{ap}).\cos\theta, \tag{2.48}$$

where G_p and G_{ap} are the conductance for parallel ($\theta = 0^\circ$) and anti-parallel ($\theta = 180^\circ$) states. Then the corresponding tunneling magnetoresistance (TMR)[2] ratio (TMR) is defined as

$$TMR = \frac{G_p - G_{ap}}{G_{ap}} = \frac{R_{ap} - R_p}{R_p}, \tag{2.49}$$

where R_p and R_{ap} are the resistances of the parallel and anti-parallel states respectively.

The traditional explanation of TMR, first shown by Julliere[2], is that it arises from

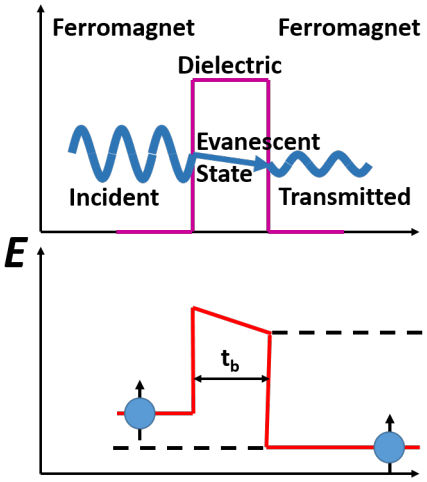

Figure 2.12: An electron tunnelling through a thin tunnel barrier. When the energy of the tunnel barrier is greater than that of the travelling electron wave (approaching from the left side of the barrier) it becomes evanescent inside the barrier and its amplitude decays. If the barrier is sufficiently thin it will emerge on the other side as a traveling wave with reduced amplitude. Figure adapted from [65]

the difference in the density of states (DOS) at the Fermi level (E_f) between the spin-up and the spin-down electrons. As spin is preserved in the tunnelling event the electron can only tunnel into a sub-band of the same spin orientation. Thus the tunnelling conductance is proportional to the product of the Fermi level DOS values of the two FMs with the same spin orientation. A change from the parallel to anti-parallel configurations of the FMs will result in an exchange between the two spin sub-bands of one the FMs for the tunnelling process. Consequently, a corresponding change in conductance will be seen, provided that the Fermi-level DOS values are different for the two spin sub-bands. Whilst Julliere's formulation had some success in predicting the TMR ratios it suffered from several fundamental defects including not taking into account the properties of the insulating barrier, a more realistic formulation can be found in reference [66].

2.14 Spin Transfer Torques (STTs)

In section 2.11 the dynamics of magnets in the absence of spin transfer torques (STTs) are discussed. Spin transfer torques arise when there is a flow of spin-angular momentum through a sample. This occurs whenever a spin current (typically created

by one magnetic thin film) is filtered by another magnetic thin film whose moment is not collinear with the first. In the process of filtering, the second magnet absorbs a component of the spin-angular momentum carried by the electron spins. There are also changes in the flow of spin-angular momentum when spin-polarised electrons pass through a magnetic domain wall or other spatially non-uniform magnetisation distributions where the spins of the charge carriers rotate to follow the local magnetisation. When the magnetisation of the FM exerts a torque on the flowing spins, altering the flow of spin angular momentum, the flowing electrons must exert an equal and opposite torque on the ferromagnet. It is this torque on the FM that is called the STT[67]. This discovery led to the development of active spintronics in which the STT is used to reorient the magnetisation of a FM[68, 69]. Traditionally such torques have been associated with the transfer of spin angular momentum between a 'polariser' FM layer and a 'free' FM layer separated by a NM spacer, mediated by a spin-polarised current flowing perpendicular to the two layers. Recently experiment[70, 71, 72, 73, 74, 75] and theory[76, 77, 78, 79, 80] have shown alternative mechanisms to produce spin torques that do not require a polariser FM layer. The mechanisms, which include the spin Hall effect (SHE), Rashba effect (RE) and Dresselhaus effect (DE), exploit SO effects to induce non-equilibrium spin accumulation, which gives rise to spin-orbit torques (SOTs) acting on the magnetisation via the interaction between s and d electrons[81].

2.14.1 The Hall Effect (HE), Spin Hall Effect (SHE) and Anomalous Hall Effect (AHE)

The Hall effect (HE) (figure 2.13.(a).) arises from the deflection of charge carriers in an applied field **H** and was measured in 1879[82] via the Hall voltage, caused by the subsequent charge accumulation. The (pure) Spin Hall Effect (SHE)[83] (figure 2.13.(c)) is a phenomenon where a spin accumulation of opposite sign arises on the lateral surfaces of a sample in which a charge current flows, due to spin dependent deflection of the carriers. This SHE was first observed in semiconductors[84, 85] but it was the subsequent observation of the SHE in metals[86] which led to a surge in interest in extracting pure spin curents from metals. The SHE arises purely from spin-orbit coupling and so requires no applied **H** field. The ratio of spin current density J_s to charge current density J_c (and therefore the strength of the SHE) is parametrized by the spin Hall angle (SHA) $\theta_{SH} = |J_s|/|J_c|$, where J_s must be expressed in units of charge. θ_{SH} is largest in heavy metals (HM), with values up to 0.4 being reported in β-W[87]. STTs due to this effect were first shown to excite spin waves within YIG/Pt films[88]. Detection

of the SHE using electrical transport measurements is not possible as the number of deflected up and down spins are the same, however the SHE has been detected directly in a GaAs sample using Kerr microscopy[89]. This method of detection is unfavourable as it puts a number of restrictions on the materials and geometries which can be used in SHE experiments (requires materials with large Kerr rotation, optical access etc). One method by which the SHE can be observed more simplistically is by placing the HM SHE material in contact with a ferromagnet (FM) layer. When current flows in the plane of a FM/HM bilayer film, the SHE causes spin current to be driven from the HM to the FM. The magnetization of the FM layer is peturbed by the spin torque (STT) resulting from the spin current in the SHE material and its magnetization state can be probed using the anomalous Hall effect (AHE) (figure 2.13.(b).). In FMs the Hall voltage consists of two contributions: the ordinary HE and an 'anomalous' part which is not proportional to **H** but to the magnetization **M** of the FM. Like the SHE the AHE arises due to spin dependent scattering, but due to the difference in the density of states for charge carriers in a FM this spin separation also leads to a charge difference on opposite sides of the FM. Like the SHE the underlying mechanism of the AHE is SO coupling. This anomalous contribution to the Hall voltage is proportional to the spin polarization (and the magnetization) and is typically much larger then the ordinary HE[90, 91].

The mechanism of the AHE has been the subject of some controversy but it is known to originate from the imbalance in the spin polarization of carriers. J_c in FMs is spin dependent and by assuming Mott's two-carrier approximation[92] a spin dependent resistivity ρ_σ can be defined as $J_\sigma = (1/\rho_\sigma)E$ (where J_σ is the current density). The spin dependence of ρ_σ may be caused by spin-dependent electronic states or by spin dependent scattering. Originally these effects were thought to result from an intrinsic magnetic field in the momentum space known as the Berry phase acquired by the moving electron (figure 2.14.(a).). Later two extrinsic mechanisms, side-jump (figure 2.14.(b).) and skew scattering (figure 2.14.(c).) due to asymmetric electron scattering from impurities were also proposed.

In order to identify which mechanism is active in a spin-orbit system the relationship between Hall resistivity (ρ_{xy}) vs longitudinal resistivity (ρ_{xx}) is typically plotted and assumed to be of the power law form $\rho_{xy} \propto \rho^\beta$. The competing theories suggest that for skew scattering $\beta = 1$ but for side jump and intrinsic deflection $\beta = 2$ and so the dominant mechanisms can be experimentally explored.

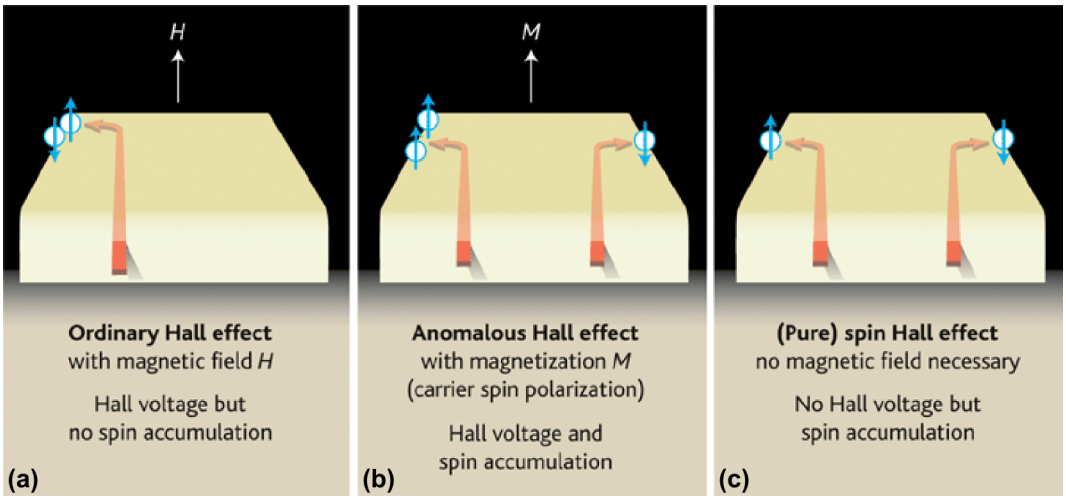

Figure 2.13: The ordinary Hall effect (a), caused by the deflection of charge carriers moving in an applied magnetic field H. Charge accumulation results in a Hall voltage but no spin accumulation as there are equal numbers of spin up and spin down carriers. The anomalous Hall effect (b), caused by the spin-dependent deflection of carriers which produces a Hall voltage and spin accumulation at the edges. The pure spin Hall effect (c) caused by spin dependent deflection of carriers gives rise to spin accumulation but produces no Hall voltage as the number of spin up and spin down electrons are the same. Figure adapted from [90].

2.14.2 The Rashba Effect (RE)

At a similar time to reports of the SHE, current induced switching was reported in Pt/Co/AlOx films with perpendicular magnetisation and was instead attributed to the RE[94]. The Rashba and Dresselhaus effects arise from broken interfacial, and bulk, inversion symmetry respectively. They are typically observed in crystals which lack an inversion center. The origins of these effects are similar, both the Rashba and Dresselhaus SO coupling lock spin to the linear momentum and split the electronic sub-bands in energy. Rashba[95] and Dresselhaus[96] realised bulk SO coupling becomes odd in the electron momentum p. Since then odd-in-p SO coupling has been confirmed across a wide variety of materials which lack inversion symmetry. The key effect of any SO coupling is that, even in the absence of an external magnetic field, electrons moving in an electric field experience a magnetic field in their frame of motion (the SO field) which couples to the electron's magnetic moment. Charge carriers in materials with Rashba SO coupling experience a momentum-dependent effective magnetic field, a spin dependent velocity correction and a geometric phase resulting from the SO

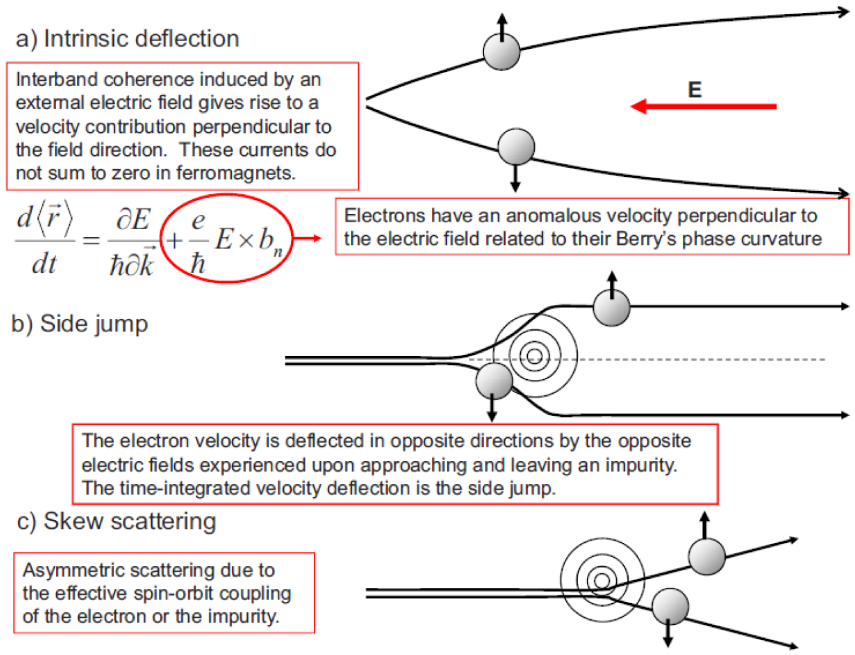

Figure 2.14: The 3 main mechanisms that can give rise to an AHE. Intrinsic deflection (a), side jump (b) and skew scattering (c). Figure taken from [93].

coupling[97]. The origins of the spin orbit coupling are outlined below following the derivation in [97]. When an electron with momentum $\mathbf{p}$ moves in a magnetic field $\mathbf{B}$, it experiences a Lorentz force in the direction perpendicular to its motion $\mathbf{F} = -e\mathbf{p} \times \mathbf{B}/m$ and posses Zeeman energy $\mu_B \sigma \cdot \mathbf{B}$, where σ is the vector of the Pauli spin matrices, m and e are the electron mass and charge respectively, and μ_B is the Bohr magneton. By analogy when this electron moves in an electric field $\mathbf{E}$, it experiences a magnetic field $\mathbf{B}_{eff} \propto \mathbf{E} \times \mathbf{p}/mc^2$ in its rest-frame, a field that also induces a momentum-dependent Zeeman energy known as the SO coupling, $\hat{H}_{SO} \propto \mu_B(\mathbf{E} \times \mathbf{p}) \cdot \sigma/mc^2$. In crystals, the electric field is given by the gradient of the crystal potential $\mathbf{E} = -\nabla V$, which produces a SO field $\mathbf{w}(\mathbf{p}) = -\mu_B(\Delta V \times \mathbf{p})/mc^2$. As the SO coupling preserves time-reversal symmetry ($\mathbf{w}(\mathbf{p}) \cdot \sigma = -\mathbf{w}(-\mathbf{p}) \cdot \sigma$), the SO field must be odd in electron momentum $\mathbf{p}$ so $\mathbf{w}(-\mathbf{p}) = \mathbf{w}(\mathbf{p})$. The odd-in-$p$ SO field only survives in systems that lack spatial inversion symmetry where broken crystal symmetry generates an out-of-plane electric field near each interface. The Dresselhaus spin-orbit coupling is beyond the scope of this thesis but the Rashba form resulting from an interfacial electric field $\mathbf{E} = E_z\hat{\mathbf{z}}$ is given by

$$\hat{H}_R = \frac{\alpha_R}{\hbar}(\mathbf{z} \times \mathbf{p}) \cdot \sigma, \tag{2.50}$$

where α_R is known as the Rashba parameter, typically 0.5^{10-11} eV m[98], (note that equation 2.50 is a p-linear approximation and does not entirely reflect the true form of the SO coupling in inversion asymmetric systems). The consequence of equation 2.50 is that when electrons flow along the x-axis, they experience an effective magnetic field along the y-axis, known as the Rashba field (B_R) shown in figure 2.15. The magnitude of the Rashba field is given by

$$B_R = \frac{2\alpha_R k_F}{g\mu_B}, \tag{2.51}$$

where k_F is the Fermi wavevector and g is the g-factor of the carriers in the conduction channel. Whilst the net torque on the local moments at each interface (in the simple case of a trilayer) typically have opposite sign the moments may experience a torque if the interfaces are dissimilar so that the cancellation of the two torques is incomplete.

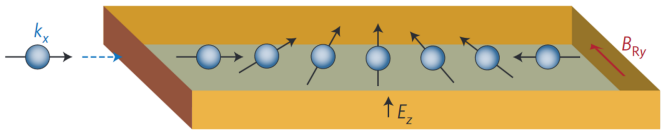

Figure 2.15: Moving electrons (k_x) with a perpendicular electric field (E_z) experience a Rashba field, B_{Ry}. In a Rashba system the spin of the moving electrons precess around the axis of the Rashba field. Figure adapted from [97].

When the electron spin is not aligned with the Rashba field, spin precession takes place with a frequency that depends on the magnitude of the field. Figure 2.15.(b) shows the precession of spin-polarised electrons injected along the x-axis, even in the absence of an applied magnetic field. A consequence of the Rashba field is the possibility to polarize flowing electrons along the direction of this field. This is known as the inverse spin galvanic effect.

2.14.3 Spin Transfer Torque (STT) Directions

Intense efforts have been made to distinguish between STTs due to the Spin Hall and Rashba effects. With a current applied parallel to the interface plane, to first order, the SHE is thought to generate a longitudinal "anti-damping" torque (also known as "Slonczewski torque" or "in-plane torque") and the Rashba effect is thought to produce a transverse "field-like" (also known as the "effective field" or "out-of-plane torque"). The configuration adopted in the discussion of STTs in thin films is that the charge current $\mathbf{j}_e$ is injected along the $\hat{\mathbf{x}}$ direction, $\hat{\mathbf{y}}$ is the in-plane direction perpendicular to

the current flow direction and $\hat{\mathbf{z}}$ is the out-of-plane direction as shown in figure 2.16.

In a simple model of the Rashba torque the Rashba field lies in $\hat{\mathbf{z}} \times \hat{\mathbf{p}}$ direction, where $\hat{\mathbf{p}}$ is a unit vector in the direction of electron momentum. In the above direction configuration the Rashba field lies in the $\hat{\mathbf{z}} \times \hat{\mathbf{x}} = \hat{\mathbf{y}}$ direction, and therefore the Rashba torque is proportional to $\hat{\mathbf{m}} \times \hat{\mathbf{y}}$. It has recently been shown that the Rashba torque $\mathbf{T}_R$ actually has both out-of-plane and in-plane components[99, 100] i.e. $T_R = T_R^{\perp}(\hat{\mathbf{y}} \times \hat{\mathbf{m}}) + T_R^{\parallel}(\hat{\mathbf{m}} \times (\hat{\mathbf{y}} \times \hat{\mathbf{m}}))$.

In a simple model of the SHE torque the injected spin due to the SHE is polarised along $\hat{\mathbf{y}}$. The transverse component is absorbed in the FM (as in spin-polarised current injection). As the spin Hall torque ($\mathbf{T}_{SH}$) is proportional to the absorbed transverse angular momentum $T_{SH} \propto \hat{\mathbf{y}} - (\hat{\mathbf{y}} \cdot \hat{\mathbf{m}})\hat{\mathbf{m}}$, this can be expressed instead as $T_{SH} \propto (\hat{\mathbf{m}} \cdot \hat{\mathbf{m}})\hat{\mathbf{y}} - (\hat{\mathbf{y}} \cdot \hat{\mathbf{m}})\hat{\mathbf{m}}$ and, by use of the BAC-CAB vector rule, can then be expressed as $T_{SH} \propto -\hat{\mathbf{m}} \times (\hat{\mathbf{y}} \times \hat{\mathbf{m}})$. As with the Rashba torque the spin Hall torque has recently been shown to contain both out-of-plane and in-plane components[101] and has the form $T_{SHE} = \theta_{SH}\mu_B j_e/e(\hat{\mathbf{m}} \times (\hat{\mathbf{y}} \times \hat{\mathbf{m}})) + \beta(\hat{\mathbf{y}} \times \hat{\mathbf{m}})$, where β is the non-adiabaticity parameter proposed by Zhang and Li[102].

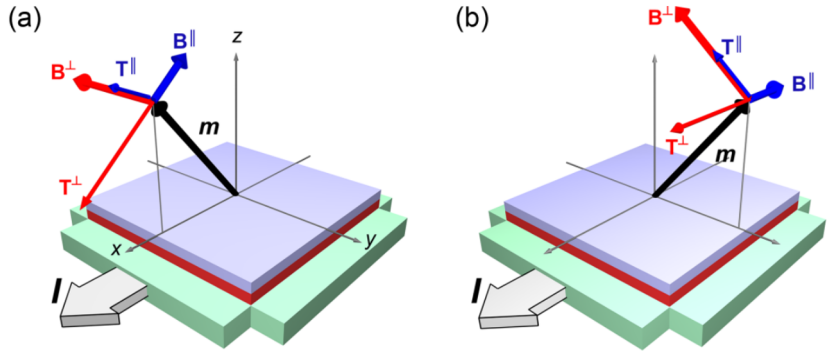

Figure 2.16: Spin-orbit torques $T^{\parallel}$ and $T^{\perp}$ and the corresponding fields $B^{\parallel}$ and $B^{\perp}$ when the magnetisation is tilted (a) parallel and (b) perpendicular to the current direction (I). Figure adapted from [103]

As both the RE and SHE can produce the same form of torque it convenient to describe the parallel $\mathbf{T}^{\parallel}$ and perpendicular $\mathbf{T}^{\parallel}$ torques, so the total torque $\mathbf{T}$ can be expressed as

$$\mathbf{T} = \mathbf{T}^{\parallel} + \mathbf{T}^{\perp} = a_j(\hat{\mathbf{m}} \times (\hat{\mathbf{y}} \times \hat{\mathbf{m}})) + b_j(\hat{\mathbf{y}} \times \hat{\mathbf{m}}), \tag{2.52}$$

where a_j and b_j are parameters that depend on the current, magnetisation, NM/FM geometry and materials.

Recent studies[104, 103] further showed that $T^{\parallel}$ and $T^{\perp}$ include significant additional contributions that depend on the magnetisation direction relative to the current and symmetry axes, which lead to the following expressions for the torques

$$\mathbf{T}^{\parallel} = \mathbf{m} \times (\mathbf{y} \times \mathbf{m}) T_0^{\parallel} + (\mathbf{z} \times \mathbf{m})(\mathbf{m} \cdot \mathbf{x})[T_2^{\parallel} + T_4^{\parallel}(\mathbf{z} \times \mathbf{m})^2], \tag{2.53}$$

and

$$\mathbf{T}^{\perp} = (\mathbf{y} \times \mathbf{m})[T_0^{\perp} + T_2^{\perp}(\mathbf{z} \times \mathbf{m})^2 + T_4^{\perp}(\mathbf{z} \times \mathbf{m})^4] + \mathbf{m} \times (\mathbf{z} \times \mathbf{m})(\mathbf{m} \cdot \mathbf{x})[T_2^{\perp} + T_4^{\perp}(\mathbf{z} \times \mathbf{m})^2], \tag{2.54}$$

where the coefficients $T_n^{\perp}$ and $T_n^{\parallel}$ represent the current-dependent torque amplitudes.

Clarifying the forms and origins of the SOTs is an ongoing debate of pressing importance since these torques have been shown to be strong enough to reverse the magnetisation of high-coercivity ferromagnetic layers with both perpendicular[74, 13, 105] and in-plane[15] anisotropies for current densities of the order $10^7 - 10^8$ A cm^{-2}, proving that SOTs have strong potential for technological applications such as the switching of magnetic-tunnel junctions, using three terminal connections to separate the read and write paths and avoid damage to the tunnel barrier[15]. The interaction of SOTs with more traditional Oersted torques has not been widely explored but SOTs have been shown to both add to[106] and oppose[107] the Oersted torque.

Chapter 3

Fabrication Techniques

3.1 Introduction

This chapter outlines the techniques utilised for the deposition and patterning of ferromagnetic multi-layered thin films. Also described are the procedures employed for the addition of on-wafer waveguides, used to deliver currents to excite magnetisation dynamics. The CrO_2 samples (section 5) and Ta/CoFeB/MgO samples (sections 6, 7 and 8) were grown at Brown University by the author and collaborators.

3.2 Thin Film Deposition

Vapour deposition processes can be broadly classified into two types. Chemical vapour deposition (CVD) involves the reaction of chemical constituents in the vapour phase on, or in the vicinity of, the surface of a heated substrate in order to form a solid deposit [108]. Physical vapour deposition (PVD) processes such as sputtering differ as they rely on material transfer from condensed-phase evaporant or sputter target sources in a vacuum [109].

3.2.1 Chemical Vapour Deposition (CVD)

CVD involves the dissociation and/or chemical reactions of gaseous reactants in an activated environment (by heat, light or plasma). The subsequent deposition involves homogeneous gas phase reactions, which occur in the gas phase, and/or heterogeneous chemical reactions which occur on or near the heated surface. These reactions lead to the formation of powders or films respectively [110].

In this study CVD is performed in a quartz reactor placed inside a traditional two-zone furnace with independent temperature control of the two zones[111, 112].

3.2.2 Physical Vapour Deposition (PVD)

In PVD, a pure source material is gasified by heat, light or electricity in an inert gas at low pressure. The target material is then carried to the substrate where it will condense on the substrate to create the desired layer. Critically no chemical reactions take place in this process.

This study utilised magnetron sputtering where the material to be sputtered is held on a 'target' plate with a negative D.C. bias. The bias attracts heavy gas ions from the plasma, on striking the target these ions eject target atoms which are thermalized by multiple collisions in the plasma before arrival at the substrate. Magnets are placed below the target trapping the electrons in small, close proximity loops due to their smaller mass relative to ions, resulting in a region of enhanced positive ion generation.

3.3 Patterning Procedures

Typically photolithography was used to pattern continuous films into smaller shapes and to define waveguides to deliver currents.

3.3.1 Mask Design for Photolithography

Photomask patterns were designed using the CAD software AutoCAD [113] and the were masks ordered from Advance Reproductions Corp (ARC)[114]. The mask base was soda-lime and had a chrome pattern coating type. For use with a Karl Suss MJB-3 mask aligner, a 4.0 " plate of 0.090 " thickness is required. Photomask tolerance for the mask is ± 0.5 μm. This proved not to be the limiting factor as human alignment of multiple masks and the 'wet' nature of the photolithography process meant feature sizes less than $\approx$ μm could not be resolved clearly.

A typical mask design is shown in figure 3.1. This mask is designed in the three layers demonstrated in (c). Alignment markers (the crosses visible in (a)) allow precise alignments of each layer. Many devices can be fabricated on a single wafer as shown in (a) and (b), and typically a level of redundancy is used to ensure the yield of key designs is as desired. Specific to the sample growth in this thesis (though true of many similar deposition processes) the highest quality area of the mask is the central region

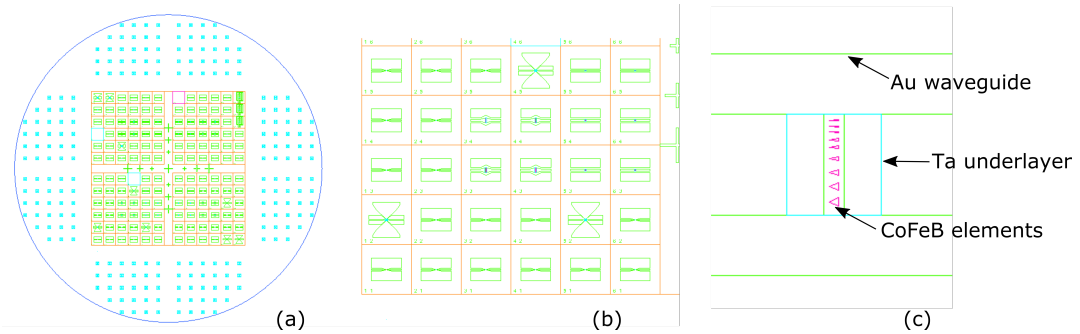

Figure 3.1: Typical mask design (a) full wafer (b) subsection (c) elements of a single device

where critical parameters such as film thickness are known best. For this reason the key designs are placed close to the center of the mask.

3.3.2 Photolithography

Photolithography is used to transfer a pattern from the partially transparent mask to the surface of the desired wafer. Typically this process involves wafer cleaning, photoresist application, soft baking, mask alignment, exposure, development and hard baking.

In this study the wafer is first cleaned to remove any traces of organic, ionic or metallic impurities. A liquid photoresist is 'spin coated' onto the material surface by dripping a small volume on to a wafer vacuum fixed on a high-speed centrifugal spinner. The desired thickness is achieved by carefully controlling the rotation speed and time.

Depending on the design requirements either a positive or negative photoresist is used. Positive photoresists undergo a structural chemical change when exposed to UV light and become more soluble to a developer solution, and so when removed the pattern remaining is where the mask was transparent. Negative resist behaves in the opposite manner and exposure to UV light causes the resist to become polymerized and more difficult to dissolve, meaning the pattern left after development is the inverse of the transparent portion of the mask. Soft baking is used to remove solvents from the photoresist coating increasing the photosensitivity. This step is often critical for a successful exposure and development. Under baking will prevent light from reaching the sensitizer meaning a portion of the hardened resist will be removed during development. Over baking can reduce the developer solubility or even destroy the

sensitizer all together.

After baking the mask is aligned over the desired area of the wafer surface and either brought into contact (high resolution but debris between the mask and wafer can damage the mask and cause defects in the pattern) or in close proximity (usually 10-25 μm gap is left). The photoresist beneath is then exposed to UV light through the pattern of the mask.

To remove the non-hardened resist the wafer is submerged in a developer solution. Typically these solutions are simple solvents such as acetone for positive resists or methyl ethyl ketone for negative resists. The timing of this step is often critical for achieving a good quality pattern as underdevelopment will leave traces of resist on the wafer surface and over development can begin to soften and remove the hardened portion of the resist.

Finally some resists require a post development hard-baking step to fully harder and improve adhesion making them more resistant to etching methods.

3.3.3 Etching

Ion beam etching is a physical etching technique which has high directionality and low material selectivity. The ion beam etcher uses a plasma, generated under low pressure by an electromagnetic field, to bombard the wafer with high-energy ions which liberate material from the surface.

For this study the ion beam etcher uses the neutral gas Ar which is ionized by electrons travelling from a hot filament to the anode grid once a critical voltage of 40 V is reached. A magnetic field of about 100 Gauss is used to trap electrons and increase the ionization rate. Etch rates are controlled by the ion flux and bombardment energy and are typically accelerated by potentials of 500-1000 V. The etch rate typically depends linearly on the ion-flux but non-linearly with bombardment energy. To prevent the build up of positively charged Ar^+ ions on the wafer plate a neutralizing filament is included after the accelerating plate.

An unwanted by-product of ion milling is the re-deposition of the etched material onto the side walls of the pattern as shown in figure 3.3. The magnitude of this effect is greatest at normal incidence but careful control and rotation of the incident angle of the ion beam can make the rate of re-deposition exactly match the rate of etching.

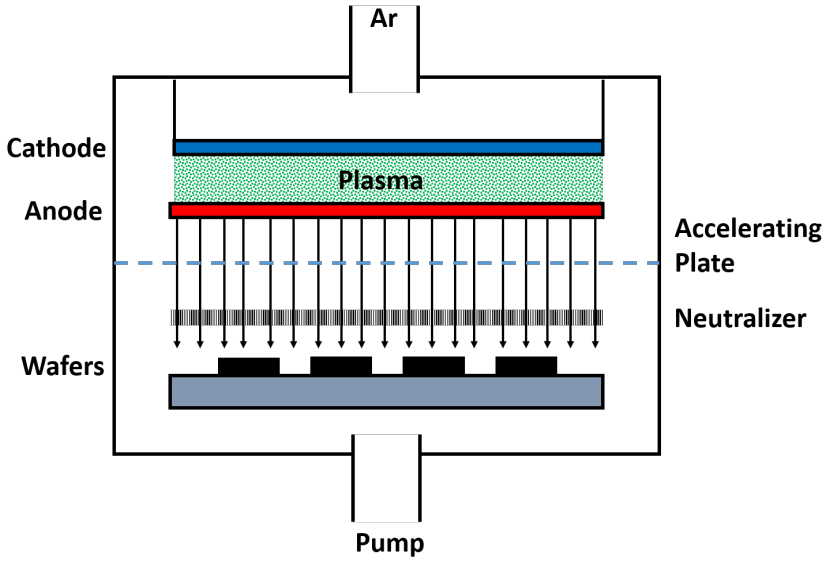

Figure 3.2: Typical reactive ion etching system.

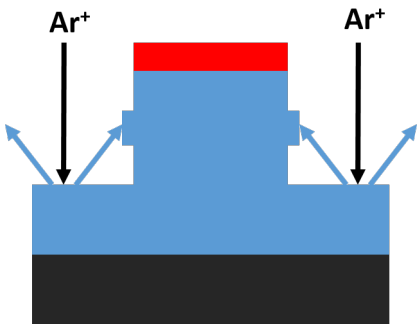

Figure 3.3: Re-deposition during ion milling.

3.4 Electrical Contacts

3.4.1 Lift Off Procedure

A lift of procedure is used in order to fabricate electrical contacts or waveguides on the wafer post patterning, without the need for a precision etch or adding unwanted metal (typically Au) to the magnetic structures. In this technique the wafers are covered with a layer of photoresist, to act as a barrier preventing the deposition of the Au directly on the wafer surface. The photoresist is patterned and developed in the target areas and sputtering used to coat the entire surface with Au. After sputtering sonication

in acetone is used to remove the protective photoresist coating along with the Au deposited on top.

3.4.2 Wire Bonding

Wire bonding is one of the methods used to make connections between the device wafer and the rest of the circuit. Generally wire bonding involves attaching a small diameter soft metal wire to a compatible metal surface without the use of solder or flux. Wire bonding can be split into three main types. Thermocompression bonding uses force, time and heat to join the materials by inter-diffusion, the wire (sometimes heated) is pressed against a hot surface for a short time to achieve the bond. Thermosonic bonding also includes the use of ultrasonics to join the two materials, the method is the same as thermocompression but additionally the wire is vibrated to increase bond adhesion. Ultrasonic bonding uses force, time and ultrasonics but without the use of heat. Devices in this study were Au bonded using a tpt HB10 wire bonder used in an ultrasonic wedge bonding mode to avoid the potentially detrimental effect heating may have on the magnetic layers.

3.5 Magnetic Thermal Annealing

The process of thermal annealing allows the atoms inside a solid to diffuse more easily so maintaining a solid at a high temperature lets it achieve equilibrium eliminating structural imperfections which would negatively impact its desired properties. In magnetic thermal annealing an external magnetic field is applied during the annealing process. One of the most important effects of this field is the reorientation of the easy axis in a FM, as this is determined by the lattice structure (except in some cases where shape or internal strain are the dominant effect). When the FM material is raised to high temperature the spins of each individual atom will align with the external field. This spin-field interaction will begin to reorganize the lattice due to the interactions between the atomic orbitals and the electron spins inside the crystal lattice (spin orbit interaction). Eventually the system will attain equilibrium within this field, causing a lattice re-orientation such that the easy axis lies parallel to the field. When the temperature is reduced, the easy axis remains locked in the field direction. This process is critical in achieving perpendicular magnetic anisotropy (PMA) in the Ta/CoFeB/MgO structures.

3.6 Chromium Dioxide (CrO_2) Thin Film Fabrication

The complete deposition procedure for CrO_2 thin films, with on-substrate waveguides, is shown in figure 3.4. Each stage is discussed in further detail in the following sections, and the process can be broadly described as follows.

(a) TiO_2 substrate cleaned and treated with HF.

(b) SiO_2 sputter deposited to cover the TiO_2 surface.

(c-d) SiO_2 patterned by photolithography.

(e-f) Underlying TiO_2 exposed by ion beam etch.

(g-h) The shape of CrO_2 elements defined by the SiO_2 layer during CVD deposition.

(j-k) Photolithography used to define the waveguide area and another ion beam etch used to expose the TiO_2 substrate

(l) Cr and Au sputtering and lift off procedure to leave waveguide pattern.

A modified patterning procedure shown in figure 3.5 was also explored. This remained identical to that shown in figure 3.4 for steps (a)-(j) but the second ion beam etch of SiO_2 (step (k)), was removed and the waveguides were deposited directly on to the SiO_2 layer. The advantage this method has over the first is a reduced chance of CrO_2 degradation due to the second ion beam etch step which occurs after CVD. This method has the potential disadvantages that the waveguide is raised slightly above the plane of the CrO_2, leading to a reduction in the Oersted excitation field (though this is likely to be negligible). The waveguides were also designed for use on a purely TiO_2 substrate and adding a second layer may reduce the accuracy of the impedance matching (though this is unlikely as the thickness of the $SiO_2 \ll$ track spacing) which is particularly difficult on TiO_2 anyway as it has a large and anisotropic dielectric constant[115, 116] (this is discussed further in section 5).

3.6.1 Titanium Dioxide Substrate Cleaning

All films in this thesis were grown on a 5 x 5 x 0.5 mm^3 (100)-oriented, single crystal rutile TiO_2 substrate.

It has been found that the CrO_2 deposition rate and uniformity is highly sensitive to the surface quality of the TiO_2 substrate so a careful substrate cleaning procedure is

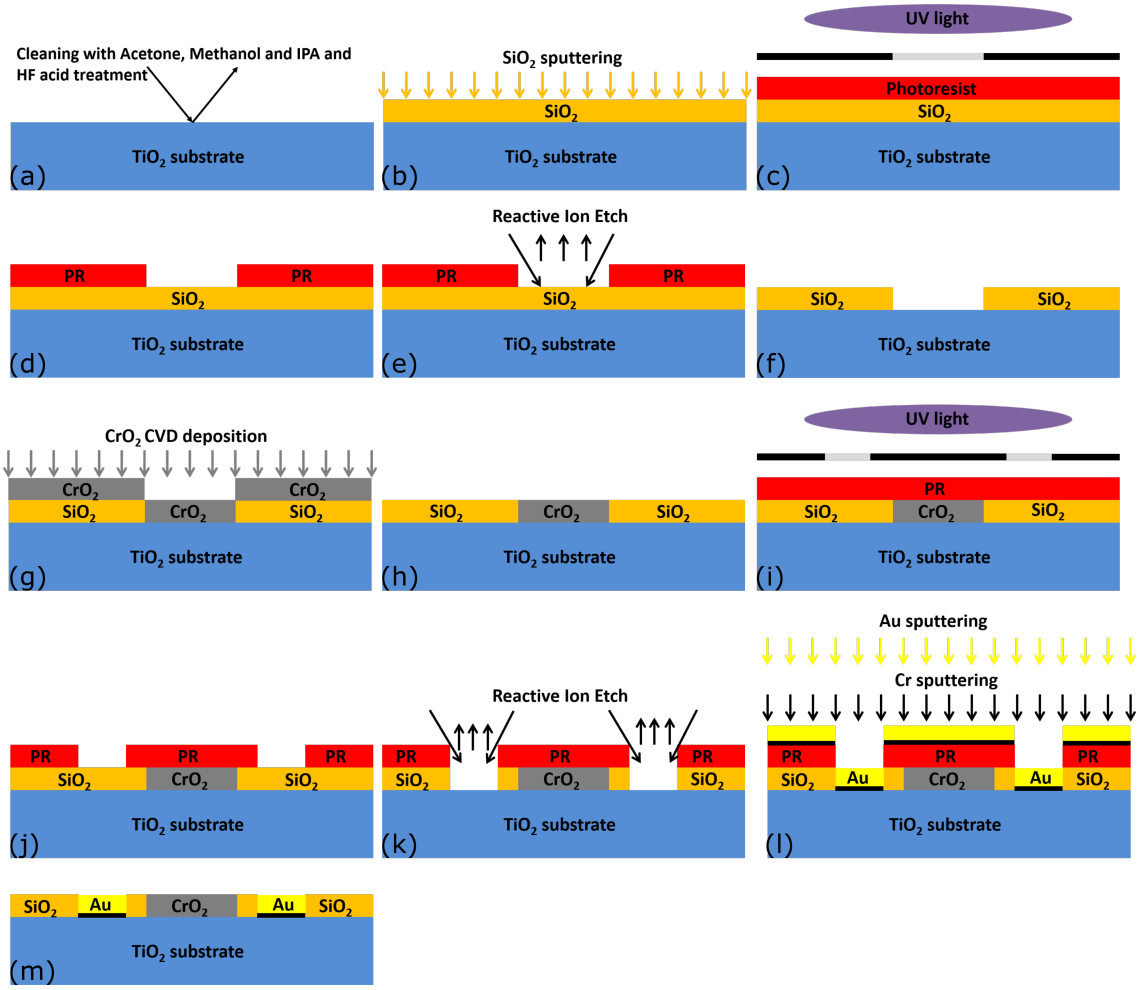

Figure 3.4: Deposition and patterning procedure for CrO_2.

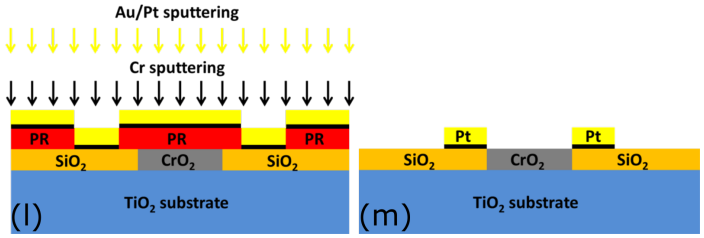

Figure 3.5: Modified deposition and patterning procedure for CrO_2.

key to a high quality deposition. It has also been reported that pretreatment of the TiO_2 substrates with hydrofluric acid (HF) gives a large enhancement to the strain of the

resultant CrO_2 films[117, 118, 119, 120, 121] which allows control of the easy axis direction and magnitude of the anisotropy.

The TiO_2 substrate is first cleaned with organic solvents (acetone, methanol and IPA) for 10 minutes each, with the containing beakers submerged in a warm ultrasonic water bath. Substrates are subsequently cleaned with distilled water then etched in a 1% HF solution for 5 minutes before being rinsed in distilled water and blown dry with N_2 gas. The substrate, precursor boat and substrate holder are then placed within the oven and heated for 20 minutes in order to burn off any remaining moisture or solvents before CVD.

3.6.2 Silicon Dioxide Deposition and Patterning

A layer of SiO_2 is sputtered on the TiO_2 substrate and patterned using photolithography and ion beam etching to act as a stencil for the growth of CrO_2. As discussed in section 5, whilst CrO_2 grows readily on a clean TiO_2 surface it will not deposit on the amorphous SiO_2 substrate. The SiO_2 thicknesses were 50 nm for growth method 1 (figure 3.4) and 500 nm for growth method 2 (figure 3.5). The thicker SiO_2 layer is possible in method 2 as no ion beam etch is required. These thickness were confirmed to ± 2 nm by XRR (shown in section 5.2.1).

3.6.3 Selective Area CVD

The TiO_2 substrate with SiO_2 stencil is placed in the centre of the substrate holder, as shown in figure 3.6, with the c-axis oriented along the direction of oxygen flow. The substrate holder is then slid along the tube to the center of the right oven, with the substrate as close as possible to the thermocouple (T.C in figure 3.6). The tube is sealed and both ovens are heated to their respective temperatures and left for 10 minutes to ensure thermal stability. The left side of the tube is then opened and the precursor boat containing 30 mg CrO_3 precursor is slid into the left oven, with the precursor as close as possible to the thermocouple. The tube is then resealed and the O_2 flow rate increased to 100 sccm. After the CrO_3 becomes a sintered solid, the vapour phase is induced (experimentally determined to be at around 10.9 minutes) and deposition begins. When deposition time is complete both ovens are turned off and opened to increase cooling rate. The O_2 flow rate is also increased to 150 sccm to further increase cooling of the system. The tube should not be opened until cooled due to significant health risks of vaporised CrO_3[122]. It has been observed that repeated depositions lead to a build-up of precursor deposits on the inner walls of the quartz tube, in subsequent

depositions solid microparticles can fall on to the surface of the substrate roughening the film[123]. The quartz tube, substrate holder and precursor boat were all cleaned with chromium etchant[124] between each deposition to minimise this effect.

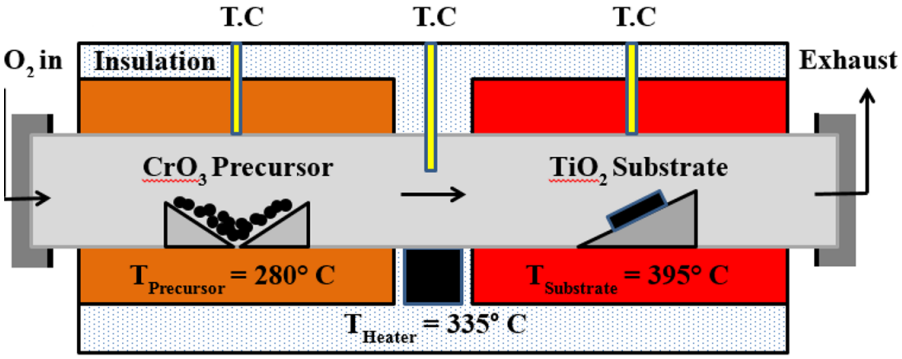

Figure 3.6: Schematic of chemical vapour deposition chamber.

3.6.4 Removal of Extraneous CrO_2

During the deposition process CrO_2 is not only deposited on the front face of the film but also on the sides and a portion of the rear, this must be removed in order for VSM to provide an accurate estimation of film thickness. Both mechanical cleaning with ultra-fine sandpaper and chromium etchant were trialled as possible methods. Mechanical cleaning removes CrO_2 from only the sample back and edges (having no significant effect on the front film surface) but does not remove material evenly and is a slow process. Chromium etchant removed material more evenly and rapidly but over time wicked on to the front surface and removed material on the front close to the edges. The optimal method was found to be a combination of the two, sanding briefly to remove some of the chromium and roughen the surface, then running the sample quickly along an etchant soaked piece of tissue to evenly remove the remaining CrO_2.

3.6.5 Au Waveguide Deposition

The final processing stage is the addition of Au waveguides to the wafer surface. In method one (figure 3.4) the SiO_2 surface is patterned using photolithography, etched by ion beam etch, and the waveguide deposited on the TiO_2 substrate, in method two the ion beam etch step is left out. Testing revealed the sputtering of a Cr base layer

significantly improved the adhesion of Au to the TiO_2 substrate, details of this are shown in section 5.2.4.

3.7 Ta/CoFeB/MgO Thin Film Fabrication

This section details the fabrication procedure for Ta/CoFeB/MgO Hall bars and devices with micron scale CoFeB elements and on wafer waveguides designed for high frequency TRSKM.

In this thesis β-Ta/CoFeB/MgO, with the CoFeB composition $Co_{40}Fe_{40}B_{20}$, is used. All samples have perpendicular magnetic anisotropy (PMA) achieved through thermal annealing.

The full growth and patterning procedure for each device type is shown in figure 3.7 (Hall bars) and figure 3.8 (high frequency). The second procedure is identical to the first but with an additional step to partially etch only the CoFeB/MgO layers to create patterned elements, leaving the Ta underlayer intact to carry a current.

The fabrication procedure for both Hall bars and patterned CoFeB elements can be broken into the following steps.

(Pre) The low resistivity silicon wafers (for Hall bars) are oxidized to grow a 2 μm thick SiO_2 layer. This step is not required for high resistivity wafers (for high frequency devices) as they are pre oxidized.

(a) Deposit Ta/CoFeB/MgO/Ta multilayers in magnetron sputtering system.

(b-c) First round of photolithography patterning and ion milling to pattern Ta/CoFeB/MgO/Ta stack into Hall bars/square regions in center of waveguide.

(e-f) (high frequency only) A second round of photolithography patterning and ion milling to pattern CoFeB/MgO/Ta layers only into shaped elements.

(g-h) Third round of photolithography patterning, gold deposition and lift-off procedure to define the Hall bar contact/waveguides.

(i) Thermal annealing with magnetic field aligned perpendicular to the sample plane to achieve perpendicular magnetic anisotropy (PMA).

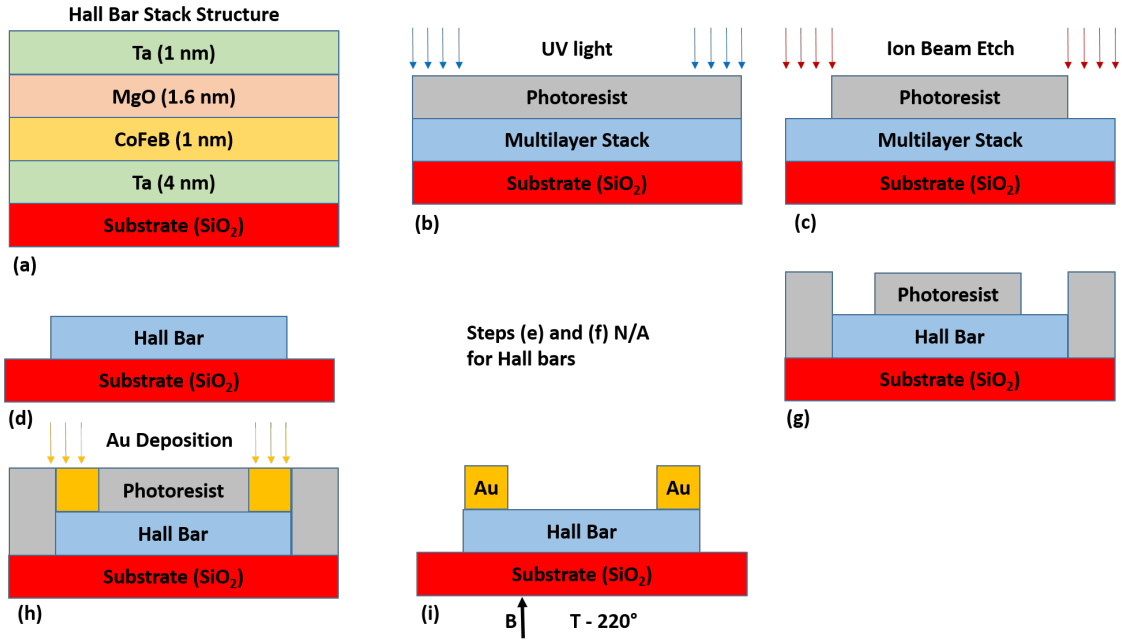

Figure 3.7: Schematic of Ta/CoFeB/MgO Hall bar deposition procedure showing (a) sputtered stack structure (b)-(g) defining Hall bar shape using photolithography and Ion beam milling (h)-(i) deposition of Au contacts and thermal annealing.

3.7.1 Sputtering

The Ta/CoFeB/MgO/Ta multilayer stacks are deposited in a single round of PVD in a magnetron sputtering system, on 2" Silicon wafers with a thickness of 275 μm. For the high frequency devices a high resistivity ($\rho \geq 1000$ Ω-cm) wafer was used in place of the standard wafers.

The system is pumped to high vacuum, 2×10^{-8} Torr as base pressure, to minimize deposition defects. Ar is used as the carrier gas, unless depositing oxides where instead Ar and O are used (in a 3:1 ratio). Typically the sputtering pressure is 4 mTorr which gives a sputtering rate of about 0.1 nm/s [125]. Throughout deposition substrates were kept at ambient temperature. During the sputtering process the substrates rotate at a constant speed about two axes to ensure uniformity. Both the face down Si substrate and face up sputtering guns have a diameter of 5 cm and are at a target-substrate distance of 9 cm with an off center spacing of 3 cm. During deposition a target rotation speed of 50 rpm ensures thickness uniformity[126]. The deposition thickness is controlled by the power applied to the sputtering target (controls rate) and the sputtering time. For the

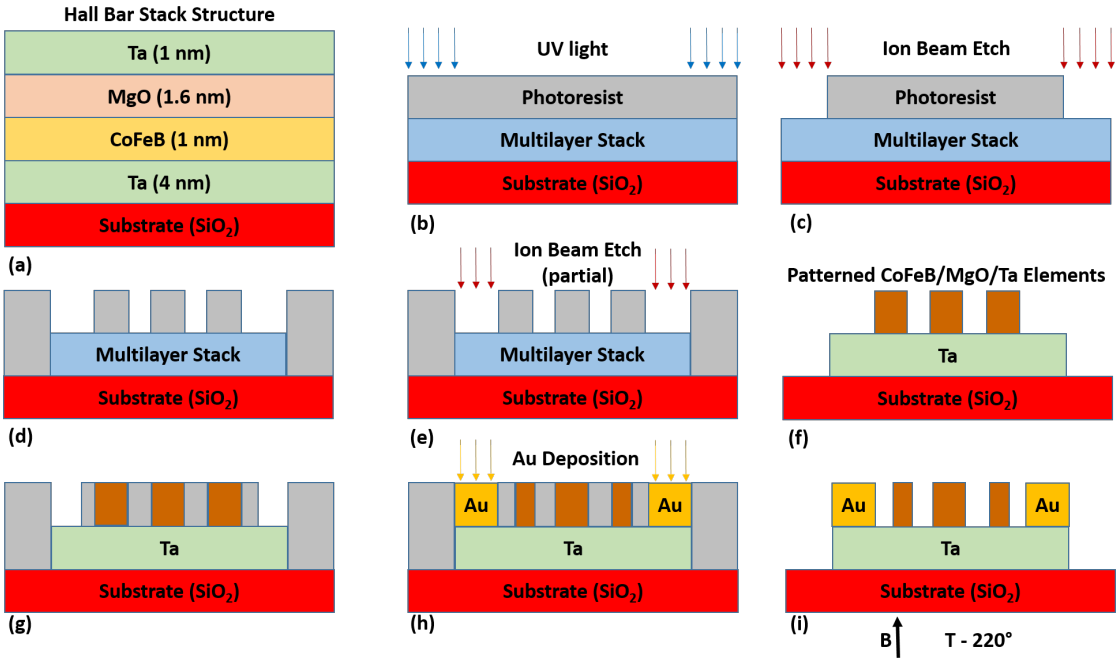

Figure 3.8: Schematic of Ta/CoFeB/MgO high frequency device deposition procedure showing (a) sputtered stack structure (b)-(g) defining CoFeB/MgO elements using photolithography and ion beam milling (h)-(i) deposition of Au contacts and thermal annealing.

multilayer stacks the following sputtering powers and times were used; Ta (4 nm) 10 W for 88 s / CoFeB (1 nm) 10 W for 25 s / MgO (1.6 nm) 120 W for 37 s / Ta (1 nm) 10 W for 22 s. The 1 nm Ta layer was used as a capping layer to prevent atmospheric oxidisation.

3.7.2 Photolithography and Etching

Once deposited, the multilayer stacks are cleaned with acetone and spin coated with the liquid photoresist AZ5214 (Clariant Inc.) at 4000 RPM for 30 seconds giving an approximate thickness of 1.2-1.4 μm. The photosensitive polymer AZ5214 can act as either a positive or negative resist dependent on baking recipe. For the first two masks (to pattern the Ta/CoFeB/MgO/Ta stack (a) and CoFeB/MgO/Ta elements (b)) the photoresist is baked for 2 minutes at 110° C resulting in it acting as a positive resist. The masks are aligned using crosses (or similar structures on mask surface) and exposed to UV light for 22 s, using a 365 nm filter, on constant power mode. This softens the resist

in the areas of mask not covered by the mask pattern. After exposure the substrate is placed in the developer AZ917 for 15 s to remove unhardened resist. This timing can vary by several seconds so the surface pattern should be inspected by eye throughout this time to prevent over/under development.

After development ion beam etching removes material in the exposed areas. As described in section 3.3.3, during the etching non-volatile material will re-deposit on the side walls of the etched channel. This effect can be reduced by varying the angle of ion beam incidence. If carefully controlled the rate of deposition can be made to exactly match the rate of etching. Empirical testing showed that variation of the angle of incidence between 45° (surface of sample is being etched but side wall accumulation rate faster than etch rate) and 10° (etching is slow but faster than side wall accumulation rate) every 10 s gives the optimal sample quality. Etching times were 170 s for the full Ta/CoFeB/MgO/Ta stack (over etching is not a concern here but under etching is) and 40 s for just CoFeB/MgO/Ta.

After the ion beam etch the hardened photoresist is removed by submersing it in acetone, methanol, IPA and DI water, each for 10 minutes, in a sonic water bath.

3.7.3 Au Contacts and Waveguide Deposition

For the final photolithography and etching, mask (c) is used to pattern Au contacts and waveguides. The photoresist is used in negative mode which adds an additional step to the process. After spin coating the resist is first soft baked at 90° C for 2 min, the mask is aligned and a 6 s UV exposure is initiated, the photoresist is then baked again at 125° C for a further 1 min (this temperature is critical for sharp patterning and should be carefully monitored). This second baking hardens the resist in the areas exposed to UV light. Development is again 15 s using AZ917 and the Au sputtering and lift off procedure defines the contacts/waveguides (detailed in 3.4.1). Throughout this process the wafer should be repeatedly checked under a microscope to ensure complete removal.

3.7.4 Thermal Annealing

Finally the wafers are annealed in order to obtain the desired PMA. The interfacial PMA between oxide and ferromagnetic metal (Fe/MgO) is attributed to the hybridization of Fe $3d$ and O $2p$ orbitals[127] for an interface of (001) orientation. It is worth noting that this is predicted by first-principles calculation and earlier experimental studies also

indicate the presence of PMA at the interface in Pt/Co/MO_X (M = Al, Mg, Ta and Ru) trilayers[128, 129].

Annealing is performed in high vacuum (below 1×10^{-6} Torr) under a magnetic field of 0.45 Tesla applied perpendicular to the sample plane. The desired vacuum is achieved after 1 hour of pumping down, the temperature is then stepped up in a multi-stage process in order to achieve smooth temperature control and to avoid overheating. A typical temperature profile for this process can be expressed as: $100^{20}_{20} + 150^{20}_{15} + 180^{15}_{15} + 200^{10}_{10} + 210^{10}_{5} + 220^{5}_{60}$ where, for instance, the 2^{nd} step is raising the temperature from 100 to 150 °C in 20 minutes with 15 minutes of waiting. The wafer is left in the chamber for 6 h of natural cooling under a field of 0.45 Tesla.

It has been shown by Qiang *et al*[126] that the PMA in the Ta/CoFeB/MgO/Ta stack structure is very sensitive to annealing temperature. Figure 3.9 shows the effect of a deviation of ± 20 °C from the optimum 220°C temperature. The as-prepared sample has sharp but disordered interfaces, which are unable to support PMA. This is improved as the annealing temperature approaches 220°C but for annealing temperatures >220°C diffusion in the interfacial region is likely the cause of PMA reduction. It is for this reason the careful control of the temperature stepping is required.

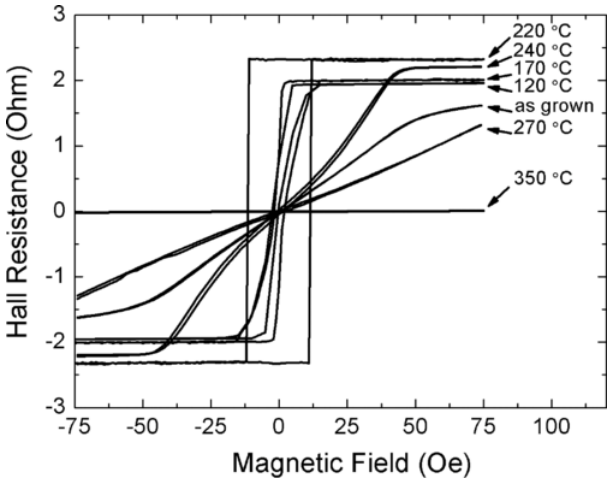

Figure 3.9: The anomalous Hall resistance of Ta(4)/CoFeB(1)/MgO(1.6) stacks vs magnetic field applied perpendicular to the stacks for a series of different annealing temperatures. (figure taken from [126])

3.8 Summary

The techniques used by the author and collaborators for the fabrication of CrO_2 and Ta/CoFeB/MgO thin films have been described. Other samples measured in this work (such as the CoMnGe films used in the spin pumping study in chapter 10) were fabricated without physical input from the author and so these procedures are beyond the scope of this thesis.

Chapter 4

Experimental Techniques

4.1 Vibrating Sample Magnetometery (VSM)

Vibrating Sample Magnetometery (VSM) was originally developed by Foner[130, 131] in the late 1950s. Since then VSM systems have increased in complexity and accuracy but the basic principle of operation has remained the same. A magnetic sample is oscillated within a uniform magnetic field **H**, inducing a voltage in a suitably placed detection (pickup) coil which is proportional to the sample's magnetic moment[132]. If a single coil is considered then the induced voltage (V) due to a local change in net flux follows from Faraday's law

$$V = -\frac{d\phi}{dx} = -\frac{d\phi}{dt}.\frac{dx}{dt}. \tag{4.1}$$

Following the analysis of Zieba and Foner[133] the flux (ϕ) produced by the magnetic dipole moment (m) of a sample due to the external field (**B**) may then be equated to the current (I) in the detection coils (the Biot-Savart Law)

$$\mathbf{B}.\mathbf{m} = I\phi, \tag{4.2}$$

and assuming that the sample is undergoing simple harmonic motion with amplitude A and frequency ω

$$\frac{dx}{dt} = A\omega\cos(\omega t). \tag{4.3}$$

Combining Eqs. 4.1, 4.2 and 4.3 gives

$$V = GmA\omega\cos(wt), \tag{4.4}$$

where G is a geometric factor. It follows that for a known amplitude and frequency of oscillation the induced current is proportional to the magnetisation of the sample[133].

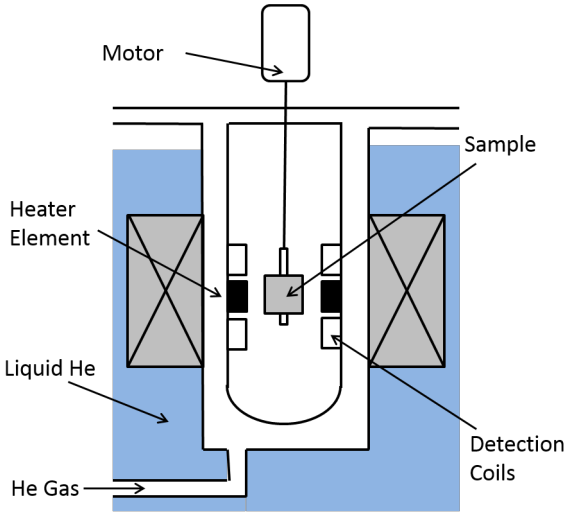

Figure 4.1: Example of a typical vibrating sample magnetometer geometry.

In this work the VSM detection coil add on for the Quantum Design Physical Property Measurement System (PPMS®), at Brown University was used to measure magnetic properties. This system has a relatively large oscillation amplitude (2 mm peak) and a frequency of 40 Hz. The system is able to resolve magnetisation changes of less than 10^{-6} emu at a data rate of 1 Hz.

4.2 X-ray Reflectivity (XRR)

X-ray reflectivity is a non-destructive, non-contact technique for structural characterization of thin films. Information about the thickness, roughness and refractive index can be be obtained by analysing the intensity of x-rays reflected at a grazing angle from the flat surface[134].

The XRR method involves monitoring the intensity of a x-ray beam reflected at 2θ as the grazing angle of the incident x-ray beam θ is varied. The reflection from the surface and interfaces is due to different electron densities in different layers of the film (which correspond to refractive indexes in traditional optics). XRR is sensitive to the material density (ρ) as ρ is proportional to the critical angle (θ) at which total internal reflection occurs, (for full equations see [136] equations (2)-(6)). For incident angles above, but close to, θ_c reflection from different interfaces gives rise to oscillations

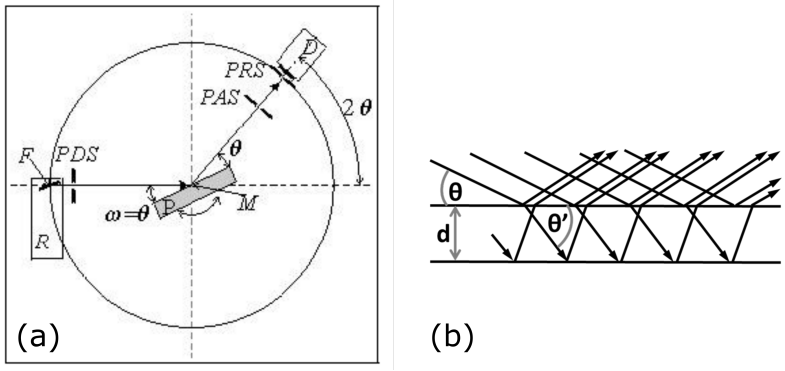

Figure 4.2: (a) Typical $\theta/2\theta$ XRR scan geometry in which both the detector and the sample rotate about the same axis MP (perpendicular to drawing). (b) Reflection from two planes separated by a distance d.

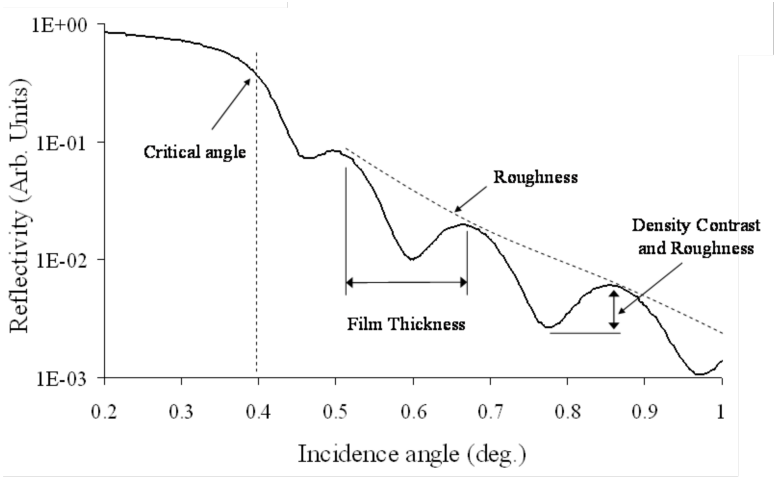

Figure 4.3: Typical $\theta/2\theta$ intensity profile with film characteristics. Figure adapted from [135].

of the x-ray intensity, measured as interference fringes. The period and decay in intensity of the interference fringes are related to the layer thickness (t) and roughness (σ_{rms}) respectively. If the interface is not perfectly sharp and smooth then the reflected intensity will deviate from that predicted by the Fresnel reflectivity[137] and can be analysed to extract these quantities where ($t \propto \lambda/(2\Delta\theta)$) and σ_{rms} is proportional to the drop in reflected intensity and goes as $I^R = I_0^R \exp(\beta\sigma_{rms}^2)$.

4.3 X-ray Diffraction (XRD)

X-ray diffraction (XRD) is a technique which can provide a wide range of information about the structure of materials including the crystal phase and texture, film thickness, grain size and stress of a sample[138].

A monochromatic beam of X-rays is incident on the crystal sample. Each atom scatters the incident x-rays in all directions but for certain orientations the scattered beams are in phase and hence interfere constructively. This behaviour occurs when the crystal lattice spacing d and the grazing beam angle θ satisfy the Bragg condition[138] $n\lambda = 2d\sin\theta$. The diffracted beam is collected by a detector as both the incident beam angle θ and the Bragg angle (2θ) (the angle between the incident and diffracted beam) are swept.

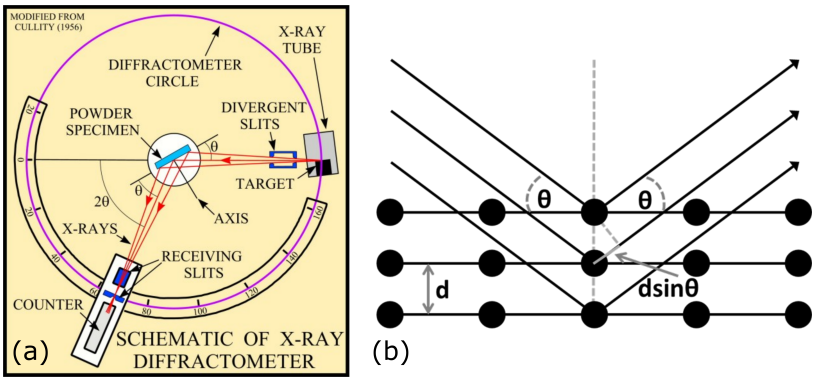

Figure 4.4: (a) Typical X-ray diffraction geometry (figure adapted from [139]). (b) reflections of X-rays satisfying the Bragg condition from multiple planes, where d is the crystal lattice spacing and θ is the reflection angle.

The position of the peaks in the resultant XRD spectrum gives information about the composition and texture of the sample. Shift of these peaks relative to those of the bulk samples arise from lattice distortions, often due to strain. In the case of thin films the peak width can be used to find the thickness, and in polycrystalline samples tells of the grain size.

4.4 Magneto-optical Kerr Effect (MOKE)

In 1845 Michael Faraday[140] observed that when linearly polarised light was passed through a dielectric medium (in this case glass), with a magnetic field applied along the axis of propagation, the axis of polarisation was rotated. He found the effect was

proportional to the strength of the magnetic field and the distance travelled within the medium. This discovery established a new fundamental interaction between electromagnetism, light and matter. In 1884 this effect, now known as the Faraday effect, was demonstrated by Kundt[141] in optically transparent ferromagnetic thin films of Fe, Co and Ni deposited on glass. He observed that the Faraday rotation was 30,000 times larger than for light transmitted through these materials than for the glass alone. Finally in 1877 Kerr[142, 143] discovered a similar effect in reflection whilst examining the polarisation of light reflected from a polished electromagnet. These effects, now known as the magneto-optical Kerr effect (MOKE) and the magneto-optical Faraday effect are both proportional to the temperature dependent magnetisation $\mathbf{M}(T)$ of the ferromagnetic material. This effect is the basis for one of the most frequently applied experimental tools in magnetism[144] due to its sensitivity, local probing nature and relative experimental simplicity[145].

4.4.1 Origins of the Magneto-Optical Kerr Effect

The films studied in this thesis were opaque and so the reflective MOKE geometry was necessary to study their properties. In parts of the following section the origins of these magneto-optical effects are discussed in terms of the Faraday effect for simplicity but the physical origins apply similarly to MOKE.

Magneto-optics is described either in the context of macroscopic dielectric theory, where the magneto-optic effect arises from the antisymmetric off-diagonal elements in the dielectric tensor, or in the context of microscopic quantum theory, where coupling between the electric field of light and the electron spin within the magnetic medium occurs through the spin orbit interaction. In the following sections both interpretations are discussed loosely following the descriptions in references [145] and [146].

4.4.2 Phenomenological Description

Maxwell expressed linearly polarised light as a superposition of two circularly polarized components and realized that the Faraday effect could be explained as a result of different propagation velocities of each component. For light propagating in a magnetized medium the two different circularly polarised modes gain different phase shifts due to their different propagation velocities, which results in the conventional Faraday rotation of the polarization plane. There is also a difference in the absorption rate for the different polarized modes which effects the ellipticity. For transparent materials

the rotation dominates the ellipticity, but for metals the ellipticity is comparable to the rotation. Generally both of these effects exist in a magnetised medium.

The response of a medium to an external field can be described by the dielectric tensor, ϵ_{ij} (with $i, j = 1, 2, 3$) which relates the displacement vector **D** to the electric field according to $\mathbf{D} = \epsilon\mathbf{E}$ and is given by

$$\tilde{\epsilon} = \begin{pmatrix} \epsilon_{ii} & \epsilon_{ij} & \epsilon_{ik} \\ -\epsilon_{ij} & \epsilon_{ii} & \epsilon_{jk} \\ -\epsilon_{ik} & -\epsilon_{jk} & \epsilon_{ii} \end{pmatrix}. \tag{4.5}$$

This tensor reduces to the dielectric constant for isotropic media, or materials with a high crystal symmetry however for ferromagnetic materials the symmetry is broken by the spontanious magnetisation (**M**). In general this tensor can be split into a symmetric and antisymmetric part $\epsilon_{ij} = (\epsilon_{ij} + \epsilon_{ji})/2 + (\epsilon_{ij} - \epsilon_{ji})/2$. As the symmetric part can be diagonalised by an appropriate rotation of the coordinate system it is clear that this has no effect on the polarization of light polarized parallel to one of the three principal axes. The dielectric tensor has to obey the Onsager reciprocal relation by magnetisation reversal, which requires the diagonal elements to be even ($\epsilon ij(M) = -\epsilon_{ij}(-M)$) and the off diagonal elements to be odd ($\epsilon_{ij}(M) = -\epsilon_{ij}(-M)$)[146]. It is these antisymmetric off diagonal elements which give rise to the Faraday rotation. To first order in the magnetisation the diagonal elements are independent of **M**, while the off diagonal elements are proportional to **M**.

To see the effect of the antisymmetric part of the dielectric tensor Qiu *et al*[145] consider a dielectric tensor in the form

$$\tilde{\epsilon} = \epsilon \begin{pmatrix} 1 & iQ_z & -iQ_y \\ -iQ_z & 1 & iQ_x \\ iQ_y & -iQ_x & 1 \end{pmatrix}. \tag{4.6}$$

The two normal modes are left-circularly polarized light with refractive index $n_L = n(1 - 1/2\mathbf{Q}.\hat{k})$ and right-circularly polarized light with refractive index $n_R = n(1 + 1/2\mathbf{Q}.\hat{k})$, where $n = \sqrt{\epsilon}$ is the average refractive index, **Q**=(Q_x, Q_y, Q_z) is called the Voigt vector[147] and is $\parallel$ to **M**, $\hat{\mathbf{k}}$ is the unit vector along the direction of light propagation. The complex Faraday rotation of the polarisation plane after the light has travelled a distance L through the medium is

$$\theta = \frac{\pi L}{\lambda}(n_L - n_R) = -\frac{\pi L n}{\lambda}\mathbf{Q}.\hat{k}. \tag{4.7}$$

It is the real part of equation 4.7 which gives rise to the rotation and the imaginary part which gives rise to the ellipticity. In the simple case where **M** lies along the z-axis and a beam of light is propagating along the z-axis, **Q** is proportional to the component of magnetization along the z-axis. The differences in the refractive indices experienced by the two modes generates the magneto-optical effect and which is proportional to Q, i.e. the consequence of these off-diagonal tensor elements is that light propagating along the z-axis with an electric field along the x-axis will experience an electric displacement along the y-axis.

4.4.3 General Formalism of the Magneto-Optical Kerr Effect

Since the majority of magnetic materials are metals it is more convenient experimentally to measure the reflected light in order to probe the magneto-optical effect. A general method for modelling the MOKE in a planar structure is to treat it as multiple magnetic layers and apply Maxwell's equations to each, with the imposition of appropriate the boundary conditions at each interface (figure 4.5).

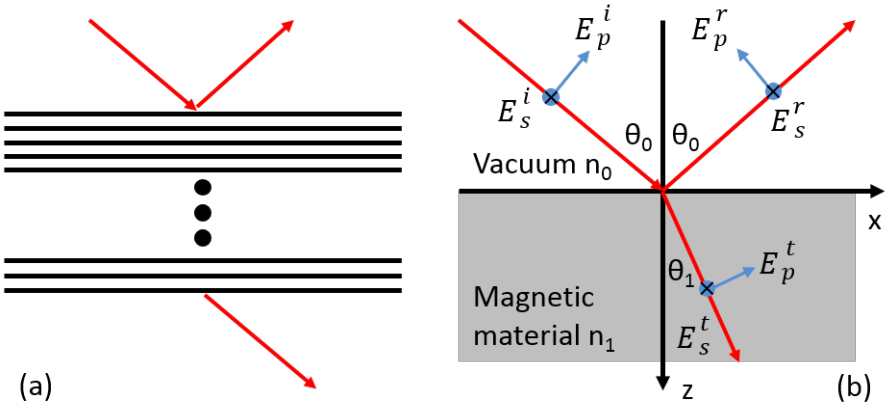

Figure 4.5: (a) Schematic of a multilayer structure (b) Definitions of the s and p directions for light reflected at the boundary between vacuum and a magnetic material.

This is done by deriving two matrices which relate the electric fields at each interface. The first, known as the 'medium boundary matrix', relates the tangential components of the electric and magnetic fields to the amplitudes of the s and p components of the electric field. The second, known as the 'medium propagation matrix', relates the s and p components of the electric field at the two surfaces of a film of thickness d. With these two matrices it is possible to calculate the magneto-optic effect under any conditions (see reference [145] appendix for details). This method can be used

to obtain the reflected electric field components $E_p^{(r)}$ and $E_s^{(r)}$ of elliptically polarized light in terms of the incident electric field E_p and E_s components using the Jones matrix formalism

$$\begin{pmatrix} E_s^{(r)} \\ E_p^{(r)} \end{pmatrix} = \begin{pmatrix} r_{ss} & r_{sp} \\ r_{ps} & r_{pp} \end{pmatrix} \begin{pmatrix} E_s^{(i)} \\ E_p^{(i)} \end{pmatrix}, \tag{4.8}$$

where r_{ij} are the optical reflection coefficients.

In the ultrathin limit (the optical thickness of the film is much less than the wavelength of the light) the magneto-optic expressions simplify further. In this limit the reflection coefficients have been calculated by Metzger *et al*[148], [149] at the interface between a vacuum and magnetic material, up to second-order in the Voigt parameter. To the first order in Q the coefficients are,

$$r_{ss} = \frac{n_0 \cos\theta_0 - n_1 \cos\theta_1}{n_0 \cos\theta_0 + n_1 \cos\theta_1}, \tag{4.9}$$

$$r_{pp} = \frac{n_1 \cos\theta_0 - n_0 \cos\theta_1}{n_1 \cos\theta_0 + n_0 \cos\theta_1} + \frac{2iQn_1 n_0 \cos\theta_0 \sin\theta_1 \mu_y}{(n_1 \cos\theta_0 + n_0 \cos\theta_1)^2}, \tag{4.10}$$

$$r_{ps} = \frac{iQn_0 n_1 \cos\theta_0 (\sin\theta_1 \mu_x - \cos\theta_1 \mu_z)}{\cos\theta_1 (n_0 \cos\theta_0 + n_1 \cos\theta_1)(n_1 \cos\theta_0 + n_0 \cos\theta_1)}, \tag{4.11}$$

$$r_{sp} = \frac{iQn_0 n_1 \cos\theta_0 (\sin\theta_1 \mu_x + \cos\theta_1 \mu_z)}{\cos\theta_1 (n_0 \cos\theta_0 + n_1 \cos\theta_1)(n_1 \cos\theta_0 + n_0 \cos\theta_1)}, \tag{4.12}$$

where θ_0 and θ_1 are the angles of incidence and refraction, n_0 and n_1 are the refractive indices of the vacuum and the magnetic material, and μ_i are the Cartesian components of the unit vector parallel to the magnetisation.

The Kerr angle Φ_K and ellipticity ϵ_K for p-and s-polarized light are then given by

$$\Phi_K^p = -Re\left(\frac{r_{sp}}{r_{ss}}\right) \text{ and } \epsilon_K^p = Im\left(\frac{r_{sp}}{r_{pp}}\right) \tag{4.13}$$

and

$$\Phi_K^s = -Re\left(\frac{r_{ps}}{r_{ss}}\right) \text{ and } \epsilon_K^s = Im\left(\frac{r_{ps}}{r_{ss}}\right) \tag{4.14}$$

respectively.

4.4.4 Microscopic Description

The optical properties of a medium are described by a dielectric tensor in which the various terms arise from the motion of electrons within the medium. We can consider a beam of linearly polarized light as a superposition of left and right circularly polarised modes with equal amplitude. If we take the classical picture, when this beam propagates through a medium its electric field generates motion of the electrons within the medium. For an isotropic medium a left-circularly polarised electric field will drive the electrons into left-circularly polarized motion and a right-circularly polarised electric field will drive the electrons into right-circularly polarized motion. The radius of the electron orbit will be the same for both left and right circular motion. Since the electric dipole moment is proportional to the radius of the orbit there will be no difference in the dielectric constants for left and right circularly polarized waves and so no Faraday rotation. If an external magnetic field is applied along the propagation direction of the electromagnetic wave there will be an additional Lorentz force acting on the electrons. This force acts to increase or decrease the radius of electron orbit dependent on whether the light is left or right circularly polarized and thus gives rise to different dielectric constants. In this way the Lorentz force of the external magnetic field can be thought of as generating the Faraday effect[150].

In this interpretation the equation of motion for the electrons under a driving magnetic field with an applied static field **B** is

$$m_e \frac{d^2\mathbf{r}}{dt^2} + \frac{1}{\tau}\frac{d\mathbf{r}}{dt} + m_e\omega_0^2\mathbf{r} = -e\mathbf{E}(t) - \frac{e}{c}\frac{d\mathbf{r}}{dt} \times B\hat{\mathbf{z}}, \tag{4.15}$$

where m_e is the electron mass, τ is the electron relaxation time and ω_0 is the natural resonance frequency. Equation 4.15 is linear and can be solved for an electromagnetic wave of frequency ω. The Cartesian components r_i, are obtained from the relation $P_i = -ner_i = (\epsilon_{ij} - 1)E_j/4\pi$ where n is the electron density, so that the dielectric tensor has the form

$$\tilde{\epsilon} = 1 + \frac{4\pi ne^2}{m} \begin{pmatrix} \frac{\gamma}{\omega^2\gamma^2 - \omega_c^2} & \frac{i\omega_e/\omega}{\omega^2\gamma^2 - \omega_c^2} & 0 \\ -\frac{i\omega_e/\omega}{\omega^2\gamma^2 - \omega_c^2} & \frac{\gamma}{\omega^2\gamma^2 - \omega_c^2} & 0 \\ 0 & 0 & \frac{1}{\omega^2\gamma} \end{pmatrix}, \tag{4.16}$$

where ω is the optical frequency, $\omega_c = eB/mc$ is the cyclotron frequency, and $\gamma = (\omega_0^2/\omega^2) - 1 - (i/\omega\tau)$ where τ is the electron relaxation time. Though this model can predict Faraday rotation in a medium with an external magnetic field it does not consider the magnetisation of the medium itself so does not predict the much

larger Faraday rotation observed in ferromagnetic materials. In order to explain the unusually large magneto-optic effect in ferromagnetic materials a quantum mechanical interpretation is required.

4.4.5 Quantum Description

Early attempts to explain the larger Faraday rotation in ferromagnets assumed an effective field alongside the applied field which Voigt calculated would need to be of the order of $10^6 - 10^7$ Oe to produce the observed Faraday rotation. This magnitude is of the order of the Weiss field[151, 152] that was postulated to account for the existence of ferromagentism. This Weiss field remained largely unexplained until after the advent of quantum mechanics when Heisenberg[153, 154] showed the exchange interaction between electrons to be the origin of the magnetism behaving as an effective field to align individual spins. This interaction cannot be used to explain the Faraday rotation as it is not coupled to the electron motion, which determines the dielectric properties of the material. Hulme[155] solved this problem in 1932 when he proposed that the spin-orbit interaction gives rise to the large Faraday rotation in ferromagnets. As an electron with momentum $\mathbf{p}$ moves in a medium it 'sees' a magnetic field as it moves through the electric field $-\nabla V$ and the spin-orbit coupling energy $(\sim (\nabla V \times \mathbf{p}).\mathbf{s})$ results from the interaction of the electron spin ($\mathbf{s}$) with this magnetic field. This interaction couples the electron's magnetic moment to its motion linking the magnetic and optical properties of a ferromagnet. The spin-orbit interaction can be thought of as an effective magnetic field vector acting on the motion of the electron. For non-magnetic materials the equal number of up and down spin electrons results in a net effect of zero, but for ferromagnets the spin imbalance at the Fermi level leads to a net effect on the orbital motion of the electrons.

Since the refractive index (and so the electron motion) is related to the complex conductivity by a constant as $\epsilon_{ij} = 1 + i4\pi\sigma_{ij}/\omega$ it is only required to calculate the conductivity, principally the off-diagonal elements, in order to obtain the magneto-optical effect. Calculation of the conductivity tensor is generally made under the assumptions that the frequency of light is much greater than the spin-lattice relaxation rate, the interaction of the electric field of the incident light with the electron is much stronger than the magnetic interaction and that the wavelength of the incident light is much larger than the atomic spacing. The final assumption is that the interaction of the electron inside the crystal with other electrons can be represented by a periodic

potential $V(r)$. Under these assumptions the Hamiltonian can be written as

$$H = H_0 + H' + H'', \tag{4.17}$$

where

$$\begin{aligned} H_0 &= \frac{p^2}{2m} + V(r) \\ H' &= \frac{\hbar}{4m^2c^2}(\nabla V \times \hat{\mathbf{p}}).\hat{\sigma} \\ H'' &= \frac{e}{mc}\mathbf{A}.\hat{\mathbf{p}}, \end{aligned} \tag{4.18}$$

where in these expressions, $\hat{\mathbf{p}}$ and $\hbar\hat{\sigma}/2$ are the momentum and spin operators of the electron, and $\mathbf{A}$ is the vector potential of the electromagnetic field inside the material. The second term in the Hamiltonian represents the spin-orbit interaction, and the third term describes the interaction of the material with the electromagnetic wave. There are two methods of calculating the conductivity tensor, the method used by Argyres[156] and that of Bennett and Stern[157].

Argyres obtained the eigenfunctions of H_0 (in the absence of the external magnetic field). He then treated the spin-orbit interaction as a perturbation to the single electron Hamiltonian to obtain the eigenfunctions of $H_0 + H'$. Finally the electromagnetic field was treated as a time-dependent perturbation (H'') acting on the electron. The conductivity tensor is then obtained from the current density operator.

Bennett and Stern obtained expressions for the weak-field Faraday effect in cubic materials for the cases of transmission and reflection by relating elements of the conductivity tensor with the optical transition rates. The macroscopic absorbed power can be written in terms of the incident electric field and the conductivity tensor. Microscopically the power absorption is due to the transition between different quantum states, which are governed by dipole selection rules. The transition rates can be calculated from Fermi's golden rule, and is proportional to the transition matrix elements of the kinetic momentum. The kinetic momentum is invariant under a Lorentz transformation and includes a term $\mathbf{s} \times \nabla\phi$ which represents the effective magnetic vector potential that results from the SO interaction. A sum taken over all transitions gives the absorbed power. The elements of the conductivity tensor can then be calculated by relating the power absorbed in terms of the transition rates to the power absorbed in terms of the elements of the conductivity tensor.

4.5 Measuring the Magneto-Optical Kerr Effect

4.5.1 Magneto-Optical Kerr Effect Geometries

There are three fundamental Kerr geometries which are defined by the orientation of the magnetisation **M** and polarisation of the incident light (E_s or E_p). In the polar Kerr configuration shown in figure 4.6.(a), **M** is oriented normal to the film plane and in the plane of the incident light and is sensitive to the out-of-plane component of the magnetisation. The longitudinal Kerr configuration,shown in figure 4.6.(b) **M** lies in the film plane and in the plane of incident light and is sensitive to the in-plane component of the magnetization. The polar and longitudinal MOKE manifests as a change in the polarization rotation (θ_K) and/or ellipticity (ϵ). The transverse Kerr configuration, shown in figure 4.6.(c) **M** also lies in the film plane but perpendicular to the plane of incident light. The transverse effect is also sensitive to the in-plane component of the magnetization but the effect and manifests instead as an **M** dependent change in reflectivity (ΔI).

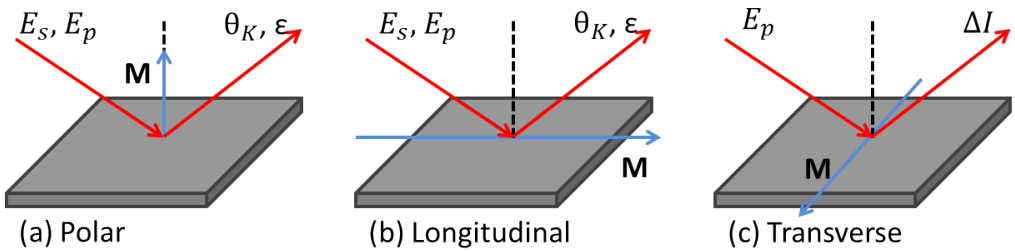

Figure 4.6: The three fundamental MOKE geometries (a) polar (b) longitudinal and (c) transverse defined by direction of magnetic field and incident light polarization.

4.5.2 Magneto-Optical Kerr Effect Detection

Static MOKE measurements were performed using a 633 nm wavelength, s-polarized, focused He-Ne laser beam. Typically the longitudinal and polar configurations were used with an angle of incidence of 45 and 0 ° respectively. The beam spot was typically focused to 200 μm and an electromagnet used to vary **H**. The light reflected from the sample was incident normal to an optical bridge detector with which the polarization rotation/ellipticity was detected. A typical example of static MOKE in the polar configuration, including the optical bridge detector is shown in figure 4.7.

Inside the bridge detector a Glan-Thompson polarising beam splitter separates

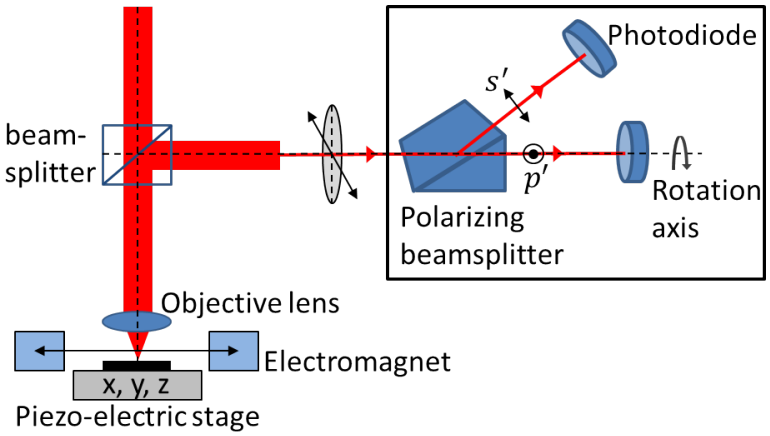

Figure 4.7: Typical scanning microscope MOKE geometry, showing the internal bridge detector optics in the inset on the right.

the light reflected from the sample into orthogonal 's' and 'p' components (note here that 's' and 'p' are defined relative to the polariser rather than to the sample). The Glan-Thompson polarising beam splitter is made of two birefringent prisms cemented together so that the optical axes of the crystals are parallel. The value of the refractive index is different along the directions perpendicular and parallel to the optical axis so rays with **E**-fields perpendicular and parallel to the optical axis will propagate with different velocities. The specific geometry of the beam splitter is designed to transmit two beams of orthogonal polarisation separated by an angle of 45°. The intensity of the beams is detected by two photodiodes and the sum and difference taken by the amplification circuitry. For maximum sensitivity the bridge detector is rotated, typically to 45° to the plane defined by **k** and the un-rotated **E**-field, so that the intensity is equally divided between the 's' and 'p' polarizations and their difference is zero. When the polarization of the incident light is rotated by the sample magnetization the difference signal will vary.

For a beam with the electric field vector incident at θ° to the x-axis (as shown in figure 4.8) its two components are given by

$$E_x^r = E^r \cos\theta \tag{4.19}$$

and

$$E_y^r = E^r \sin\theta. \tag{4.20}$$

As the beam intensity is proportional to the square of the amplitude of the **E**-field, the

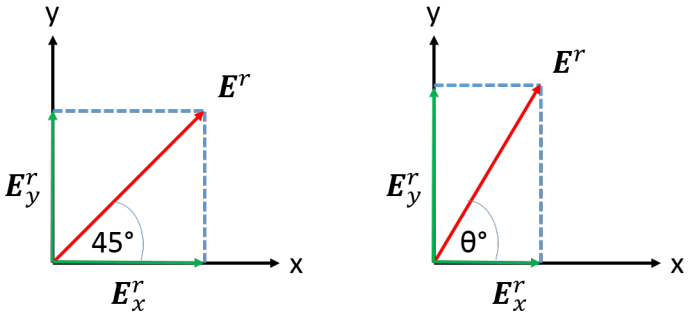

Figure 4.8: Rotation of the **E**-field components.

sum of the two diode outputs is proportional to the beam intensity and the difference gives the quantity

$$\Delta I = (E^r)^2(\cos^2\theta_K - \sin^2\theta_K) = (E^r)^2\cos(2\theta_K). \tag{4.21}$$

As θ_K is usually $\ll 1^\circ$, if the incident angle is $\approx 45^\circ$ then

$$\Delta I \propto \cos(45 + \theta_K + 45 + \theta_K) \propto \cos(90 + 2\theta_K) \tag{4.22}$$

and so under the approximation $\cos(\phi) \approx \phi$ close to $\phi = 90$

$$\Delta I \propto 2\theta_K \tag{4.23}$$

and so the Kerr rotation, and therefore the change in magnetisation direction, can be calculated from the difference in the two beam intensities.

In typical dynamic measurements, the magnetization does not lie within the plane of incidence as shown in figure 4.6 but instead precesses around a direction set by an external magnetic field. In this case it is necessary to resolve the change in the three Cartesian components of the magnetization namely M_x, M_y and M_z. For sensitivity to these three components a vector bridge detector is required. The critical difference between this form of detector and that shown in figure 4.7 is that the photo-diodes are replaced by quadrant-photodiodes. As shown in figure 4.9 a quadrant-photodiode is split into four equal sections which react independently to the incident light.

Like in the case of the simple bridge detector the beam incident on the vector bridge detector is split by a Glan-Thompson polarising beam splitter to fall on two separate quadrant photodiodes. When the incident beam is incident on the center of

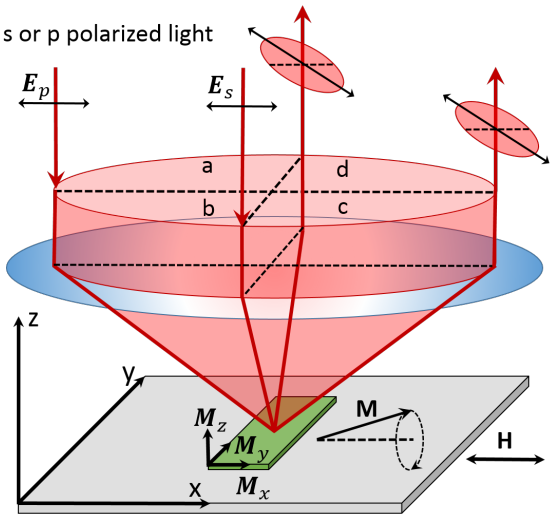

Figure 4.9: s or p polarised light focused through an objective lens onto a magnetic sample. The quadrant photodiodes are positioned so as to collect the different portions of the beam labelled a, b, c and d.

the quadrant-photodiode it is split into four equal parts arbitrarily labelled a, b, c and d. The beam incident on the $a+b$ half is reflected back to the $c+d$ half and the beam incident on the $c+d$ half will be reflected back to the $a+b$ half. The intensity sensed by each half of the quadrant photodiodes will be $I_{c_1+d_1}$ and $I_{c_2+d_2}$ and $I_{a_1+b_1}$ and $I_{a_2+b_2}$.

The longitudinal component of the Kerr rotation, due to M_x is equal to the intensity difference

$$\Delta I_x = I_{c_2+d_2} - I_{c_1+d_1} \tag{4.24}$$

for the $c+d$ beam, and

$$\Delta I_{-x} = I_{a_2+b_2} - I_{a_1+b_1} \tag{4.25}$$

for the $a+b$ part. Reversing the beam direction reverses the sign of the Kerr rotation. Both halves of the beam contain a polar component due to the M_z. So a subtraction of ΔI_x and ΔI_{-x} leaves no polar component, so

$$|\Delta I_x - \Delta I_{-x}| = 2|\Delta I_x|. \tag{4.26}$$

The same argument holds true for the $b+c$ and $a+d$ halves allowing detection of M_y.

Due to the opposite sign of the longitudinal components, they will disappear if the four quadrants are added together. This allows detection of the polar component due

to M_z as

$$|\Delta I_z| = I_{a_2+b_2+c_2+d_2} - I_{a_1+b_1+c_1+d_1}. \tag{4.27}$$

4.5.3 Time Resolved Scanning Kerr Microscopy

Time resolved scanning Kerr microscopy (TRSKM)[158] can be used to investigate magnetization dynamics on a time-scale theoretically determined by the width of the laser pulse (on the order of 100 fs). In practice the temporal resolution of the TRSKM system utilised in this thesis was the jitter in the current pulse generator $\approx$ 50 ps. This technique is capable of resolving dynamics in the GHz range. By focusing the beam this technique also allows sub-μm scale resolution.

The magnetization is first perturbed from its equilibrium orientation by a magnetic field, typically generated by a current pulse travelling along a micro-scale strip line, in close proximity to the sample. This thesis does also touch briefly on a laser induced thermal demagnetization which re-orients the magnetic field by reducing the magnetization and anisotropy field, therefore re-orienting the effective field acting on the magnetization. Pulses from an ultra-fast mode locked laser are then used to probe the magnetization state at some time t after the excitation, via the MOKE. By varying the delay between excitation pulse and optical probe a full profile of the evolution of the magnetization dynamics over several ns can be built up.

In this study the light source was a mode locked Ti:sapphire laser (Spectra-Physics Tsunami) with an 80 MHz repetition rate (details of mode-locking can be found in ref [159]). The Tsunami produces sub 100 fs pulses at a wavelength of $\approx$800 nm. At this wavelength the power was typically 0.6 W meaning each pulse had energy of $\approx$ 8 nJ. The beam diameter was 2 mm with a divergence of $\approx$ 1 mrad.

In the most simple configuration the laser was mode locked to an electrical impulse generator (Pico Second Pulse Labs PSPL 3600) by a master clock (Atlantec low phase noise oscillation instrument). The pulse generator is modulated at a kHz frequency. The relative delay t between electrical pulse and laser probe is varied using a mechanical delay line, consisting of a retro-reflector mounted on a 1-D stepper stage as shown in figure 4.10. The delay in the probe beam comes from the increase in path length as the translation stage is stepped. From the retro-reflector the probe beam passes to a beam expander (to ensure a uniform illumination of the rear of the microscope obhective) before being re-focused on the sample surface. The reflected beam is re-collimated and a beam splitter delivers it to the bridge detector. The electrical output from the bridge detector is passed to a series of lock-in amplifiers[160, 161], whose reference frequency

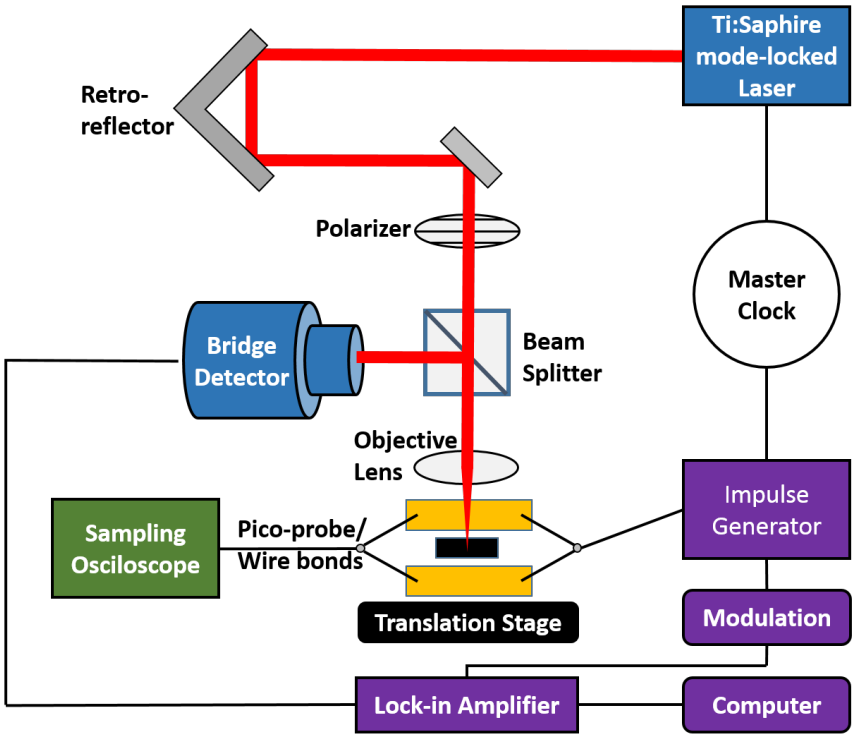

Figure 4.10: Schematic of a typical time resolved scanning Kerr microscopy set up. The clock illustrates how a master oscillator used to synchronise the electrical pump and the laser probe.

is the same as the modulation frequency, before being recorded by a computer. An in depth description of this experimental set up can be found in reference [159].

One fundamental limit of the set up shown in figure 4.10 is that some magnetic dynamics take place on a longer time-scale than the 4 ns it is possible to measure with the mechanical retro-reflector. In cases such as this it is necessary to 'pick' the laser pulse down to a lower repetition rate in order to fully capture the samples response. An example of one such method is shown in figure 4.11. The beam passes through an electro-optic modulator which contains a potassium dideuterium phosphate crystal and a polariser and operates based on the Pockel's effect[162] to block, in the case of figure 4.11, every 7/8 pulses. After the pulse picker a 90/10 beam splitter allows the majority of the beam to continue its path along the same path as is figure 4.10. The other portion of the beam is sent into a photodiode and the output of this is converted to a transistor-transistor logic (TTL) pulse[163], in order to trigger the electrical pulse side of the experiment at the same repetition rate as the picked laser. The TTL pulse is

passed to a delay generator (Stanford Research Systems DG645) which in turn triggers the impulse generator (Avtech AVP-AV-HV3 Ultra High Speed Pulse Generator). The delay generator is digitally controlled in order to vary the time between the electrical pump and laser probe and can sweep the full time between probe pulses (100 ns at 10 MHz). In this experiment the uni-polar electrical pulse is then split into two pulses using a power divider, and each is sent down a different cable of carefully selected length. In one cable section a pulse inverter reverses the pulse polarity before the two pulses are recombined to form a bi-polar pulse. Figure 4.11 also demonstrates the set up of the oscilloscope to measure the electrical pulse reflected from a device, in this case the device is not connected in transmission but in a 'shorting' configuration, both configurations were used in this work. In this configuration a directional coupler sends the return/reflected pulse from the device to the oscilloscope, which is also triggered from the delay generator, in order to match the repetition rate.

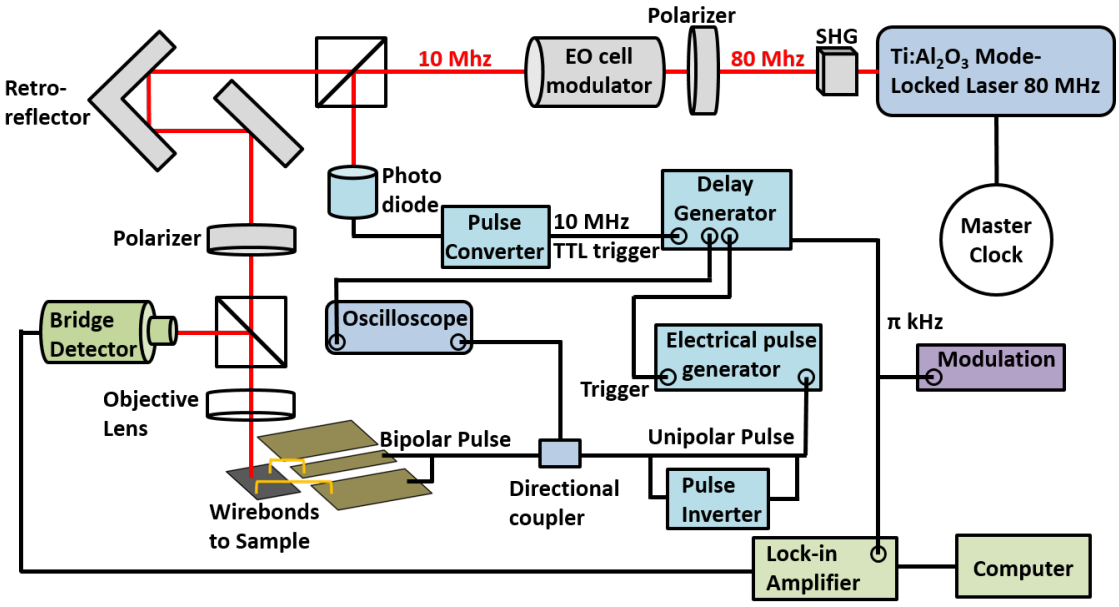

Figure 4.11: Schematic of a typical time resolved scanning Kerr microscopy set up for use when magnetisation dynamics occur between 12.5-1 μs.

4.6 Vector Network Analyser Ferromagnetic Resonance

4.6.1 Vector Network Analyser Operation

A vector network analyser (VNA) combines a broadband frequency source (up to the GHz range) with electronics to measure the amplitude and phase of electromagnetic waves both transmitted and reflected from a device under test (DUT). The broadband microwave source, typically a 'wobble generator' emits a microwave wave, here labelled V_0 of frequency f. A power splitter divides V_0 into a reference wave V_{ref}, which is guided to the detection scheme, and another wave V_{inc}, which is guided to the DUT. At the DUT there is typically partial transmission (V_{trans}) and reflection (V_{refl}) of V_{inc}. By means of a directional coupler these components are also guided to the detection scheme as shown in figure 4.12.

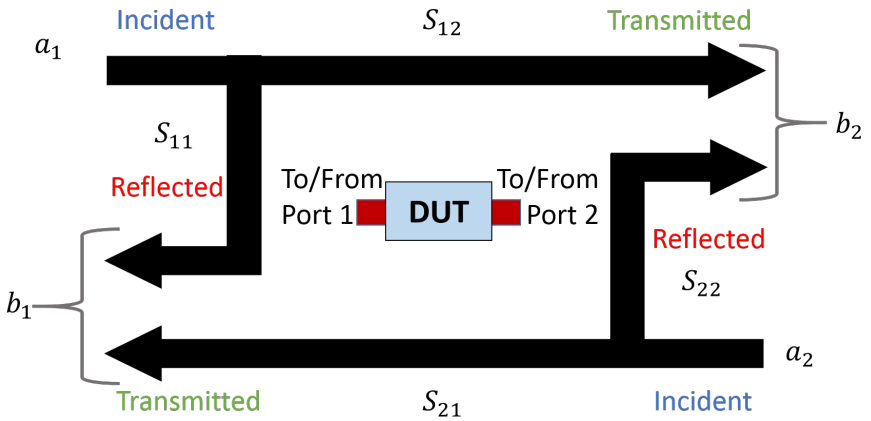

Figure 4.12: Definition of S-parameters for a 2-port measurement.

The behaviour of the DUT is typically described using the scattering parameters or S-parameters which describe the relative transmission and reflection of V_{inc}. An N-port device has N^2 S-parameters, so a two-port device as typically used in the measurements described in this thesis has four S-parameters. The naming convention for S-parameters is that the first number following the "S" is the port where the signal emerges, and the second number is the port where the signal is applied. So S_{12} is a measure of the signal coming out of port 1 relative to the r.f. stimulus measured at port 2 i.e. the signal transmitted from port 1 to 2. When the numbers are the same such as S_{11} this indicates

a reflection measurement of the signal coming out of port 1 relative to the r.f. stimulus measured at port 1[164]. Measurement of the S-parameters requires measurement of V_{inc}, V_{trans} and V_{refl} when the output is terminated in a perfect impedance matched load (a load that equals the characteristic impedance of the test system). Under these conditions the S-parameters are defined as

$$\begin{aligned} S_{11}(\omega) &= \frac{V^1_{refl}(\omega)}{V^1_{inc}(\omega)} & S_{12}(\omega) &= \frac{V^2_{trans}(\omega)}{V^1_{inc}(\omega)} \\ S_{21}(\omega) &= \frac{V^2_{trans}(\omega)}{V^1_{inc}(\omega)} & S_{22}(\omega) &= \frac{V^2_{refl}(\omega)}{V^2_{inc}(\omega)} \end{aligned} \tag{4.28}$$

or

$$\begin{aligned} S_{11} &= \frac{b_1}{a_1}\Big|_{a_2=0} & S_{12} &= \frac{b_1}{a_2}\Big|_{a_1=0} \\ S_{21} &= \frac{b_2}{a_1}\Big|_{a_2=0} & S_{22} &= \frac{b_2}{a_2}\Big|_{a_1=0} \end{aligned}. \tag{4.29}$$

4.6.2 Vector Network Analyser Ferromagnetic Resonance (VNA-FMR) Measurements

In its simplest terms the Vector Network Analyser ferromagnetic resonance measurement (VNA-FMR) works by applying a time varying r.f. magnetic field ($\mathbf{h}_{rf}$) to the sample which exerts a torque on its magnetisation $\mathbf{M}$ driving precession. The exertion of torque on $\mathbf{M}$ by $\mathbf{h}_{rf}$ can be measured as an energy absorption by the sample. The energy absorbed is at a maximum when the system is at FMR with $\omega = \omega_r$.

According to the Landau-Liftshitz-Gilbert (LLG) equation (section 2.11) when the equilibrium magnetization is disturbed by a perturbing field then $\mathbf{m}$ strives to align parallel to the effective magnetic field ($\mathbf{H}_{eff}$) in order to minimize energy. The resultant motion of $\mathbf{m}$ is a precession around $\mathbf{H}_{eff}$ following a damped helical trajectory until alignment with $\mathbf{H}_{eff}$ is obtained. When $\mathbf{h}_{rf}$ is added to $\mathbf{H}_{eff}$ it causes a disturbance of the equilibrium that excites the magnetization, and a transverse component of the magnetization arises. The total magnetization is then at a small angle with respect to its former direction parallel to the magnetic field $\mathbf{H}_{eff}$. At the resonance condition $\mathbf{h}_{rf}(\omega) = \mathbf{h}_{rf}(\omega_r)$ the r.f. field coincides with the precessional frequency of the magnetization and spin resonance occurs and the angle between $\mathbf{m}$ and the effective field vector increases. Since the dynamic susceptibility ($\tilde{\chi}$) connects the magnetization $\mathbf{M}$ with the magnetic field ($\mathbf{H}$) as

$$\tilde{\chi} = \frac{\delta \mathbf{M}}{\delta \mathbf{H}}, \tag{4.30}$$

then any change in this angle affects $\tilde{\chi}$. As the dynamic susceptibility of the sample is linked to the energy absorption from $\mathbf{h}_{rf}$, this provides a useful method to gain

information about $\tilde{\chi}$.

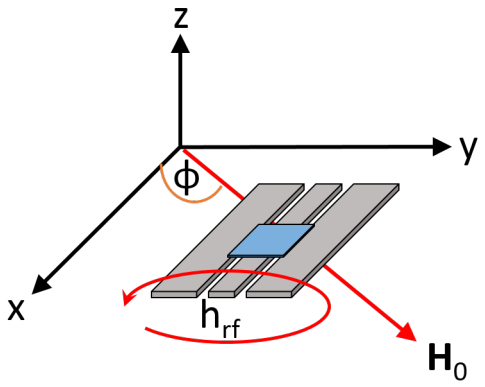

Figure 4.13: Direction of the perturbing field $\mathbf{h}_{rf}$ and the applied field H_0 relative to the waveguide.

An expression $\tilde{\chi}$ (a full derivation is beyond the scope of this thesis and can be found in[165]) can be found by inserting the full effective magnetic field $\mathbf{H}_{EFF} = \mathbf{H}_{eff} + \mathbf{h}_{rf}$ into the LLG equation. Several simplifying assumptions are made, that the excitation field of the waveguide only has components in the y-z plane and $\mathbf{h}_{rf}^{y} \gg \mathbf{h}_{rf}^{z}$, only terms where $\mathbf{m}$ has a linear time dependence are considered, and the resonant frequency ω_r can be introduced from the Kittel formula[43] as

$$\omega_r^2 = \omega_M \omega_H (1 + \frac{2K}{\mu_0 M_s^2}) + \omega_H^2, \tag{4.31}$$

where $\omega_M = \gamma \mu_0 M_s \cos(\phi)$, $\omega_H = \gamma \mu_0 H_0 \cos(\phi)$, K is the anisotropy constant, μ_0 is the vacuum permeability and M_s is the saturation magnetisation. Under these assumptions equations for the real $\tilde{\chi}^R$ and imaginary $\tilde{\chi}^I$ components of the dynamic susceptibility can be derived[165] and expressed as

$$\tilde{\chi}^R = \frac{\omega_M(\omega_M(1+\frac{2K}{\mu_0 M_s^2}) + \omega_H)(\omega_r^2 - \omega^2) + \alpha^2\omega^2\cos^2(\phi)(\omega_M(1+\frac{2K}{\mu_0 M_s^2}) + 2\omega_H)}{(\omega_r^2 - \omega^2)^2 + \alpha^2\omega^2\cos^2(\phi)(\omega_M^2(1+\frac{2K}{\mu_0 M_s^2})^2 + 4\omega_r^2)} \tag{4.32}$$

and

$$\tilde{\chi}^I = \frac{\omega_M \alpha\omega\cos(\phi)(\omega_M^2(1+\frac{2K}{\mu_0 M_s^2})^2 + \omega_r^2 + \omega^2 + \omega_M(1+\frac{2K}{\mu_0 M_s^2})\omega_H)}{(\omega_r^2 - \omega^2)^2 + \alpha^2\omega^2\cos^2(\phi)(\omega_M^2(1+\frac{2K}{\mu_0 M_s^2})^2 + 4\omega_r^2)}, \tag{4.33}$$

where α is the damping constant. These equations break the susceptibility down according to the complex formula $\tilde{\chi} = \tilde{\chi}^R + i\tilde{\chi}^I$ and are valid only for thin films when the external field is applied in the film plane. In this derivation any anisotropy in the plane of the film is neglected.

As shown in figure 4.14 the real part of the susceptibility is antisymmetric and is equal to zero at resonance. Whilst this is true for small damping, it is worth noting that the shape can deviate slightly for larger damping due to the second order damping term in the numerator. The imaginary part of the susceptibility has a Lorentzian shape with a maximum at the resonant condition $\omega = \omega_r$. It is this part of the susceptibility which corresponds to the energy absorption from $\mathbf{h}_{rf}$ by the sample.

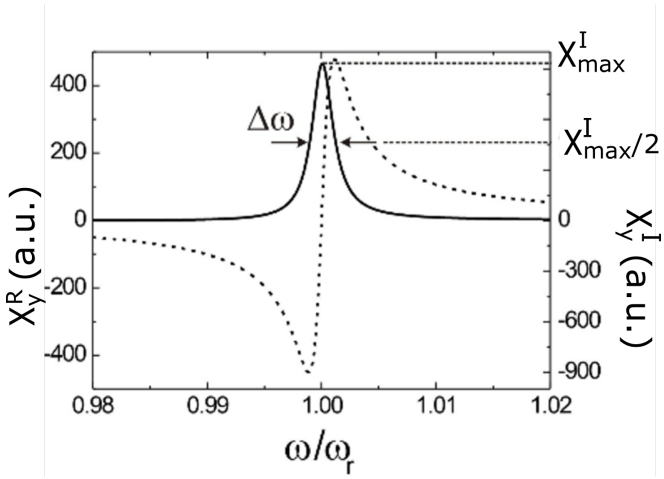

Figure 4.14: Example of the real (dashed line) and imaginary (solid line) part of the complex susceptibility as a function of frequency. Figure adapted from reference [166].

The full width of the imaginary susceptibility at half maxima ($\Delta\omega$) is related to the damping parameter by

$$\alpha = 2\Delta\omega(2\omega_H + (1 + \frac{2K}{mu_0 M_s^2})^2\omega_M). \tag{4.34}$$

In the work presented in this thesis typically the Gilbert damping parameter α was instead extracted from the frequency dependent linewidth $\Delta H(\omega)$ (Full width half maxima (FWHM)). Lattice imperfections can contribute an inhomogeneous broadening $\Delta H(0)$ to the FMR linewidth. The intrinsic Gilbert damping parameter can be isolated

from this broadening effect through the equation[167]

$$\Delta H(\omega) = \Delta H(0) + \frac{2\alpha\omega}{\gamma}. \tag{4.35}$$

4.7 Vector Network Analyser Ferromagnetic Resonance Experimental Set up

The VNA-FMR set up utilised in this thesis comprises a Vector Network Analyser connected to a high bandwidth waveguide and an in-plane quadrupole electromagnet. The VNA serves as both source and detector of the microwave frequency perturbing field $\mathbf{h}_{rf}$ orthogonal to the current direction ($\hat{\mathbf{y}}$) whilst the in-plane electromagnet provides a bias field H_0 along the current direction ($\hat{\mathbf{x}}$). The VNA sweeps through a frequency range of 0-26.5 GHz and H_0 can be varied from 0.0-1.5 kOe.

The VNA-FMR set up is shown in figure 4.15, the signal from the VNA signal out port is guided via microwave coaxial cables to pins soldered to a coplanar waveguide impedance matched to 50 Ω. The waveguide pitch and signal line width varies but typically the signal line width lies between 200 and 500 μm.

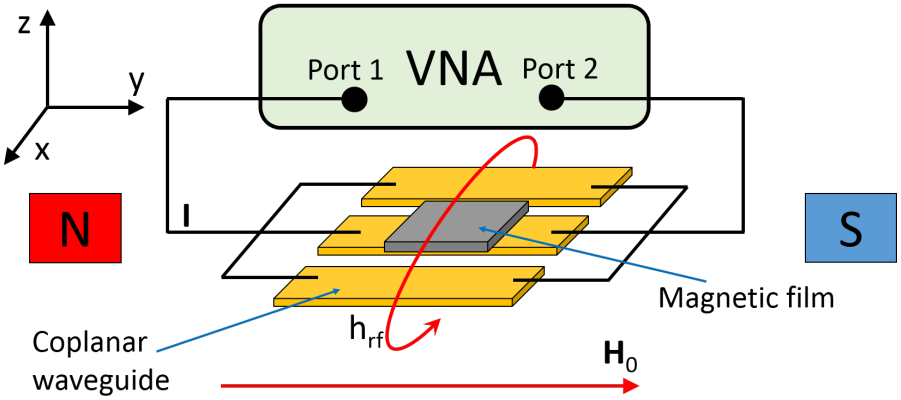

Figure 4.15: Typical experimental set up for VNA-FMR experiments.

The sample is placed 'face down' i.e. with the magnetic layers in close proximity to the waveguide. In order to prevent any shorting of the waveguide and current flow through the sample a thin layer of photoresist ($< 1\mu$m) is spin coated onto the waveguide prior to the experiment.

Typically measurements are performed by stepping field values and sweeping the desired frequency range, this is considerably quicker and more stable than stepping

frequency and sweeping field. All four S-parameters are recorded simultaneously (discussed in section 4.6.1). For each field value a reference measurement is made at high field and subtracted. At high fields the FMR resonance occurs outside of the desired frequency range so by subtracting the high field measurement only the lower field FMR is left and any artefacts caused by the waveguide and coaxial cables are removed.

4.7.1 Design of Waveguides for TRSKM and Vector Network Analyser Ferromagnetic Resonance Measurements

In the experiments discussed in this thesis a wave of a certain frequency is guided to the sample location to provide $\mathbf{h}_{rf}$. A coplanar waveguide (CPW) consisting of a signal line flanked by two ground planes is used to facilitate this (figure 4.16). This geometry is favoured due to its planar structure and relatively low loss. At the measurement frequencies the CPW cannot support pure TEM waves due to the inhomogeneity inherent between the underlying dielectric and air and instead can be though of as a quasi-TEM wave with additional **E** field components in the direction of propagation up to 40-100 GHz depending on the geometry and substrate[168].

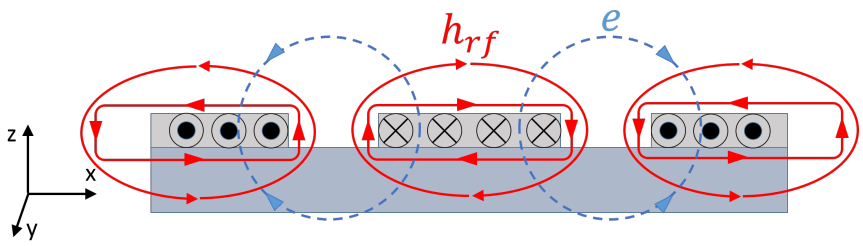

Figure 4.16: Illustration of the magnetic field $\mathbf{h}_{rf}$ and electric field **e** generated by a current travelling along the metal strips of a coplanar waveguide (CPW). $\mathbf{h}_{rf}$ is transverse in-plane at the centre of the strips and perpendicular to the strip plane near the edges, while **e** lies perpendicular to $\mathbf{h}_{rf}$

A critical parameter in CPW design is the characteristic impedance (Z_0), a response function which determines the relation between the electric and magnetic fields of an EM wave. For the simplest case of a wave propagating in the $\hat{\mathbf{y}}$ direction (defined in figure 4.15) in a vacuum then the characteristic impedance (Z_0) is defined as[169]

$$Z_0 = \frac{E_x}{H_z} = \frac{V_0}{I_0}. \tag{4.36}$$

In this case the impedance is independent of any spatial coordinates and time. For a wave guided along a transmission line there is a dependence on the spatial coordinates and time and it is easier to use the mode voltage ($V_0(x,t)$) and mode current ($I_0(x,t)$) to describe the TEM wave as

$$V_0(x,t) = Ae^{(i\omega t - \gamma x)} + Be^{(i\omega t + \gamma x)}, \tag{4.37}$$

$$I_0(x,t) = \frac{A}{Z_0}e^{(i\omega t - \gamma x)} - \frac{B}{Z_0}e^{(i\omega t - \gamma x)}. \tag{4.38}$$

For the case when a voltage propagates along a transmission line terminated with an impedance Z_L, at $x = 0$ then

$$Z_L = \frac{V|_{x=0}}{I|_{x=0}} = Z_0\frac{A+B}{A-B}, \tag{4.39}$$

which may be solved for the reflection coefficient $R = A/B$ so that

$$R = \frac{Z_0 - Z_L}{Z_0 + Z_L}. \tag{4.40}$$

From equation 4.40 it is clear that only when the load impedance is matched perfectly to the characteristic impedance of the transmission line will no wave reflection occur. Each deviation from this matching along the transmission line causes a backscattering of the EM wave, reducing the total transmission. For the experiments performed in this thesis all components were matched to the industry standard characteristic impedance of 50 Ω.

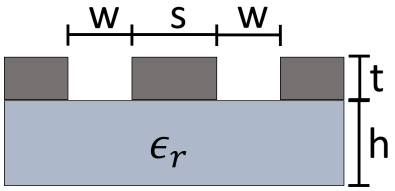

Figure 4.17: Parameters which may be used to vary the characteristic impedance of a coplanar waveguide (CPW).

The impedance of the CPW can be matched to 50 Ω by carefully controlling the parameters shown in figure 4.17. Typically the relative permittivity (ϵ_r) and substrate thickness (h) are fixed and the metal thickness (t) is limited to less than a few μm. This

means the easiest parameters to vary are the signal line width (s) and the distance from the ground plane to signal line (w). The tuning of these parameters was performed using the tool in reference [170].

Chapter 5

Ferromagnetic Resonance of CrO_2 Thin Films Patterned by Selective Area Chemical Vapour Deposition

The work in this chapter was published by Chris Durrant *et al* in reference [171].

5.1 Introduction

Chromium Dioxide (CrO_2) is a highly attractive material for spintronic applications[3, 4], due to its near 100% spin polarization[5]. The realisation of CrO_2 based spintronic devices requires both the fabrication of high quality elements on a sub-micron scale, and a comprehensive understanding of their dynamical properties. Fabrication of patterned CrO_2 structures is however a complex task since CrO_2 readily decomposes to Cr_2O_3 when traditional post deposition patterning processes, such as argon-ion milling[6], wet etching, reactive ion etching (RIE)[7] and focused ion beam milling[8] are used. Selective-area chemical vapour deposition (CVD) of epitaxial CrO_2 onto rutile TiO_2 substrates through pre-patterned amorphous SiO_2 stencils provides a promising alternative, but the dynamic properties of such structures have yet to be confirmed.

Previous studies of CrO_2 nano-structures have explored their magnetotransport[172, 173], and micromagnetic[174, 175], properties. Ferromagnetic resonance (FMR) measurements[120, 176], have been performed upon continuous CrO_2 films but were not extended to patterned elements. Ultrafast dynamics, including precession, have been measured in all-optical pump-probe setups[177, 178], but with the additional complication that optical heating

fundamentally alters the magnetic properties of the sample. In particular epitaxial $CrO_2/TiO_2(100)$ films possess a large uniaxial anisotropy, with an in-plane easy axis, that has a strong temperature and thickness dependence[179].

In the present study, Au coplanar striplines (CPS) were deposited around CrO_2 elements, grown by selective area CVD (detailed in section 3.6), to facilitate high frequency measurements by vector network analyser ferromagnetic resonance (VNA-FMR) and time resolved scanning Kerr microscopy (TRSKM). Such measurements are challenging due to the large anisotropic dielectric constant of the rutile TiO_2 substrate[115, 116], and the small precession amplitude resulting from the strong uniaxial magnetic anisotropy. We explore the dynamical response observed by different measurement techniques and compare the dynamical properties of continuous and patterned films to confirm the efficacy of the selected area CVD technique.

5.2 Fabrication of Continuous CrO_2 Thin Films

Patterned CrO_2 films were grown in a traditional two-zone CVD furnace[179] on 5x5x0.5 mm (100)-oriented single crystal rutile TiO_2 substrates[116] through a 50 nm thick SiO_2 stencil layer. The stencil was formed by sputter deposition of SiO_2 followed by a combination of photolithography and reactive ion etching. The substrate plus stencil were then cleaned and baked at 185 °C for 30 minutes before CVD of CrO_2.

5.2.1 Thickness and Deposition Rate

In order to calibrate the CrO_2 growth rate, continuous films were deposited with varying deposition times. The samples were then mounted in a vibrating sample magnetometer VSM (detailed in section 4.1) with their b-axis aligned parallel to the field. Hysteresis loops from $\pm$20 kOe were taken at 300 K and a linear fit made to the extreme field ends of the curve, where the CrO_2 is fully saturated as shown in figure.5.1. The magnetic susceptibility (χ) of the TiO_2 substrate is calculated from the gradient of this fit and the paramegnetic background subtracted. The CrO_2 thickness (in nm) is then calculated from the intercept (P_{incpt}) of this fit with the y-axis (zero field) and the saturation magnetisation (M_s) (measured by Miao *et al* to be 475 emu/cm^3[111]) from

$$t = \frac{P_{incpt}}{M_s \times CSA}. \tag{5.1}$$

Using this method the thickness of the film in figure 5.1. was estimated to be $t = 27$ nm.

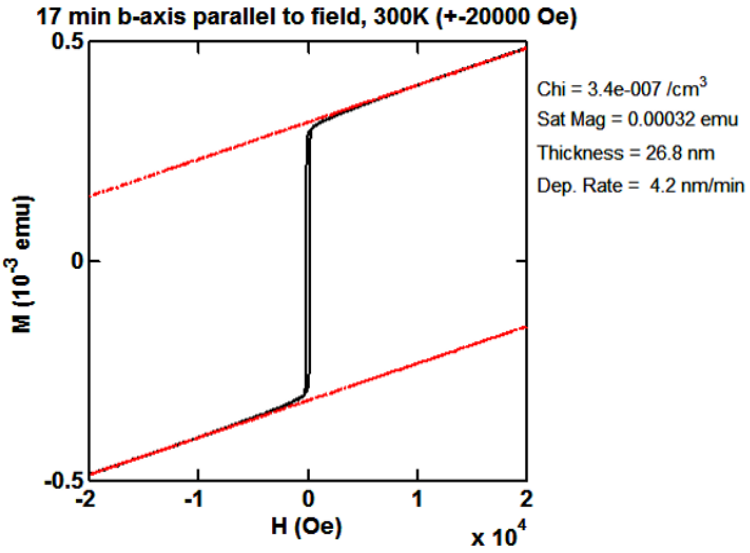

Figure 5.1: Typical VSM hysteresis curve used to estimate the thickness of a CrO_2 layer.

Whilst the VSM provides a good estimation of the film thickness, it has several limitations. The deposition of CrO_2 on the side and back walls of the sample (detailed in section 3.6.4) will contribute to the VSM signal if not fully removed, leading to an overestimation of the film thickness. Removal of unwanted CrO_2 is a delicate process and conversely over removal will lead to an underestimation of film thickness. In order to confirm the accuracy of the VSM thickness measurement X-ray reflection (XRR) (detailed in section.4.2) was utilized. This method provides a more accurate estimation of thickness but was considerably slower and infeasible for a large number of samples. A typical XRR curve is shown in figure 5.2.

From the XRR curve the thickness is extracted from the following equation

$$d = \frac{n\lambda}{2\sin\theta} \tag{5.2}$$

$$d = \frac{n\lambda}{2\cos\theta\Delta\theta} \tag{5.3}$$

as θ is small, $\cos\theta \to 1$, $n = 1$ and $\lambda = 1.5418 \times 10^{-10}$ m so

$$d = \frac{1.54 \times 10^{-10}}{2\Delta\theta}. \tag{5.4}$$

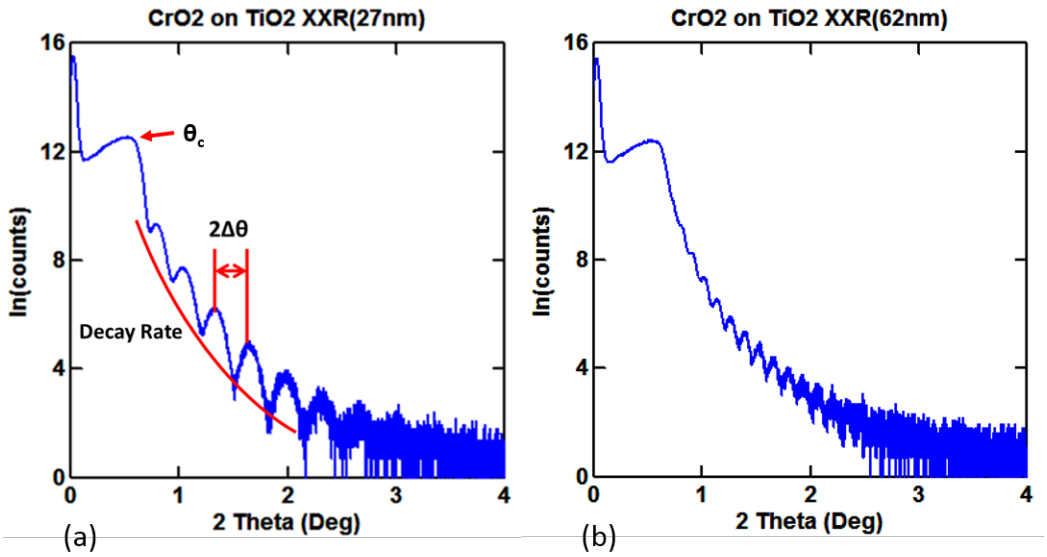

Figure 5.2: XRR curves for continuous CrO_2 films with 27 nm (a) and 62 nm (b) estimated thicknesses (from VSM).

Using this method a comparison can be made between the two techniques

Deposition time (min)	VSM thickness (nm)	XRR thickness (nm)
17	27	29
20	39	43
23	42	45
22.5	44	46
23.5	62	69

Table 5.1: CrO_2 layer thickness measured by VSM and XRR.

From table 5.1 it can be seen that VSM provides a reasonable estimation of film thickness, the differences of a few nm may be due to some variation across the film surface, or may be due to over or under removal of the CrO_2 deposited on the sides and back of the film. As the VSM appears to consistently underestimate the thickness this could be an indication of a magnetic dead layer at the upper or lower surface of the film.

As can be seen in figure 5.2, $\Delta\theta$ is relatively easy to extract when the film thickness is thin (a) however as the thickness increases the spacing of the peaks narrows and the film shown in (b) is close to the limit where it is still possible to resolve individual peaks. For this reason VSM was used to estimate thickness of all remaining films. Though film

thickness was measured for each film achieving the desired thickness by controlling the O_2 flow rate was difficult. The flow rate was set by eye using a reading ball flowmeter and the deposition time varied to set the thickness. A more accurate method to control flow rate such as a digital flowmeter or even a valve fixed to a suitable flow rate would have made estimation of the thickness pre-deposition considerably more accurate.

5.2.2 Film Purity

The purity of the CrO_2 phase was confirmed by X-ray diffraction (XRD), as described in section 4.3. An XRD spectrum for a 213 nm CrO_2 continuous film is shown in figure 5.3.

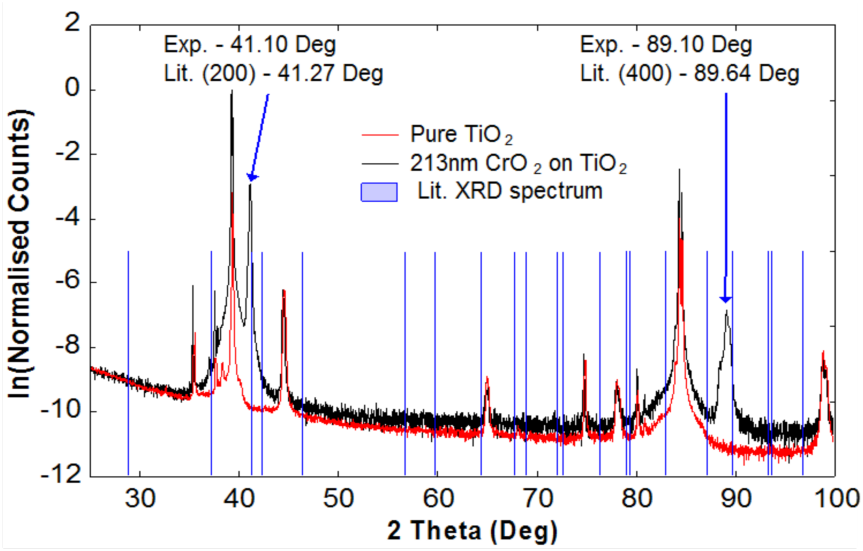

Figure 5.3: Typical XRD spectrum for a 213 nm continuous CrO_2 film on a TiO_2 substrate (black), compared to the spectrum from a pure TiO_2 substrate (red). Vertical blue lines indicate expected peaks in the CrO_2 spectrum (note these lines only indicate the position, and not the magnitude of the expected peaks). Blue arrows indicate the largest peaks arising from the CrO_2 layer.

By comparing the observed peaks in the CrO_2 (black) spectrum which do not correspond to peaks from the TiO_2 substrate (red) it is clear that the peaks at 41.1° and 89.1○ arise purely from the CrO_2 layer. These peaks can be compared to the expected peaks for CrO_2 with the bulk lattice constant, the vertical blue lines. It should be noted that as the film is (100) oriented only (n00) are expected to be observed, not peaks at all of the vertical blue lines. The observed peaks correspond to the 200 and 400 CrO_2 planes, although there is a small shift from the angles of 41.3 and 89.6○ expected

for CrO_2 with the bulk lattice constant. This shift arises from the strain at the TiO_2 interface[139]. Critically there is no observable decomposition into Cr_2O_3 as there are no strong peaks other than those arising from TiO_2 and CrO_2.

5.2.3 CrO_2 Vibrating Source Magnetometer Hysteresis Loops

Two competing contributions to the magnetic anisotropy are expected in CrO_2 thin films. The magnetocrystalline anisotropy is a volume effect and is an intrinsic property of the material. It favours the magnetic easy axis aligned along the in-plane *c* direction as observed for bulk samples [180] and thick films[112]. There is also a strain anisotropy for films grown on treated TiO_2. This is induced at the TiO_2/CrO_2 interface, being caused by the lattice mismatch being larger along the *b* direction (3.91%) than the *c* direction (1.44 %)[112], and favours the alignment of the easy axis along the *b* direction. As the strain anisotropy arises from the interface it is thickness dependent. It has been shown to dominate the magnetocrystalline anisotropy, orienting the easy axis in the *b* direction for thinner films. As the film thickness increases the magnetocrystalline anisotropy has been shown to dominate, orienting the easy axis in the *c* direction. This effect is shown in Figure 5.4.

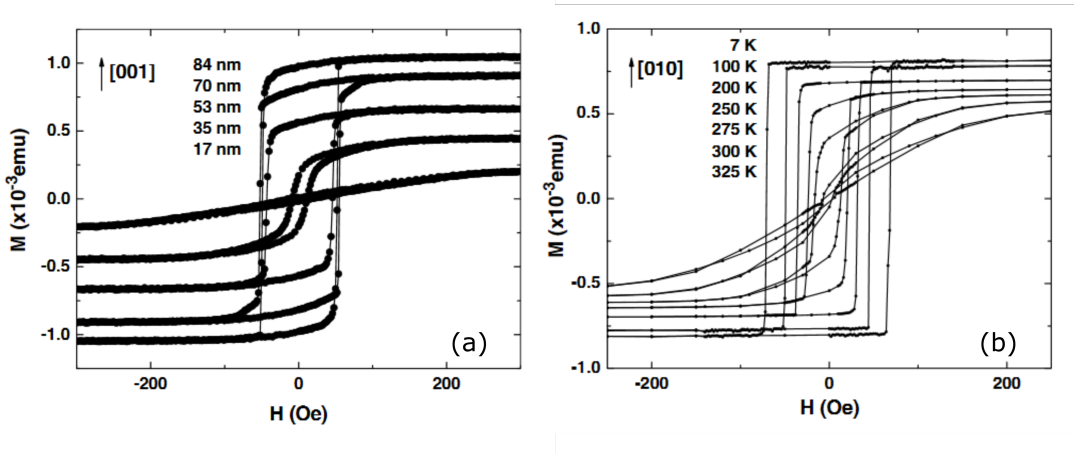

Figure 5.4: (a) Hysteresis loops showing the orientation of the easy axis move from the *c* to the *b* axis for CrO_2 films with decreasing film thickness (b) Hysteresis loops showing the evolution of the easy axis direction into the hard axis direction with increasing temperature for a 47 nm film. Figures taken from reference [121].

Figure 5.5 shows VSM hysteresis loops for a range of CrO_2 thicknesses from 6 to 213 nm. It is immediately obvious that there is no thickness dependence of the easy axis direction. According to figure 5.4 a rotation of the easy axis from the *c* direction to the

b direction is expected for films $\lesssim$ 53 nm. No significant rotation is observed at 300 K for films between 6 and 44 nm. This suggests that in these films the magnetocrystalline anisotropy dominates the strain anisotropy. Assuming that the bulk properties of these films are similar to those previously reported it is likely that the strain is lower than expected, as is discussed further in section 5.2.4.

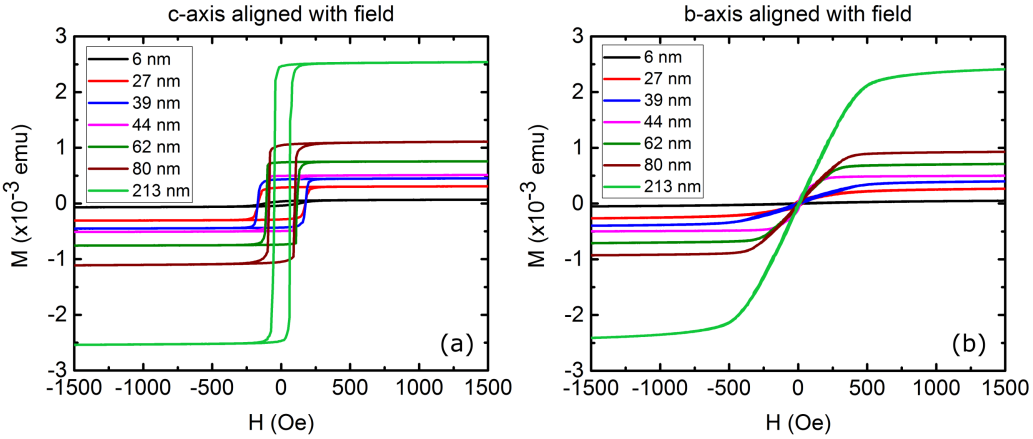

Figure 5.5: Hysteresis loops at 300 K for increasing CrO_2 film thickness for the external field aligned parallel to the *c*-axis (a) and *b*-axis (b).

The temperature dependence of the *c*-axis and *b*-axis hysterisis loops is shown in figure 5.6 for films with thickness of 6, 44 and 213 nm. For the 44 nm intermediate thickness film there is a clear rotation of the easy axis from the *c* direction at 323 K, to the *b* direction at 7 K (figure 5.6.(c-d).). At 7 K the easy axis has almost rotated fully to the *b* direction. There is still evidence of the opening of the loop in (c) and rounding of the loop in (d) suggesting the easy axis has not fully rotated into the field direction. This effect may arise from a competing strain through the thickness of the film. Close to the TiO_2/CrO_2 interface the strain is proportionally higher than at the opposite CrO_2/air interface. At a certain depth into the film the strain anisotropy and crystalline anisotropy balance each other resulting in a near zero effective anisotropy in this region. This 'soft' layer is sandwiched between the top and bottom 'harder' layers. The anisotropy of the top layer is dominated by the crystalline anisotropy and has an easy axis along the *c* direction. The anisotropy of the bottom layer, dominated by the epitaxial strain, has an easy axis along the *b* direction. Miao *et al* propose that the middle section in such a system will assume a spin configuration of a 90° domain wall[111]. For the 213 nm film the effect of the multiple layers can be seen clearly if one focuses on the small section around $H = 0$ in figure 5.6.(f), which is shown clearly

in figure 5.7. Though the hard axis remains in the *c* direction for all temperatures, the contribution of the strained layer is seen as an open section of the loop close to zero field (note here that a misalignment of field could also produce a similar effect but films were aligned by eye to within a few degrees). Perhaps surprisingly the 6 nm film does not show such a strong dependence of its easy axis on temperature. It would be expected that at 6 nm the easy axis would remain in the *b* direction for all temperatures but instead remains in the *c* direction. This anomalous behaviour may be caused by inhomogeneous/patchy growth (backed up by visual inspection) as the film is considerably thinner. An inhomogeneous growth may induce other competing anisotropy effects such as shape anisotropy which may dominate other terms.

A room temperature thickness dependence of the easy axis would be an added dimension to explore in the dynamic study, but was not critical to those measurements. It was impractical to carry out dynamic measurements at low temperature and so patterned films were only fabricated at a small number of thicknesses as behaviour was fairly uniform at room temperature. Time constraints did not allow exhaustive testing of the reasons for a lack of thickness dependent anisotropy but the following section details a few simple tests that were carried out.

5.2.4 Strain testing

The HF treatment of the TiO_2 substrate has been reported as being critical to the epitaxial strain[121, 118, 181] as it can enhance the surface smoothness of the TiO_2 substrate thus leading to the growth of epitaxially strained CrO_2 films. The HF treatment procedure was explored as a potential candidate for the lack of strain anisotropy. As stated in section 3.6.1. the TiO_2 substrate was immersed in a 1% HF solution for 5 minutes prior to CVD. In figure 5.8.(a) and (b) we show the results of increasing HF immersion time and HF concentration respectively (for the same growth time). It is clear from (b) that an increase in HF concentration from 12.5 % to 25.0 % leads to a faster (larger *M*) and more strained (more square loop) growth. As concentration was increased up to 50% the strain and growth rate began to decrease. An increase in treatment time at lower concentrations (shown in 5.8.(a)) also increased the strain, evident in the steeper slope of the hysteresis loop for the 10 minute immersion compared to the 5 minute.

Figure 5.9 shows the increase in strain when HF concentration and immersion time were increased. The increase in strain is very clear from the hysteresis loop shape when the field is aligned in the *b*-direction, with the 25 %, 10 minute sample showing a much steeper slope than the 1 %, 5 minute sample. Another effect of the increased

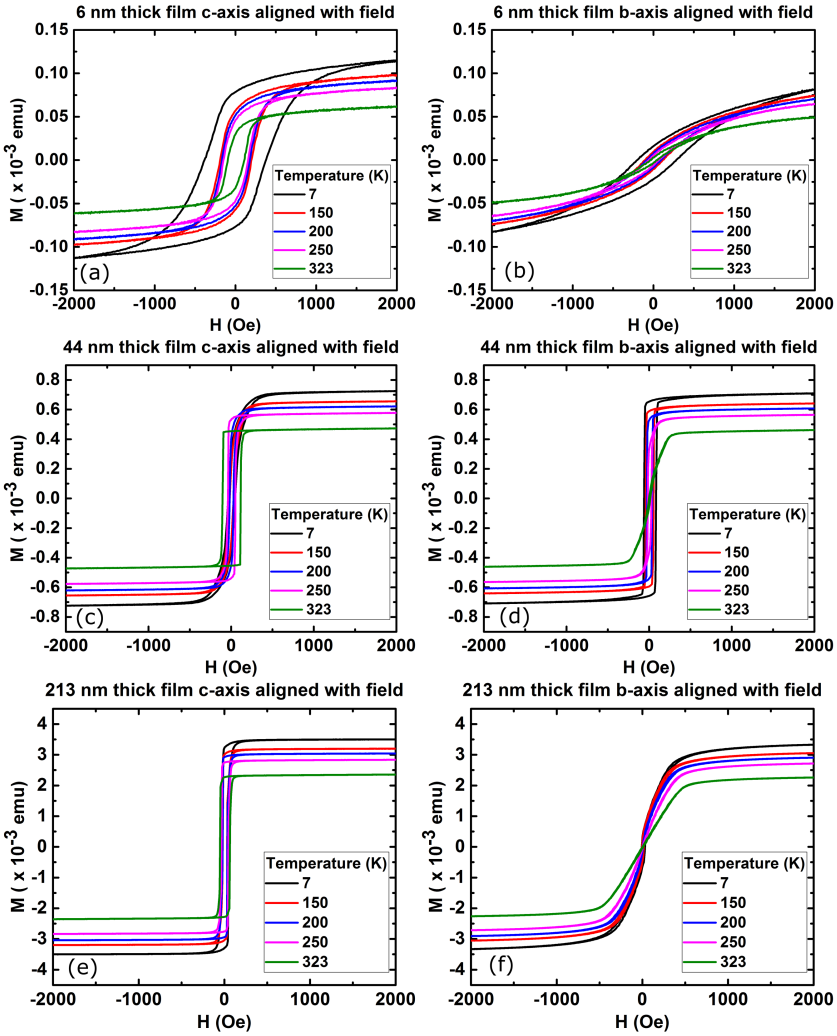

Figure 5.6: Hysteresis loops at increasing temperatures for CrO_2 film thickness of 6 nm, (a) and (b), 44 nm, (c) and (d), and 213 nm, (e) and (f), for the external field applied parallel to the *c*-axis and *b*-axis.

treatment is a lower coercivity, seen clearest when the field is aligned in the *c*-axis direction. Though the strain has been increased there is still no full rotation of the easy axis to the *b*-direction as should be expected for this $\approx$ 27 nm film.

Annealing the TiO_2 substrate prior to CVD was also also tested as a potential method for increasing film strain. After HF treatment substrates were annealed at 500° K for 30-120 minutes and one at 950° K for 240 minutes. All films showed a visible reduction in CrO_2 growth quality and uniformity so this approach was not pursued further.

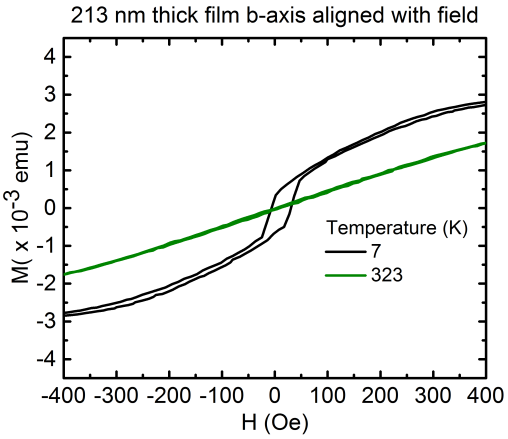

Figure 5.7: Hysteresis loops at 7 and 323 K for a 213 nm CrO_2 film with the external field aligned in the direction of the *b*-axis.

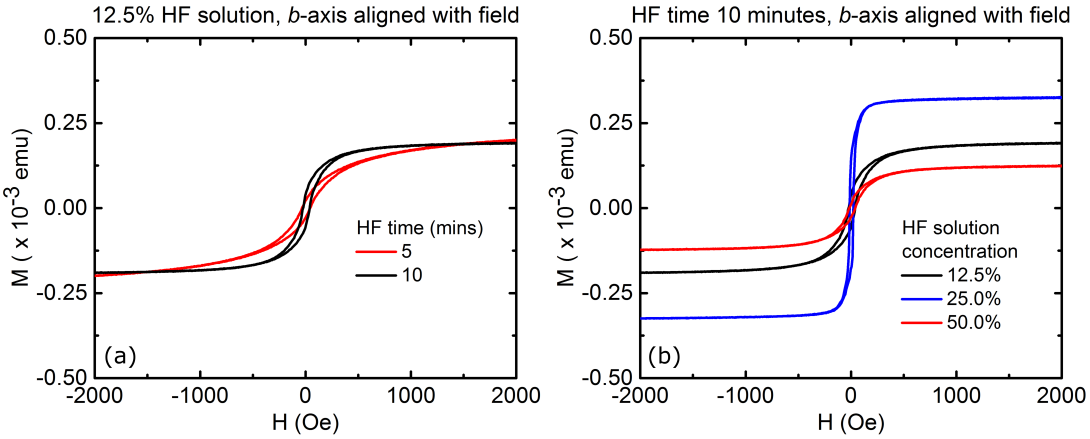

Figure 5.8: VSM hysteresis loops for CrO_2 films with different HF treatment times (a) and concentrations (b) prior to a 17 minute CVD ($\approx$ 27 nm under 1% HF, 5 minutes condition).

Due to time constraints as a visitor to Brown University (where samples were fabricated) a decision was made to not spend time re-optimising the CVD growth process to maximise strain. Highly strained CrO_2 would have provided an additional parameter to explore, however the novel dynamic measurements could be performed on unstrained films and attaining high quality patterning and waveguides was deemed a higher priority.

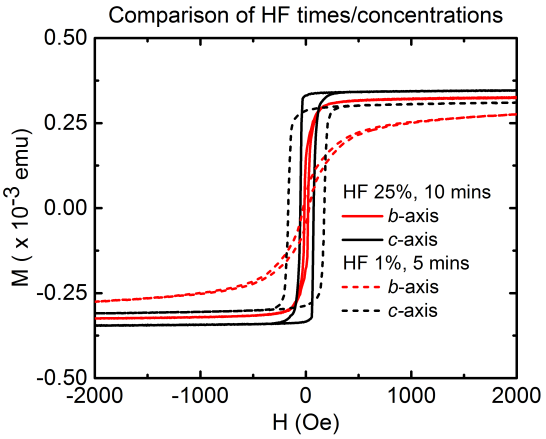

Figure 5.9: VSM hysteresis loops showing the comparison of ≈ 27 nm CrO_2 films with HF treatments of 1%, 5 minutes (as used for the majority of growths) and 25 % for 10 minutes.

5.3 Fabrication of Patterned CrO_2 Thin Films

To facilitate high frequency current pulsed excitation the CrO_2 was patterned by selective area CVD (section 3.6.3) and Au waveguides deposited around the elements (section 3.6.5). In this study the coplanar strip-line (CPS) waveguide type was used to avoid passing current through the CrO_2, an example of two typical devices is shown in figure 5.10.

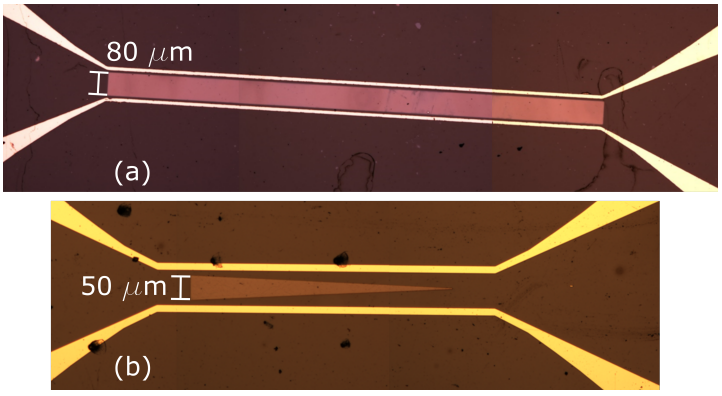

Figure 5.10: CrO_2 patterned by selective area CVD into (a) strip and (b) wedge shapes with on-substrate Au waveguides.

The dielectric constant of TiO_2 varies with crystal phase, temperature, electric field and critically is anisotropic[182, 183, 184, 185]. The design of 50 Ω impedance, planar waveg-

uides (discussed in section 4.7.1) relies on an accurate knowledge of the permittivity of the substrate layer, and waveguide dimension calculations typical assume a single isotropic value. The anisotropic and variable dielectric constant of TiO_2 made it likely waveguides were not perfectly impedance matched and significant reflections of the pulse current were expected.

Wire-bonding to the Au waveguide contact pads was initially difficult as severe tear-out occurred for the majority of the bonds (shown in figure 5.11). Visual evidence suggested an adhesion problem between the TiO_2 and Ti layers, not between the Au and Ti layers. This may have arisen from the nature of the oxide-metal interface, or possibly just surface contamination.

Figure 5.11: Au waveguide contact pad post wire bonding, highlighting tearing out of bonds.

The literature suggested that the replacement of Ti with Cr or Ru would increase adhesion[186, 187],and also reduce contact resistance. To test this, four samples were grown, two with Cr and two with Ru, replacing the Ta layer. One of each of the samples with replaced metal later were cleaned pre-deposition whilst the others were not, as shown in table 5.2. The samples were then sonicated and subjected to scratch and tape adhesion tests; a sharp dental pick was pressed into and run over the sample surface and 3M Scotch® tape was placed over half the sample and ripped off, the results of this test are shown in table 5.2.

Material	Result	Conclusion
Cr on pre-cleaned TiO_2	High adhesion quality, no loss	Best base layer candidate
Ru on pre-cleaned TiO_2	Good adhesion quality, minimal loss	Viable substitution for Cr
Cr on un-cleaned TiO_2	Poor adhesion quality, removed in testing	Unsuitable
Ru on un-cleaned TiO_2	Large area loss just due to sonication	Unsuitable

Table 5.2: Influence of Cr and Ru layers on Au adhesion to SiO_2 substrate

Based on these results Cr was selected as the best base layer candidate, and so all subsequent samples were fabricated with Cr 20 nm/Au 100 nm waveguide layers. For this composition all wire bond contacts were strong and stable.

5.4 MOKE and VNA-FMR Study of CrO_2 Thin Films

Continuous films were fabricated with thicknesses in the range $d = 27$ to 1200 nm. Two patterned strips of 80 μm width and 2 mm length were grown for which $d = 55$ and 250 nm. Strips were oriented with the long edge along the [001] axis, which is expected to be the hard axis for t >50 nm[179]. The CPS track width and separation were chosen to be 21 μm and 100 μm respectively and were intended to achieve a characteristic impedance of 50 Ω although significant error can be expected since the dielectric constant of the TiO_2 is anisotropic and poorly characterised[182, 183, 184, 185].

5.4.1 Comparison of Static Magnetic Properties

The static magnetic properties of both continuous and patterned CrO_2 films were first investigated by longitudinal magneto-optical Kerr effect (MOKE) measurements performed with a 633 nm wavelength s-polarized focused laser beam. Hysteresis loops were recorded with field applied in the [001] (*c*) and [010] (*b*) directions.

Typical MOKE hysteresis loops with **H** applied in the [010] and [001] directions, for both patterned and continuous films, are shown in Figure 5.12. All samples show strong uniaxial anisotropy with a [001] easy axis. A difference in loop height is observed for the easy and hard axis due to the birefringent nature of the film and substrate. Hard axis loops for patterned samples (Figures 5.12.(b) and (c)) deviate from the expected linear shape, probably due to slight misalignment of **H** from the hard axis and mixing of first and second order Kerr effects. Note here that similar behaviour was seen for the majority of measurements made on continuous films, but many measurements were performed on the continuous films with minor rotations of the sample relative to **H** and in a very narrow rotation angle window the expected hard axis loop was obtained, these results are those shown in figures 5.12. The hard axis saturation field, $H_k = 2K_u/M_S$ where K_u is the uniaxial anisotropy constant and M_s is the saturation magnetization, was extracted from the loops and used in the fitting of dynamic results. This anisotropy field increases with film thickness as previously reported[120, 176].

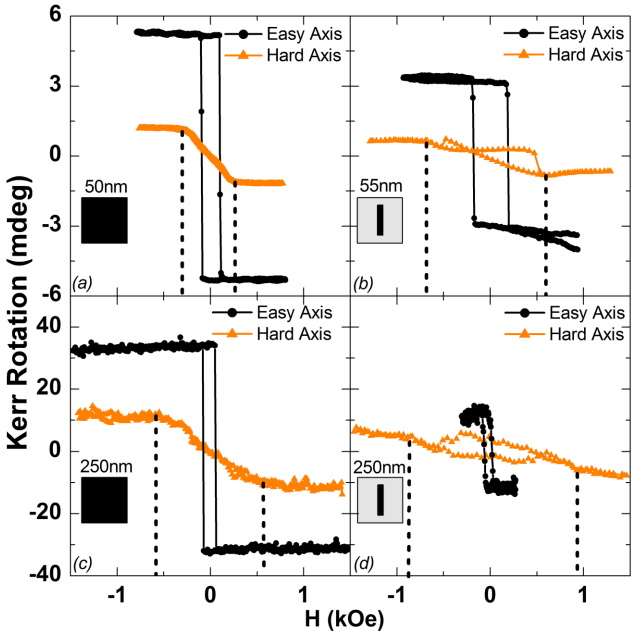

Figure 5.12: MOKE loops with field along the easy [001] and hard [010] axes for (a) $d =$ 50 nm continuous (b) $d = 55$ nm, 80 μm wide strip (c) $d = 250$ nm continuous (d) $d =$ 250 nm, 80 μm wide strip, CrO_2 samples. Dashed lines indicate H_k in each case.

5.4.2 Comparison of Dynamic Magnetic Properties

VNA-FMR measurements were made on continuous films by placing the samples face down on a 50 Ω coplanar waveguide (CPW) with 500 μm signal track width. An 100 nm layer of photoresist was used to prevent the sample short circuiting the CPW. The scattering matrix parameters of the composite structure were recorded as the field was swept between 0 and 1.3 kOe. VNA-FMR measurements were also attempted upon the patterned elements using wire bonding to connect to the CPS, but no measurable response was observed, presumably due to poor impedance matching and the small amplitude of precession.

Instead, TRSKM measurements were performed on the patterned samples using the setup described in Ref [188] (described in section 4.5.3). The CPS was connected to a 50 Ω coplanar waveguide (CPW) by wire bonds and the sample magnetization excited by the magnetic field associated with 6 V, 70 ps FWHM pulses supplied to the CPS. Time resolved polar MOKE measurements were made at 80 MHz repetition rate with laser pulses of 800 nm wavelength and 100 fs duration. A static field of 0 to 0.9 kOe was applied parallel to the [010] hard axis. No measurable signal was observed

when the field was applied parallel to the easy axis, due to the higher frequency and lower amplitude of precession.

Finally, all- optical pump-probe measurements were made on selected continuous films using the setup described in reference [189]. Optical pumping was performed with s-polarized pulses of 50 fs duration, 800 nm wavelength, and 2.26 mJ/cm^2 fluence at near normal incidence. Time resolved Kerr rotation measurements were made with an s-polarized 800 nm wavelength probe pulse incident at 45°. Pump and probe beams were focused onto the sample surface with spot sizes of 135 μm and 40 μm respectively. Again a measurable precession response was only observed when a static field of 0.22 to 1.8 kOe was applied in the [010] direction.

The oscillatory part of the Kerr rotation signals were fitted to the form

$$\theta_k \propto \theta_0 \cos[2\pi f_0 t + \phi] exp(-t/\tau), \tag{5.5}$$

where θ_0, f_0, $1/\tau$ and ϕ are respectively, the amplitude of precession, the frequency, the relaxation rate, and the initial phase of the precessional signal. In the all-optical and TRSKM experiments, intense optical and electrical pulses respectively are used to perturb the magnetic state on time scales short compared to the period of precession. After excitation, the magnetization is no longer parallel to $\mathbf{H}_{eff}$, the total effective field acting on the magnetization and a damped precession ensues. If material parameters modified by the excitation relax sufficiently slowly compared to its period, the precession may be described by the Landau-Lifshitz-Gilbert equation,

$$\frac{\partial \mathbf{M}}{\partial t} = -|\gamma| \mathbf{M} \times \mathbf{H}_{eff} + \frac{\alpha}{M}(\mathbf{M} \times \frac{\partial \mathbf{M}}{\partial t}), \tag{5.6}$$

where α is the phenomenological damping parameter, $\gamma = 2.8 \times \pi \times g$ MHz/Oe is the gyromagnetic ratio of the electron, and g is the spectroscopic splitting factor. In the limit $\alpha \ll 1$, the apparent damping parameter α, which contains contributions from all damping processes present, is given by[189].

$$\alpha = \frac{2}{|\gamma|(H_\alpha + H_\beta)} \frac{1}{\tau}, \tag{5.7}$$

where H_α and H_β are effective fields that include the anisotropy and demagnetizing fields[189]. For a frequency domain measurement such as VNA-FMR, the relaxation rate $1/\tau$ is replaced by the half width at half maximum frequency $\Delta\omega_{FWHM}/2$.

The results of VNA-FMR measurements performed on a 250 nm continuous film are

presented in Figure 5.13. The effect of the uniaxial in plane anisotropy is immediately apparent from panels (a) and (e). With **H** applied along the [001] (easy) axis, the FMR frequency increases monotonically with $|\mathbf{H}|$, while for the [010] axis a minimum is observed as $|\mathbf{H}|$ approaches the hard axis saturation field. Cross-sections through the grey scale plot may be taken as a function of field, as in the lower panels, or frequency. In the latter case the absorptive (imaginary) component of the scattering matrix representing transmitted power S_{12} was fitted to a Lorentzian function, and the linewidth used to calculate α.

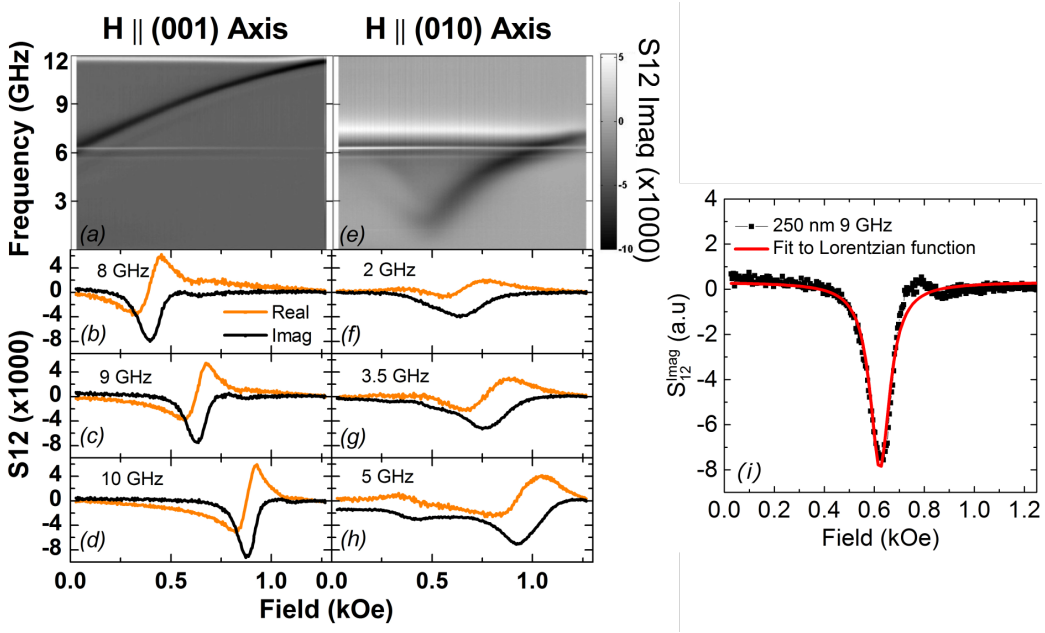

Figure 5.13: VNA-FMR measurement of 250 nm continuous film, with **H** parallel to (001) in (a)-(d) and (010) in (e)-(h). (a) and (e) show S_{12}^{Im} while both S_{12}^{Re} and S_{12}^{Im} are plotted against field for selected frequencies in the remaining panels. (i) shows a typical fitting of a Lorentzian function to $\mathrm{Im}(S_{12})$. Note here that the horizontal band arises from the high field reference measurement described in section 4.6.

Since attempts to measure the patterned elements by VNA-FMR proved unsuccessful, TRSKM was used to perform time domain measurements on samples with $d = 55$ and 250 nm. The time resolved polar MOKE response of a $d = 55$ nm strip is displayed in Figure 5.14.(a). **H** was again applied parallel to the [010] axis and **H** varied from 0 to 0.9 kOe. The shape of the first anti-node is generally rather unclear. Measurements of the transmitted and reflected electrical pulse confirmed the presence of secondary pulses of lower amplitude resulting from poor impedance matching

between the SMA to CPW connector and the CPS on the sample chip. This can lead to a partial coherent suppression/enhancement of the precession. However these effects appear to be confined to the first few hundred ps of the measurement, and so fitting to equation 5.5 was performed from the first clear peak in the signal.

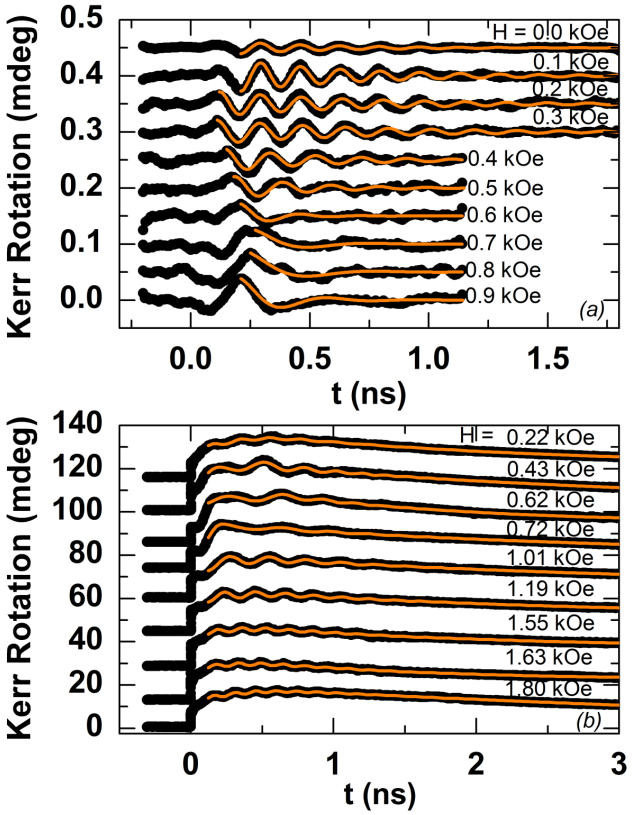

Figure 5.14: (a) TRSKM measurements of a $d = 55$ nm, 80 μm wide CrO2 strip. (b) All-optical measurements of a $d = 250$ nm continuous CrO2 film. Fitted curves are shown in orange.

Finally, all-optical measurements were performed on a $d = 250$ nm continuous film for comparison. The transient polar Kerr rotation is plotted in Figure 5.14.(b) for the field applied along the [010] hard axis. A partial ultrafast demagnetisation occurs within the first few ps, after which the uniaxial anisotropy field is reduced, initiating precession of the magnetization. The maximum Kerr signal occurs after $\approx$300 ps, reflecting a slower demagnetization process associated with the half metallic character of the CrO_2[178]. Following the measurement the data were fitted to the sum of equation. 5.5 and a slowly varying background term. In addition a term bt^2 was

added to the argument of the cosine function to account for chirp that occurs as the values of magnetic parameters such as M_s and K_u gradually relax.

The precession frequencies and effective damping parameters obtained from the three dynamical measurement techniques are compared in Figure 5.15. The same characteristic field dependence of the frequency is observed in all cases when the field is applied parallel to the hard axis. Indeed the optical experiments only yielded measurable signals in this configuration since the frequency is lower and the amplitude of precession greater. The VNA-FMR measurements show that α is only weakly field dependent when **H** is applied along the [001] (easy) axis but varies strongly when **H** is along the [010] (hard) axis. Specifically we observe an increase in α with decreasing precession frequency as $|\mathbf{H}|$ approaches H_k. Above H_k, the variation of α is consistent with the linear dependence reported by others[177]. Qualitatively similar behaviour is observed for all samples although the size of the uniaxial anisotropy and damping differs most significantly between the $d = 50$ and 55 nm samples, perhaps reflecting a sensitivity to substrate conditions.

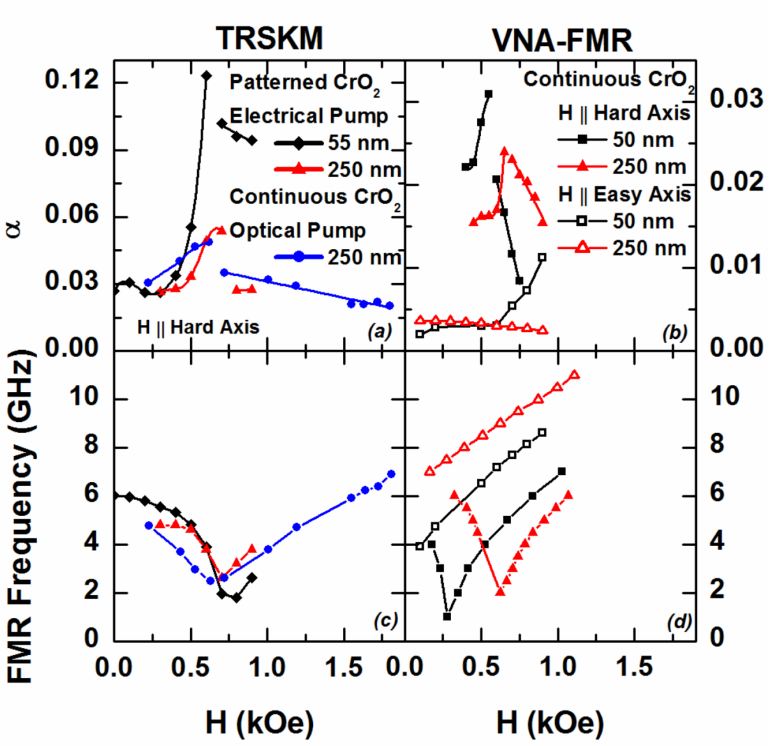

Figure 5.15: Field dependence of the effective damping parameter α measured for continuous and patterned films in 3 separate experimental geometries (a) electrically and optically pumped TRMOKE (b) VNA-FMR. The field dependence of the precessional frequency (c) electrically and optically pumped TRMOKE (d) VNA-FMR. Lines are guides to the eye.

5.5 Summary and Future Work

In summary the efficacy of selective area CVD has been demonstrated for the fabrication of highly spin-polarized CrO_2 thin films. The need for careful control of the surface quality of the TiO_2 substrate has been highlighted as critical for the growth of highly strained CrO_2. The large uniaxial in plane anisotropy observed in continuous and patterned epitaxial CrO_2 thin films, and the dielectric properties of their TiO_2 substrates, make characterization of their dynamic properties challenging. Nevertheless, by comparing results obtained from complementary dynamical measurement techniques it has been shown that continuous and patterned CrO_2 samples exhibit essentially similar dynamic magnetic properties. If the large anisotropy field can be accommodated this bodes well for the use of CrO_2 spintronic devices such as spin batteries and ideal magnetic tunnel junctions. Recently first principles calculations have shown CrO_2 to be a viable candidate for magnetic tunnel junctions comprising graphene[190], CNT[191] and SiCNT[192] between CrO_2 layers. This study shows that realisation of these devices on a micron or nano scale is a real possibility.

Chapter 6

Current Induced Switching in Ta/CoFeB/MgO Films With Perpendicular Magnetic Anisotropy

The work in this chapter was published by Chris Durrant *et al* in reference [193].

6.1 Introduction

The ever growing demand for higher density and faster processing speeds has led to great advances in the field of data storage in the last few decades[194]. The discovery of tunnelling magnetoresistance (TMR)[195] has made magnetic tunnel junctions (MTJs) one of the leading candidates for next generation high density magnetic random access memories (MRAMs)[9].

Traditional MRAM requires an external magnetic field, generated by a current, to induce switching during the read/write procedure. Recently there has been great interest in switching the memory bit directly by using spin transfer torques (STT) generated by charge currents[10, 11]. Conventional STT switching requires current to be injected directly through a tunnel barrier. However, recent studies have utilised the torques generated by spin Hall and Rashba effects to switch elements with an in-plane current, leading to smaller write currents for equivalent thermal stability, and avoiding degradation associated with passing high current densities through a tunnel barrier[12]. To date these phenomena have been investigated mostly in layered structures containing HM/FM/Ox sub-units in which the ferromagnetic (FM) layer is sandwiched between

a heavy metal (HM) and an oxide (Ox)[15, 196, 197, 198, 14, 199, 73]. Spin-transfer torque magnetic random-access memory (STT-MRAM), has been explored as a replacement for dynamic random access memory (DRAM) and may provide performance comparable to DRAM main memory with an average 60% reduction in main memory energy[200]. With main memory energy now accounting for as much as 30% of overall system power [201, 202] STT-MRAM has the potential to significantly reduce the operational cost of computing systems.

It has been demonstrated that the Ta/CoFeB/MgO sub-unit, already widely used in MTJs with in-plane anisotropy [203, 204], could fulfil the three criteria required for high performance MTJs for STT-MRAM, namely high tunnelling magnetoresistance (TMR), low switching current, and high thermal stability for small device dimensions.

As discussed in section 2.13 a large TMR is critical to an efficient MTJ. TMR ratios as high at 120% [205] have already been reported in Ta/MgO/CoFeB/MgO/CoFeB/Ta stacks and 162% 162% in similar stacks with additional Mo layers[206].

A thermal stability factor of greater than 40 is required for non volatility over 10 years on a bit level[207] i.e.

$$E/k_BT > 40, \tag{6.1}$$

where k_B the Boltzman constant, T is the temperature and E is the energy potential between the two states given by

$$E = M_S H_K V/2, \tag{6.2}$$

where M_S is the saturation magnetisation, H_K is the anisotropy field and V the volume of the free layer. As the dimension is reduced V is reduced and so the anisotropy energy density

$$K = M_S H_K/2, \tag{6.3}$$

must be sufficiently high for thermal stability. Whilst there are a number of material combinations with perpendicular magnetic anisotropy (PMA) which satisfy this condition they typically make use of $L1_0$-ordered (Co,Fe)-Pt alloys with a high spin-orbit interaction. This is problematic as the critical current I_C required for magnetization switching for perpendicular MTJs is proportional to

$$I_C = \alpha \frac{\gamma e}{\mu_B g} M_S H_K V = 2\alpha \frac{\gamma e}{\mu_B g} E, \tag{6.4}$$

where α is the magnetic damping constant, γ is the gyromagnetic ratio, e the electron

charge, μ_B the Bohr magneton and g a function of the spin polarisation of the tunnel current and the angle between the magnetisations of the reference and free layers. Inspection of (6.4) reveals that low switching current requires a low α for a given E. The aforementioned noble metals typically have a large α due to a high spin-orbit interaction and so are unsuitable as they require high I_C. The Ta/CoFeB/MgO combination has shown I_C as low as 49 μA with sufficiently large perpendicular, interface induced anisotropy to lead to stable bits with dimensions as low as 40 nm diameter[205] with switching voltages of 290 mV at 50 ns[208] (in the range required for STT-MRAM) [209] making it a perfect candidate for high performance MTJs.

It is worth noting that for an in-plane MTJ E in (6.4) is replaced by the demagnetising energy E_{Demag} and it is for this reason that materials with a perpendicular magnetic anisotropy (PMA) are desired for a low I_C.

A critical parameter for obtaining low I_C is a large spin Hall angle θ (section 2.14.1). With a large θ metals can efficiently convert a longitudinal charge current (J_C) to a transverse spin current (J_S), which in turn exerts a strong torque on the magnetization state. Large θ values have been observed in a range of materials including Pt ($\theta = 0.07$[210, 211, 212]), β-W ($\theta = 0.33 - 0.4$[213, 87]) and β-Ta ($\theta = 0.14$[126, 15]). The metastable β forms of Ta and W are more difficult to stabilise but display much larger intrinsic resistivities (and therefore larger Θ than their more stable α forms.

With TMR ratios of 120% in Ta/MgO/CoFeB/MgO/CoFeB/Ta[205] stacks and 162% in similar stacks with additional Mo layers[206], switching currents of $3 - 6 \times 10^6$ A/cm^2 for similar devices[18, 22], and good thermal stability for devices with 40 nm diameter[205], Ta/CoFeB/MgO is indeed a viable candidate for next generation STT-MRAM.

Critical for effective STT device fabrication is a deeper understanding of the underlying switching mechanisms, which have recently been the subject of much debate. Kim *et al*[198] report a strong HM and FM thickness dependence of both the Rashba spin orbit field and the spin Hall torques. Torrejon *et al*[17] also report a strong thickness dependence of their relative contributions to the switching, with spin Hall torque dominating for thicker HM underlayers. The relative contributions made by these effects are also influenced by capping layer thickness[19] and temperature[18]. In this study we combine scanning Kerr imaging with electrical transport measurements to gain further insight into the switching process. Crucially, current pulses of constant amplitude are applied so that the evolution of intermediate magnetic states can be probed under constant current conditions. This study focuses on the current induced switching properties of β-Ta/$Co_{40}Fe_{40}B_{20}$/MgO in which PMA has been achieved through thermal annealing.

6.2 Fabrication of Ta/CoFeB/MgO Thin Film Hall Bars and Experimental Techniques

Fabrication of MgO/CoFeB/Ta Hall bars has been described in section 3.7. The stack structure and optical microscope pictures of the 20 x 140 μm^2 Hall bars, with 5 μm wide contact pads are shown in figure 6.1.

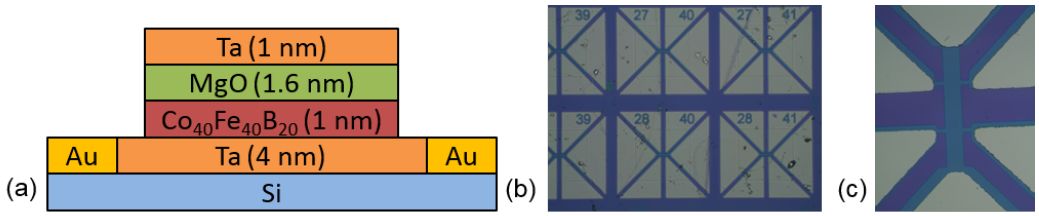

Figure 6.1: (a) Hall bar stack structure. (b) Hall bar wafer with Au contact pads. (c) Single Hall bar.

For magnetotransport measurements wire-bonding was used to connect the Hall bar to two 50 Ω coplanar waveguides (CPWs) (figure 6.2.(a)). The 50 Ω waveguides were not a requirement for the quasi DC measurements discussed in section 6.3) but are crucial for the pulsed experiments discussed in section 7. The waveguides were connected to a Keithley 6221 current source and Keithley 2182A nanovoltmeter. A constant D.C. current $I_{test} = 0.1$ mA was applied along the direction parallel to the long edge of the Hall bar ($\hat{\mathbf{z}}$) and the Hall resistance was measured across the contacts perpendicular to the current ($\hat{\mathbf{x}}$) as shown in figure 6.2.(c). In this way the magnetization between the contact pads was probed via the anomalous Hall effect (AHE). The Hall bar and CPWs were placed in a scanning Kerr microscope so that the magnetisation within a sub-micron region could be probed via the magneto-optical Kerr effect (MOKE), simultaneously with the Hall resistance measurements. The MOKE measurement was performed by focusing the beam from a 633 nm He-Ne laser onto the sample surface with a 40X objective lens, and recording the optical rotation of the back-reflected beam using a simple optical bridge detector as shown in figure 6.2.(b).

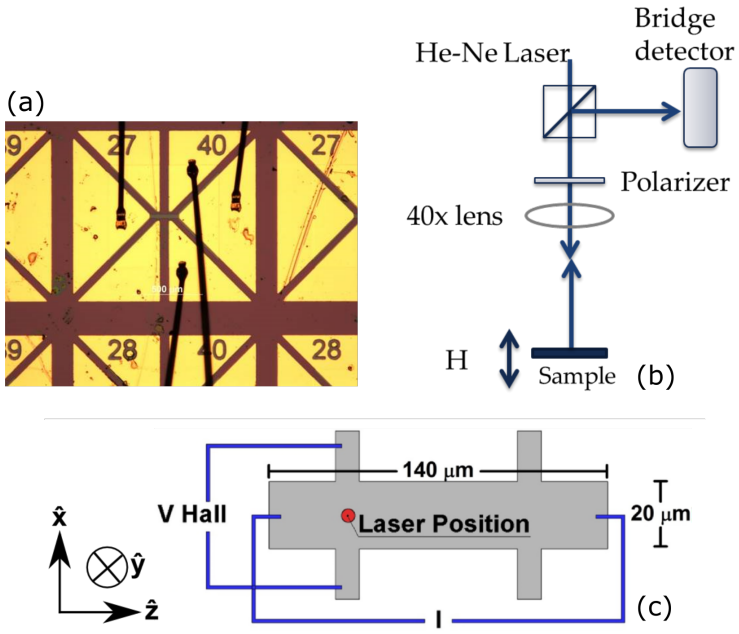

Figure 6.2: (a) Wirebonds to contact pads. Experimental geometry for (b) polar MOKE and (c) Hall resistance measurements.

6.3 Results and Discussion

6.3.1 Field Induced Switching Measured by MOKE and Hall Resistance

Using an out-of-plane ($\hat{\mathbf{y}}$) field the saturation Kerr rotation (figure 6.3.(a)) and Hall resistance (figure 6.3.(b)) were found for each of the bistable out-of-plane magnetisation **M** states. These results were used to confirm full magnetization reversal had occurred in subsequent current induced switching experiments. The devices showed a particularly low ($\approx$ 10 Oe) perpendicular coercive field. The small difference in coercive field between figure 6.3.(a) and (b) is probably due to the measurements being made at different times and therefore under slightly different conditions e.g. the temperature in the laboratory may affect the coercivity given that the depinning of domain walls is thermally activated. The Hall resistance measured during the application of the in-plane field used to set the initial **M** state is shown in figure 6.3.(c). The crossover observed at $\pm$ 600 Oe is due to the $< 1^{\circ}$ tilt of the field w.r.t. the sample plane.

Whilst the Hall resistance is a useful tool to quickly assess the behaviour of an entire region of a device, as it represents a spatial integral of the domain state within the material between the Hall contacts, utilising the MOKE allows behaviour of much

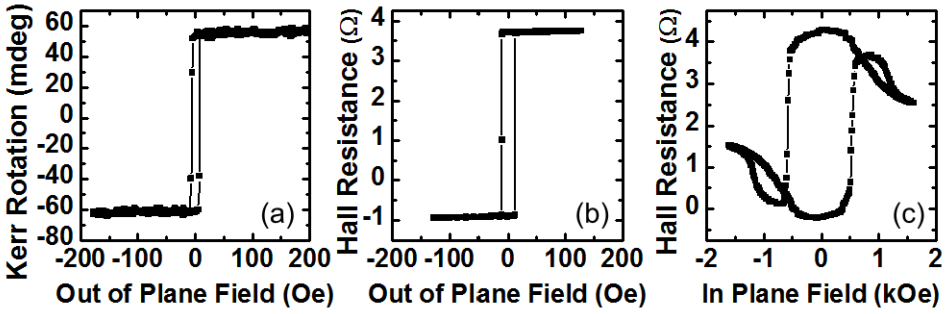

Figure 6.3: Kerr Rotation (a) measured mid-way between the contact pads as shown in figure 6.2.(c), and Hall resistance (b) between the contact pads during sweeping of an out-of-plane ($\hat{\mathbf{y}}$) magnetic field. (c) shows the Hall resistance measured during sweeping of an in-plane magnetic field applied along the direction of the current ($\hat{\mathbf{z}}$).

smaller regions to be probed.

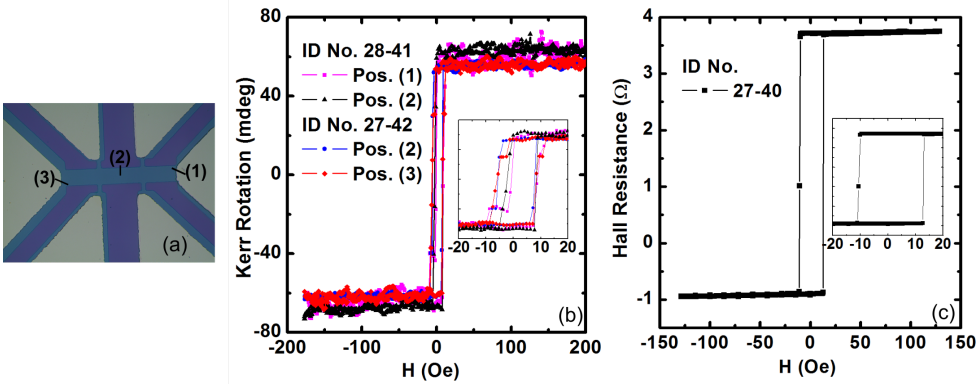

Figure 6.4: Comparison of Kerr rotation (b) and Hall resistance (c) during sweeping of an out-of-plane field for two nominally identical Hall bars arbitrarily labelled 28-41 and 27-42 with the laser focused at different positions on the Hall bar shown in (a).

In figure 6.4.(b) the MOKE is used to assess the uniformity of the response along the length and across the width of the Hall bar. Another advantage of the MOKE technique is that it allows the exploration of multiple devices without physical disruption of the measurement geometry, and so provides a method of quickly testing the uniformity of multiple devices on a wafer. This would be challenging via the Hall effect as it would require electrical connection (in this case wirebonding) of a new device and so removal from the experimental setup. The response of different devices tested on the wafer show uniform behaviour with low coercive fields of 10 Oe, a key requirement for low I_C, observed using both methods. The result of probing different spatial positions

on the device is shown in figure 6.4.(b), and again relatively uniform behaviour is observed. Some stepped structure close to the coercive field can be seen within the inset to figure 6.4.(b). As there are no energetically viable intermediate states between the two out-of-plane configurations it seems likely that this is a result of sampling multiple domains and the resultant intermediate Kerr rotation being a sum of domains in the $+\hat{\mathbf{y}}$ and $-\hat{\mathbf{y}}$ directions.

Using the same experimental setup as figure 6.2.(b) the field was swept in the plane of the sample both $\parallel$ and $\perp$ to the 0.1 mA measurement current I_m (the directions shown in figure 6.5.b) and the results are shown in figure 6.5.a.

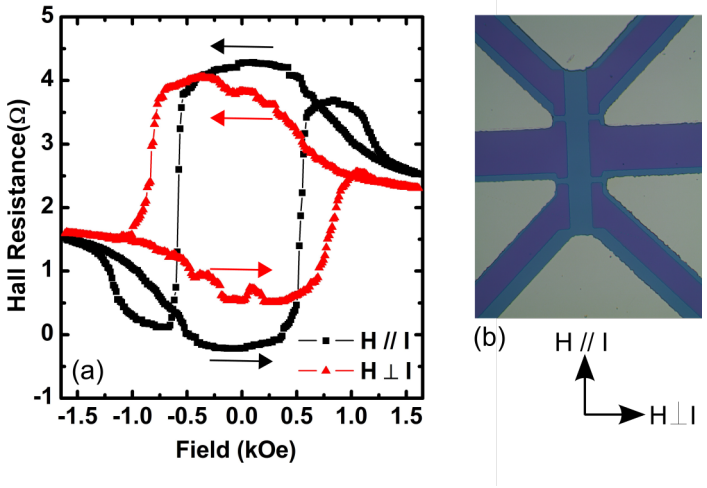

Figure 6.5: Hall resistance (a) measured using 0.1 mA D.C. current for fields swept in the sample plane $\parallel$ and $\perp$ to the current direction as shown in (b). Arrows on (a) indicate the field history.

In both cases in-plane fields of 1.6 kOe were insufficient to rotate the magnetisation fully in-plane, demonstrating the presence of a large out-of-plane anisotropy. The difference in shape of the loops is not indicative of a difference in in-plane anisotropy but instead gives insight into the imperfect alignment of the in-plane field. By taking the perpendicular coercive field as 10 Oe (figure 6.4) simple trigonometric arguments show that a tilt angle of $\sin^{-1}(10\text{ Oe}/600\text{ Oe}) = 1^\circ$ would be enough to see the hysteretic behaviour, and a difference in tilt angle of as little as $0.15^{\{circ}$ could cause the difference in loop shape between the field directions. These small variations in angle are due to a slight tilt during mounting or simply misalignment of the magnet poles relative to the sample mount.

The effect of this small misalignment proved useful for subsequent experiments due to the geometry of the scanning magneto-optical Kerr microscopy (SMOKE) apparatus. The SMOKE contains a quadrupole in-plane magnet and the addition of a 5th pole, to set the magnetization state with an out-of-plane field, before removing it to apply in-plane fields was impractical. Instead for all subsequent measurements a large in-plane field was used to set the initial perpendicular magnetisation in the $\hat{\mathbf{z}}^+$ and $\hat{\mathbf{z}}^-$ directions. This direction was reproducible due to a slight ($< 1°$) tilt of the applied field relative to the plane of the Hall bar. Unless otherwise stated the field was then reduced to remanence (≈ 7 Oe) along the direction of current flow. All measurements were performed at room temperature.

6.3.2 Current Induced Switching Measured by Hall Resistance

After setting the magnetization to the out-of-plane state corresponding to a Hall resistance of 3.20 Ω, the in-plane field was reduced to 50 Oe, parallel to the current direction. The magnetization was switched using current pulses (I_p) of 5 s duration and amplitude ± 5.0 mA as shown in figure 6.6. This current corresponds to a current density of 8.3×10^{13} A/m^2 in the CoFeB and 4.2×10^{13} A/m^2 in the Ta layer. The Hall resistance was measured before and after I_p (the functionality to measure during the pulse was later added) using $I_{test} = 0.10$ mA.

In figure 6.6.(a). we observe a full magnetization switch in agreement with the perpendicularly saturated Hall resistance seen in figure 6.4. Subsequent pulses of the same polarity, shown in (b), do not reverse the magnetisation. When the pulse polarity is reversed the magnetization is switched into the opposite perpendicular direction (c) and again further pulsing of the same polarity does not switch the magnetization (d). The repeatability of this process is shown in (e) which documents an identical switching event to (a).

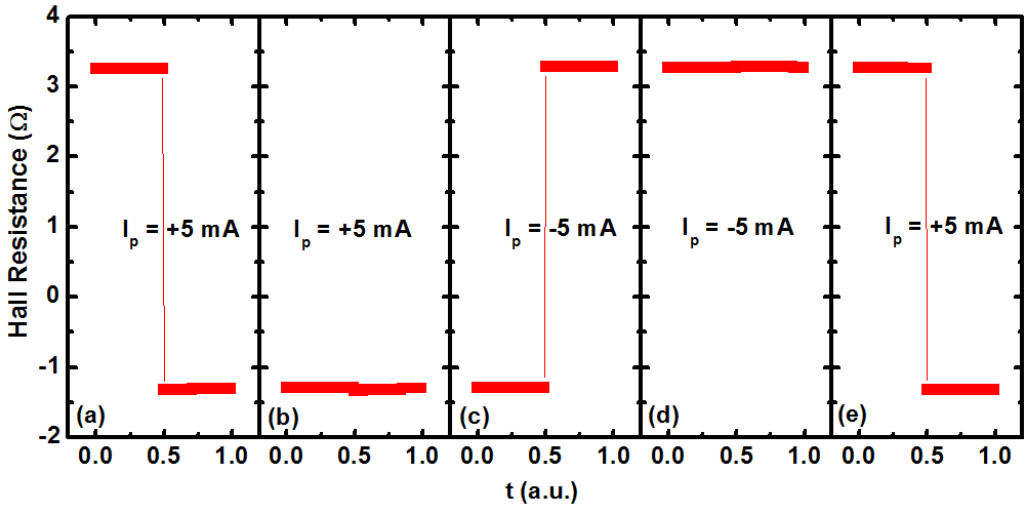

Figure 6.6: Hall resistance of a single Hall bar before and after perpendicular magnetization switching induced by current pulses (I_p) of 5.0 s duration and amplitude $\pm$5.0 mA. Note that t is in arbitrary units as the Hall resistance was not recorded during the pulse itself, the Hall resistance is simple measured before and after the pulse with a D.C. current (I_{test}) of 0.10 mA.

6.3.3 Time Resolved Current Induced Switching Measured by MOKE and Hall Resistance - Constant Time Varying Current

The functionality to record Hall voltage during the switching pulse was added. In the magnetotransport measurements shown in figure 6.7.(a) the initial magnetisation state ($\mathbf{M}^-$) was measured with a small D.C. current $I_{test} = 0.10$ mA and found to correspond to a Hall resistance of $-1.25\ \Omega$. The magnetization was switched towards the opposite bistable state ($\mathbf{M}^+$), which corresponds to a Hall resistance of 3.25 Ω, by current pulses $I_p = 2.00 - 10.00$ mA with a duration of 3.0 s. I_{test} was then applied once more to measure the final magnetisation state. Throughout this process the Kerr rotation (figure 6.7.(b)) was continuously monitored at a position mid-way between the Hall contacts shown in figure 6.2.(c). The Hall resistance is expected to vary symmetrically about 0 Ω, and the 1 Ω offset is due to a slight misalignment of the Hall contacts. The longitudinal resistance of the bonded Hall bar was 2 kΩ, so a 1 Ω offset corresponds to a 0.05 % longitudinal misalignment of the Hall contacts, which is within the tolerance of the photolithographic fabrication procedure.

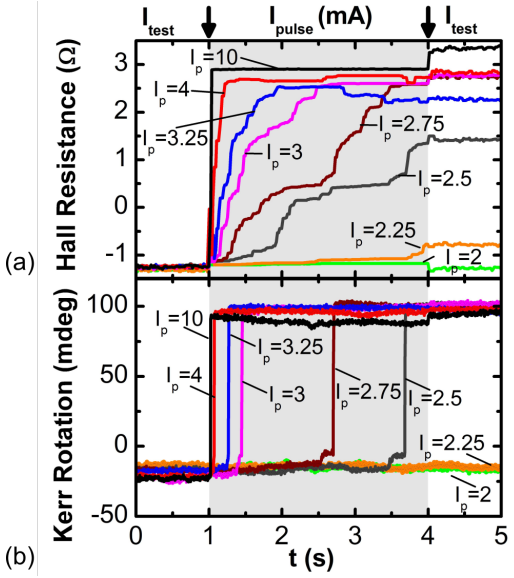

Figure 6.7: Hall resistance (a) between the contact pads shown in figure 6.2.(c) as the device undergoes magnetization switching induced by current pulses of 3 s duration with amplitude I_p = 2.00-10.00 mA, triggered at t = 1 s (darker background on graph). Hall resistance is measured using a current of 0.1 mA both before (t = 0.0-1.0 s) and after (t = 4.0-5.0 s) application of the pulse. (b) shows the simultaneous measurements of the Kerr rotation within a sub micron region mid-way between the Hall contacts, also shown in figure.6.2.(c).

For $I_p > 6.00$ mA, switching occurred on a time-scale < 1 μs, faster than the resolution of the measurement technique (which was limited by GPIB transfer rate in this experimental setup). By reducing the pulsed current to the range $I_p = 2.25 - 5.00$ mA switching occurs considerably more slowly allowing the change in Hall resistance to be easily observed within the 3 s pulse duration. Due to the strong PMA, an intermediate Hall resistance value corresponds to a domain state in which the magnetisation points either in or out-of-plane. The intermediate Hall resistance is effectively equivalent to a line integral of all **M** states between the contact pads. This is confirmed by the Kerr rotation shown in figure 6.7.(b) where the local **M** switches instantaneously between the two states. Switching in figure 6.7.(b) coincides with large steps in the Hall resistance, which are most clear for currents in the range $I_p = 2.50 - 4.00$ mA. This implies that a large area (length equal to a few μm) switches simultaneously. Whether the switching is due to a single domain or a collection of smaller domains is difficult to determine as for $I_p = 2.50$ and 2.75 mA a small step before full switching can be seen in the Kerr rotation (figure 6.7.(b)). This must be due to either the full switching of a small domain, less than the size of the laser spot, or else the laser has been positioned on a domain wall at the edge of a larger domain.

For the highest currents (seen for $I_p = 10.00$ mA in figure 6.7.(a)), the final Hall resistance is slightly larger than that observed for lower currents. This is probably due to the magnetization of the contact pad regions being more strongly pinned and requiring higher currents to switch than the body of the device. For higher currents (again seen clearly for $I_p = 10.00$ mA) the Hall resistance shows full switching occurs within μs, however the final Hall resistance measured with I_{test} is larger than the Hall resistance measured during the pulse. This behaviour may be due to the perpendicular component of the Oersted field (in the $\hat{\mathbf{y}}$ direction) opposing reversal on one edge of the device during I_p. This field will be significantly lower during I_{test}, when full reversal finally occurs. The role of the Oersted field will be discussed further in the final section of this chapter.

For the lowest currents < 2.25 mA no switching occurs. The switching process is stochastic in nature, as shown in Fig. 6.8, and for repeated measurements switching was observed for a critical current of $I_c = 2.6 \pm 0.2$ mA, where the stated uncertainty indicates the full range of values for which complete switching was observed. Other studies have attributed the switching entirely to the giant spin Hall effect and so calculate critical current densities from the current in the Ta layer. Based on typical resistivities of $\rho_{CoFeB} = 100$ $\mu\Omega$cm and $\rho_{Ta} = 200$ $\mu\Omega$cm[126], 2/3 of the current is expected to flow through the Ta layer. This yields $I_c = 1.73 \pm 0.1$ mA and a critical

current density of $2.16 \pm 0.2 \times 10^6$ A/cm^2. Although the critical parameter values are expected to depend upon both the temperature and the characteristic measurement time, the calculated critical current density is similar to values of $3 - 6 \times 10^6$ A/cm^2 reported previously for the same material[18, 22]. Indeed the critical current density is of comparable magnitude to the values reported for MTJs with in-plane anisotropy[207] and for giant magnetoresistance (GMR) spin-valve sensors[214].

The present experiment demonstrates the strong dependence of the switching speed on I_p. Care must therefore be taken in comparing with previous studies that have used different protocols to extract I_c. For example, the current may be swept at a given rate and the Hall voltage measured simultaneously. However, in this case, if the sweep rate is too high, details of intermediate states, such as those observed in figure 6.7(a) for $I_p = 2.5$ mA, may be lost and the critical current may be overestimated.

6.3.4 Time Resolved Current Induced Switching Measured by MOKE and Hall Resistance - Constant Current Varying Time

During the experiments in which I_p was varied, the Hall resistance trace and the time of switching observed in the Kerr signal were not always the same for repeated switching measurements made with identical I_p. Figure 6.8 highlights the stochastic nature of this process showing 5 switching processes under nominally identical conditions for $I_p = 2.75$ mA. The parameters for this experiment were identical to those discussed for figure 6.7 but the pulse length was increased to 5.0 s so that full switching could be obtained within the duration of the pulse at a lower I_p value.

In the transport measurements shown in figure 6.8.(a) the Hall resistance is similar in each event for the first 1.0 s of the pulse. The Hall resistance then diverges between $2.0 - 4.5$ s before reaching the same saturation state in the final $4.5 - 6.0$ s. The divergence coincides with a large step in the Hall resistance which occurs at the same time as the large change in Kerr rotation seen in figure 6.8.(b). As the Kerr rotation probes only the centre of the device (figure.6.2.(c).), it can be inferred that for the first 1.0 s of the pulse, domains at the edges of the Hall bar switch more easily than the magnetisation at its centre, and that switching follows a similar 'path' in each event (reasons for this are to be discussed and shown in figure 6.10). The switching of the central region, observed as a large step in Hall resistance and change in Kerr rotation, occurs later in the pulse and appears more random than the switching of the edge of the device.

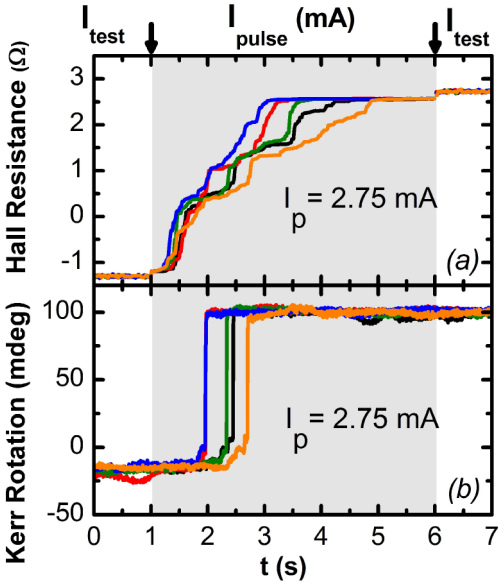

Figure 6.8: Hall resistance (a) between the contact pads shown in figure 6.1.(c) as the device undergoes 5 switching events under identical conditions induced by 5.0 s duration current pulses, with amplitude I_p = 2.75 mA, triggered at t = 1.0 s (darker background on graph). The Hall resistance is measured before (t = 0.0 − 1.0 s) and after (t = 6.0 − 7.0 s) the pulse using a current of 0.1 mA. (b) shows the simultaneous measurement of the Kerr rotation within a sub micron region mid-way between the Hall contacts, also shown figure.6.2.(c).

6.3.5 Static Imaging During Current Induced Switching

For further insight into the domain configuration during switching, scanning MOKE images were acquired for a series of stable (on the time-scale of the imaging experiment) domain configurations during the switching process. Figure 6.9.(a) shows the Hall resistance values at which the images (b) to (h) were taken. It was not feasible to image a single switching event as the 'mid' states (with **M** close to 50/50 in and out-of-plane) were unstable over the imaging time (several hours). Images were instead taken on either side of this unstable middle region for the two separate partial switching events shown in figure 6.9.(a). Image (h) was subtracted from the remaining images to suppress topographic features and optimise the magnetic contrast. The strong dark and light contrast across the bottom of the bar in (h) may be associated with the incomplete removal of photoresist in that region.

Figure 6.9.(b) shows $\mathbf{M}^-$ corresponding to a Hall resistance of -1 Ω. As I_p is applied, the formation (c) and growth (d) of large domains of $\mathbf{M}^+$ is observed. These

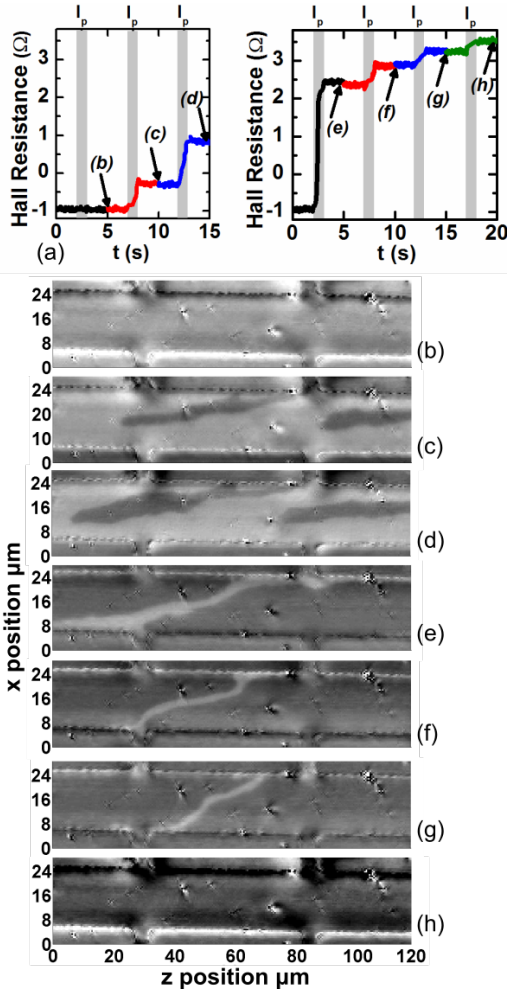

Figure 6.9: (a) Hall resistance values between the contact pads shown in Fig.6.1.(c) for the magnetic domain state images shown in (b) to (h). Darker background in (a) indicates pulse on, lighter background indicates test current on.

domains appear to grow from the edge of the Hall bar and remain pinned at more than one site (e.g. z = 60 μm x = 24 μm). For the second set of stable states the majority of **M** lies in the $\mathbf{M}^+$ direction. The large reversed domain seen in (e) is in a similar position to the domain seen in (c) and (d) and also appears pinned at the same site. This domain then shrinks in (f) and (g) while remaining pinned until a full reversal to $\mathbf{M}^+$ is observed in (h).

To a first approximation the Hall resistance should be proportional to the integral of the out-of-plane component of **M** evaluated along a line between the contact pads. The value of this integral can be compared to the percentage of reversed magnetization

along the same line within the corresponding image. The minimum Hall resistance of -1.25 Ω corresponds to 0% reversed magnetization while the maximum 3.25 Ω corresponds to 100%. The percentage of reversed magnetization inferred from the Hall resistance and Kerr images respectively are (c) 26 and 23%, (d) 39 and 41%, (e) 78 and 77%, (f) 88 and 87%, and (g) 96 and 95%. The magnetic states inferred by the two methods are therefore seen to be in excellent agreement.

Reverse domains appear to form first at the edge of the device for which x = 24 μm, as observed in (b) to (d), and then grow towards the center. When reversal is close to completion the largest portion of the original domain state appears to be located on the opposite edge of the device, as seen clearly in (e) around x = 4 μm. This may again be due to the presence of the Oersted field, with the $\hat{\mathbf{y}}$ component of this field (B_y) having peak magnitude but opposite polarity at the two long edges of the device.

6.3.6 Modelling of Oersted Fields

Many studies of similar structures do not discuss the presence of Oersted fields. Some studies[13, 14] do calculate the in-plane component of the Oersted field (B_x) and conclude that it does not have any significant effect upon the switching since B_x is about 1 order of magnitude smaller than the effective fields generated by spin-torques (ref [13] calculates 0.3 Oe/mA for a 20 μm wide bar) and this field often acts to oppose the spin-torques[15].

We demonstrate in the model shown in figure 6.10 that while B_x is indeed small B_y can become comparable to the 10 Oe coercive field shown in figure 6.4 and so may have a significant effect on the switching process, at least in the absence of an external field applied to the structure.

The Hall bar cross section (20 μm x 4 nm Ta and 1 nm CoFeB) was modelled by filling it with wires of radius r as shown in figure 6.10.(a). The space in and around the bar was broken into a grid and the field calculated at each point from the Biot-Savart law

$$\mathbf{B}(r) = \frac{\mu_0}{4\pi} \int_C \frac{I d\mathbf{l} \times \mathbf{r}'}{|\mathbf{r}'|^3}, \tag{6.5}$$

where $d\mathbf{l}$ is a vector whose magnitude is the length of the differential element of the wire in the direction of conventional current, $\mathbf{r}' = \mathbf{r} - \mathbf{l}$ the full displacement vector from the wire element ($\mathbf{l}$) to the point at which the field is being computed ($\mathbf{r}$) and μ_0 is the permeability of free space.

A uniform current density was assumed in each layer. The current density in each layer was calculated assuming $\frac{2}{3}I$ in the Ta layer and $\frac{1}{3}I$ in the CoFeB (as discussed in the previous section), and the current in an individual wire was adjusted to take

account of the packing fraction (4/3). The current was assumed to flow perpendicular to the cross sectional plane, shown in figure 6.10.(a) in the $\hat{\mathbf{z}}$ direction. Each layer was assumed to have a thickness equivalent to five wire diameters ($r_{CoFeB} = 1/10$ nm and $r_{Ta} = 4/10$ nm) in order to optimise computation time. Further increase in the number of wires contained within the layer made negligible difference to the calculated field. The minimum wire radius tested was $r_{CoFeB} = 1/32$ nm but little change in the result was observed when wire radius was $r_{CoFeB} < 1/10$ nm and so five wires through each of the CoFeB and Ta thicknesses were used to minimise computation time.

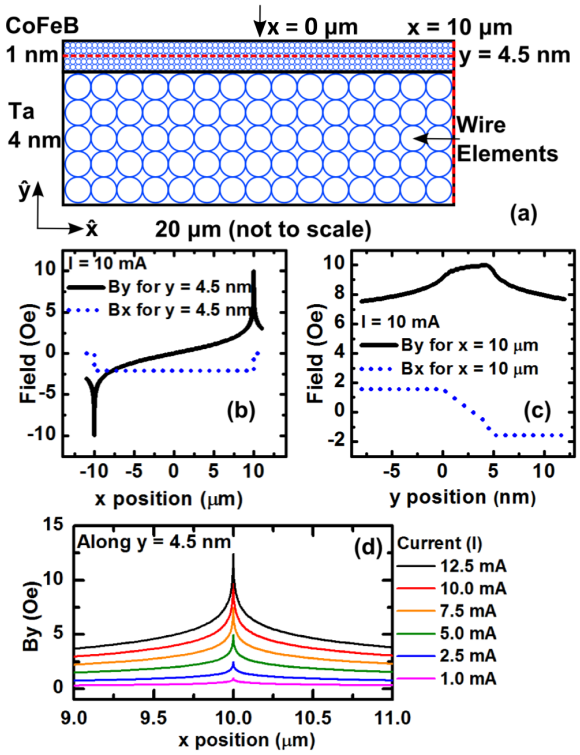

Figure 6.10: Geometry (a) for calculation of Oersted fields in Ta/CoFeB layers modelled as an array of wire elements. (b) shows how the in (B_x) and out-of-plane (B_y) components of the Oersted field vary across the width of the Hall bar along a line through the center of the CoFeB layer. (c) shows the variation of these fields across the thickness of the layers at the edge of the Hall bar where the out-of-plane field has maximum value. (d) shows how the out-of-plane field varies with current along a line through the center of the CoFeB layer close to the edge of the Hall bar.

In figure 6.10 the $\hat{\mathbf{x}}$ direction has again been defined along the width of the Hall bar (20 μm) while $\hat{\mathbf{y}}$ lies perpendicular to the plane. Figure 6.10.(b) shows B_y and B_x along

a line through the center of the CoFeB layer at y = 4.5 nm for $I_p = 10$ mA. The field profile is as expected for a current carrying strip[215] and B_x is in good agreement with fields calculated in ref.[13]. We observe a sharp peak in B_y with height of about ± 10 Oe close to the edges of the bar. These fields are comparable to the 10 Oe out-of-plane coercive fields observed for this device in figure 6.3. The magnitude of the Oersted field varies little through the thickness of the CoFeB layer as shown at the field peak around (x = 10 μm), in figure 6.10.(c). These results in conjunction with figure 6.9 may explain the domain behaviour at the edges of the device. On one edge B_y aids the reversal of domains whilst on the opposite edge it opposes reversal. This effect may be lessened as I_p and hence B_y are reduced as shown in figure 6.10.(d). Even for $I_p = 5$ mA the Oersted field is still about 50% of the coercive field, and so is still likely to influence the switching process.

With recent interest in resolving the contributions of several mechanisms to the switching of similar devices, this result shows that Oersted fields may not always be discounted when interpreting the relative contribution of each switching mechanism, and also that care must be taken when designing devices of this type. A simple method of minimising B_y, so as to explore only the spin-torque contributions to the switching, is therefore to perform a post deposition etch to remove CoFeB at the edges of the Hall bar, leaving only the Ta underlayer. In the majority of recent studies the HM underlayer has been thicker than the FM layer and so carries the majority of current, meaning that perpendicular Oersted fields in the FM would be effectively minimised by this approach. Another approach to studying the spin transfer torque is to apply an in-plane external magnetic field to the structure, so that switching occurs via coherent rotation[126] of magnetization rather than by domain nucleation and growth.

6.3.7 Wide Field MOKE

Due to the slow speed of the switching at low currents an attempt was made to observe the switching of the entire device using a wide-field CCD camera and a polariser. Figure 6.11 shows two images at $I_p = \pm 10$ mA, these currents correspond to a full switch of the magnetization to each of the fully saturated states (figure 6.7).

No clear difference in contrast is observed between images (a) and (b). An argument could be made that image (b) has a darker contrast however the entire image appears darker overall. A difficulty of this method was the strong reflection from the Au contact pads surrounding the Hall bar, this reflection was considerably stronger than that from the dark Ta/CoFeB/MgO and dominated the colouring of the image, even

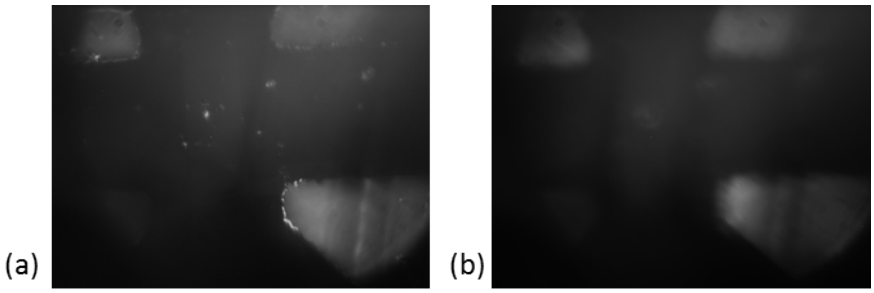

Figure 6.11: Wide-field MOKE images of a Ta/CoFeB/MgO Hall bar with **M** saturated in the z^- (a) and Z^- (b) directions.

when extensive post-processing was employed. With no clear difference between the saturated reference states this method was not pursued further for the measurement of intermediate states.

6.4 Summary and Future Work

Current induced switching in perpendicularly magnetised Ta/CoFeB/MgO layers was studied by simultaneous Kerr microscopy and electrical transport measurements, focusing on currents close to the critical value for switching. For zero applied magnetic field we find the switching to be a stochastic domain wall driven process, the speed of which is strongly dependent upon the value of the applied current. The nucleation of reverse domains appears to begin at one edge of the device, before these domains then grow towards the center of the Hall bar. Modelling the Oersted field through the cross section of the Hall bar reveals that the out-of-plane component is comparable to the 10 Oe out-of-plane coercive field of the CoFeB, suggesting that the Oersted field may assist the initial domain nucleation on one edge of the Hall bar while opposing reversal on the other edge.

With recent interest in utilising Ta/CoFeB/MgO layers in perpendicular magnetic tunnel junctions this study highlights the need for careful consideration of the Oersted field when analysing potential contributions to the switching process. Minimisation of the Oersted field contribution, to facilitate study of spin-torques, can be achieved by etching the CoFeB layer at the edge of the device, although it may also be possible to utilise these fields to improve switching efficiency in future technologies.

Chapter 7

Time-Resolved Scanning Kerr Microscope Studies of Spin Orbit Torque Induced Magnetisation Dynamics in Ta/CoFeB/MgO Hall Bars

7.1 Introduction

The work in this chapter builds on the work of chapter 6 but employs the TRSKM measurement geometry to further explore the torques acting upon a HM/FM Hall bar with the structure Ta/CoFeB/MgO. Whilst the background and motivation remains similar, utilising TRSKM opens up the potential for directly observing the time dependence and direction of any SOTs which may be present in current induced switching. As discussed in section 2.14.3 it has been demonstrated that both field-like and anti-damping-like current induced torques may be present in the Ta/CoFeB/MgO trilayer[74, 197, 73, 107]. Initially the anti-damping torque was thought to be due to the SHE[15] however it has also been shown that the RE can produce torques of a similar form[216, 197]. Initially the field-like torque was thought to arise from the RE[73] however it has also been shown that the SHE can produce torques of a similar form[217]. The potential torques are further complicated by the presence of an Oersted torque in the FM, due to currents in the HM, which has the same symmetry as the field-like torque but has been shown to

either oppose or add to the SOT term. The total torque in the FM layer can be expressed as

$$\mathbf{T} \propto \mathbf{T}^{\parallel} + \mathbf{T}^{\perp} = a_j(\hat{\mathbf{m}} \times (\hat{\mathbf{y}} \times \hat{\mathbf{m}})) + b_j(\hat{\mathbf{m}} \times \hat{\mathbf{y}}), \tag{7.1}$$

where $\hat{\mathbf{y}}$ lies in the plane of the sample and perpendicular to $\hat{\mathbf{x}}$, the direction of the current, $\hat{\mathbf{m}}$ is a unit vector parallel to the magnetisation and a_j and b_j are parameters that depend on the current, magnetisation, NM/FM geometry and materials. As discussed in section 2.14.3 it has also been shown that higher order contributions to these torques may also be present which have the form shown in equations 7.10 and 7.9. Efforts have been made to separate the contributions from these two torques by studying their dependence on layer thickness[16] An additional field-like torque in the same direction as the Oersted torque has been observed in Py/Pt layers[106]. However a similar field-like torque which oppposes the Oersted torque[107], has been observed in ultra-thin Co/Pt bilayers. This suggests that at least the field-like torque is sensitive to the details of sample composition and thickness. There remain many open questions about SOTs in HM/FM structures which challenge our current understanding of spin-orbit physics. Answering these questions will open up the possibility of exploiting new classes of materials and enhance technologies that can exploit the resulting magnetisation dynamics.

7.2 Experimental

Wire-bonding was used to connect the same Hall bar measured in chapter 6 to a single 50 Ω CPW. One end of the Hall bar was connected to a CPW signal line so that the Hall bar shorted the CPW. The signal line was connected to a 7 V Picosecond Pulse Labs (PSPL) electrical impulse generator and the ground plane connected to a 50 Ω terminator. Between the generator and the CPW was a directional coupler which redirected the current reflected from the device under test (DUT) to a sampling oscilloscope. Monitoring this reflected pulse was especially important in this experiment as the Hall bars were not designed for high frequency, pulsed current measurements. Therefore the impedance matching was expected to be poor, and therefore the amplitude of the reflected pulse was expected to be high. Figure 7.1 shows a pulse reflected from an SMA open, before connection to the waveguide and DUT, compared to the reflection after connection.

The reflected pulse from the SMA open (figure 7.1.(a)) had $\approx 1/3$ of the magnitude of the input pulse from the PSPL. This can be compared to the reflection from the

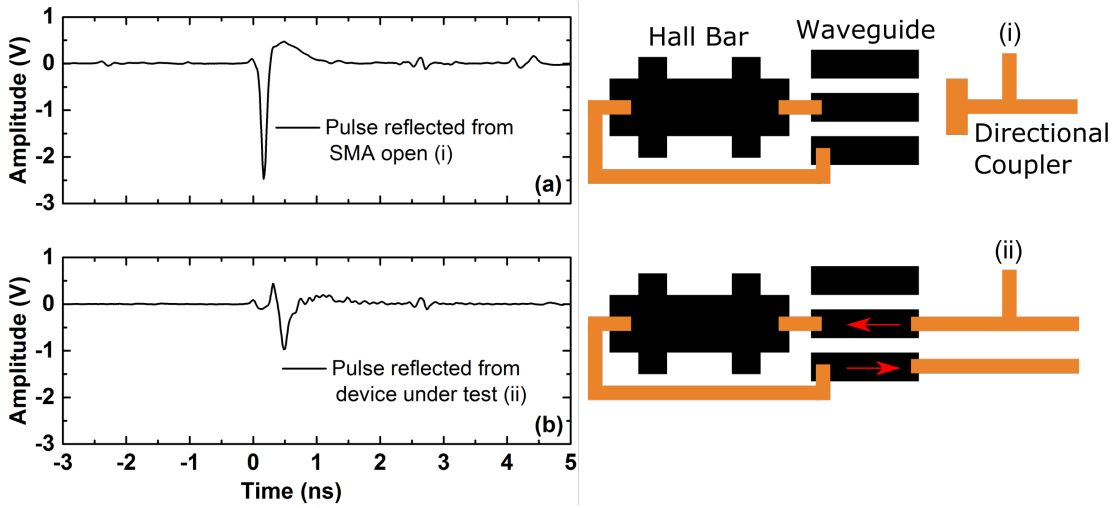

Figure 7.1: Electric pulse reflected from (a) SMA open immediately prior to device under test and (b) from Hall bar. Figures on the right show configurations of waveguide, Hall bar and directional coupler. Red arrows represent the direction of current flow.

DUT (figure 7.1.(b)) to give some sense of the pulse delivered to the Hall bar. Whilst not perfect, it can be assumed that the difference in reflected pulses between the connected and disconnected states corresponds to the pulse delivered to the device. Approximately 1/3 of the pulse is reflected by the device so the characteristic impedance can be calculated from $R = (Z_L - 50)/(Z_L + 50)$. Under these assumptions $Z_L = 100\Omega$ which corresponds to a current density of 1.5 A/cm^2.

The experimental geometry for the measurement of magnetisation precession within the TRSKM is shown in figure 7.2, the basic principles of this experiment are described in section 4.5.3.

This TRSKM set up does not have the functionality to apply a static out-of-plane field to set the perpendicular magnetisation state. The magnetisation cannot be reset between experiments by current pulses as TRSKM is a stroboscopic measurement, meaning that though the first pulse can switch **M** from one perpendicular state to the opposite state, subsequent pulses will have no effect on the magnetization direction (as shown in figure 6.6). Using a unipolar pulse from the 80 MHz, 7 V, PSPL pulse generator meant that switching of **M** between the $\hat{\mathbf{z}}^-$ and $\hat{\mathbf{z}}^+$ states could not be observed. Instead an in-plane field is used to perturb the equilibrium direction of **M** from the perpendicular direction and the current induced precession measured.

Both the simple (out-of-plane component of **M** only) and vector (in-plane and out-of-

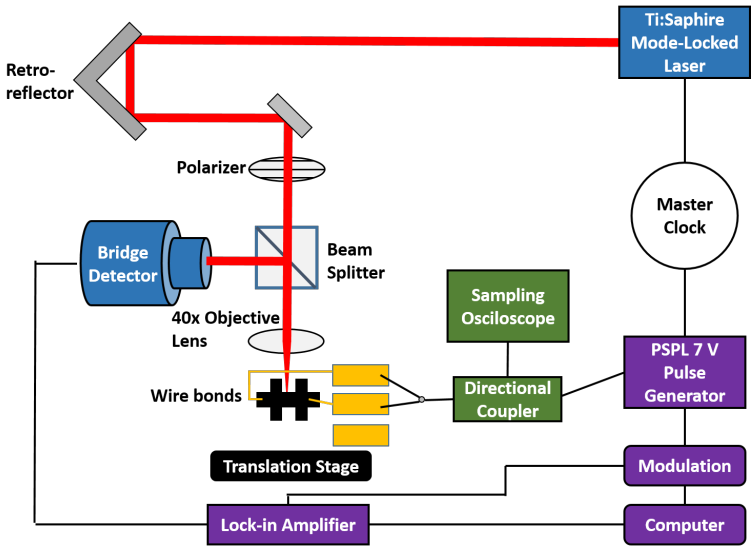

Figure 7.2: Experimental set up for time-resolved scanning Kerr microscopy measurements of precession dynamics in Ta/CoFeB/MgO Hall bars.

plane components of **M**) bridge detectors were used in this study. The advantage of the vector bridge is its sensitivity to all three Cartesian components of the magnetization. However the sensitivity is approximately a factor of $\times 10$ less than the sensitivity of the simple bridge. With the precession amplitude being relatively small in the following experiments the detector of choice reflects the goal of the measurement. Figure 7.3 shows the directions of the magnetization components, position of the focus laser spot and the current direction, used throughout this experiment unless otherwise stated.

Unless otherwise stated the laser is focused at the mid-point of the Hall contacts closest to the contact pad bonded to the waveguide signal line. M_z is defined as the component of magnetisation perpendicular to the sample plane, the in-plane component of the magnetisation parallel to the direction of current flow (and the long edge of the Hall bar) is defined as M_x and the in-plane component of the magnetisation perpendicular to the direction of current flow (and the short edge of the Hall bar) is defined as M_y.

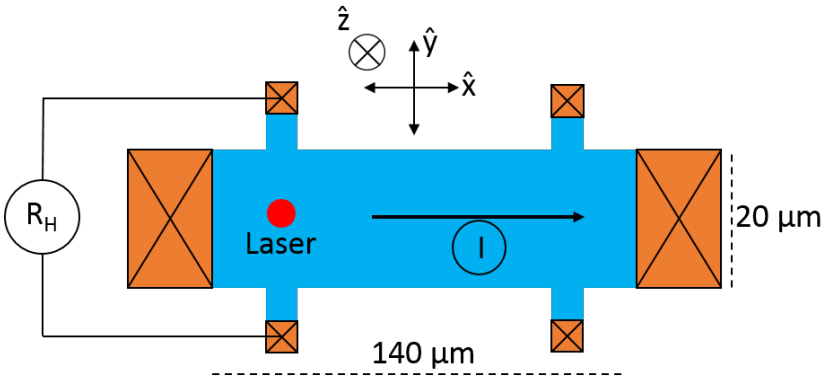

Figure 7.3: Coordinate system and measurement geometry for TRSKM studies of a Hall bar, showing current direction (**I**) and laser spot position (red dot). The Hall contacts used for the work in section 6 are shown for comparison.

7.3 Results

7.3.1 Static Hysteresis

In the pseudo-time-resolved experiments discussed in chapter 6, it was found that the perpendicular magnetisation state could be reproducibly set by an in-plane field due to a slight tilt of the applied field relative to the Hall bar plane. In order to assess the viability of this when samples were mounted in the TRSKM experiment the static response of the Hall bar to an in-plane field was explored. For this measurement only the out-of-plane component of the magnetisation was probed (due to the increased sensitivity of the simple bridge detector). If a magnetic sample with PMA is subjected to an in-plane field, the idealised out-of-plane hysteresis loop will show a maximum in M_z at zero field and the magnetisation will be slowly dragged in plane. This is contrary to the behaviour seen in figure 7.4 which shows hysteresis loops for fields applied parallel ($\hat{\mathbf{x}}$) and perpendicular ($\hat{\mathbf{y}}$) to the long edge of the Hall bar.

All loops show a combination of features indicative of fields applied parallel ($\hat{\mathbf{x}}$ or $\hat{\mathbf{y}}$) and orthogonal ($\hat{\mathbf{z}}$) to the measured component of magnetisation. Unlike other hysteresis loops shown in this thesis, which are typically an average of multiple field sweeps, single nominally identical field sweeps are plotted together to highlight the stochastic behaviour of the magnetisation. With the field applied in the $\hat{\mathbf{y}}$ direction, perpendicular to the long edge (c, f), the orientation of the magnetisation is repeatable between each sweep, however when the field is applied in the $\hat{\mathbf{x}}$ direction, parallel to the long edge (a-b, d-e), the magnetisation does not always follow the same path for

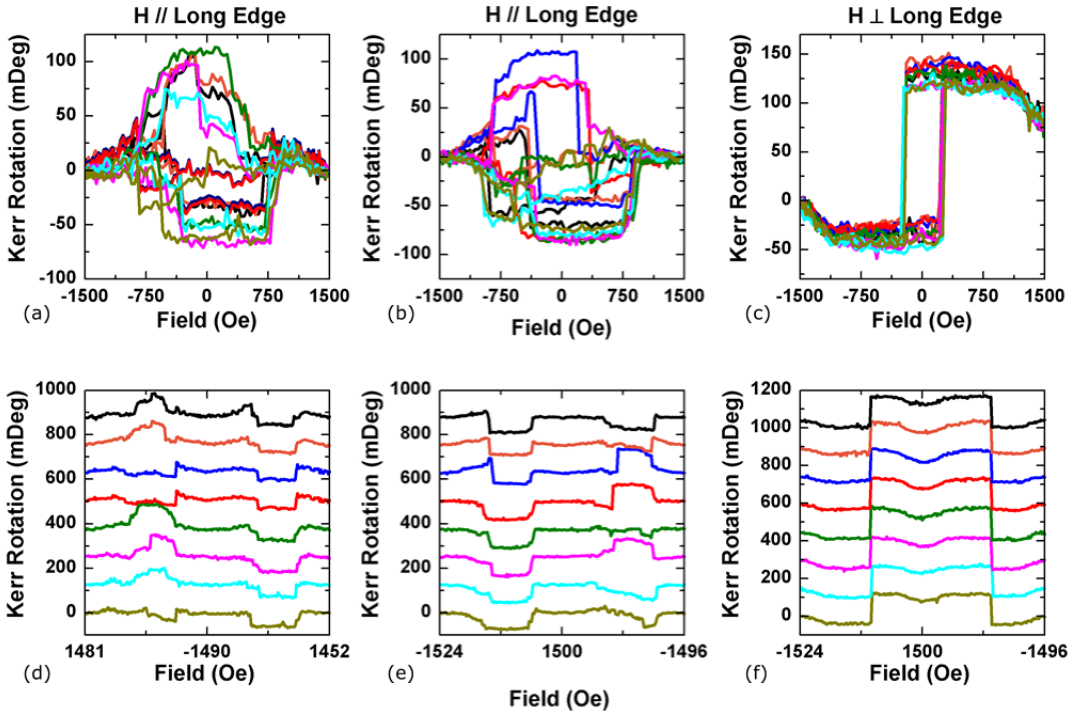

Figure 7.4: Repeated hysteresis loops under nominally identical conditions measuring the response M_z to an in-plane field applied (a-b, d-e) parallel ($\hat{\mathbf{x}}$) and perpendicular (c, f) ($\hat{\mathbf{y}}$) to the long edge of the Hall bar. Typical hysteresis loop plots are shown in (a-c), for clarity (d-f) show 'unwrapped' and offset loops. For $\mathbf{H} \parallel$ to the long edge loops are shown with the initial saturation in the positive (a, d) and negative (b, e) directions.

each of the repeated field sweeps.

First the repeatable (c, f) behaviour will be analysed. The orientation of the magnetisation $\mathbf{M}$ from the hysteresis curves shown in figure 7.4 is a function of the anisotropy energy density ϵ_α and the magnetostatic interaction energy density ϵ_m (discussed in section 2.7). The anisotropy energy density for a film with magnetic anisotropy constant K_u whose magnetic moment makes an angle θ with the easy axis direction (which is perpendicular to the plane) is given by

$$\epsilon_\alpha = -K_u \cos^2 \theta. \tag{7.2}$$

In the absence of an external field the energy minima occur when θ is aligned parallel to the easy axis (90°). When an external field ($\mathbf{H}$) is applied, $\mathbf{M}$ makes an angle θ with the easy axis (figure 7.5.(a)). When ($\mathbf{H}$) is applied in an in-plane direction then the

angle between (**H**) and (**M**) is $\theta_H = \pi/2 - \theta$. In this configuration ϵ_m is given by

$$\epsilon_m = -\mathbf{M}.\mathbf{H} = -MH\cos\Big(\frac{\pi}{2} - \theta\Big). \tag{7.3}$$

Assuming saturation magnetisation (M_s), the competition between the anisotropy energy (acting to keep the magnetisation parallel to the easy axis) and the interaction energy (acting to align the magnetisation with the external field) dictates the total energy density of the system to be

$$\epsilon_t = -K_u\cos^2\theta - MH\cos\Big(\frac{\pi}{2} - \theta\Big). \tag{7.4}$$

When the magnetic field is applied in the direction opposite to the magnetization vector, and is large enough to overcome the anisotropy energy, the moment will jump over the energy barrier (figure 7.5.(c)) and stay in the opposite direction when the field is removed, this condition is known as the flipping field. Stoner and Wohlfarth[218] showed this field can be found from the condition that $d\epsilon_t/d\theta = 0$ and $d^2\epsilon_t/d\theta^2 = 0$.

For the condition

$$\frac{dE}{d\theta} = 0 \quad \text{then} \quad \cos(\theta) = 0 \quad \text{or} \quad \sin(\theta) = \frac{MH}{2K_u}. \tag{7.5}$$

The responses of the vector components of **M**, M_z and M_x are given by

$$M_x = M\sin(\theta) \tag{7.6}$$

and

$$M_z = M\cos(\theta) \tag{7.7}$$

respectively, so

$$M_z^2 = M^2 - M_x^2 = M(\sqrt{1-\sin^2\theta}) = M\Big(\sqrt{1-\Big(\frac{MH}{2K}\Big)^2}\Big). \tag{7.8}$$

The expected response of M_z for a sample with PMA to a tilted in-plane magnetic field is shown in figure 7.5.(c).

The similarity can be seen between the expected hysteresis loop shape shown in figure 7.5.(c) and the observed shape when the field is applied parallel to the long edge of the Hall bar shown in figure 7.4.(c). For the field range applied in this direction (the maximum of the TRSKM system) it is clear that M_s is never reached as the extremums of the curve do not reach the same Kerr Rotation value. When the field is applied

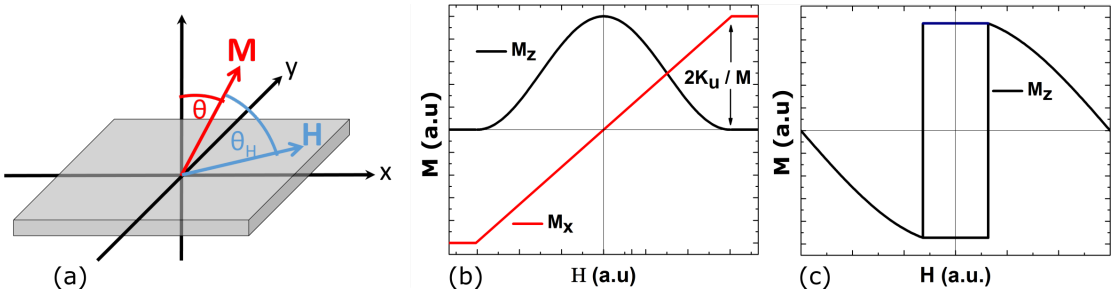

Figure 7.5: (a) Magnetisation orientation of a sample with PMA under the influence of a bias field applied along the $\hat{\mathbf{x}}$ direction. (b) Idealised magnetic hysteresis loops for the M_x and M_z magnetisation component for a sample with PMA for an in-plane bias field along the $\hat{\mathbf{x}}$ direction. (c) Expected out-of-plane M_z magnetic hysteresis loop for a sample with PMA for an in-plane bias field along the $\hat{\mathbf{x}}$ direction, with a tilt along the $\hat{\mathbf{z}}$ direction.

perpendicular to the long edge, though the magnetisation does not follow the the same path for each iteration the shape is broadly similar. The widening of the flipping field in (a) and (b) and general shape implies the out of plane field component is reduced in this direction. This most likely means that the relative tilting of the field, which has origins in a slight tilt in the sample mounting, is less in this direction. By comparing the 280 Oe perpendicular switching field when the bias is applied in-plane (figure 7.5) to the 10 Oe perpendicular switching field when bias is applied out-of-plane (figure 6.3), a tilt of $\arcsin(10/280) \approx 2^\circ$ is deduced. A tilt in the mounting of the sample may be induced by an uneven mounting of the sample to the sample mount with double sided tape. The sample mount is secured to the piezoelectric stage by a single screw, offset to one side of the sample as shown in figure 7.6. The small angle tilt may have occurred due to the this asymmetry in mounting.

The stochastic nature of this process implies that the switching in this direction may not be a coherent rotation but instead may be a domain wall process. The difference between loops may be caused by either the domain structure being different in each iteration, or potentially that whilst the domain structure is consistent the laser positioning is on, or close to a domain wall so that minor positioning drift means a different domain is measured for each field sweep. It is worth noting that the 'unwrapped' loops shown in (d) and (e) show that sweeps from negative to positive fields produce consistent and repeatable magnetisation orientations. It is the positive to negative field sweeps which are stochastic, the reason for this is not known.

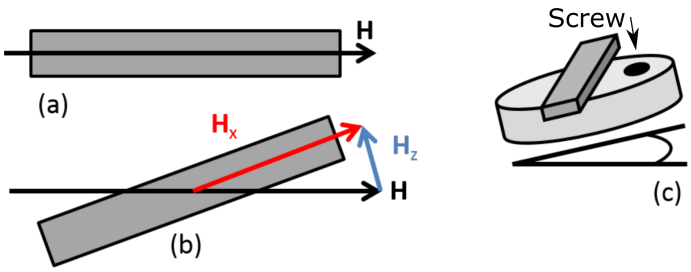

Figure 7.6: (a) Idealised in-plane field, (b) in-plane field with sample tilted relative to the applied field. Note that arrows on this diagram show the direction of the applied magnetic field relative to the sample and are not magnetic field lines. (c) tilting of sample mount due to the offset screw hole (black circle).

7.3.2 Time Resolved Scanning Kerr Microscopy (TRSKM)

Effect of Bias Field

Once the dependence of the ground state upon in-plane field was determined, vector resolved TRSKM was performed using the geometry described in figure 7.2. Figure 7.9 shows the variation of the three Cartesian components of the magnetisation in response to pulsed electrical excitation for fields of 0-900 Oe applied in-plane, along the current direction $\hat{\mathbf{x}}$. Due to the stochastic response with the field applied in this direction (shown in figure 7.4) for each measurement the field was first saturated in the order -1400 Oe $\rightarrow$ 1400 Oe $\rightarrow$ measurement field, unless otherwise stated the field history for all subsequent measurements is a similar bipolar high field saturation then reduction to measurement field. The laser spot is positioned in the center of the Hall contacts (figure 7.3).

In this field configuration independent of whether the magnetisation lies out-of-plane ($\hat{\mathbf{z}}$) or in-plane ($\hat{\mathbf{x}}$ or $\hat{\mathbf{y}}$) in the $\hat{\mathbf{x}}$ direction, a torque on $\mathbf{M}$ is expected due to Oersted field excitation as well as any SOTs. The oscillation amplitude of the out-of-plane component of the magnetisation M_z, is strongly dependent on the bias field. This behaviour is to be expected since an increase of the bias field drags the magnetisation in-plane and increases the M_z component of the precession. There is also a slight increase/decrease in precession frequency. An unexpected behaviour occurs for the largest in plane fields ($\mathbf{H} \geq 750$ Oe) where a secondary oscillation appears to be present, with a lower frequency than the more clearly visible higher frequency oscillations. This can be observed as a positive offset to the higher frequency oscillations and can be seen clearest at ($\mathbf{H} = 900$ Oe). By taking a fast Fourier transform (FFT) of the Kerr rotation

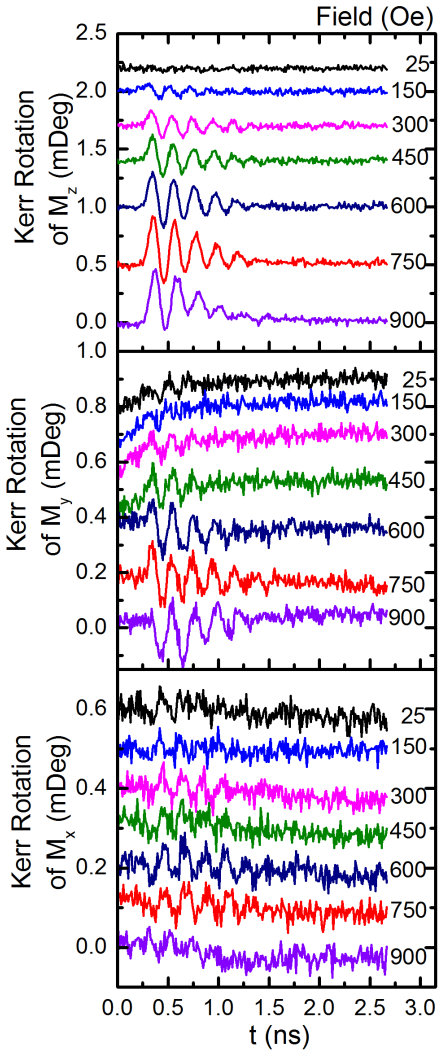

Figure 7.7: Vector time resolved Kerr microscopy of a Hall bar with bias fields 0-900 Oe applied in-plane along the direction of the excitation pulse ($\hat{\mathbf{x}}$). The laser is positioned in the center of the Hall contacts shown in figure 7.3

of the polar magnetisation component it is possible to view the components of the oscillatory signal in the frequency domain, as shown in figure 7.8. In this regime it is clear that in addition to the higher frequency precession centred around 4.8 GHz an additional lower frequency precession can be seen which is highly sensitive to the bias field. This behaviour is investigated further in figure 7.10.

The in-plane magnetisation perpendicular to the current direction M_y follows a similar dependence to M_z increasing in oscillation amplitude with increased field. It is

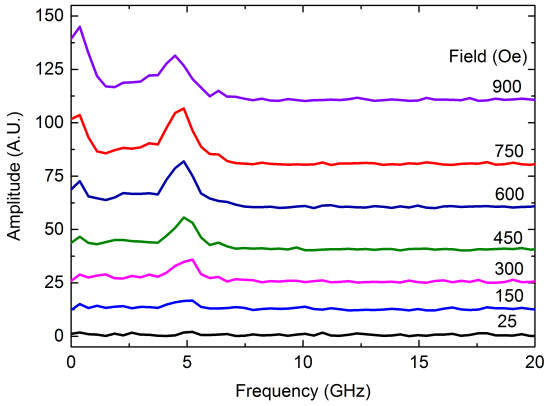

Figure 7.8: Frequency components of the oscillation of the polar magnetisation component shown in figure 7.7.

difficult to separate the potential torques which may be causing this precession as both the Oersted torque and field-like SOT act in the $\hat{\mathbf{y}} \times \hat{\mathbf{m}}$ direction (though the field-like torque has been shown to oppose the Oersted torque[107]. It may be argued that for H= 900 Oe there is a similar secondary oscillation seen a slight shifting of the primary oscillations in the negative direction. The in-plane magnetisation parallel to the current direction M_x shows the least variation in precession amplitude with bias field, showing a small increase up to H = 750 Oe but then almost disappearing at H = 900 Oe.

Effect of Laser Position

The spatial variance of the TRSKM signal was investigated across and along one end of the Hall bar at positions shown in figure 7.9.(c) and (d) with an in-plane field **H** = 600 Oe in the $\hat{\mathbf{x}}$ direction. No significant precession variation can be seen in positions across (a) and along (b) the device. This implies that whilst **H** = 600 Oe is not a large enough field to saturate the in-plane magnetisation there is no evidence of a domain structure, at least on the scale of the position steps in this measurement. This fact is highlighted as domain structure was observed in the pseudo-time resolved imaging (section 6) and in the devices designed for high-frequency TRSKM (section 8). Positions at the extreme edges of the device were not measured so no signs of out-of-plane Oersted fields were observed. This measurement implies that the TRSKM measurements at different bias fields (figure 7.7) are representative of the behaviour of the majority of the device.

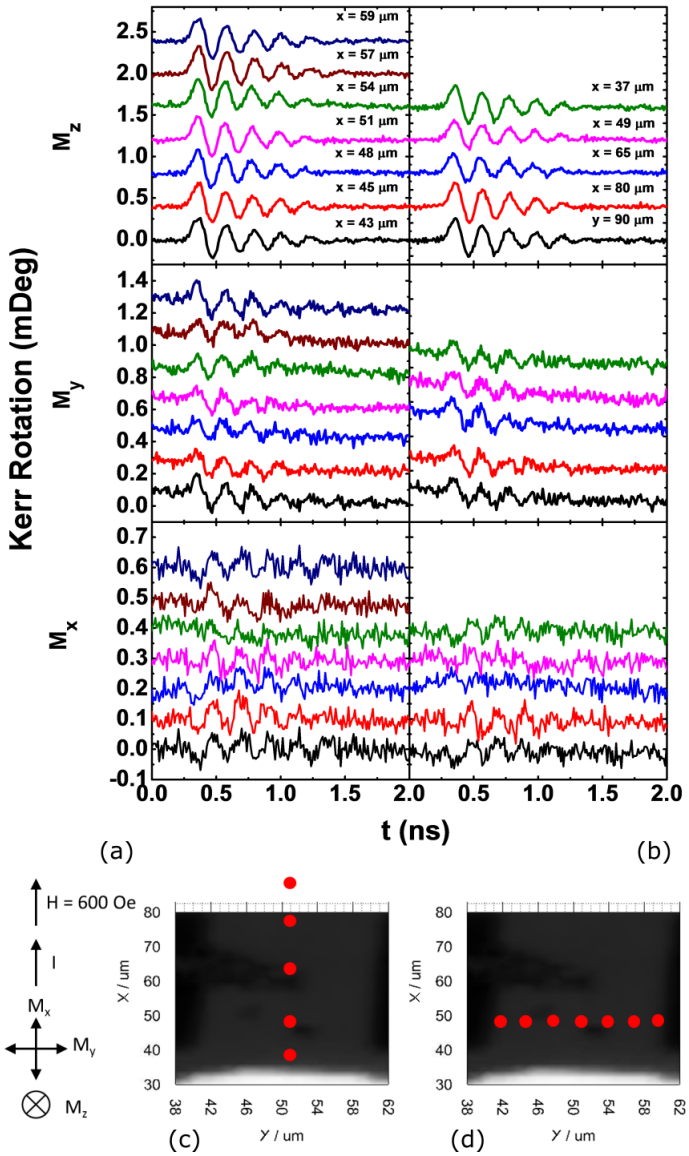

Figure 7.9: Vector time resolved Kerr microscopy at different positions across (a, c) and along (b, d) a Hall bar with an in-plane bias field of 600 Oe applied in-plane along the direction of the excitation pulse ($\hat{\mathbf{x}}$).

Effect of Field Direction and Polarity, and Current Direction and Polarity

In figure 7.7 it was shown that for bias field values H $\geq$ 750 there appeared to be a secondary oscillation visible with a lower frequency than the primary oscillations. The amplitude of this secondary oscillation also appeared to increase with increasing field.

This phenomena was explored further by increasing bias fields up to the high limits of the magnet, rotating the in-plane bias field direction and polarity, and reversing the pulsed current direction. Figure 7.10 shows the oscillation of the out-of-plane magnetisation component M_z (note here the simple bridge detector was used for its increased sensitivity) for bias fields of -1300 to 1300 Oe applied both parallel and perpendicular to the current direction.

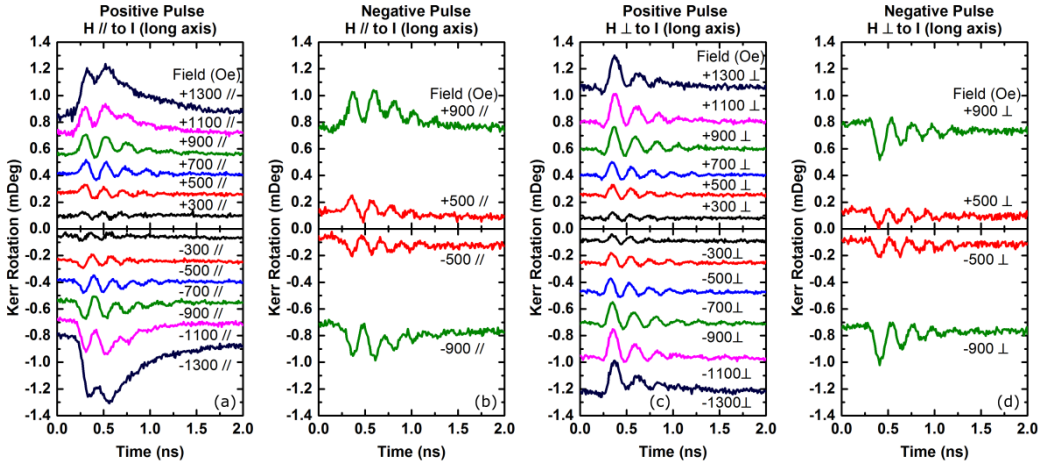

Figure 7.10: Time resolved Kerr signals acquired with the laser spot in the center of the Hall contacts shown in figure 7.3, for a positive pulse with an in-plane bias field applied (a) parallel to $\hat{\mathbf{x}}$ and (c) perpendicular $\hat{\mathbf{y}}$ to the current direction, and for the reversed (negative) pulse direction with an in-plane bias field applied (b) parallel $\hat{\mathbf{x}}$ and (d) perpendicular $\hat{\mathbf{y}}$ to the current direction.

In order to interpret figure 7.10 it is useful to assess the position of the magnetisation prior to the excitation pulse at each field value. The hysteresis loops shown in figure 7.4 imply that when the field is applied parallel to the current direction ($\hat{\mathbf{x}}$) as in figure 7.10.(a) and (b) that for $H = \pm 300$ Oe the magnetisation lies out-of-plane, between $H = \pm 300 - 700$ Oe the magnetisation lies between the out-of-plane and in-plane directions, and for $H = \pm 900 - 1300$ Oe the magnetisation is fully in-plane along $\hat{\mathbf{x}}$. For fields applied perpendicular to the current direction ($\hat{\mathbf{y}}$) as in figure 7.10.(a) and (b) the hysteresis loops shown in figure 7.4 imply that the magnetisation remains largely out-of-plane for $H = \pm 300 - 700$ Oe and lies in an intermediate state between the $\hat{\mathbf{z}}$ and $\hat{\mathbf{y}}$ directions for $H = \pm 700 - 1300$ Oe.

To interpret the potential torques acting on the magnetisation it is useful to examine the direction of magnetisation deflection under the inversion of bias field (and therefore $\mathbf{m}$) and the direction of current flow. In figure 7.10.(a) and (b) where the field is applied

parallel to the current direction ($\hat{\mathbf{x}}$) reversing the bias field direction causes a 180° phase shift of the oscillation of M_z. However reversing the current direction does cause a 180° phase shift of the oscillation of M_z for a given bias field. This behaviour is directly opposite to that seen in figure 7.10.(c) and (d) where the field is applied perpendicular to the current direction ($\hat{\mathbf{y}}$). Here reversing the bias field does not cause a 180° phase shift of the oscillation of M_z. However, reversing the current direction causes a 180° phase shift of the oscillation of M_z for a given bias field.

In order to assess the expected symmetry of the torques $T^{\perp}$ and $T^{\parallel}$ (discussed in detail in 2.14) the expected spin accumulation ($\delta\mathbf{m}$ which denotes the induced magnetisation assosciated with the spin accumulation) in a system with rotational symmetry about the z-axis, and mirror symmetry for all planes perpendicular to the x-y plane, can be considered. Here we follow the arguements of Garello *et al* given in the supplementary material of reference [197].

Consider an applied current driven by an electric field ($\mathbf{E}$) in the x-y plane that leads to $\delta\mathbf{m}$. $\delta\mathbf{m}$ induces a change in the exchange field ($\mathbf{B}^{xc}$) in the ferromagnet, which acts as an effective magnetic field on $\mathbf{m}$, given by $\mathbf{B}^{I} = (\mathbf{B}^{xc}/m)\delta\mathbf{m}$. The resultant torque given by $T = \mathbf{m} \times \mathbf{B}^{I}$. Since the torque only depends on the component of $\mathbf{B}^{I}$ perpendicular to $\mathbf{m}$ then here $\mathbf{B}^{I}$ and $\delta\mathbf{m}$ denote only the perpendicular to $\mathbf{m}$ components of the effective field and spin accumulation.

When $\mathbf{E}$ lies along the $\hat{\mathbf{x}}$ direction and the magnetisation lies in the x-z plane (figure 7.11.(a) and (b)) there are two possible components of $\delta\mathbf{m}$, one perpendicular to the plane $\delta\mathbf{m}^{\perp}$ in the $\hat{\mathbf{y}}$ direction and one in the x-z plane $\delta\mathbf{m}^{\parallel}$. Whilst $\mathbf{E}$ is invariant under a reflection in the x-z plane $\mathbf{m}$ must be inverted as it is an axial vector[197] and so the component of the axial vector $\delta\mathbf{m}^{\parallel}$ is inverted but $\delta\mathbf{m}^{\perp}$ is invariant. This means $\delta\mathbf{m}^{\parallel}$ must be an odd function of $\mathbf{m}$ whilst $\delta\mathbf{m}^{\perp}$ must be an even function. Mirror reflection at the y-z plane followed by a rotation about the $\hat{\mathbf{z}}$ axis by 180° leads to the same conclusion. There is no symmetry operation which forbids either $\delta\mathbf{m}^{\perp}$ or $\delta\mathbf{m}^{\parallel}$, owing to the structure inversion symmetry. For example, if there was inversion symmetry, $\mathbf{E}$ would change under inversion while $\mathbf{m}$ and $\delta\mathbf{m}$ would remain unchanged. Therefore inversion symmetry would dictate that both $\mathbf{E}$ and $-\mathbf{E}$ lead to the same spin accumulation, meaning that, in such a case the linear response of the spin accumulation would be zero.

Consider instead the case that $\mathbf{E}$ is along the $\hat{\mathbf{x}}$ direction and the magnetisation in the y-z plane (figure 7.11.(c) and (d)). Now $\delta\mathbf{m}^{\perp}$ lies in the y-z plane and $\delta\mathbf{m}^{\parallel}$ lies in the $\hat{\mathbf{x}}$ direction. Within linear response $\delta\mathbf{m}$ must change sign upon inversion of $\mathbf{E}$. Again $\delta\mathbf{m}^{\perp}$ must be an even function of $\mathbf{m}$ as, for an inverted $\mathbf{E}$ *and* inverted magnetisation

$\delta\mathbf{m}^{\perp}$ is inverted. Similarly, $\delta\mathbf{m}^{\parallel}$ must again be an odd function. Mirror reflection at the x-z plane followed by a rotation about the **z** axis by 180° leads to the same conclusion.

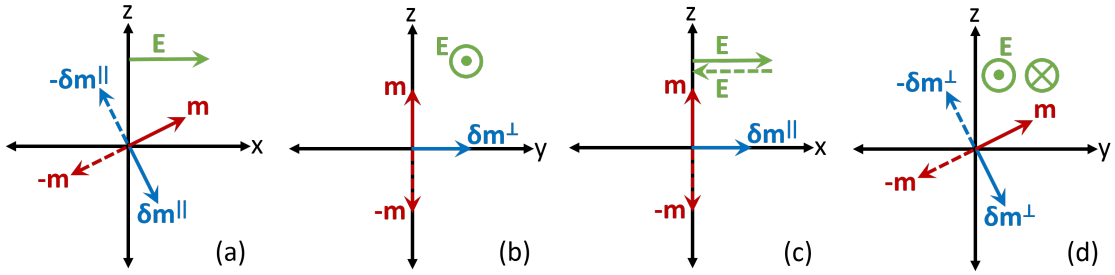

Figure 7.11: Examples of transformations of the electric field **E**, ,magnetisation **m** and the spin accumulation $\delta\mathbf{m}$ under mirror reflections in the x-z and y-z planes. (a) shows magnetisation in the x-z plane, (b) shows magnetisation in the x-z plane viewed on the y-z plane. (c) shows magnetisation in the x-z plane, (d) shows magnetisation in the x-z plane viewed on the y-z plane. This figure is a reproduction from reference [197] supplementary material.

The torque directions observed in figure 7.10 can be assessed in terms of the configurations of **m** and **E**. In figure 7.10.(a) and (b), which correspond to magnetisation in the x-z plane (figure 7.11.(a) and (b)), a 180° phase shift of the oscillation of M_z is induced upon reversal of **M** for all fields. As $\delta\mathbf{m}^{\perp}$ is an even function of **m** it can be inferred that the torque caused in figure 7.10.(a) is caused by spin accumulation due to the odd function of **m**, $\delta\mathbf{m}^{\parallel}$. With the magnetisation in the y-z plane in 7.10.(c) and (d) (figure 7.11.(c) and (d)) reversal of the magnetisation direction does not cause a 180° phase shift of the oscillation of M_z. This behaviour implies that the torque on **M** in this case is caused by an odd function of **m** and so it can be inferred that in this case the spin accumulation is $\delta\mathbf{m}^{\perp}$. In both cases reversing the current direction is expected to reverse the sign of the spin accumulation as reversing the direction of **E** simply reverses sign of pre factors[219] in equation 7.1. A reversal in the precession direction of M_z is observed when the magnetisation is in the y-z plane as expected. However reversal of **E** does not change the precession direction when the magnetisation is in the x-z plane. One possible explanation of this may be that the current density in the first pulse was large enough to switch the direction of **m**, subsequent pulses had no further effect on **m**, so in this case the reversal of **E** in this case *also* corresponds to a reversal of **m**. This could be explored further by a systematic reduction of pulse amplitude, though this will reduce the amplitude of the signal, once the current density is reduced below J_c no

switching will occur.

It has also been shown by Garello *et al*[197] that SOTs present in Ta/CoFeB/Mgo trilayers contain not only the field-like and anti-damping like components but also higher order effects with different directional dependences not explained by current models of the spin Hall and Rashba effects and give the following equations as the minimal set of terms required to model the action of field-like and anti-damping like torques

$$\mathbf{T}^{\parallel} = \mathbf{m} \times (\mathbf{y} \times \mathbf{m}) T_0^{\parallel} + (\mathbf{z} \times \mathbf{m})(\mathbf{m} \cdot \mathbf{x})[T_2^{\parallel} + T_4^{\parallel}(\mathbf{z} \times \mathbf{m})^2], \tag{7.9}$$

and

$$\mathbf{T}^{\perp} = (\mathbf{y} \times \mathbf{m})[T_0^{\perp} + T_2^{\perp}(\mathbf{z} \times \mathbf{m})^2 + T_4^{\perp}(\mathbf{z} \times \mathbf{m})^4] + \mathbf{m} \times (\mathbf{z} \times \mathbf{m})(\mathbf{m} \cdot \mathbf{x})[T_2^{\perp} + T_4^{\perp}(\mathbf{z} \times \mathbf{m})^2]. \tag{7.10}$$

The relative magnitudes of the SOTs have also been shown to have a strong angular dependence. In one study Lee *et al*[219] show for two-dimensional free-electron and tight-binding models with Rashba spin-orbit coupling, the field-like torque acquires nontrivial dependence on the magnetisation direction when the Rashba SO coupling becomes comparable to the exchange interaction. They also find the antidamping-like torque acquires nontrivial angular dependence when the Rashba SO coupling is comparable or stronger than the exchange interaction. Without detailed information about the nanoscopic interface structure and information about the in-plane oscillation directions it is impossible to formulate a full model of the SOTs and fully describe their origins.

In addition to the primary high frequency oscillations a secondary oscillation, with a lower frequency, is seen for all field configurations and the magnitude of this has a strong dependence on the bias field strength. The relative increase in the secondary oscillation amplitude is different for fields applied in different directions, with the much stronger signal seen in 7.10.(a), where the field is applied in the $\hat{\mathbf{x}}$ direction, compared to 7.10.(c) where the field is in the $\hat{\mathbf{y}}$ direction. The origins of this behaviour may lie with the initial orientation of the magnetisation. In figure 7.4 it was shown that the *effective* anisotropy field (which here accounts for any tilt of the ferromagnet) is larger with the field applied in the $\hat{\mathbf{y}}$ direction. It therefore seems reasonable to assume that for a given field, comparison between the precession signals obtained in the two field geometries is also a comparison between magnetisations with different angles from the $\hat{\mathbf{z}}$ direction. If the torque causing the secondary oscillations is sensitive to the magnetisation direction then this would explain the different dependence on bias field

strength since this corresponds to a different ground state for each field direction.

Alternatively observed dynamics of M_z in figure 7.10 are consistent with the magnetisation precessing (the primary oscillations) about an effective field vector which is rotating out-of-plane at a lower frequency (the secondary oscillation). Figure 7.12 shows this precession of $\mathbf{m}$ as $\mathbf{H}_{eff}$ rotates out-of-plane.

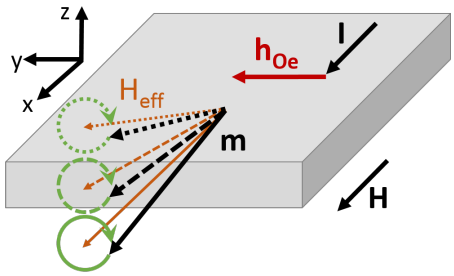

Figure 7.12: Illustration of the current induced precession dynamics observed in a Ta/CoFeB/MgO Hall bar with an in-plane field applied in the direction of current flow.

There are several difficulties in determining the origins of the secondary oscillation. The first is a lack of knowledge of the pulse profile within the device. As discussed previously the Hall bar used in this experiment was not designed for high frequency measurements and therefore may produce significant reflections of the current pulse at the wirebonding interfaces. Unfortunately the device geometry did not allow for measurement of the transmitted pulse. There is a precedent for broadening and attenuation of the current pulse, and therefore a long relaxation time, due to loss from an *n*-type Si substrate[220]. However if the origin of the secondary oscillations is pulse broadening then the broadening would *also* have to be highly sensitive to the bias field magnitude and direction, which is unlikely.

Many recent studies have focused on the direction and magnitude of SOTs, and current induced switching has been demonstrated using sub ns pulses[221] measuring the initial and final states. The time-scales on which the SOTs act have not been explored. One possible interpretation of the data in 7.10 is that the two precession signals are induced by separate torque mechanisms which affect the magnetisation on different time scales. It is possible that the high frequency oscillation is induced by the in-plane Oersted field as the magnetisation is quickly 'kicked' by the field as the current pulse enters the under-layer. The slow deflection caused by SOTs as these occur due to diffusive processes so the induced motion may rise and fall on a slower time-scale, which is dependent on the spin-relaxation rate. If it is true that in such systems different torques act on different time-scales, then this experiment may allow

for the temporal separation of the SOTs, making their origins easier to determine.

7.4 Summary and Future Work

The torques acting on a large scale Hall bar device were investigated by TRSKM as a function of position, bias field direction and current direction. Despite measurement difficulties due to incompatibility of the device design with the high frequency current pulses used in the TRSKM experiment, and measurement of only the polar component of the magnetisation, torques were shown to be strongly dependent on the bias field polarity and direction. Torques due to spin accumulation in the $\delta\mathbf{m}^{\parallel}$ direction were shown to dominate when magnetisation lies in the x-z plane (parallel to the current direction) and torques due to spin accumulation in the $\delta\mathbf{m}^{\perp}$ direction were shown to dominate when magnetisation lies in the y-z plane (perpendicular to the the current direction). The reversal of current direction was shown to reverse the direction of the torque when the magnetisation lies in the x-z plane however unexpectedly no reversal of the torque direction was observed upon current reversal when the magnetisation lies in the y-z plane. However this may be explained by an initial current induced switching of $\mathbf{m}$. Between positions separated by $\approx 3\mu$m no variation in the precession of any of the three Cartesian components of the magnetisation was observed, implying that torques act uniformly across and along the Hall bar. A secondary precessional signal at a frequency an order of magnitude lower than the typical Oersted field induced oscillations typical of this TRSKM measurement may be evidence that different torques present in this system act on different time-scales.

There has been significant recent interest in understanding the torques acting on HM/FM structures especially in current induced switching procedures. There remain many open questions about the nature of SOTs and the effects which generate them and it seems that current linear models of field-like and anti-damping like torques due to the spin-Hall and Rashba effects may be insufficient to fully describe recent experiments. This study further demonstrates the complexity and difficulty of this task. Further understanding of the torques at work requires the fabrication of devices designed for excitation by high frequency current pulses which have minimal effect on the pulse profile. Reducing the size of these devices and decreasing the pulse reflection and loss will allow for larger current densities, potentially increasing the torques, inducing a larger rotation of the magnetisation and allowing full vector resolution of the magnetisation dynamics, a crucial requirement if an improved description of the torques in such systems is to be obtained. This process and its results is discussed in

section 8.

Chapter 8

Time-Resolved Scanning Kerr Microscope Studies of Spin Orbit Torque Induced Magnetisation Dynamics in Patterned Ta/CoFeB/MgO Ultra Thin Films

8.1 Introduction

The work in this chapter builds upon the studies described in chapters 6 and 7. Therefore introductory information regarding the torques acting on the Ta/CoFeB/MgO trilayer system can be found at the beggining of these chapters. This chapter utilises time-resolved scanning Kerr miscroscopy (TRSKM) which is an ideal tool for investigating the potential of the Ta/CoFeB/MgO structure for use in MRAM. Whilst many recent studies have focused on the critical current densities (J_c) required for current induced switching, many have used DC currents, or very long (on the time-scales of MRAM) duration current pulses. For use in MRAM Yagami *et al*[222] state that for CoFeB structures (without PMA), in the current perpendicular to plane (CPP) geometry, the duration of pulsed switching currents (τ_p) for STT switching are required to be of the order of $\tau_p = 5$ ns. They found that J_c decreased logarithmically with increasing τ_p from 1 μs to 5 s, and attributed this behaviour to the increased probability of thermal activation. It is not immediately obvious what the effect of reducing τ_p to sub ns

time-scales will have on J_c for SOT switching, but reduction to time-scales less than the thermal activation time is likely to increase J_c. The stroboscopic nature of TRSKM allows very short < 1 ns pulses to be applied, whilst the spatial resolution of TRSKM allows the investigation of the domain nucleation and propagation processes associated with thermal activation.

A key development in this chapter over the similar experiment presented previously in chapter 7 is that devices were specifically designed for high frequency excitation, unlike the Hall bars which were trialled for the TRSKM experiment in chapter 7. Several key parameters which have the potential to affect the magnetisation dynamics were controlled within the new design. The dimensions of the waveguide and Ta under layer which carry the excitation current pulse determine the current density within the Ta/CoFeB layer. The size and shape of the CoFeB/MgO elements most likely affects the nucleation and propagation of domains. The position of the CoFeB/MgO elements on the Ta under layer can affect the magnitude and direction of Oersted torques acting upon them, as an out-of-plane component of the Oersted field exists at the Ta under layer edge.

In Ta/CoFeB/MgO structures there has been a wide variation of the J_c values reported with values in the range $10^{10} - 12^{12}$ A/m^2 across similar stack structures[20, 21, 15, 22, 18]. One key similarity between these current densities is that they are all smaller than the values predicted by the macrospin model. A potential reason for the variation and consistent overestimation of the macrospin model is that there may be multiple switching regimes, including switching by coherent reversal, incoherent reversal and domain nucleation and propagation, these will also be affected by Joule heating. Which switching regime occurs is expected to have a strong dependence on device size[23, 24] and τ_p. The effect of τ_p, amplitude and external field on the switching probability and critical current (I_c) in Pt/Co/AlO$_x$ dots with lateral dimensions of 90 nm was explored by Garello *et al*[21]. For $\tau_p = 180$ ps to ms range they observed two distinct switching regimes, a short-time intrinsic regime, where I_c scaled linearly with the inverse of pulse length, and a long-time thermally assisted regime where I_c varied weakly. In both regimes the results are explained by the magnetisation reversal proceeding by nucleation and fast propagation of domains and the obtained I_c was 3-4 times smaller than expected for a single domain model. The affect of device size on J_c was explored by Zhang *et al*[25], in Ta/CoFeB/MgO structures miniaturised from a micrometer-sized wire to a 30 nm dot. They observed an order of magnitude increase of J_c from micrometer to 80 nm scales but no further increase from 80 nm to 30 nm and attribute this behaviour due to the transition from a domain nucleation and propagation process to

a single domain switching process. In both of these experiments the Hall resistance across contact pads was used to determine the magnetisation state, so whilst a domain nucleation and propagation process can be inferred it could not be directly measured. In this study TRSKM provides an opportunity to verify these claims and explore the spatial variance of the domain structure for different device sizes, shapes and current densities.

8.2 Design of Ta/CoFeB/MgO Planar Devices for High Frequency Pulsed Current Experiments

The Hall bars used in chapter 7 were not designed for high frequency excitation. Whilst it was possible to connect them to a pulse generator via wire bonding, significant pulse reflection was expected as they did not have optimal 50 Ω impedance matching. In light of this a second generation of devices was fabricated using planar CPW waveguides designed to be connected via picoprobes instead of wirebonds. The waveguides were designed with a 50 Ω characteristic impedance to match the impedance of the picoprobes and SMA cables connecting the device to the pulse generator.

The first generation of Ta/CoFeB/MgO Hall bars were relatively large (20 x 140 μm) as they were designed primarily for electrical Hall resistance measurements. The devices in this chapter, designed with optical experiments in mind, were made considerably smaller and crucially the CoFeB/MgO layer was patterned whilst leaving the Ta layer intact to contact to the Au waveguide and carry a current. The fabrication process was the same as in previous chapters and patterning was achieved with an additional, carefully controlled, ion-beam etching step (the full fabrication procedure is discussed in detail in section 3.7) to etch only the CoFeB/MgO layers. The CoFeB/MgO layer was patterned into shapes including ellipses, rectangles, wedges, notched strips and arrays. Elements were designed to explore how various parameters such as the shape anisotropy and notches would affect domain nucleation and propagation. Modelling in chapter 6.3.6 suggested that out-of-plane Oersted fields may play a role in the switching process. In an attempt to separate this effect from the SOT mechanisms the majority of elements were patterned to leave a few μm between the edges of the Ta layer (the edges that are parallel to the current direction) and the CoFeB/MgO elements. In order to further explore the effect of out-of-plane Oersted fields a small number of devices comprising identically shaped elements at different distances from the edge of the Ta layer were also fabricated. Most commercial applications of SOT based memory

devices will require miniaturisation to the nm scale, for this reason the CoFeB elements were fabricated to have considerably smaller dimensions from 0.25-10 μm (the lower bound here is set by the resolution of the photolithographic fabrication process) than the 140 $\times$ 20 μm Hall bars in previous chapters. Some Hall bars we also fabricated on the same wafers as the patterned devices to facilitate electrical measurements used for preliminary testing.

Another factor taken into consideration when designing the high frequency devices was the DC resistivity of the Ta layer. The DC resistivity of the Hall bars was relatively large ($\approx$ 3500 Ω) due to the comparatively high length to width ratio (140:20 μm) of the Hall bars and the relatively high resistivity of the Ta layer (200 $\mu\Omega$cm[126]). The high frequency devices had a maximum length to width ratio of 1:1 (the minimum ratio was 3:20) so the maximum DC resistance was expected to be equal to the sheet resistance of 500 Ω.

8.2.1 Waveguides

Typically a Picosecond Pulse Labs 4050B pulse generator is used for the TRSKM experiments at Exeter University. The output from this generator has a fixed amplitude of 7 V giving a total delivered current of 7 V/50 Ω = 140 mA. Though attenuation could be used to vary the amplitude, a limited range of attenuators meant a careful choice of Ta under layer thickness (t_{Ta}) and width (w_{Ta}) was necessary to control the current density. Another potential choice of pulse generator was the Avtech AVP-AV-HV3-C pulse generator. This could be used to supply a variable voltage up to 40 V (800 mA). This pulse generator must be triggered at 1 MHz so picking of the probe beam from 80 MHz down to 1 MHz is also required, making use of the 2 ns mechanical delay line (described in section 4.5.3) more difficult for this experiment. Picking can also significantly increases the signal to noise ratio, however this can be offset by a larger precession amplitude due to the potentially larger pulse amplitude. Measurements at 1 MHz would also allow a bipolar pulse to be used, which has the potential to switch the magnetisation backwards and forwards between the two perpendicular states between laser pulses.

A list of the fabricated Ta under layer widths is shown in table 8.2.1 along with the expected current density and in-plane Oersted fields when used with the PSPL pulse generator. In each case the impedance is assumed to be perfectly matched at 50 Ω and the pulsed current fixed at 7 V. It should also be noted here that the current and Oersted fields in the CoFeB layer are not taken into account in this estimation.

w_{Ta} (μm)	t_{Ta} (nm)	I (A)	J (A/cm^2)	B (T)	H (Oe)
1.0	4	0.14	3.50×10^8	8.80×10^{-2}	8.80×10^2
2.5	4	0.14	1.40×10^8	3.52×10^{-2}	3.52×10^2
5.0	4	0.14	7.00×10^7	1.76×10^{-2}	1.76×10^2
10.0	4	0.14	3.50×10^7	8.80×10^{-3}	8.80×10^1
20.0	4	0.14	1.75×10^7	4.40×10^{-3}	4.40×10^1
50.0	4	0.14	7.00×10^6	1.76×10^{-3}	1.76×10^1
100.0	4	0.14	3.50×10^6	8.80×10^{-4}	8.80×10^0
200.0	4	0.14	1.75×10^6	4.40×10^{-4}	4.40×10^0

Table 8.1: Current densities and Oersted fields around Ta strips of varying width, calculated from a 7 V pulsed current and 50 Ω impedance

Previous studies have reported critical switching current densities of $10^{10} - 12^{12}$ A/m^2[20, 21, 15, 22, 18], if the full current is delivered to the Ta strip then the critical current density should lie between strip widths of 50 and 100 μm. For redundancy a range of strip widths above and below these values were fabricated. Imperfect impedance matching will lead to a portion of the current being reflected (I_r) equal to

$$I_r = \frac{Z_2 - Z_1}{Z_1 + Z_2} \tag{8.1}$$

where Z_2 is the impedance of the connecting cable (50 Ω) and Z_1 is the impedance of the waveguide. To ensure a large enough current density, even if reflections occured, smaller Ta strips of 1.0, 2.5, 5.0 and 10.0 μm were fabricated, which, assuming full current is delivered will have a current density far exceeding J_c. A second reason for fabricating narrower Ta strips is that, though switching occurs at J_c, studies have shown that switching occurs more rapidly at higher current densities[193]. One disadvantage of the thinner waveguides is an increased susceptibility to defects, another disadvantage is an increased difficulty in photomask alignment. Three separate photolithography steps were required to fabricate a single set of devices. Photomask alignment must be consistent in all three steps to ensure electrical connection and correct positioning of devices. Alignment was performed by eye under a microscope and, despite alignment markers and careful checking, alignment to within a few μm was challenging. The wider Ta widths $\geq 50\mu$m had the advantage of being significantly easier to align during photolithography. Wider strips also allowed multiple CoFeB/MgO elements to be designed on a single waveguide. Multiple devices allow for much easier measurement in the TRSKM experiment, as sample mounting and probe landing is a time intensive

process. Multiple devices on the same signal line also allows a more consistent comparison between devices as the current density is more likely to be consistent across the same signal line than between nominally identical signal lines. A small number of devices with Ta widths of 200.0 μm, wider than those in the critical current range for the 7 V pulse generator, were also fabricated. These samples were designed for use with the Avtech pulse generator, which can generate higher pulse amplitudes than the PSPL.

Waveguides were designed to accommodate a 125 μm pitch picoprobe at each end, and then to match the Ta signal line width in the central region of the waveguide. For Ta widths $< 50\mu$m the waveguides taper as shown in figure 8.1.(b). For Ta widths of 50 and 100 μm, waveguides were designed to remain as straight tracks, as shown in figure 8.1.(c). Finally for the widest Ta widths of 200 μm the signal line had to widen, as the ends of the waveguide have to remain narrow enough to accommodate the 125 μm pitch probes, as shown in figure 8.1.(d). In order to maintain a constant 50 Ω impedance as the signal line width varied the signal-ground plane spacing also had to vary. The required ratio of signal line width to signal-ground plane spacing was calculated using an online RF and microwave circuit calculation tool[170].

Contacts for Hall bars were also required and were fabricated in three different configurations. Contacts pads for wire bonding contacts are shown in figure 8.1.(e). In order to use picoprobes for Hall resistance measurements a more complex design was required, as shown in figure 8.1.(f).

8.2.2 CoFeB/MgO Elements

The multilayer stack structure for high frequency devices is shown in figure 8.3.(g). The Hall bars measured by TRMOKE in chapter 7 were composed of Ta (4 nm)/CoFeB (1 nm)/MgO (1.6 nm)/Ta (1 nm) layers grown on a relatively low resistivity (100) Si substrate ($\rho \geq 500$ Ωcm). In this chapter several modifications to the stack structure were trialled. The first was growth on a relatively high resistivity (100) Si substrate ($\rho \geq 1000$ Ωcm), this was expected to reduce pulse attenuation and broadening. All other substrate parameters (diameter 50.8 mm, thickness 275 μm) remained identical between substrate types. The second modification was an increase in the thickness of the Ta under layer from 4 nm to 8 nm, this variation was made as there was potential for the additional ion-beam etching step, used to pattern the CoFeB/MgO/Ta top layers to over etch and also remove the Ta under layer. By increasing the thickness of the Ta under layer more material was present ensuring that even if over etched by a few

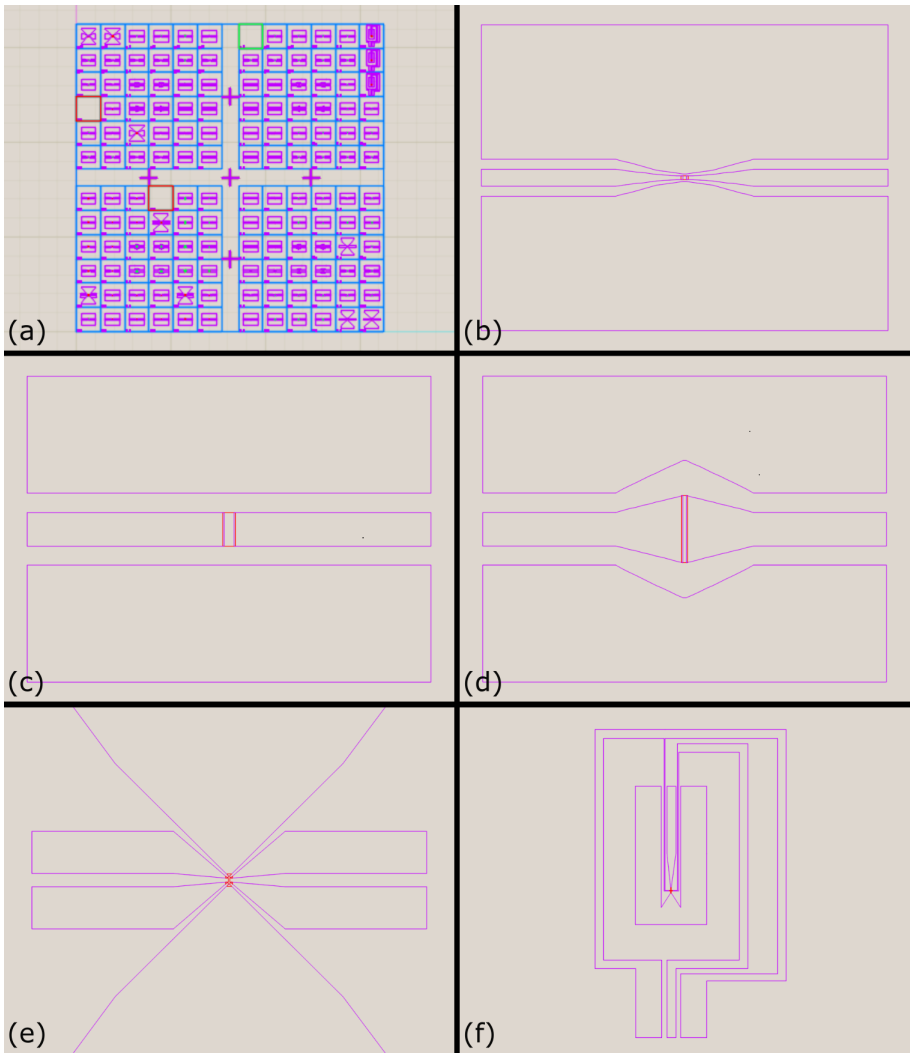

Figure 8.1: (a) 1" Photomask, containing 144 devices split into four quadrants defined by the central cross. Examples waveguides for Ta under layer widths of (b) 10 μm, (c) 100 μm and (d) 200 μm. Hall bar with (e) wirebonding contact pads and (f) picoprobe contact pads.

nm there would still remain an electrical connection to the waveguides. The potential four combinations of stack structure from these variations are low/high ρ Si/Ta (4/8 nm)/CoFeB (1 nm)/MgO (1.6 nm)/ Ta (1 nm) are shown in figure 8.2.

Examples of CoFeB/MgO elements are shown in 8.3.(a-f). The varying circle sizes from 0.25-10 μm radii shown in (a) were designed to explore the potential transition between multi-domain and single domain behaviour. It should be noted that a previous

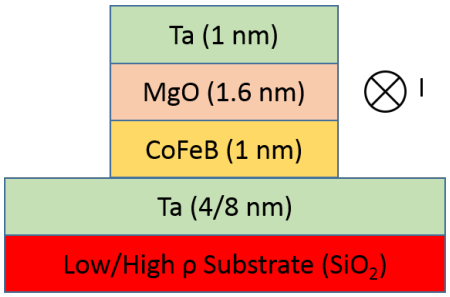

Figure 8.2: Illustration of the stack structure and current direction for Ta/CoFeB/MgO devices designed for TRSKM.

study inferred that single domain behaviour occurred for device dimensions $\leq$ 80 nm[25]. However considerable variations in behaviour of the Ta/CoFeB/MgO structure have been reported for nominally similar compositions, which implies the response is highly sensitive to growth and measurement conditions. It may still be possible to observe the single domain transition, and if not a reduction in the number of domains, even in the relatively larger devices.

The varying length to width ratio ellipses shown in (b) were designed to explore the effects of shape anisotropy. In order to achieve deterministic SOT switching in ferromagents with PMA, an external bias field is typically required. Zero external field deterministic switching has been achieved by engineering a tilted anisotropy[223]. The shapes in (b) were designed to explore whether zero field deterministic switching could be achieved by offering a favourable switching direction by controlling the shape anisotropy. The arrays with varying separation shown in (c) were designed to explore the interaction distance between separate elements, a potentially crucial parameter for SOT memory applications. The identical strips with varying position on the Ta under layer shown in (d) were designed to explore the effect of out-of-plane Oersted fields discussed in chapter 6. If these fields do have an effect on the magnetisation, the dynamics at the edge of the Ta signal lines should show a different behaviour to those in the center. The triangles with varying base width shown in (e) were also designed to explore the effects of shape anisotropy when the anisotropy is relative to the current direction i.e. the triangles were oriented so the current pulse would either reach the narrow or wide end of the triangle first. The strips with notches shown in (f) were designed to explore the possibility of trapping propagating domains.

Two main factors dictate the suitability of a device for TRMOKE. A large amplitude, un-broadened pulse must reach the CoFeB/MgO elements to excite magnetisation

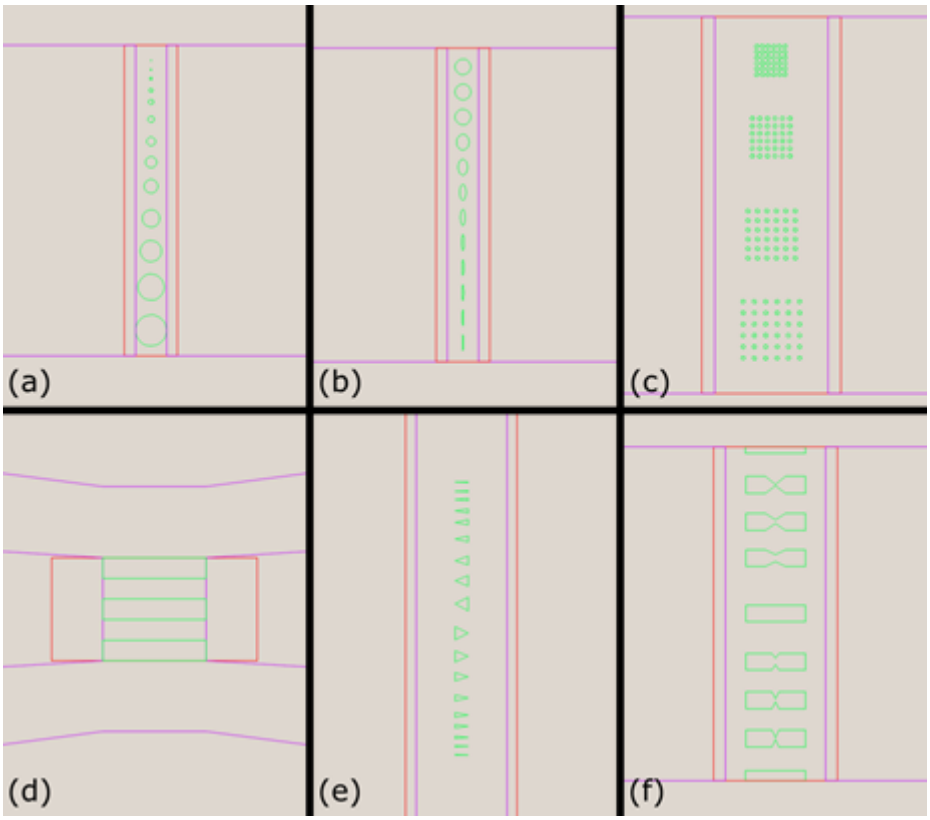

Figure 8.3: Examples of Ta/CoFeB/MgO stack element types consisting of (a) varying circle size, (b) ellipses with one varying dimension, (c) arrays of circles with varying separations, (d) rectangular strips of varying position, width and separation, (e) wedges with varying taper angles and (f) notched rectangles.

dynamics, and the Kerr rotation response must be large enough to detect. Both of these factors were tested across the various device types to assess the most suitable candidate for TRMOKE.

8.2.3 Pulse Profile on Different Substrates and Waveguide Types

In order to ensure correct impedance matching, and to assess which substrate type gave the highest quality pulse profile, probes were landed on different substrate/waveguide types and the reflected and transmitted pulses recorded. The apparatus for this test comprises a pulse generator (PSPL), connected via picoprobes to the measured device. The pulse transmitted through the device was connected directly to a fast oscilloscope, triggered at the same frequency as the pulse generator. A directional coupler was used

to direct the pulse reflected from the device to the same oscilloscope. The original pulse (the pulse from the pulse generator before passing through the waveguide) was measured by direct input to the oscilloscope. The original, transmitted and reflected pulses for signal lines tapering/widening to 10/200 μm on high resistivity substrates are shown in figure 8.4. The lengths of the Ta under layer for the 10 and 200 μm wide signal lanes were 10 and 30 μm respectively.

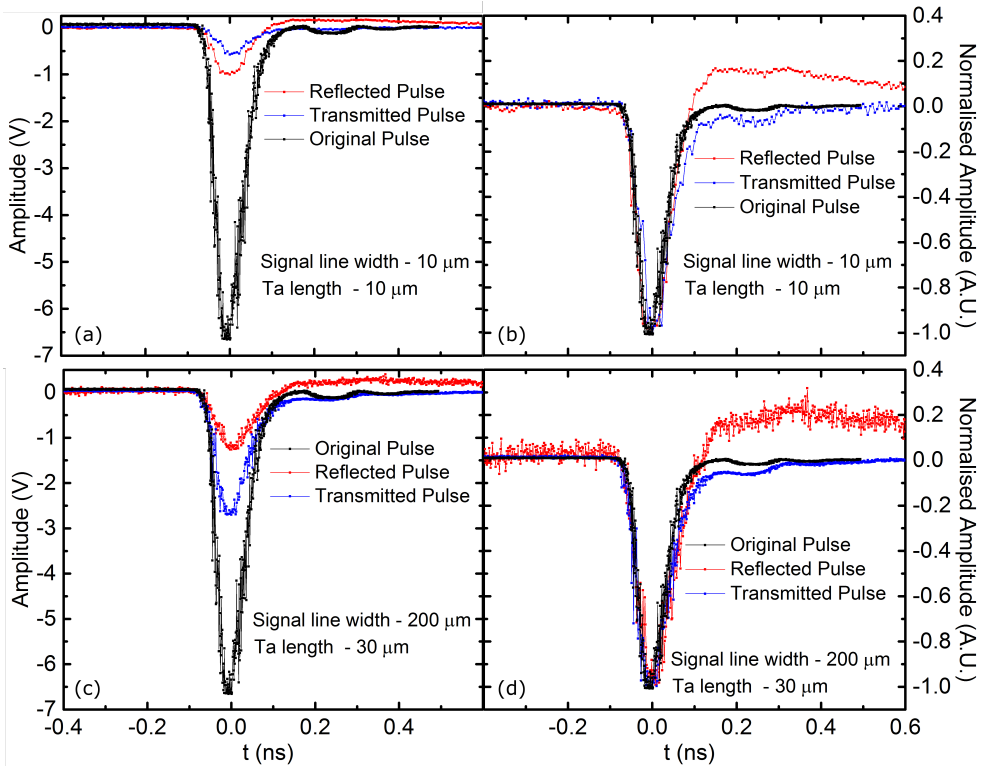

Figure 8.4: Comparison of original, transmitted and reflected pulses in Ta/CoFeB/MgO samples on high resistivity Si substrates. Top panels (a) and (b) show measurements for signal line tapering to a width of 10 μm and a length of 10 μm. The bottom panels (c) and (d) show measurements for signal line widening to a width of 200 μm and a length of 30 μm. Left panels (a) and (c) show calibrated pulse amplitudes and right panels (b) and (d) show normalised amplitude.

For both the 10 μm (a, b) and 200 μm (c, d) signal line widths the reflected pulse is acceptably small $\approx$ 15 %. The normalised plots (b, d) show that on high resistivity substrates no significant broadening of the transmitted pulse occurs, as the transmitted width is comparable to the original pulse width. It is clear from the calibrated amplitude plots (a, c) that the wider signal line has a larger transmitted pulse. This behaviour is

consistent with measurements on other signal line widths. This behaviour is expected as the wider signal lines typically had a lower resistance leading to a lower loss and attenuation of the pulse. The transmitted pulse gives a lower limit on the pulse amplitude at the CoFeB/MgO elements. A pulse will typically experience exponential attenuation along a lossy line, as the CoFeB/MgO elements are halfway along the waveguide the pulse at the sample elements is likely larger than the transmitted pulse. The transmitted pulse may also not be a direct measurement of waveguide efficiency as the pulse energy is absorbed in the excitation of magnetisation dynamics. As the CoFeB/MgO elements are not comparable between waveguide types the transmitted pulse may not be a direct comparison of efficiency between waveguide types. However this absorption is typically negligible compared to the exponential attenuation so for the purposes of comparison this effect is not taken into account.

The original, transmitted and reflected pulses for signal lines tapering/widening to 10/200 μm on low resistivity substrates are shown in figure 8.5.

On low resistivity substrates, for both the 10 μm (a, b) and 200 μm (c, d) signal line widths, the reflected pulse is again acceptably small but shows a greater dependence on signal line width, with the 10 μm signal line reflecting $\approx$ 25 % of the original pulse and the 200 μm signal line reflecting $<$ 10 % of the original pulse. As expected the low resistivity substrates caused a greater broadening of the pulse, though the effect is still minor. This can been seen clearly in the normalised plots (b, d) and occurs primarily on the trailing edge of the pulse. The majority of the high amplitude region of the transmitted pulse retains the same width as the original pulse so this substrate type, whilst not as ideal, is still a viable candidate for TRSKM.

Electrical measurements on samples with 4 nm Ta under layers suggests that, with careful calibration of the ion-beam etch rate, there is no over etching of the Ta under layer as electrical connection is observed for devices with both 4 and 8 nm thickness, and the DC resistance of the Ta under layers is close to the expected value. This means that electrically both $t_{ta} = 4$ and $t_{ta} = 8$ nm samples are suitable candidates for TRSKM.

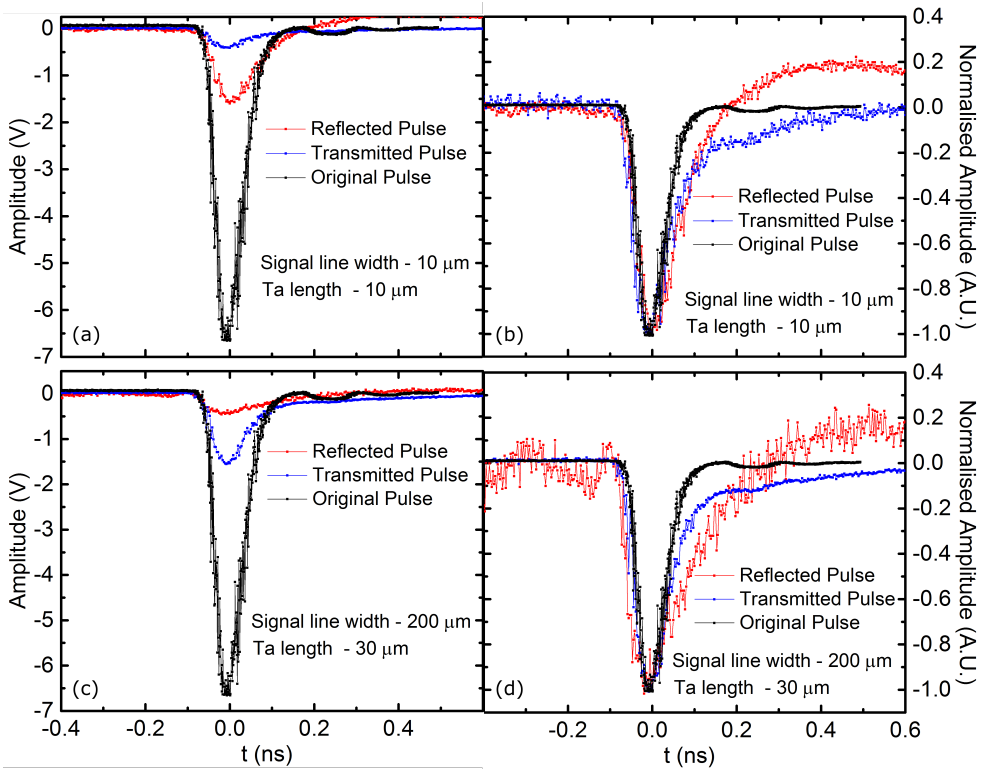

Figure 8.5: Comparison of original, transmitted and reflected pulses in Ta/CoFeB/MgO samples on low resistivity Si substrates. Top panels (a) and (b) show measurements for signal line tapering to a width of 10 μm and a length of 10 μm. The bottom panels (c) and (d) show measurements for signal line widening to a width of 200 μm and a length of 30 μm. Left panels (a) and (c) show calibrated pulse amplitudes and right panels (b) and (d) show identical pulses with normalised amplitude.

8.2.4 Kerr Rotation of CoFeB Grown on Different Substrates with Different Ta Layer Thickness

The second important parameter in determining the suitability of a device for TRSKM is the magnitude of the Kerr response. If pulsing induces a large motion of the magnetisation but the Kerr response is low this may still be impossible to detect. To determine which material combination showed the largest Kerr rotation the static MOKE response of the polar magnetisation component to an out-of-plane field was tested using the geometry shown in figure 4.7. Due to fabrication difficulties the first generation of devices did not contain the combination of high resistivity Si with a 4 nm Ta under layer. The MOKE response of the three other combinations is shown in figure 8.6. Each of the panels shows the response of three nominally identical ~1 x 1 cm devices grown on nominally identical wafers but grown in different sputtering runs.

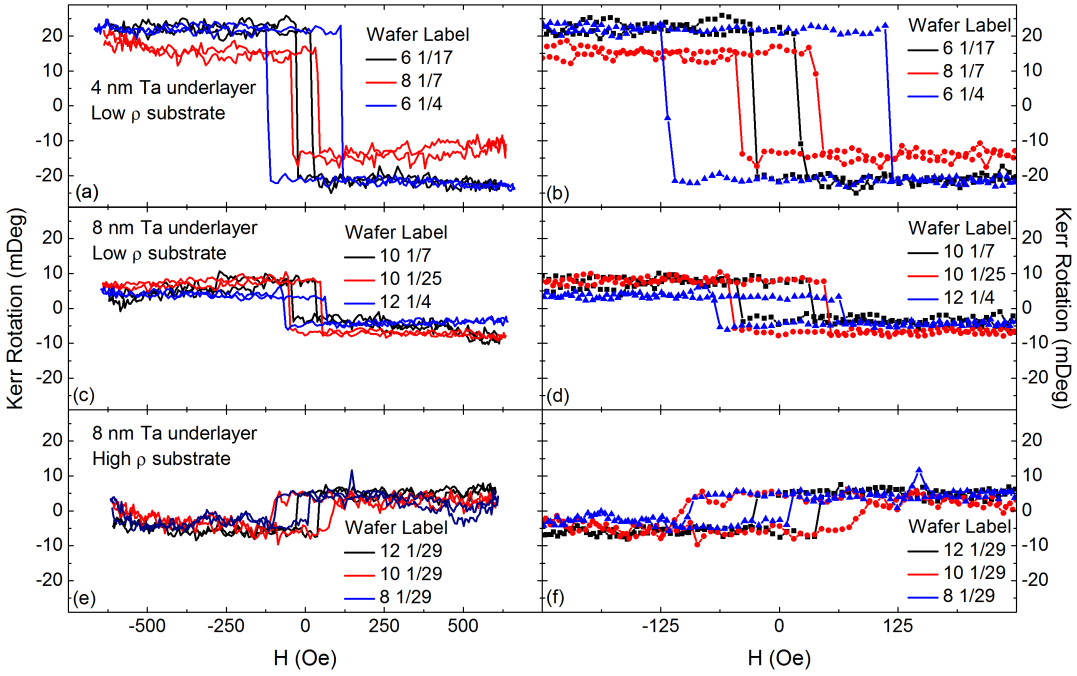

Figure 8.6: Polar Kerr rotation of Ta/CoFeB/MgO stacks, with a swept out-of-plane field. Shown is a comparison between 4 nm (a-b) and 8 nm Ta under layers (c-f), on low resistivity (a-d) and high resistivity (e-f) substrates. Right hand plots (b, d, f) show the low field region of (a, c, e) for comparison. The three measurements shown on each plot were made on nominally identical devices on nominally identical wafers, but grown in different sputtering runs.

It is immediately clear from figure 8.6 that CoFeB grown on a $t_{Ta} = 4$ nm under layer

gives a consistently larger MOKE response than CoFeB grown on a $t_{Ta} = 8$ nm Ta under layer. Though some variation is seen between different sputtering runs, which can be seen if the red loop is compared to the black and blue loops in (a), the MOKE response of CoFeB grown on 4 nm Ta was consistently $\times 2$ larger than CoFeB grown on 8 nm under layers. There may be several reasons for this increased response. The thickness of the Ta under layer may affect the growth quality of the CoFeB layer. However in this case it is more likely that the increase in signal is due to multiple interactions of the laser beam with the CoFeB layer, amplifying the Kerr response. Multilayer optical interference if difficult to model but it is more likely that the thermal oxide layer of the Si substrate (oxidisation is performed at Brown and may not be well controlled), combined with the Ta layer thickness determines the magnitude of the amplification. No significant variation in the magnitude of the Kerr response is observed between the low (b) and high (c) ρ substrates with identical Ta under layer thickness. However the sign of the Kerr rotation is reversed on high ρ substrates. The perpendicular coercive field (H_c) shows a surprisingly large variation between nominally identical devices. This difference is most pronounced for CoFeB on the 4 nm Ta under layer when comparing between the black and blue loops in (c) but is also visible for CoFeB with the 8 nm under layer in (d) and (f). H_c depends mainly on domain nucleation and structure, which are governed by defects. Variations between nominally identical films are likely caused by differences in defects.

The data from the pulse and MOKE response testing suggested that the optimal combination was growth on a high ρ substrate (best pulse profile) and a 4 nm Ta under layer (strongest MOKE response). Unfortunately this was the combination which was lost due to fabrication difficulties in the first generation of devices. A second generation of devices was fabricated to include this potentially optimal combination, along with a second series of 4 nm Ta under layers grown on low ρ substrates.

For this second generation of devices the pulse profile was consistent with measurements made on the first generation. However the MOKE loops shown in figure 8.7 show a significant difference in the Kerr rotation response. A much larger difference in Kerr rotation between the high and low ρ wafers was seen in this generation of devices where the magnitude of the Kerr response was $\approx \times 8$ greater on low ρ wafers than high ρ wafers. A potential reason for this may be that the high ρ wafers inhibits multilayer interference within the Ta under layer.

For this generation of devices MOKE microscopy was also employed to compare the response of the continuous (~1 x 1 cm) and patterned (10.0 x 10.0 μm) devices. This experiment was complicated by difficulties in device selection for CoFeB/MgO

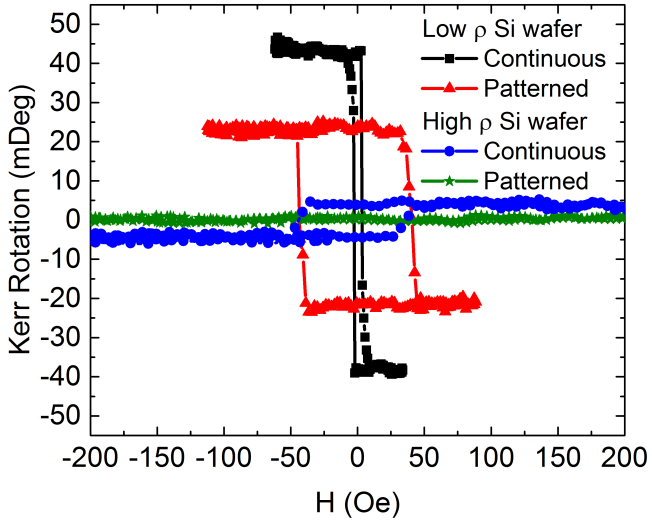

Figure 8.7: Polar Kerr rotation of Ta/CoFeB/MgO stacks with a 4 nm Ta under layer, with a swept out-of-plane field. This shows a comparison between low and high resistivity substrates, and un-patterned (1×1 cm square) and patterned (10.0×10.0 μm square).

elements grown on high ρ substrates. The sample yield on both low and high ρ substrates was not perfect (an estimate of the average percentage yield is not possible as this varied between photolithography and sputtering runs). Devices were first examined under an optical microscope to select appropriate candidates for MOKE microscopy. CoFeB/MgO elements grown on low ρ substrates were optically distinct from the Ta under layer. Unfortunately this was not true of the CoFeB/MgO elements grown on high ρ substrates. This meant it was difficult to know whether patterned elements were present, but not visible against the under layer, or had simply been lost in the fabrication process. Due to the time involved in switching between potential devices in the MOKE microscope, it was not feasible to test a large number of devices on the high ρ substrate. Of the patterned CoFeB/MgO elements on high ρ substrates that were measured, any MOKE signal was comparable to experimental noise. Patterned devices on low ρ substrates showed a much stronger signal than those on high ρ substrates. However, as illustrated in figure 8.7, the amplitude of the Kerr rotation was typically lower than the continuous regions and H_c was typically much larger. H_c is strongly dependent on domain nucleation processes, it is likely that in smaller devices there are less choices of nucleation sites and stronger pinning at the device edges.

As fabrication was performed at Brown University it was beyond the scope of this thesis to investigate the origins of these variations and optimise the growth procedure

in order to increase uniformity. Only two wafers of each substrate resistivity were fabricated in the second generation, so the sample size is too small to assume the observed behaviours are representative of the patterning procedure. The best candidates for TRSKM were selected from the second generation of devices. Though the pulse profile was slightly worse on the low ρ substrate, this substrate type was selected as no Kerr rotation for CoFeB/MgO on high ρ substrates was observed.

8.2.5 Current Induced Switching

Hall bars like those measured in chapter 6 were grown on the same wafers as the high frequency devices. Electrical transport measurements were made on these Hall bars to ensure current induced magnetisation switching occurred. Figure 8.8 shows the Hall resistance of a Hall bar with an 8 nm Ta under layer, as current is swept from I = -0.01 to 0.01 A. Bias fields of H $= \pm 50$ Oe were applied in-plane, parallel to the current direction. Switching is observed at approximately 0.0028 A which corresponds to a current density of 1.75×10^6 A/cm^2.

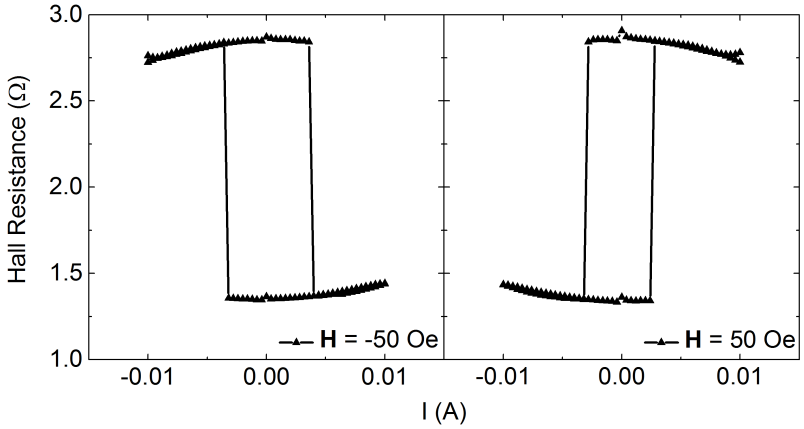

Figure 8.8: Hall resistance of a Ta/CoFeB/MgO Hall bar measured during sweeping of a current from I = -0.01 to 0.01 A. A bias field of H= ± 50 Oe is applied in-plane parallel to the current direction

8.3 Ground State Measurements of Ta/CoFeB/MgO Patterned Elements for TRSKM

8.3.1 Device Geometry

The device selected for TRSKM showed a strong polar MOKE signal (40 mDeg full loop height) with a reasonably un-broadened transmitted pulse of 850 mV. The straight waveguide design was selected as this had the lowest chance of impedance mismatch and had a reflected pulse amplitude of 700 mV. The device dimensions are shown in figure 8.9. The Ta under layer was 100 μm wide and 30 μm long. The CoFeB elements were squares designed with a side length of 0.5-10.0 μm. However visual inspection indicated that the smallest CoFeB/MgO square edge that had been successfully patterned and sputtered was 1.6 μm long. A rounding of the square edges was also observed with decreasing edge length

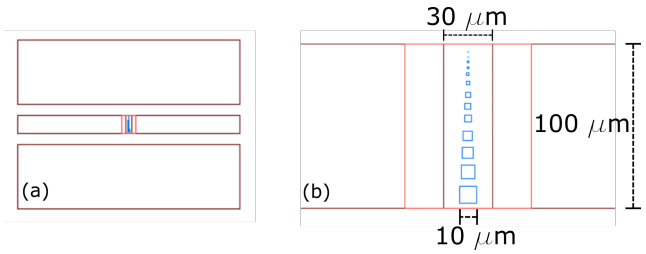

Figure 8.9: Specifications of Ta/CoFeB/MgO device for TRSKM, (a) full waveguide (b) central region of the waveguide including 30 x 100 μm Ta under layer (red) and square CoFeB elements with side lengths from 0.5-10.0μm (blue).

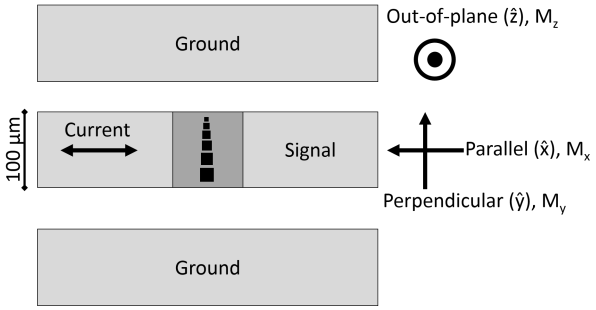

Figure 8.10: Orientation of Ta/CoFeB/MgO device in the TRSKM experiment. The components of the magnetisation measured by the vector bridge are defined relative to the current direction.

The coordinate system used to describe the vector resolved components of the

magnetisation is shown in figure 8.10. This follows the same convention as similar studies with $\hat{\mathbf{x}}$ defined as the in-plane direction parallel to the direction of current flow, $\hat{\mathbf{y}}$ defined as the in-plane direction perpendicular to the direction of current flow and $\hat{\mathbf{z}}$ defined as the out-of-plane direction (orthogonal to the x-y plane). The components of the magnetisation vector $\mathbf{M}$ in these directions are defined as M_x, M_y and M_z respectively.

8.3.2 Ground State Response to In-Plane Fields

Prior to dynamic measurements the ground state of the largest CoFeB/MgO element, a 10.0×10.0 μm square, in response to an in-plane field was explored by scanning Kerr microscopy (SKM) imaging of the polar magnetisation component (figure 8.11) and vector resolved hysteresis (figure 8.12). In the experiments described in chapter 7 the out-of-plane magnetisation state was deterministically set by a nominally in-plane field, which was possible due to a slight tilt of the sample mount, which meant the field also had an out-of-plane component. This was explored as a potential method to control the ground state magnetisation for the high frequency devices. However the patterned devices showed a typically larger out-of-plane coercive field than the Hall bars measured previously, and so it was expected that a larger in-plane field or larger sample tilt relative to the in-plane field would to be required.

Figure 8.11 shows the polar component of the ground state magnetisation response to static in-plane fields applied in the (a) $\hat{\mathbf{x}}$ and (b) $\hat{\mathbf{y}}$ directions. The field history for both field directions is a saturation to a high negative -1500 Oe field before reduction then back to 0 Oe field, then the measurement fields are stepped in the direction defined by the dashed arrows in figure 8.11 from 0 Oe to 500 Oe, and back to 0 Oe. Fields above 500 Oe were not explored as a single domain state was reached between 200 and 300 Oe. For both in-plane field directions large domains form at low fields. As these samples have PMA it is assumed that the contrast seen in 8.11 shows domains oriented in the $\pm\hat{\mathbf{z}}$ directions, with some canting as the field is applied in-plane. As the field strength is increased the size of the domains decreases. Around $H = 200$ Oe the domain size becomes smaller than the scanning step size (1/3 μm). For $H > 200$ Oe the domain structure disappears as the anisotropy field is overcome. In order to ensure that the magnetisation was saturated in-plane for the TRSKM measurements, fields of 500 Oe were used. A comparison of domain structure between fields applied in the (a) $\hat{\mathbf{x}}$ and (b) $\hat{\mathbf{y}}$ directions reveals that the domain structure does not appear to have a strong dependence on field direction, and interestingly the orientation of the

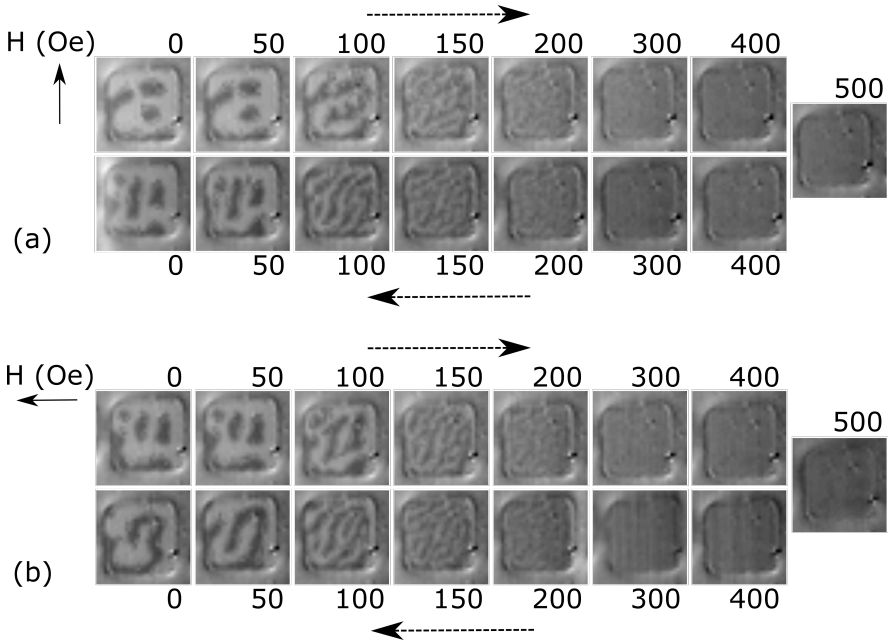

Figure 8.11: Images of the ground state magnetisation of a 10.0 x 10.0 μm Ta/CoFeB/MgO square. (a) shows the out-of-plane component of the magnetisation upon application of an in-plane field, parallel to the signal line ($\hat{\mathbf{x}}$). (b) shows the out-of-plane component of the magnetisation upon application of an in-plane field, perpendicular to the signal line ($\hat{\mathbf{y}}$). Dashed arrows show the order in which the fields were set.

domain walls appears to favour a diagonal direction for $H = 100 - 150$ Oe regardless of field orientation or polarity. The position and shape of the domains is broadly similar between field directions and polarities with an especially strong pinning observed at the bottom (from the readers perspective) edge of the square. The insensitivity to field orientation and polarity and lack of positional variation implies that the domain structure is defined by strong pinning intrinsic to the structure of the material. It is not clear from these measurements whether the domain state would still form after the magnetisation is reset by an out-of-plane field. There is no capacity to apply an out-of-plane field to set the perpendicular magnetisation state in the TRSKM so it is unclear whether an out-of-plane saturation field would lead to a single out-of-plane domain state after the field was removed. It is also unclear whether the domains would form in response to the in-plane field if the sample began in the single perpendicular domain state. This is complicated by the fact that, prior to the static field swept measurements, a pulsed current excitation was used to check for a TRMOKE signal.

It was suggested by collaborators that repeated pulsing with the same pulse polarity may induce a 'striped' domain state. Without applying an out-of-plane field to reset the magnetisation state it is difficult to say with certainty whether the striped domain state is initially set by the pulsing and the in-plane fields simply modify this state, even once the pulse is removed.

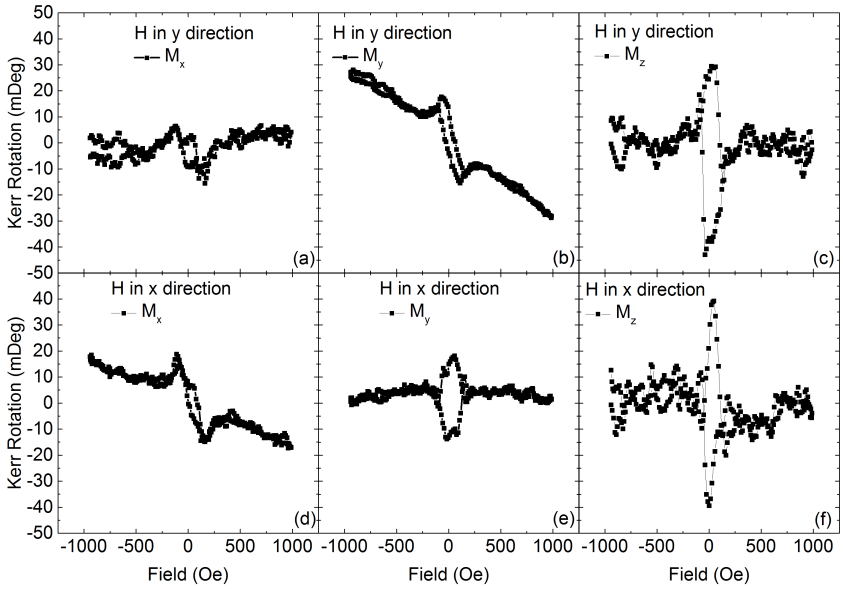

Figure 8.12: In-plane field, vector resolved hysteresis loops with the laser spot focused at the center the a 10.0 x 10.0 μm square shown in figure 8.9.(b). In (a-c) the field was applied perpendicular to the signal line ($\hat{\mathbf{y}}$) and in (d-e) the field was applied parallel to the signal line ($\hat{\mathbf{x}}$).

Figure 8.12 shows in-plane field vector hysteresis loops with the laser spot focused on the center of the 10.0 $\times$ 10.0 μm CoFeB/MgO square. The response of M_z (c and f) to in-plane fields is, as expected, similar when the field is applied in the $\hat{\mathbf{x}}$ or $\hat{\mathbf{y}}$ directions. These loops imply that the magnetisation is dragged fully in plane for H ~75 Oe. This behaviour is not consistent with the images shown in figure 8.11 where a perpendicular domain state is still clearly visible at about H ~75 Oe. However as the domain size clearly reduces for increasing fields, the smaller the domain size the more adjacent domains are likely to be under the beam spot. If multiple domains oriented in opposite out-of-plane directions contribute to the Kerr rotation the resultant average will be close to zero. An asymmetry is visible at the switching field in the loops for polar components (c, f) similar to the modelled loops for an out-of-plane field with an in-plane component shown in figure 7.5, this implies there may again be a slight tilting

of the sample relative to the in-plane field. As the coercive field was shown to be much larger in the patterned devices than the Hall bars this component does not have quite such a pronounced effect on the hysteresis loop as in section 7.3.1. It could also be that **M** cants within the domain or domain walls, as suggested by the M_x and M_y loops. The behaviour of the loops for the in-plane magnetisation components deviates further from the idealised loops for a single domain state in response to an in-plane field. With the field applied along a certain in-plane direction the magnetisation component along that direction is expected to produce a 'standard' hysteresis loop (maximum Kerr rotation at the saturation field and an open loop at low fields), and no change in the component of the magnetisation orthogonal to that direction is expected. For both field directions the shape of the hysteresis loop for the component of the magnetisation along the field direction is close to the expected shape, however there is a continued increase in Kerr rotation past the Kerr rotation. This effect may be caused by a mechanical motion induced by high fields. Some hysteretic behaviour is also observed for the component of the magnetisation orthogonal to the field direction. There are multiple possible reasons for this effect. Imperfect alignment of the in-plane field relative to the polarisation of the laser would mean a component of the field lay in the direction orthogonal to the measured magnetisation component. The remanent magnetisation state may be canted. The process of domain nucleation involves a rotation of the in-plane magnetisation components in the direction orthogonal to the field. A final explanation may be that this effect is an experimental artefact caused by breakthrough of the polar component to the in-plane bridge detector channels, due to poor alignment. This is unlikely as it is clearly visible when comparing (e) and (f) that the anisotropy field is larger for the in-plane loop, if the signal was breakthrough from the polar channel then the same anisotropy field would be expected for the in-plane components.

8.4 TRMOKE of Ta/CoFeB/MgO Patterned Elements

The TRMOKE measurement geometry for the following experiments was identical to the set up used to measure Hall bars in chapter 7 but with the device connected to the pulse generator via picoprobes instead of wire bonds. TRMOKE was performed with the laser spot focused in the center of a 10.0×10.0 μm square unless otherwise stated. Initially an in-plane field was applied along the current direction $\hat{\mathbf{x}}$. This field configuration was likely to induce the largest precession amplitude as, for all field strengths, the magnetisation remains orthogonal to the Oersted field direction, meaning, as well as any SOT induced dynamics, an Oersted torque would also act

on the magnetisation. Figure 8.13 shows the current induced oscillation of the three Cartesian components of the magnetisation with an in-plane bias field H = 0 − 1000 Oe in the $\hat{\mathbf{x}}$ direction.

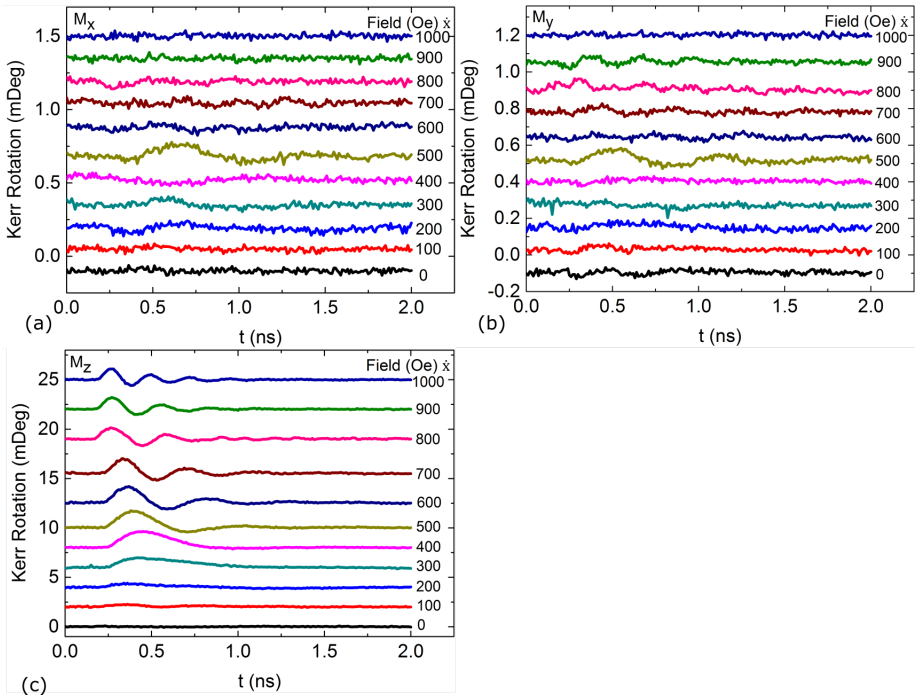

Figure 8.13: Vector resolved TRSKM measurements with the laser spot focused at the center of the 10.0 x 10.0 μm square shown in figure 8.11. Fields from 0 to 1000 Oe were applied in-plane and parallel to the current direction ($\hat{\mathbf{x}}$) and the M_x (a), M_y (b) and M_z (c) components of the magnetisation were recorded.

As the bias field is increased from H = 0 − 200 Oe the oscillation frequency of M_z decreases, this behaviour is expected as the in-plane bias field competes with the PMA field, and the minimum precession frequency occurs when the magnetisation is dragged in-plane with the in-plane field is close to the PMA field. The ground state measurements show that this condition occurs between H = 200 and H = 300 Oe. As the bias field is increased further from H = 200 − 1000 Oe the oscillation frequency of M_z steadily increases again because the effective field increases in the magnetisation direction. A considerably smaller oscillation amplitude was observed for the in-plane components of the magnetisation at all fields, with the maximum in-plane oscillation amplitude observed at H = 500 Oe. This was one reason H = 500 Oe was first selected for TRSKM. At low fields, the domain structure demonstrated in figure 8.11 means it is difficult to state whether the oscillations observed with the laser focused in a single

position are representative of the behaviour of the entire device. As the bias field is varied, domain nucleation and motion may result in the laser spot being focused on domains of opposite polarisation at different fields. For in-plane fields greater than the saturation value the behaviour measured in the center of the device is more likely to be an accurate representation of the whole device as it is in a single domain state. This was a second reason that H = 500 Oe was the initial field value chosen for imaging.

In chapter 7 it was shown that SOTs due to parallel and perpendicular spin accumulations have an even and odd symmetry in **M**. Figure 8.14 compares the oscillatory response of the Cartesian components of **M** with bias fields applied along $\hat{\mathbf{x}}$ and $-\hat{\mathbf{x}}$. The M_z component of the precession signal undergoes a 180° phase shift when the bias field (and therefore **M**) polarity is reversed, indicating the direction of out-of-plane magnetisation deflection is dependent on the initial orientation of **M**. The symmetry of the in-plane components of the magnetisation in **M** is more difficult to analyse due to the increased signal to noise ratio however, broadly, the oscillations of the in-plane components do not undergoes a 180° phase shift when the bias field and therefore **M**) polarity is reversed (compare for example the M_y component at H = ±500 Oe). Whilst at first thought this behaviour may seem unexpected it is consistent with the precession direction remaining constant *in polar coordinates* i.e. if the precession direction for positive fields (and therefore **M** in the $\hat{\mathbf{x}}$ direction) is defined as anti-clockwise then the precession direction for negative fields (and therefore **M** in the $-\hat{\mathbf{x}}$ direction) is also anticlockwise. If the magnetisation is assumed to be saturated in plane in the $\pm\hat{\mathbf{x}}$ direction (in reality there may also be some component of the magnetisation in the $\hat{\mathbf{y}}$ and $\hat{\mathbf{z}}$ directions if there is tilting of the field or an incomplete saturation), then to first order the field-like and Oersted torques will *initially* act in the $\hat{\mathbf{x}} \times \hat{\mathbf{y}} = \hat{\mathbf{z}}$ or $-\hat{\mathbf{x}} \times \hat{\mathbf{y}} = -\hat{\mathbf{z}}$ directions, whilst the anti-damping torque will act in the $\hat{\mathbf{x}} \times (\hat{\mathbf{y}} \times \hat{\mathbf{x}}) = \hat{\mathbf{y}}$ or the $-\hat{\mathbf{x}} \times (\hat{\mathbf{y}} \times -\hat{\mathbf{x}}) = \hat{\mathbf{y}}$ direction this is consistent with the behaviour observed in figure 8.14. As the magnetisation precesses the torque directions will change over time, a full model must be developed to describe the instantaneous torques on this system.

TRMOKE was also performed with a bias field applied parallel to $\hat{\mathbf{y}}$ i.e. in-plane perpendicular to the current direction. In this field configuration field-like torques which are proportional to $\hat{\mathbf{M}} \times \hat{\mathbf{y}}$ are not expected to be present once **M** is dragged fully in-plane. The laser spot was again focused in the center of the device and the results are shown in figure 8.15.

A smaller oscillation amplitude of M_z, M_y and M_x is observed for all bias field strengths. The largest oscillations occur for $H = 150 - 200$ Oe at approximately the perpendicular anisotropy field. As discussed, no torques with the $\hat{\mathbf{m}} \times \hat{\mathbf{y}}$ form

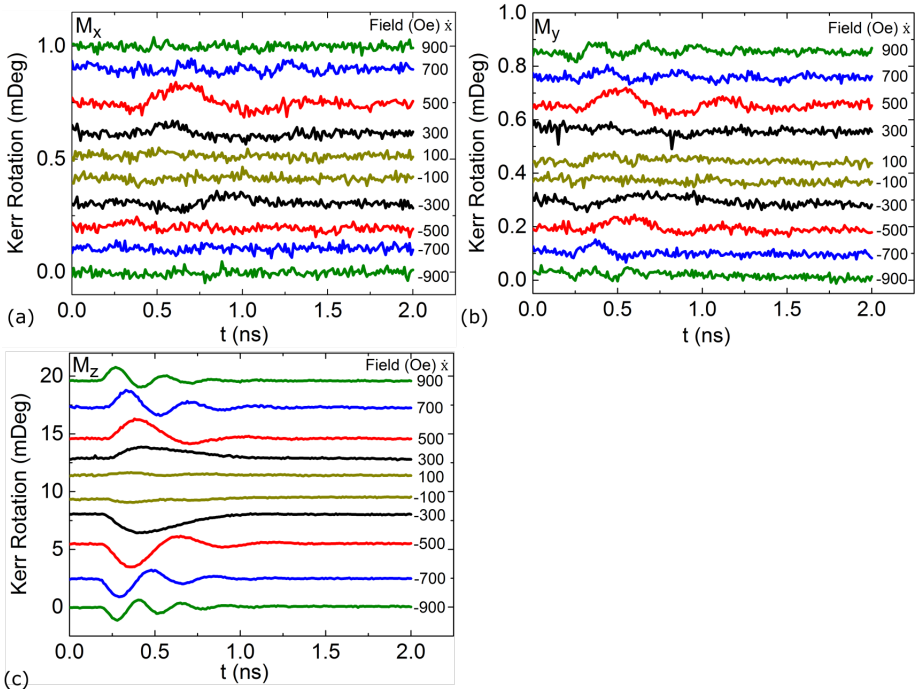

Figure 8.14: Vector resolved TRSKM measurements with the laser spot focused at the center of the 10.0 x 10.0 μm square shown in figure 8.11. Fields were applied with both negative and positive polarity from -900 to 900 Oe, in-plane and parallel to the current direction ($\hat{\mathbf{x}}$) and the M_x (a), M_y (b) and M_z (c) components of the magnetisation were recorded.

are expected when the magnetisation lies in the $\hat{\mathbf{y}}$ plane. There is still evidence of precession at fields above the perpendicular anisotropy field though with considerably lower amplitude than observed with the field applied along the current direction. This may indicate some component of $\mathbf{M}$ is present in the $\hat{\mathbf{x}}$ or $\hat{\mathbf{z}}$ directions which induces this small torque. The strongest in-plane signal was observed at H= 100 Oe. This was selected as the measurement field for the second set of TRSKM images.

After taking TRSKM images (shown later in this section) it was observed that the behaviour of the center of the square was not representative of the entire square. A different signal (which is not labelled a 'precession' as no $\pm$ oscillation is seen, only a deflection of the magnetisation in a single direction) was observed at the edges of the device. The relative amplitude of this signal was larger than the central region and varied in amplitude dependent of the strength and orientation of the bias field. This can be seen clearest in the TRSKM images shown in figure 8.18.(a). In order to explore this effect further TRMOKE was performed with H= 500 Oe applied parallel to the

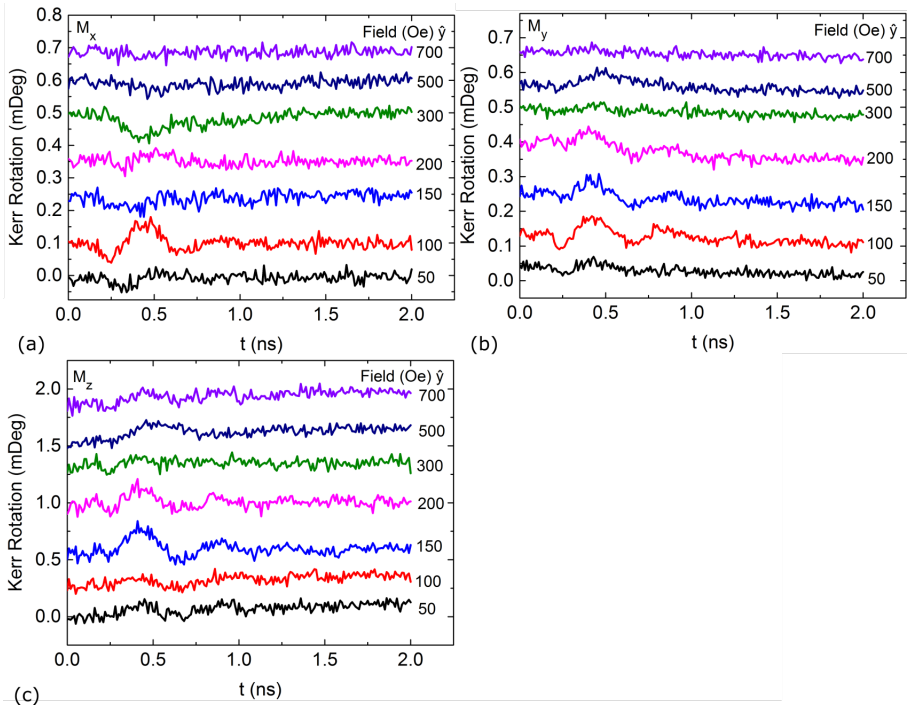

Figure 8.15: Vector resolved TRSKM measurements with the laser spot focused at the center of the 10.0 x 10.0 μm square shown in figure 8.11. Fields were applied with both negative and positive polarity from -900 to 900 Oe, in-plane and perpendicular to the current direction ($\hat{\mathbf{y}}$) and the M_x (a), M_y (b) and M_z (c) components of the magnetisation were recorded.

current direction and the laser spot was focused on each of the edges of the square, mid way between the corners. This is shown in figure 8.16 where the notations 'left', 'top', 'right' and 'bottom' are used to denote which edge the laser spot was focused on and are correct from the readers perspective when viewing the images.

The relative amplitudes of the M_z signals are reasonably consistent with the laser spot focused on different edges. However the amplitudes of the in-plane components are strongly dependent on which edge the laser spot is focused on. Large amplitude M_x components are observed when the laser was focused on the top and bottom edges with almost no M_y signal. The opposite is true when the laser spot is focused on the left or right edges where the amplitude of M_y is much greater than M_x. The shape of the signals is also markedly different to those observed at H= 500 Oe, with the laser spot focused in the center of the square (figures 8.13 and 8.14). This effect is highlighted in figure 8.17 where the edge and center signals are plotted together. Focusing on the oscillation of M_z in figure 8.17, when the laser is positioned at the square center (a)

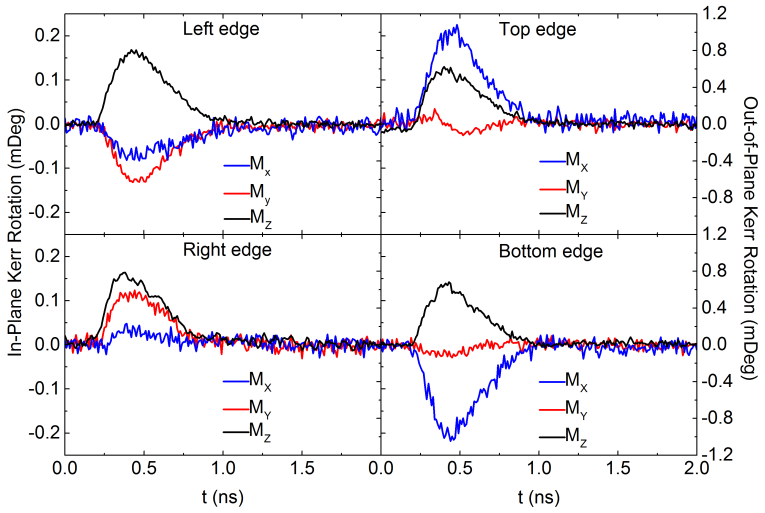

Figure 8.16: Vector resolved TRSKM measurements with the laser spot focused on each of the four edges, mid way between the corners, of the 10.0 x 10.0 μm square shown in figure 8.11. Here 'left' and 'right', correspond respectively to smaller and larger x values, and 'bottom' and 'top' correspond respectively to smaller and larger y values and denote the measurement edge as defined by the orientation in figure 8.11. A 500 Oe positive, in-plane field was applied parallel to the current direction ($\hat{\mathbf{x}}$) and the M_x, M_y and M_z components of the magnetisation were recorded.

three distinct oscillations are visible before they are damped out. Taking FFTs of these oscillations yields an oscillation frequency of 1.5 GHz. With the laser positioned at the edges of the device (b, c) only a half cycle of oscillation is observed (if the signal is in fact oscillatory) and a FFT yields a lower oscillation frequency of 0.5 GHz. The shape and frequency of the edge signal is comparable to the signal seen at the center of the square at the lower field of H= 300 Oe in figure 8.13, which might indicate a higher PMA at the edges such that competition between this higher PMA and the bias field produces similar behaviour to a lower PMA and lower bias field. This may also be evidence that domains are pinned more strongly at the edges of the square.

8.5 TRSKM of Ta/CoFeB/MgO Patterned Elements

TRSKM imaging was initially performed on the 10.0×10.0 μm^2 square, with H= 500 Oe applied parallel and perpendicular to the current direction. H= 500 Oe was shown to give the strongest response of the in-plane components in TRMOKE. The TRMOKE measurements shown in section 8.4 were used to select time delays for TRSKM. The

time delays which are shown in figure 8.17 were selected to capture the dynamic response of the magnetisation at key points throughout the oscillation. The dashed lines in figure 8.17 correspond to the time delays shown in figure 8.18.

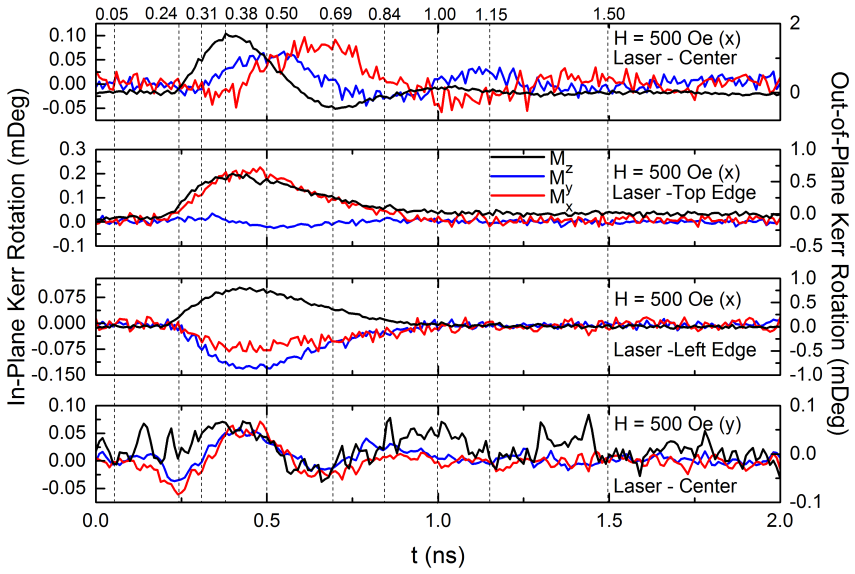

Figure 8.17: Vector resolved TRMOKE measurements showing time delays at which the images in figure 8.18 were taken. The laser beam spot was focused at either the center (a, d) or the edge (b, c) of the 10.0 x 10.0 μm square shown in figure 8.11. H= 500 Oe was applied in-plane in the $\hat{\mathbf{x}}$ (a, b, c) or $\hat{\mathbf{y}}$ (d) directions. The dashed lines indicate the time delays for imaging, the exact times are shown along the top of panel (a).

The magnetic contrast in figure 8.18 is scaled to clearly show the domain structure. The oscillation amplitude varies between different bias field directions and different components of **M**. Therefore the contrast is comparable for the same component of the magnetisation at different time delays, but not between different bias field directions, or between different components of the magnetisation i.e. the contrast for M_x at t = 0.05 ns and t = 0.38 ns, with **H** in the $\hat{\mathbf{x}}$ direction, is comparable. However contrast for M_x at t = 0.38 ns and M_y at t = 0.38 ns with **H** in the $\hat{\mathbf{x}}$ direction is not comparable, and neither is the contrast for M_x at t = 0.38 ns with **H** applied in the $\hat{\mathbf{x}}$ and $\hat{\mathbf{y}}$ directions. The banding visible in some of the reflectivity images is caused by a drift in laser power intensity. This effect was well correlated to the cycle of the air conditioning in the lab. The banding does not propagate through to the magnetic images as the optical polarisation bridge detector is immune to variations in laser intensity to first order.

A larger oscillation amplitude is observed when **H** is applied in the $\hat{\mathbf{x}}$ direction

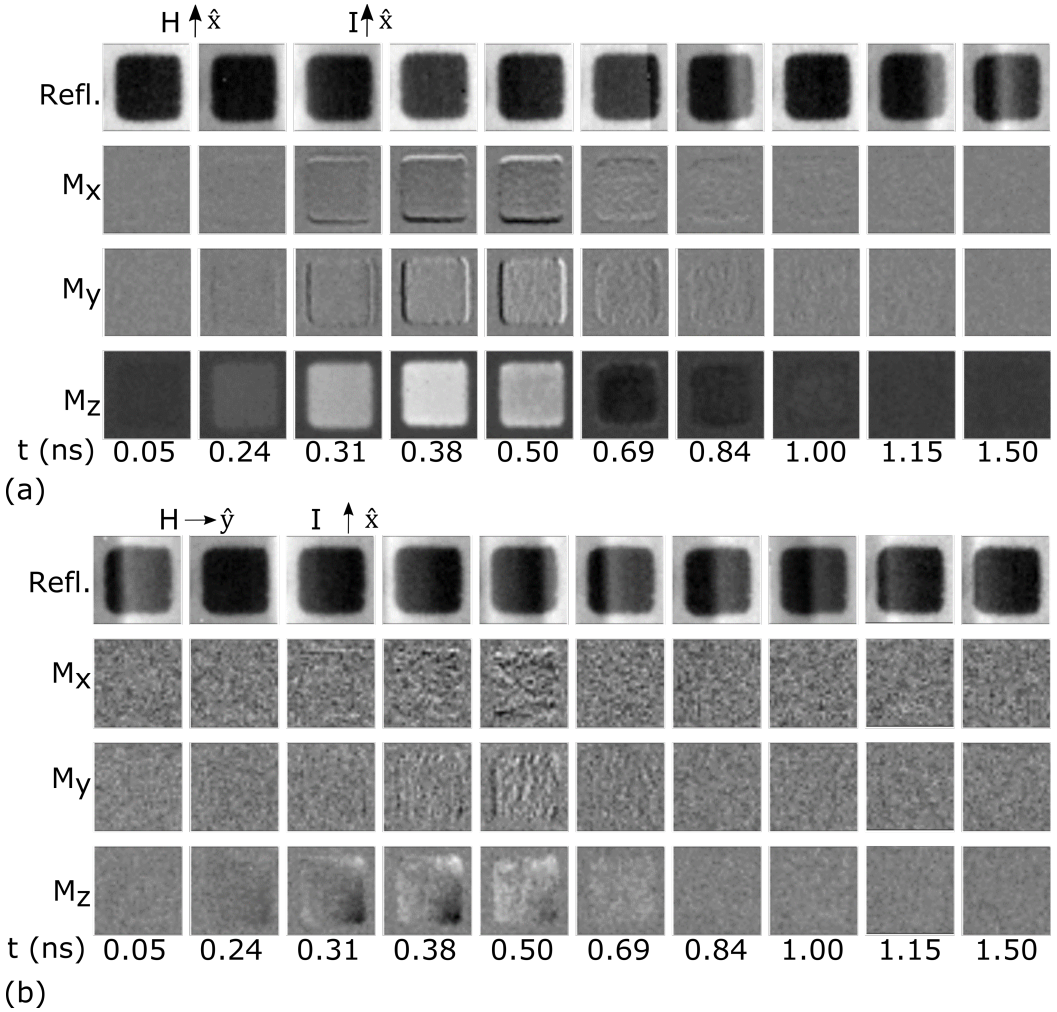

Figure 8.18: Vector resolved images showing the magnetisation state of a 10.0 x 10.0 μm Ta/CoFeB/MgO square at different time delays relative to an excitation current pulse with a constant bias field of 500 Oe applied in-plane (a) parallel ($\hat{\mathbf{x}}$) and (b) perpendicular ($\hat{\mathbf{y}}$) to the current direction.

(shown in figure 8.18.(a)) compared to when the field is applied in the $\hat{\mathbf{y}}$ direction (shown in figure 8.18.(b)).

First the dynamics with **H** applied parallel to the current (figure 8.18.(a)) will be discussed. The light contrast in the images will be defined as the +ve direction and the dark contrast defined as the -ve direction. The response of M_z is uniform for t = 0.05-0.38 ns where the pulse causes a large positive out-of-plane deflection of the magnetisation. The reversal of M_z at the center of the square can be seen to begin at ~0.41 ns in figure 8.17.(a). Therefore for the next image at t = 0.50 ns (shown in figure

8.18.(a)) the deflection direction of the magnetisation reverses, there is a subtle variation in contrast between the edges (lighter) and central region (darker) indicating that the magnetisation rotated towards the -ve direction (becoming more in-plane) faster at the center of the device than the edges. This contrast becomes more pronounced at t = 0.69 ns where the central region of the square has now been deflected to the -ve direction direction (dark contrast) whilst the edges of the device remain in the +ve direction (light contrast). This opposing edge-center orientation persists at t = 0.84 ns as the magnetisation relaxes back to the in-plane ground state from t = 0.84-1.50 ns. This behaviour is consistent with the TRMOKE measurements made with the laser spot focused on the edges or central region of the square. Comparison of these laser positions in figure 8.17 (comparing M_z between (a) and (b-c)) shows that whilst the central region of the square oscillates between the +ve and -ve directions the edge magnetisation deflects only in the +ve direction.

The response of the in-plane components is non-uniform at all delays, with a much larger signal amplitude observed at the edges of the square compared to the central region. For M_x opposite signal polarity is observed at the top and bottom of the square and opposite polarity of M_y is observed at the left and right edges. Before moving forward with the interpretation of these results the likelihood that this is a 'real' magnetic effect will be discussed. The strong localisation of this interesting behaviour to the device edges should prompt some questioning as to whether this effect could be caused by the step in height of the sample surface. Any change in surface hight may give rise to scattering of the laser beam and may change it's polarisation, producing an artificial Kerr rotation. First it should be observed that the edge contrast only occurs at specific time delays. Prior to the pulse and after the magnetisation has relaxed no edge contrast is seen. This eliminates the possibility that scattering from the device edge is producing a constant artificial Kerr rotation. However there is still the possibility that whilst the current pulse is propagating through the device the applied field exerts a force upon the conduction tracks that results in mechanical motion of the sample. However it is far from clear that the mechanical response time should be comparable to the duration of the current pulse, and a constant background signal would be the more likely outcome. In order to exhaustively demonstrate that this is a purely magnetic effect, TRSKM images were taken on non-magnetic edges of the device, at time delays before arrival of the pulse (t = 0.00 ns) and at delays where maximum edge contrast was observed (t = 0.50 ns). The first of these measurements was performed on the substrate/Ta edge and is shown in figure 8.19.

The reflectivity from the substrate and Ta are very similar, however the edge can

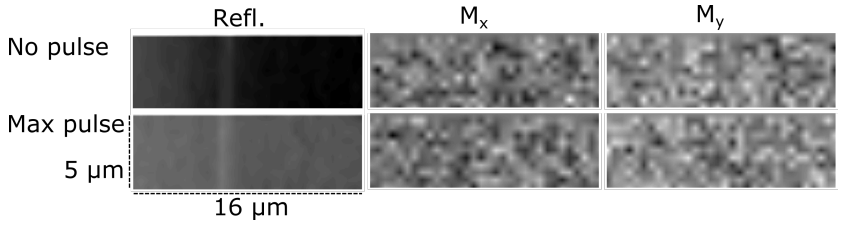

Figure 8.19: Images of the non-magnetic Ta/substrate edge before arrival of the pulse and at maximum pulse amplitude.

be seen as light band in the reflectivity. No difference in contrast with no pulse, or at maximum pulse, can be seen for either the M_x or M_y components of the magnetisation. No change in magnetic contrast in this measurement implies the change observed in figure 8.18 is a magnetic effect. The same experiment was performed on the edges of the Au waveguide and the results are shown in figure 8.20.

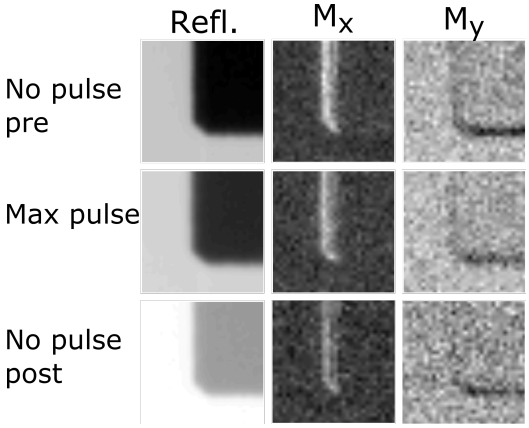

Figure 8.20: Images of the non-magnetic Au/Ta edge before the pulse, at maximum pulse amplitude and after the pulse.

A strong contrast is observed in the magnetic channels on the Au waveguide edge. However this has some fundamentally different characteristics to the contrast observed on the magnetic edges in figure 8.20. Unlike the magnetic edge contrast the Au edge contrast does not depend on the pulsed current. The same edge contrast is seen before, during and after the pulse. There is some dependence of the Au edge contrast on the laser intensity. In the three images the intensity of the edge contrast appears well correlated with the reflected intensity. This is another sign that the origins of this contrast are not the same as those for the magnetic edge in figure 8.20, which do not depend on laser intensity. The final difference between the Au and magnetic edge

contrasts is the bridge detector channel in which they appear and the sign of the contrast. The M_x magnetic edge contrast manifests at the top and bottom edges of the CoFeB/MgO square but this manifests on the left Au edge and not the bottom. The M_y magnetic edge contrast manifests on the left and right edges of the CoFeB/MgO square but manifests most strongly on the bottom Au edge. The Au edge contrast is likely caused by a very strong scattering from the highly reflective Au that also has a comparatively large height change. As no time varying contrast is observed on non-magnetic edges this implies the contrast in figure 8.18 is a real magnetic effect.

The shape and time dependence of the edge and center signals are similar to the 'primary' and 'secondary' superimposed oscillations discussed in chapter 7. Now these signals are spatially separated whereas the primary and secondary oscillations were measured in the same position on the Hall bar. This may be further evidence that torques with different origins act on different time-scales. Another potential explanation is that the squares are not spatially uniform and the PMA is different at the edges of the sample. As the field-like torque goes as $\hat{\mathbf{m}} \times \hat{\mathbf{y}}$ whilst the anti-damping torque goes as $\hat{\mathbf{m}} \times (\hat{\mathbf{y}} \times \hat{\mathbf{m}})$ a uniform response is expected if $\mathbf{M}$ is uniform across the square. However if the PMA is different at the square edges then $\mathbf{M}$ may be not be the same at the center and the edges, so non-uniform torques may be present. A similar Kerr imaging edge contrast with opposite sign on opposite edges due to the SHE in semiconductors was observed by Kato *et al*[89]. The polarisation they observed was out-of-plane, as is consistent with the Spin Hall effect for current flow in the film plane. However in our films the CoFeB layer is also conducting, and actually has a lower resistivity $\rho_{CoFeB} = 100\ \mu\Omega$cm than the Ta layer $\rho_{Ta} = 200\ \mu\Omega$cm[126]. This is likely to mean there is a component of the charge current which flows out-of-plane at the edges of the square as illustrated in figure 8.21. A vertical charge current close to the CoFeB edges could lead to an in-plane spin polarisation which would instead cause an in-plane rotation of the magnetisation.

When the field is applied perpendicular to the current direction ($\hat{\mathbf{y}}$), shown in figure 8.18.(b), the precession amplitude is lower than for the parallel configuration. A considerably different deflection of M_z is observed in this configuration. Whilst in figure 8.18.(a) initially the response was uniform from t = 0.05-0.38 ns, in (b) large regions of positive and negative contrast form, with the upper right and lower left corners deflecting in the positive direction and the lower right corner deflecting in the negative direction. In the ground state measurements (figure 8.11) a preferred direction of domain wall formation along the same upper right to lower left diagonal was observed. The in-plane components of the magnetisation do not show such a strong

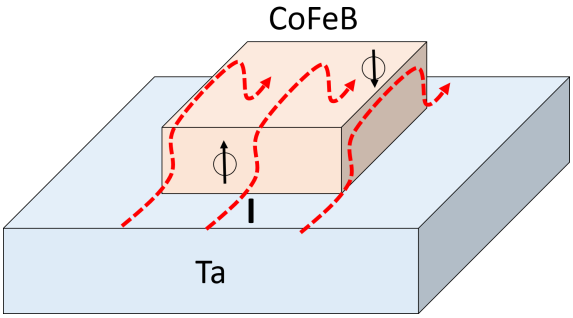

Figure 8.21: Spin accumulation due to vertical current flow in CoFeB element.

edge contrast as in (a) however some evidence is visible at t = 0.50 ns for both M_x and M_y. There is clear evidence of incoherent precession seen as a horizontal banding of M_x and vertical banding of M_y. This banding follows the same directional dependence as the edge contrast observed in (a). Again if the magnetisation is saturated in the $\hat{\mathbf{y}}$ direction no torques are expected, the time dependent signal again implies there may be some component of the magnetisation in the $\hat{\mathbf{x}}$ or $\hat{\mathbf{z}}$ directions.

TRSKM was also performed with a smaller in-plane field (H = 100 Oe) applied both parallel and perpendicular to the current direction. The ground state images shown in figure 8.11 suggested that at H= 100 Oe a striped perpendicular domain state formed and so these lower field measurements allow a comparison of dynamics when the ground state is in the $\hat{\mathbf{z}}$ direction (at H= $\pm$100 Oe) and the $\hat{\mathbf{x}}$ and $\hat{\mathbf{y}}$ directions (at H= 500 Oe). The time delays selected for imaging are shown in figure 8.22, delays were selected to capture key features in the TRMOKE traces.

TRSKM images at H= 100 Oe are shown in figure 8.23. Also shown are static images of the ground state acquired simultaneously to the time-resolved images, these images do not have any dependence on delay time. Many of these images are obscured by laser intensity drift however several are largely unaffected. The ground state for **H** applied in the $\hat{\mathbf{x}}$ direction can be seen most clearly in figure 8.23.(a) at t = 1.00 ns and the ground state for **H** applied in the $\hat{\mathbf{y}}$ direction can be seen clearest in figure 8.23.(b) at t = 0.23 ns.

The magnitudes of the signal amplitudes for different bias field directions are more similar in figure 8.23 (H= 100 Oe) than in figure 8.18 (H= 500 Oe). This allowed the contrast to be scaled to the same limits for the **H** applied parallel to the $\hat{\mathbf{x}}$ and $\hat{\mathbf{y}}$ directions whilst maintaining visible domain contrast in figure 8.23, and so a comparison of signal amplitudes is possible between figure 8.23 (a) and (b). Generally

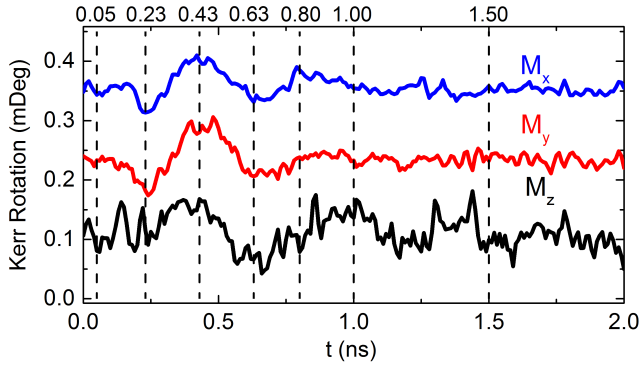

Figure 8.22: Vector resolved TRSKM measurements showing time delays at which the images in figure 8.23 were taken. The laser spot was focused at the center of the 10.0 x 10.0 μm square shown in figure 8.11 with a 100 Oe in-plane field applied in the $\hat{\mathbf{y}}$ direction. Dotted lines indicate the time delays for imaging.

the signal amplitude is larger at H= 100 Oe with the bias field applied perpendicular to the current (figure 8.23.(b)) than with the field applied parallel (figure 8.23.(a)). This behaviour is opposite to that observed at H= 500 Oe where the signal amplitude is much larger with the bias field applied parallel to the current (figure 8.18.(a)) than with the field applied perpendicular (figure 8.18.(b)).

When H= 100 Oe is applied in the $\hat{\mathbf{x}}$ or $\hat{\mathbf{y}}$ directions in figure 8.23, a striped domain structure is observed for the ground state of M_z, with domains aligned in the $\pm\hat{\mathbf{z}}$ direction with some canting to the bias field direction. The dynamic response of M_z is strongly dependent on the bias field direction. When $\mathbf{H}$ is applied in the $\hat{\mathbf{x}}$ direction at the onset of the current pulse the magnetisation rotates in the same direction for both +ve and -ve M_z domain stripes, this can be seen clearly in figure 8.23.(a) between t = 0.43-0.80 ns. However when $\mathbf{H}$ is applied in the $\hat{\mathbf{y}}$ direction at the onset of the current pulse the magnetisation rotates in different directions for the +ve and -ve M_z domain stripes, this can be seen clearly in figure 8.23.(b) between t = 0.43-0.80 ns. In order to elucidate the origin of this difference the expected *initial* field-like ($\hat{\mathbf{m}} \times \hat{\mathbf{y}}$) and antidamping-like ($\hat{\mathbf{m}} \times (\hat{\mathbf{y}} \times \hat{\mathbf{m}})$) torques were calculated for an arbitrarily canted magnetisation and the results are shown in table 8.2. It is important to note here that as the magnetisation is deflected these torque directions no longer apply. In the small angle limit the torque directions remain approximately constant however when the precession angle is large a more complete model is required.

Both the modelled field-like and antidamping-like initially generate either zero, or small out-of-plane torques with a direction which does not depend on the direction of

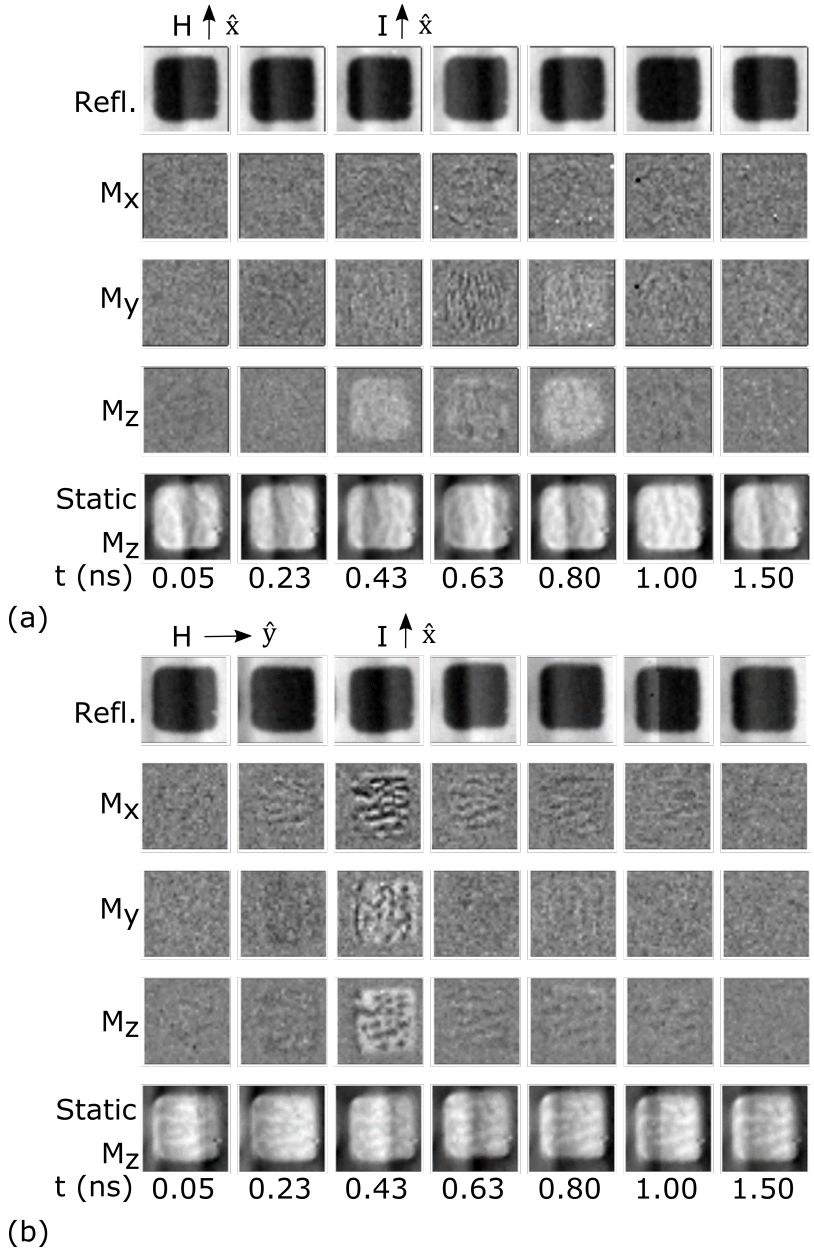

Figure 8.23: Vector resolved images showing the magnetisation state of a 10.0 x 10.0 μm Ta/CoFeB/MgO square, at different time delays relative to the arrival of an excitation current pulse, with H= 100Oe applied in-plane (a) parallel ($\hat{\mathbf{x}}$) and (b) perpendicular ($\hat{\mathbf{y}}$) to the current direction.

m. This is consistent with the ground state independent rotation direction of M_z seen in figure 8.23.(a). The calculated directions of the in-plane components of the torque are

$\hat{\mathbf{m}}$	$\hat{\mathbf{y}}$	$\hat{\mathbf{m}} \times \hat{\mathbf{y}}$	$\hat{\mathbf{m}} \times (\hat{\mathbf{y}} \times \hat{\mathbf{m}})$
(0.2 0 0.8)	(0 1 0)	(-0.8 0 0.2)	(0 0.68 0)
(0.2 0 -0.8)	(0 1 0)	(0.8 0 0.2)	(0 0.68 0)
(0 0.2 0.8)	(0 1 0)	(-0.8 0 0)	(0 0.64 -0.16)
(0 0.2 -0.8)	(0 1 0)	(0.8 0 0)	(0 0.64 -0.16)

Table 8.2: Initial field-like and antidamping-like torques for samples with out-of-plane magnetisation canted in-plane.

dependent on the direction of **m** for the field-like torque but not for the antidamping-like torque. This suggests that in this simple picture the opposite deflection directions of +ve or -ve ground states seen in figure 8.23.(b) must be due to the field-like torque term, as only this term has antisymmetry in **m**. This oversimplified picture demonstrates how the TRSKM results may be used to discern the torque directions in such systems. These results will not be correct for large angle precession or full switching, and so a numerical model must be developed in order to asses the instantaneous torque directions to further explore the underlying mechanisms. This theoretical treatment is currently being developed.

The oscillation amplitude of the in-plane components is larger with **H** applied in the $\hat{\mathbf{y}}$ direction. The rotation direction of the magnetisation is influenced by the ground state direction. Figure 8.24 shows the ground state and dynamic magnetisation components in the configuration corresponding to maximum contrast (H= 100 Oe in the $\hat{\mathbf{y}}$ direction at t = 0.43 ns). The ground state domain structure is highlighted in red and overlaid on the TRSKM images of the dynamic components.

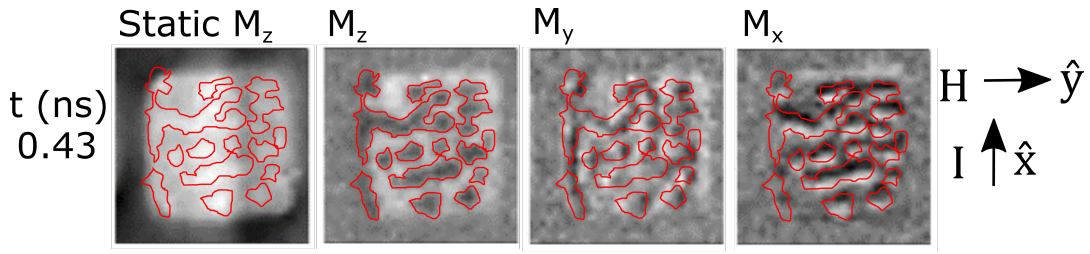

Figure 8.24: TRSKM images from figure 8.23.(b) at t = 0.43 ns with ground state domain structure highlighted in red and overlaid onto the dynamic magnetisation components.

Without this highlighting it is not immediately clear where the stripes seen in figure

8.23.(b) lie in relation to the ground state. This highlighting reveals that the rotation direction of M_z corresponds directly to the ground state $\hat{\mathbf{z}}$ direction. The behaviour of the in-plane components is subtly different, M_x rotates in opposite directions dependent on which vertical (from the readers perspective) edge of the domain is examined, this can been seen as a dark contrast at the top edges of the highlighted overlay and a light contrast at the bottom edges. The rotation direction of M_y is slightly more difficult to discern however a similar general trend appears to be present but with light dark contrast visible in the horizontal direction.

A comparison of the dynamic response of square elements with varying edge length from 1.6 - 10.0 μm was also explored via TRSKM. Figure 8.25 shows the dynamic response of the squares at t = 0.5 ns, the time delay corresponding to maximum contrast in figure 8.18. A bias field of H= 500 Oe was applied parallel to the current direction, these measurements also investigated the effect of reversing the bias field direction. The advantage of the wide waveguide design is that multiple square edge lengths can be measured simultaneously without having to remove the sample from the microscope and remount, making direct comparison of magnetic contrast easier. However the principle difficulty of this measurement is the long imaging times required to capture all devices in a single scan. Position steps small enough to capture the domain behaviour combined with a position range large enough to measure multiple devices meant imaging times were many hours. Over such long imaging times the TRSKM system is susceptible to focus and positional drift. Due to this the images shown in figure 8.25 are split in two and a smaller step size was used to capture dynamics in the 1.6-3.6 μm edge length squares than for the 4.4 - 10.0 μm edge lengths.

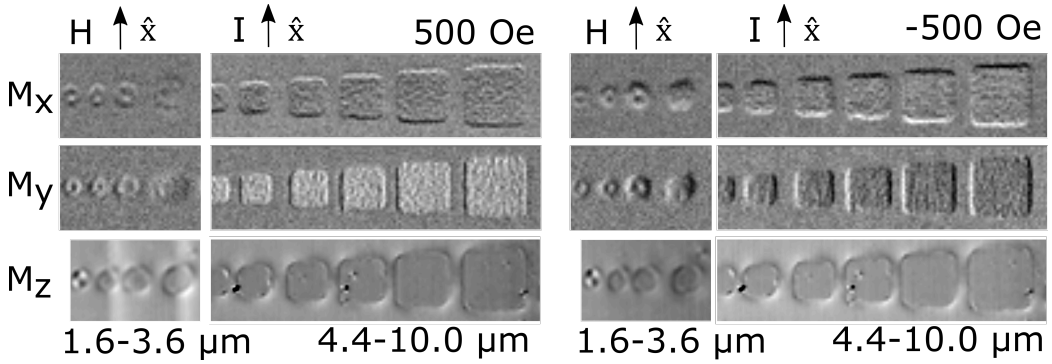

Figure 8.25: TRSKM images Ta/CoFeB/MgO squares with edge lengths from 1.6-10.0 μm with a $\pm$500 Oe in-plane bias field parallel to the current direction ($\hat{\mathbf{x}}$). The 1.6-3.6 μm images were taken separately to the 4.4-10.0 μm images in order to achieve a smaller position step size.

A reversal of bias field reverses the edge contrast for the in-plane magnetisation components. It is also apparent from comparison between field polarities that whilst the rotation of the central portion of the device is not as large as at the edges the direction of rotation also reverses for reversed fields. This can be seen most clearly by comparing M_y for the 4.4-10.0 μm squares for different field directions. The central portion of the square has a light contrast relative to the Ta under layer for H= 500 Oe but has dark contrast relative to the Ta under layer for H= -500 Oe.

The general dynamics are consistent for square edge lengths between 4.4 - 10.0 μm, with a grainy but largely uniform contrast seen in the central region of the squares and strong opposite contrast at the edges. As the square edge length is reduced below 3.6 μm strong opposite contrast is also observed in the central region of the element. The origins of this contrast may lie with a change in the shape of the device. The fidelity of the photolithography process appears reasonable for squares with edge lengths down to 4.4 μm (though some rounding of the edges occurs). As the edge length of the square is reduced further the rounding becomes more pronounced and the smallest 'squares' are actually circles. To illustrate this further a more detailed image of the smallest element (1.6 μm) was taken and is shown in figure 8.26. The reflectivity image in this figure shows that the edges have been rounded until the device is circular and also a change in reflectivity is observed at the center of the device indicating that for this device either there is no CoFeB/MgO at the center or some residual photoresist is still present.

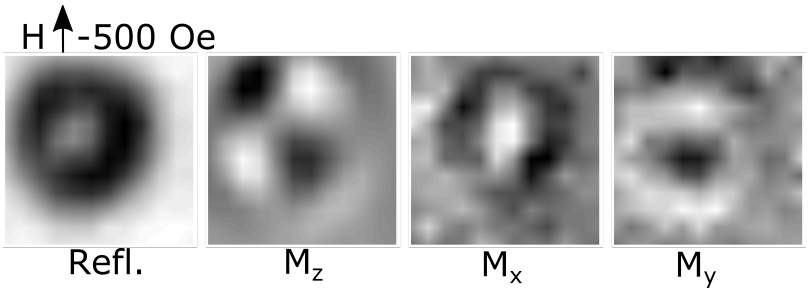

Figure 8.26: TRSKM images of a Ta/CoFeB/MgO square with edge lengths 1.6 μm with a 500 Oe in-plane bias field parallel to the current direction ($\hat{\mathbf{x}}$).

For this device the M_z component has a distinct domain structure not observed for larger devices. A strong M_z domain structure is observed in +ve and -ve directions in four clear quadrants of the image. The center of the ring of domains is in the same position as the light region in the reflectivity image. More experiments would be required to assess the origins of this behaviour but this shape/size may show consider-

ably different behaviour to the larger squares. This final measurement demonstrates consistent behaviour for devices down to 4.4 μm. Below this the resolution of the photolithography patterning technique becomes comparable to the device size. Higher resolution patterning techniques such as E-beam lithography will be required to further reduce device dimensions.

8.6 Summary and Future Work

In recent years the Ta/CoFeB/MgO trilayer has been used extensively to study SOTs. In SOT switching J_c has regularly been measured to be below the values predicted by the macrospin model and this has been attributed to domain nucleation and propagation, however this can only be inferred from the electrical measurements as they do not have spatial resolution. A significant portion of the recent work has focused on relatively large devices, and have used DC or long, on the time-scales of STT memory technology, pulsed currents. Spin-transfer torque technology will require the miniaturisation of devices and significant reduction in current duration. These reductions are likely to cause transition from the domain nucleation and propagation regime observed in current-induced switching, to the incoherent and coherent rotation switching regimes. In an effort to move closer to the device dimensions and current durations required for memory technology small scale devices were designed specifically for high frequency excitation. Several key magnetic parameters of these devices such as the coercive field were shown to vary between nominally identical devices fabricated in different sputtering runs. The sensitivity of SOTs to the ferromagnetic and heavy metal structure has been well documented, and so efforts must be made to reduce this variance and carefully control the deposition and patterning procedure if SOT devices are to be used commercially. Patterning the CoFeB/MgO layer independently of the Ta under layer allowed patterned element dimensions to be reduced and to be fabricated away from the edge of the Ta under layer, minimising the out-of-plane Oersted field contribution to the torque. The signal line dimensions were also reduced significantly increasing the current density and allowing full vector resolution of the magnetisation dynamics in the TRSKM. The magnetisation dynamics of $1.6 - 10.0$ μm squares were found to be highly sensitive to bias field direction and polarity, and also showed strong spatial variations. Again signals with two distinct time-scales were observed which may be further evidence that different torques in such systems do not have the same characteristic time-scales. Many more interesting questions were raised by this study, in particular why TRSKM images showed a strong bipolar contrast at the edges the square when the

magnetisation was saturated in-plane along the direction of current flow. Interpretation of these results is ongoing. However this may be evidence of a spin-accumulation at the lateral edges of the square or evidence of an in-plane spin accumulation generated by the spin Hall effect as charge current flows in the out-of-plane direction into the conducting CoFeB. Another key result in this study was the observation that, for a multi-domain ground state with a small in-plane canting either in or orthogonal to the direction of current flow, the direction of polar rotation was dependent on the direction of canting. A model of the SOTs is currently being developed which, when applied to these results should allow a qualitative determination of the dominant SOTs in this structure.

This study demonstrates the efficacy of the TRSKM technique for exploring SOTs and lays the groundwork for further studies. A wide range of devices was fabricated to explore the effects of device size (to explore switching regimes), shape anisotropy (to aid deterministic zero field switching), element separation (to explore stray field interaction distances), position (to explore the effects of Oersted fields) and notched designs (to trap domains). Time constraints only allowed time-resolved study of a limited number of devices. However this experiment has since been taken up by colleagues who have this large parameter space to explore. A key future development of this work is the application of a lower frequency, large bipolar pulsed current. The bipolar current will allow imaging of the current-induced switching between the perpendicular magnetic states providing this occurs in less than the 1 μs time delay between picked laser pulses. This experiment is currently being set up and shows promising results. The device dimensions in this study stretched the limits of the photolithography patterning procedure. In order to reduce to the nano-scale another patterning technique such as e-beam lithography will need to be utilised.

Chapter 9

Development of a Vector Network Analyser Ferromagnetic Resonance (VNA-FMR) Experiment

9.1 Introduction

At the outset of the studies described in this thesis the vector network analyser ferromagnetic resonance (VNA-FMR) experimental set-up was in its infancy. This chapter details the specifics of development of technique with a focus on the processing and interpretation of the data generated by this experiment. The basic geometry and theory of the VNA-FMR technique is described in section 4.6. However an amount of post-experimental processing was required in order to extract meaningful information from experimental data. VNA-FMR is a powerful technique which can be used to quickly measure magnetisation dynamics over a wide frequency and field range. VNA-FMR can be used to measure the dependence of frequency on applied field and damping parameters for a large number of samples, on time scales that would be impossible for the optical techniques described elsewhere in this thesis. However the speed and efficiency of this technique means that, typically, large data sets are generated. As a level of processing is required to convert the raw data into a form from which useful magnetic information can be extracted, the size of the data sets means that this conversion is often only feasible programmatically. This chapter discusses some of the difficulties in performing and automating this processing due to systemic error and experimental noise, and the steps taken to overcome them. Many of the issues discussed may seem trivial to overcome with a level of human input and judgement but

it must be remembered that this is often infeasible due to the size of the data sets, and so processing methods must be algorithmic and robust over a wide range of potential conditions. Robust algorithmic processing also has the advantage of consistency and repeatability.

9.2 Analysis of Vector Network Analyser Ferromagnetic Resonance (VNA-FMR) Data

As described in section 4.6.2 the magnetic damping parameter (α) can be extracted from the frequency dependent FWHM linewidth $\Delta H(\omega)$. In this thesis $\Delta H(\omega)$ is found by fitting a Lorentzian function to the absorptive (S^{Imag}) part of the transmission S-parameters. It is also possible to extract the FWHM from the peak to peak ($\Delta Hpp(\omega)$) of the dispersive (S^{Real}) components of the S-parameters through the relation $\Delta H(\omega) = \sqrt{3}\Delta Hpp(\omega)$, although due to the specifics of this experimental set up this is more challenging. It is also possible to extract the damping from the reflective S-parameters, S_{11}^{Imag} and S_{22}^{Imag}, however the signal is typically clearest in the transmission parameters S_{12}^{Imag} and S_{21}^{Imag}. For ease of notation it is assumed that $S_{12}^{Imag} \simeq S_{21}^{Imag}$ and so S_{12}^{Imag} is used to denote the transmission parameter in this chapter. A level of processing is required to convert the raw data into into a form where this fitting is possible. This chapter details these processing procedures and for consistency the steps are illustrated with the series of CoMnGe/Ag/NiFe spin valve stacks discussed further in chapter 10.

Figure 9.1 shows typical 'raw' S_{12}^{Imag} and S_{12}^{Real} data generated by the VNA-FMR experiment. It should be noted that in this context the 'raw' data has undergone a level of processing at the experimental level. The inbuilt VNA calibration has been applied to remove any frequency dependent phase shift associated with the VNA electronics and SMA cables connecting the VNA and the device under test (DUT). A high field background subtraction is also applied at each measurement field such that $S_{12}(\mathbf{H}) = S_{12}(\mathbf{H}_{measure}) - S_{12}(\mathbf{H}_{ref})$ in an attempt to remove any systemic background and leave only the FMR signal.

There are three effects evident in figure 9.1 which mean a simple Lorentzian curve cannot be fit to S_{12}^{Imag} in order to extract α.

1. A phase change associated which the electrical length of the waveguide, evidenced in figure 9.1 as a frequency dependent dark and light banding.

2. The overlap of FM_1 and FM_2 resonances, evidenced at low field in figure 9.1 (note that this only occurs in samples with multiple magnetic layers).

3. A field dependent non-linear background, this is difficult to see in figure 9.1 but is illustrated clearly as a deviation from the expected zero outside of the FMR range in figure 9.2.

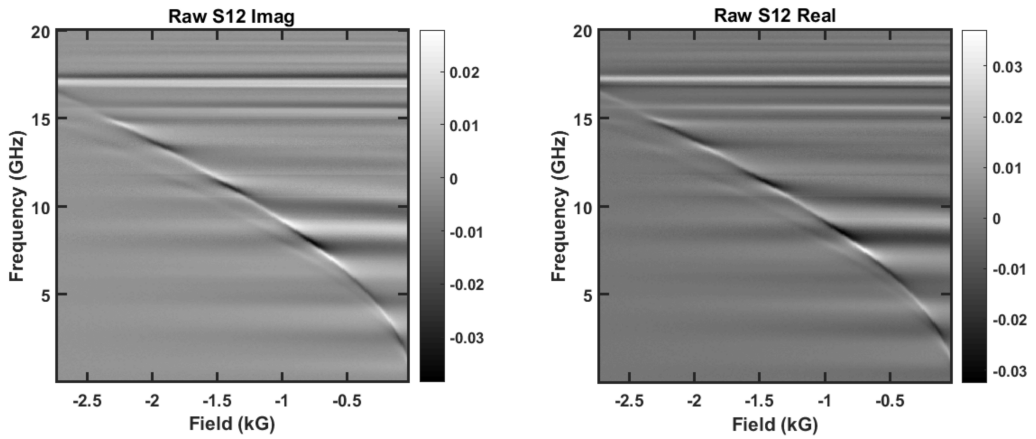

Figure 9.1: Typical raw VNA-FMR measurement of a Ta(5 nm)/NiFe(1.8 nm)/Ag(6 nm)/CoMnGe(5 nm)/Ag(2 nm)/Ta (3 nm) with **H** perpendicular to $\mathbf{h}_{r.f.}$

9.2.1 Calibration of Vector Network Analyser Ferromagneitc Resonance (VNA-FMR) Data at an Experimental Level

The following section describes attempts made to calibrate the above effects at an experimental level.

Experimental calibration of phase shift

In theory it is possible to remove the frequency dependent phase shift of the r.f. signal using the inbuilt calibration routines of the VNA. However, using a standard calibration kit, this is only effective to the ends of the cables connected to the DUT. The calibration routine first measures the frequency dependence of the cable response with 'open', 'short' and 50 Ω 'load' connections. Difficulties arise because this routine then also requires a 'through' connection between ports 1 and 2. If this connection is made with the calibration kit's known 'through' standard then the electrical length and frequency dependence of the DUT are not taken into account, and so any phase change associated with the DUT is not accounted for. For a two-port measurement it is possible to use the DUT as an unknown 'through', however this requires the S-parameters to fulfil the

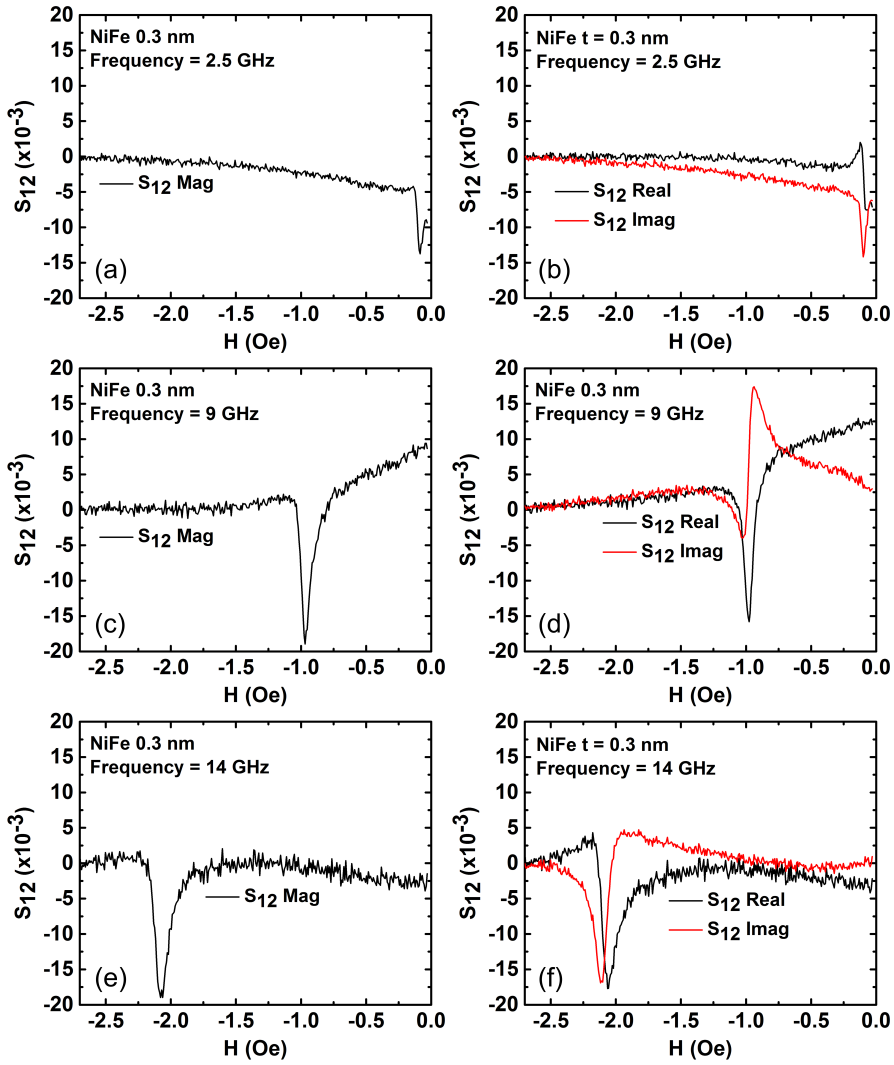

Figure 9.2: Typical raw VNA-FMR measurement of Ta(5 nm)/NiFe(1.8 nm)/Ag(6 nm)/CoMnGe(5 nm)/Ag(2 nm)/Ta (3 nm) with **H** perpendicular to $\mathbf{h}_{r.f.}$. Line scans extracted from figure 9.1 at 2.5 GHz, (a) and (b), 9 GHz, (c) and (d), and 14 GHz (e) and (f). Left side plots ((a), (c), (e)) show the transmission S-parameter magnitude S_{12}^{Mag} and right hand plots ((b), (d), (f)) shown the transmission S-parameter real and imaginary components S_{12}^{Imag} S_{12}^{Imag} and S_{12}^{Real}, in order to illustrate phase rotation and field dependent background.

reciprocity condition $S_{12} = S_{21}$[224]. In practice using the DUT as the calibration through yielded a poor result suggesting $S_{12} \neq S_{21}$. This is probably due to asymmetries in the waveguide and connections causing small, directional dependent variations in

reflection and transmission. A further problem with this type of calibration is the effect of the sample and its position. The DUT comprises not only the waveguide but also the sample placed on top of it. The permittivity of the sample can also have a frequency dependent effect upon signal transmission as the waveguides are designed assuming an air interface on the top side (discussed in section 4.7.1) meaning that if the calibration is performed with only the waveguide then the addition of the sample can invalidate it. One option then is to calibrate with the sample on the waveguide. If this calibration is performed with the magnetic layers in contact with the waveguide (which avoids any need to reposition the sample) then the calibration also removes the low field FMR response (the FMR response remains due to remanent fields). Depending on the frequency/width of the FMR resonance, this may remove a significant portion of useful data. Attempts were made to calibrate with the sample on the waveguide, with the magnetic layers in contact, at very high fields (above the reference field) to force the FMR resonance out of the measurement range, however this calibration was also unsuccessful, likely due to the field dependent background discussed in sections 9.2.1 and 9.3.1. The final method attempted was to calibrate with the sample on top of the waveguide but inverted so that the magnetic layers were far from the r.f. field. This configuration worked well to fully remove any phase shift background however when the sample in flipped back again so that the magnetic layers were placed back in contact for the measurement, a phase shift was re-introduced suggesting either small shifts in the sample position and orientation, or differences in the effective permittivity were large enough to invalidate the calibration.

Due to the difficulties in calibrating out the phase shift at an experimental level, it was instead removed in post experiment processing by rotating S^{Real} and S^{Imag} by a frequency dependent phase difference ϕ in the Argand plane. A detailed description of this process is given in section 9.3.2.

Experimental design to avoid FMR overlap

For samples with a single magnetic layer there is no potential for the overlap of FMR modes. When multiple magnetic layers are present in the sample stack (such as the CoMnGe and NiFe layers in this example) then overlap of the two resonances (F_1 and F_2) resonances requires a more careful treatment when extracting parameters such as α, especially when this process requires a rotation in the Argand plane. One simple method to avoid this complication is a careful choice of layer composition and thickness to avoid this overlap altogether (at least in the experimental frequency range).

As sample composition is often bound by other constraints then a multi-peaked Lorentzian fitting function can be used instead. Again there are additional complications to this process, especially when signal to noise ratios are low, and the resonances are close to overlap, as detailed in section 9.3.3.

Experimental removal of field dependent background

Whilst not immediately obvious from figure 9.1, there is field dependent background, which is seen most clearly in the S-parameter magnitude. This background can be seen more clearly in figure 9.2 where S_{12}^{Mag} (a, c and e) deviates from the expected 0, clearest close to H = 0 Oe, whilst the FMR resonance is clearly visible at a much higher field. The non-linearity of this background is evidenced in the negative and positive gradients in (c) and (a) receptively. This background appears reduced when the resonance occurs at a higher field (e) meaning the origins likely lie with the subtraction of a high field reference measurement ($S_{12}(\mathbf{H}) = S_{12}(\mathbf{H}_{measure}) - S_{12}(\mathbf{H}_{ref})$). Typical experiments are performed by stepping the field and sweeping frequency, so that variations in magnet temperature, mechanical drift etc are likely to be much smaller between the high field measurements and the subtracted higher field reference, than between the low field measurements and the relatively much higher field reference. This background can have significant effects on the quality of the Lorentzian fit, and can make robust phase rotation difficult at low fields. Attempts were made to remove this background at an experimental level by running the entire measurement with the magnetic layers in close proximity to the waveguide then flipping the sample and running the entire experiment again, subtracting the data with magnetic layers far from the waveguide (flipped) as a background from the first measurement. This method was not effective due to complications with the frequency dependent phase shift. Running the experiment without the magnetic layers close to the waveguide involved the removal or flipping of the sample, altering the frequency dependence of the S-parameters. This meant that a phase shifted background was subtracted from the data, altering the expected shape of the FMR resonance.

Removal of this background was instead performed in post-experimental processing. Due to the non linearity and field dependence of this background, fitting a general form for subtraction was not possible. Instead a subtraction was made at each measurement frequency, for which the form of the background was assumed to be approximately linear in the reduced field range close to the resonance. Further details are discussed in section 9.3.1.

9.3 Post Experimental Processing of Vector Network Analyser Ferromagnetic Resonance (VNA-FMR) Data

This section shows the results of several different procedures, both experimental and in post-experimental processing, that were attempted to extract useful material parameters from VNA-FMR experiments. The main focus is the removal of all background effects and phase shifts in order to fit a Lorentzian function to the transmission parameter S_{12}^{Imag} of the form

$$y(x) = \frac{2A}{\pi}\frac{\Gamma}{4(x-x_0)^2+\Gamma^2} + y_0, \tag{9.1}$$

where A is the amplitude, x_0 is the center (peak) and Γ determines the peak width. The frequency dependent full width at half maxima (FWHM) linewidth $\Delta H(\omega)$ is then related to the Gilbert damping constant α by the equation.

$$\Delta H(\omega) = \Delta H(0) + \frac{2\alpha\omega}{\gamma}, \tag{9.2}$$

where γ is the absolute value of the electron spectroscopic splitting factor. An initial approach was to simply increase the complexity of the fitting function in order to incorporate the systematic background effects. Variations of a multi-peaked (to incorporate multiple FMR modes) asymmetric (to incorporate the phase rotation) Lorentzian combined a high order polynomial or exponential (to describe the non linear background) was used, with the general form for n magnetic layers described by

$$y(x) = \sum_{i=1}^{n} \frac{2A_i}{\pi}\frac{\Gamma_i\cos(\theta_i) + (x-x_{0,i})^2\sin(\theta_i)}{4(x-x_{0,i}) + \Gamma_i^2} + g_i(x), \tag{9.3}$$

where $g_i(x)$ is a phenomenological function which describes the field dependent background and θ_i is the rotation angle of the real and imaginary components in the complex plane. Typical results from this type of fitting are shown in figure 9.3.

This method produced mixed results, working fairly well for measurements without a strongly field dependent background (a and b) but it was not effective at certain phase rotations, especially when a larger background was present (c). It must be stressed again that 'effective' here means a fitting method that must be programmatically robust for a wide range of possible conditions due to the size and variance of data sets generated. Here over parametrization allows the fitting function to reach inaccurate local minima before the 'correct' solution can be converged upon. Efforts were made to increase the complexity of the fitting code and function seeding, however after several iterations it

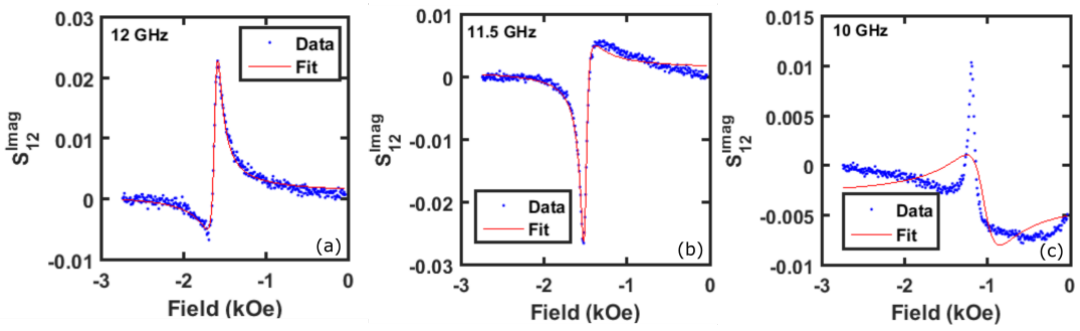

Figure 9.3: Fitting an asymmetric Lorentzian with a polynomial background to VNA-FMR data from a Ta(5 nm)/NiFe(0.3 nm)/Ag(6 nm)/CoMnGe(5 nm)/Ag(2 nm)/Ta (3 nm) thin film at (a) 12 GHz, (b) 11.5 GHz and (c) 10 GHz.

became evident that this would be more difficult than removing the systematic effects before fitting a more simple function.

The steps to remove experimental artefacts before fitting are as follows (note some steps are mutually exclusive).

1. Import raw VNA-FMR data with high field reference measurement subtracted.
2. Subtract field dependent background either by
   (a) Experimental subtraction of repeated measurements without magnetic layers in close proximity to waveguide.
   (b) Post processing subtraction of an approximately linear background in the reduced field region of the FMR mode (best method).
3. Rotate data in the Argand plane under the condition for correct phase rotation of
   (a) Maximising the magnitude of the S_{12}^{Imag} peak.
   (b) Maximising the magnitude of difference between the S_{12}^{Real} peaks.
   (c) A combination of both conditions taking the moments about the real and imaginary axes (best method).
4. Fit a Lorentzian function to S_{12}^{Imag} which may be a
   (a) Simple single Peak Lorentzian
   (b) Multi-peaked Lorentzian
5. Fit frequency dependent linewidth to extract α using equation 9.2.

9.3.1 Removal of Field Dependent Background

Experimental removal of field dependent background

Attempts were made to remove the field dependent background by subtracting a repeat measurement without the magnetic layers in close proximity to the waveguide from the measurement with layers in contact. The aim was to remove all features except the FMR due to the magnetic layer. To keep all other conditions as constant as possible during the reference measurement the sample is inverted and placed in the same position as for the FMR measurement Adding a small marking to the waveguide during the FMR measurement helps to make the positioning as close as possible. The result of a typical subtraction is shown in figure 9.4

This background subtraction typically works better at some frequencies than others. As shown previously, the background is considerably higher at low frequency. This can be seen most clearly as a decrease of constant slope in S_{12}^{Mag} at 4 GHz (figure 9.4 (a)). In this case the background subtraction (b) has done an excellent job of removing the slope with the S_{12} lying close the expected $S_{12}^{Imag} = 0$ outside of the FMR region. At other frequencies the effectiveness of the subtraction is not so clear. Between (c) and (d) the subtraction appears to have improved the quality of S_{12}^{Real} but has acted to increase the background in S_{12}^{Imag}. At higher frequencies, such as 12 GHz shown in (e), there is typically little or no field dependent background. In this case the subtraction (f) actually increases the effective low field background in both S_{12}^{Real} and S_{12}^{Imag}.

Overall the effectiveness of this method is limited as the subtraction must be effective across the entire frequency range, or problems can occur with the rotation and Lorentzian fitting further down the line. For some samples and frequency ranges this method is effective but the appropriateness must be considered on a case by case basis which is not good for robust algorithmic processing.

Post experimental removal of field dependent background

When an experimental background subtraction is not possible a phenomenological subtraction provides a simple alternative. In a field range extending just beyond the FMR peaks (as shown in figure 9.5) the non-linear background can be approximated as linear and subtracted. This procedure was difficult to fully automate as the frequency dependent mixing of S_{12}^{Real} and S_{12}^{Imag}, combined with the background makes creating generalized conditions to identify peak position, and the appropriate width of the FMR mode difficult. Instead this process was semi-automated which allowed a level of

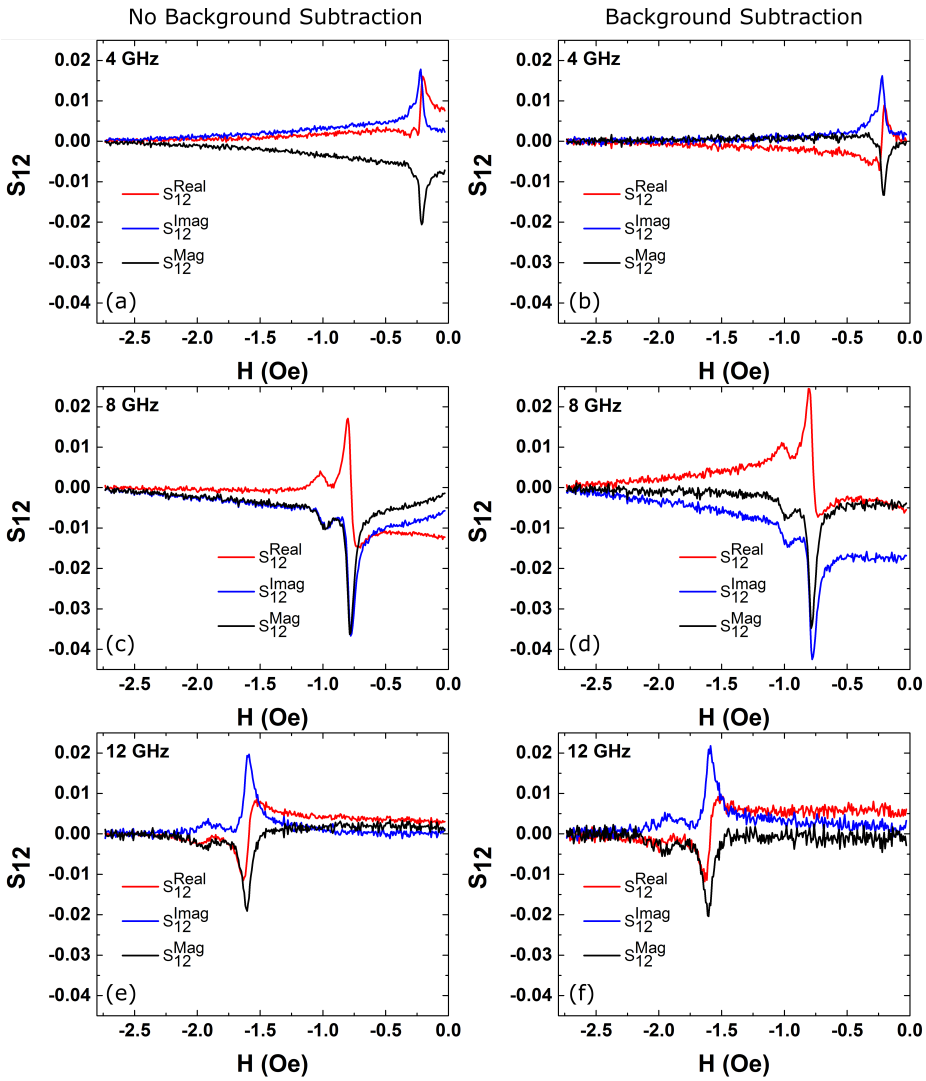

Figure 9.4: Typical raw FMR measurements of Ta(5 nm)/NiFe(1.8 nm)/Ag(6 nm)/CoMnGe(5 nm)/Ag(2 nm)/Ta (3 nm) at 4 GHz (a) 8 GHz (c) and 12 GHz (e). The result of subtracting a reference measurement during which the sample is inverted are shown in (b), (d) and (f).

human judgement to decide the width of the FMR peak and, whilst slower than fully automated processing, remained adequately fast. A script was created using Matlab's 'ginput()' which allows a user to input the peak position and extremum of the linear background. The human judgement allows cases of extreme background and difficult phase rotations to be easily dealt with whilst still retaining the speed of programmatic processing.

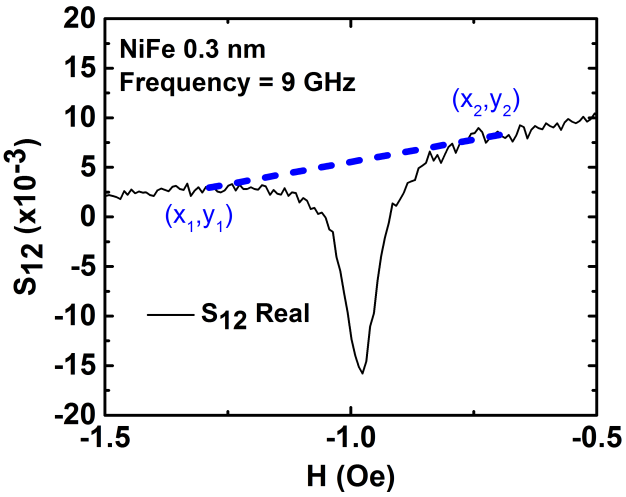

Figure 9.5: Example of linear background subtraction for a Ta(5 nm)/NiFe(0.3 nm)/Ag(6 nm)/CoMnGe(5 nm)/Ag(2 nm)/Ta (3 nm) stack at 9 GHz. The (X,Y) co-ordinates show points between which the linear background fit is applied and demonstrate the approximate linearity of the background over a small field region close to the FMR peak

Typical results of this linear subtraction are shown in figure 9.6. Whilst more time consuming, this method works well for a wide range of frequencies giving the most symmetric shape on either side of the peak close to the expected transmission of $S_{12}^{Imag} = 0$ outside the FMR range.

9.3.2 Removal of Frequency Dependent Phase Shift

As discussed, experimental calibration of the frequency dependent, phase shift is difficult but it can be removed in post processing. The phase shift causes a rotation of the complex S-parameters within the Argand plane and and as such can be 'undone' by simply reversing this rotation using the rotation matrix

$$\mathbf{R} = \begin{bmatrix} \cos(\theta) & -\sin(\theta) \\ \sin(\theta) & \cos(\theta) \end{bmatrix}. \tag{9.4}$$

Equation 9.4 rotates points in the Argand plane counter clockwise through an angle θ about the origin. The position of the S_{12} points are represented by a column vector $\mathbf{v}$

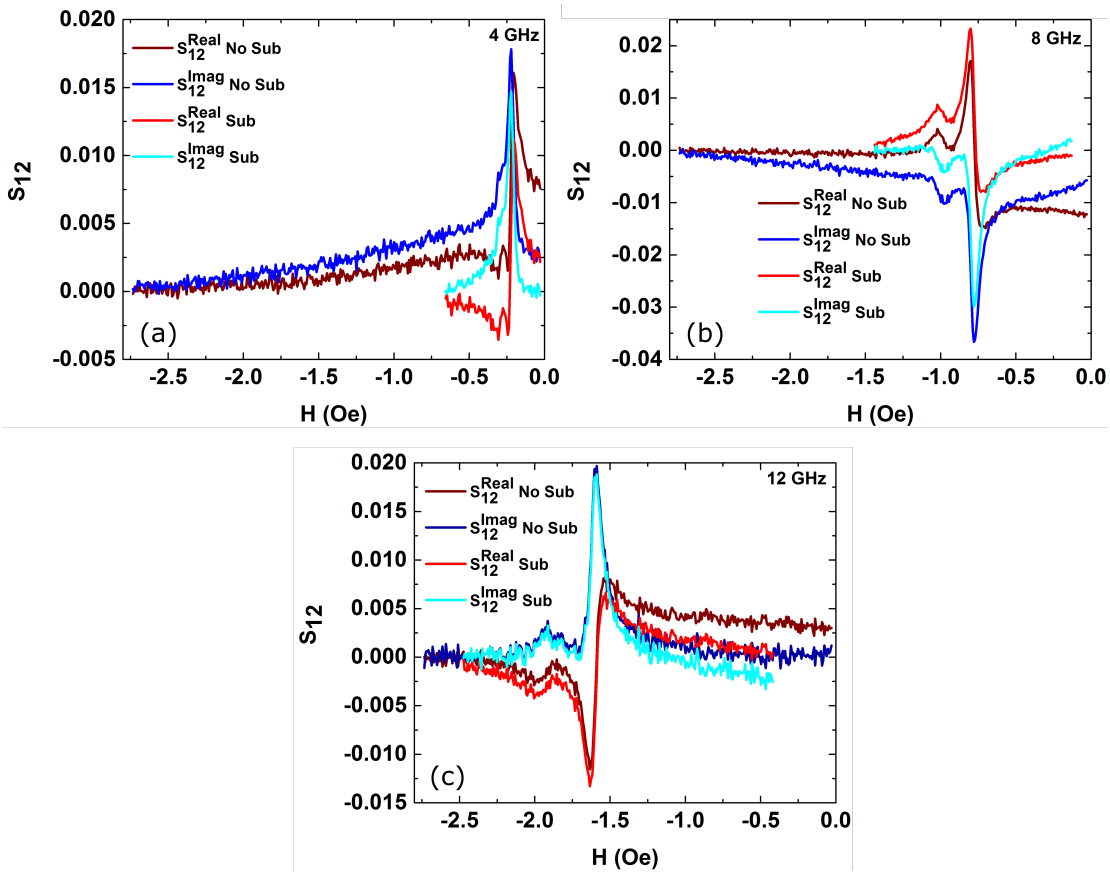

Figure 9.6: Typical pre and post linear background subtraction VNA-FMR measurements of Ta(5 nm)/NiFe(1.8 nm)/Ag(6 nm)/CoMnGe(5 nm)/Ag(2 nm)/Ta (3 nm) at 4 GHz (a) 8 GHz (b) and 12 GHz (c).

and the rotated vector is obtained by using the matrix multiplication **Rv** yielding

$$\begin{bmatrix} S_{12}^{Real'} \\ S_{12}^{Imag'} \end{bmatrix} = \begin{bmatrix} \cos(\theta) & -\sin(\theta) \\ \sin(\theta) & \cos(\theta) \end{bmatrix} \begin{bmatrix} S_{12}^{Real} \\ S_{12}^{Imag} \end{bmatrix} \tag{9.5}$$

or

$$S_{12}^{Real'} = S_{12}^{Real}\cos(\theta) - S_{12}^{Imag}\sin(\theta) \tag{9.6}$$

and

$$S_{12}^{Imag'} = S_{12}^{Real}\sin(\theta) + S_{12}^{Imag}\cos(\theta) \tag{9.7}$$

Results of this rotation are shown in figure 9.7

The correct rotation angle was defined by the conditions discussed in section 4.6.2,

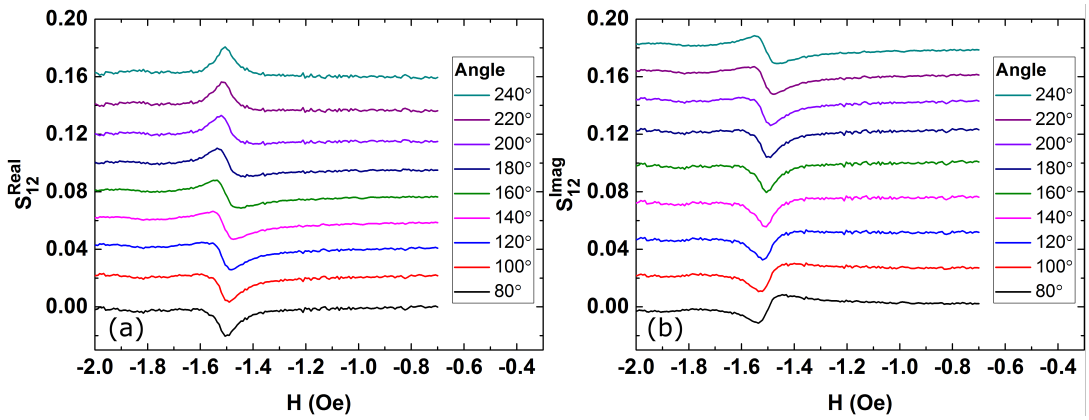

Figure 9.7: Phase rotation of S_{12}^{Real} (a) and S_{12}^{Imag} (b) through a 180° half cycle in Ta(5 nm)/NiFe(0.9 nm)/Ag(6 nm)/CoMnGe(5 nm)/Ag(2 nm)/Ta (3 nm) at 8 GHz.

namely that the absorption of $\mathbf{h}_{rf}$ by the samples follows the same dependence as the susceptibility χ shown in figure 4.14. It is clear from figure 9.7 that the induced phase shift causes an effective mixing of the S_{12}^{Real} and S_{12}^{Imag} components. As the phase shift is cyclic over a period of 2π then the signal can be 'un-mixed' by finding and applying the correct rotation angle for each frequency. Using the expected shape shown in figure 4.14 the condition for the correct rotation angle is a minimum (or maximum as this simple represents a further rotation of $n\pi$ and does not affect the linewidth) in the peak of S_{12}^{Imag} at the point where the magnitude of the S_{12}^{Real} gradient is at its maximum. A more robust method for rotation in the case of noisy data is to use the moments of each point when both components are plotted on the same plane. Using this method the correct rotation angle is when the average weight of S_{12}^{Real} points is zero about the imaginary (vertical) axis, and the average weight of S_{12}^{Imag} points is zero about a horizontal (when plotted as in figure 9.8) line bisecting the imaginary axis at $\pm$ (a shift of $n\pi$ and does not affect the linewidth) the average radius of the circles shown in figure 9.8. The correct rotation condition is illustrated in figure 9.8.(a) by plotting both S_{12} components on the same plane. Figure 9.8.(b). shows the result of a correct rotation which, for this specific frequency, was 157°. An advantage of plotting S_{12}^{Imag} as a function of S_{12}^{Real} is that any offset, arising as an experimental artefact, is clearly visible as a shift of the circle of circles in figure 9.8.(a). This provides another method to phenomenologically remove any background signal, by fitting a larger circle encompassing the outermost points (furthest from the central region where smaller circles overlap) then applying a linear subtraction to shift the center of this larger fitted circle to $(0,0)$. This method of removing backgrounds was the most robust for fully automatic processing and so

appropriate for very large data sets, however the previous method of subtracting a linear background close to the FMR peak, whilst more time consuming, remained the most consistent processing method and so was used for smaller data sets.

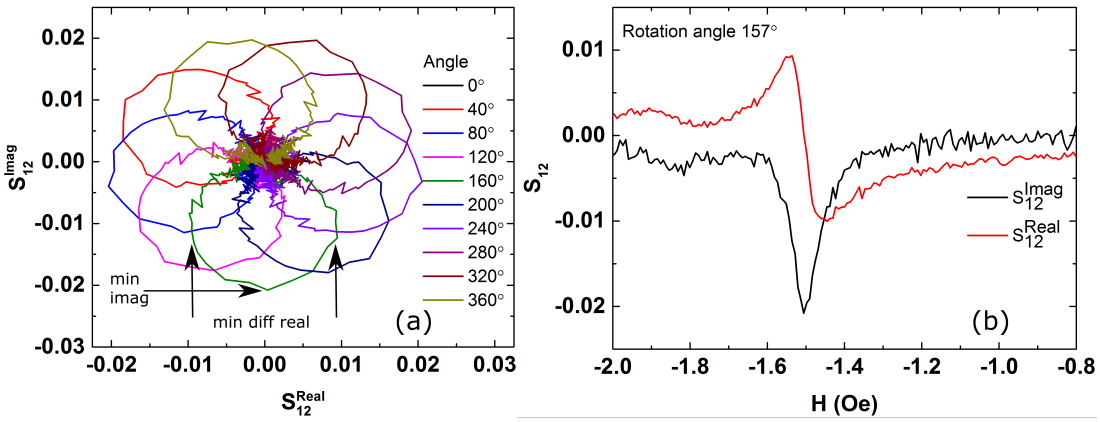

Figure 9.8: Example of phase rotation condition (a) and correctly rotated FMR curves (b) for a Ta(5 nm)/NiFe(0.9 nm)/Ag(6 nm)/CoMnGe(5 nm)/Ag(2 nm)/Ta (3 nm) film.

9.3.3 Fitting Lorentzian Function to Extract Frequency Dependent Linewidth

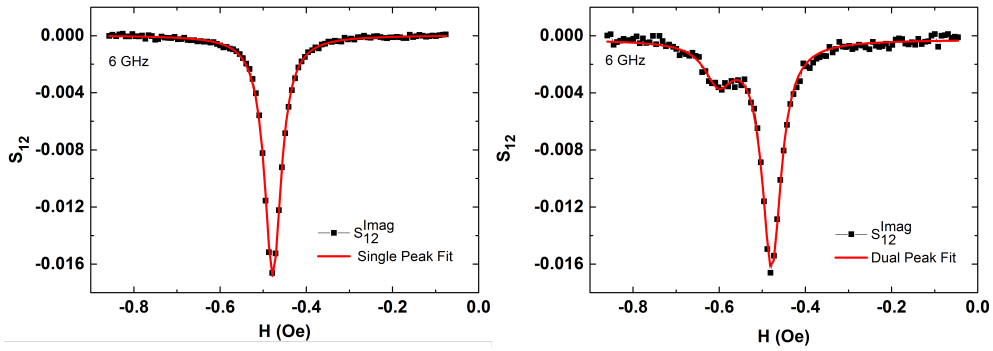

Figure 9.9: Fitting a single (a) and double (b) peaked Lorentzian function to Ta(5 nm)/NiFe(t nm)/Ag(6 nm)/CoMnGe(5 nm)/Ag(2 nm)/Ta (3 nm) measured by VNA-FMR where t = 0.3 nm and 1.8 nm respectively.

As discussed in section 4.6.2 the Gilbert damping parameter α can be extracted from the frequency dependent FMR linewidth $\Delta H(\omega)$ using equation equation 9.2. Once the systemic experimental effects have been removed it is simple to fit a Lorentzian function to S_{12}^{Imag} (equation 9.1). Programmatic seeding of this function is made considerably easier by the prior removal of experimental artefacts requiring only the peak position

and an approximate linewidth. Figure 9.9 shows an example of this fitting for (a) a single peak (one magnetic layer) and (b) double peak (two magnetic layers) after background removal and phase rotation.

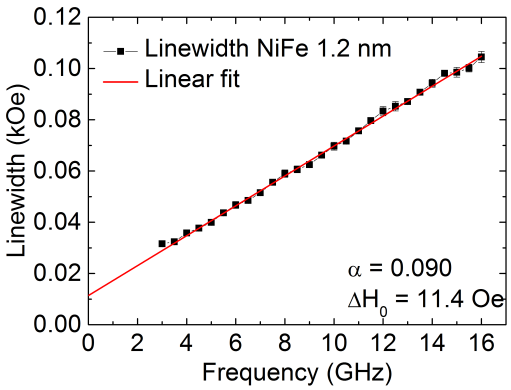

Figure 9.10: Extraction of α and ΔH_0 from the frequency dependent linewidth in a Ta(5 nm)/NiFe(1.2 nm)/Ag(6 nm)/CoMnGe(5 nm)/Ag(2 nm)/Ta (3 nm) thin film measured by VNA-FMR.

The final step in extracting α and ΔH_0 is to plot H(ω) against frequency and convert the gradient to α using equation 9.2 and equate ΔH_0 to the zero field offset. A typical example of this is shown in figure 9.10.

9.4 Summary and Future Work

In summary this chapter has detailed the difficulties in extracting magnetic parameters from the VNA-FMR experiment and the steps taken to formulate a robust algorithm for post experimental processing. Whilst this chapter does not present any novel developments to physical theory the work completed here has facilitated the studies in other chapters of this thesis and the work of other members of the Exeter magnetism group. The fitting algorithm and methods detailed here will facilitate ongoing measurements and future developments to the VNA-FMR system.

Chapter 10

Spin pumping and spin transfer torque in Ta/Ag/Co_2MnGe (5 nm)/Ag (6 nm)/$Ni_{81}Fe_{19}$ (0 - 5 nm)/Ag/Ta spin valve structures

This work has been submitted for publication in Physical Review B.

10.1 Introduction

The discovery that a spin-polarized current could exert a torque (STT) on a nano-scale ferromagnet (FM) has led to the development of a whole new class of electronic devices[225]. Pure spin currents can circumvent the constraints placed on traditional electronics and have the potential to allow low-power and high-bandwidth information transfer[26, 27]. Crucial to the development of smaller and more efficient devices is a strong understanding of the mechanisms by which spin currents can be generated, such as the spin Hall effect,[226, 227] and how these currents propagate through ultra-thin films. Detection of pure spin current has been achieved through measurement of effects induced by the spin current, such as spin-torque driven magnetic precession[28, 29] and the inverse spin Hall effect[30, 31, 32]. Very recently methods have been devised to detect the local spin density by means of soft x-ray probes[33].

One mechanism by which the generation and propagation of spin current can be studied is precessional spin pumping. In a spin valve comprising a ferromag-

netic/normal/ferromagnetic (FM_1/NM/FM_2) metal hybrid structure, magnetic precession in the 'source' layer (FM_1) pumps pure spin current into the adjacent non-magnetic layer (NM)[228]. A non-local damping of FM_1 may then result from spin scattering in the NM. Further damping may occur with the addition of the second ferromagnetic 'sink' layer (FM_2) on the opposite interface of the NM. This allows FM_1 to pump spin current across the NM and into FM_2 where the transverse component of the spin current can be absorbed, in a similar manner to the absorption of the spin carried by a charge current[229]. The absorption of the spin current leads to a STT on the sink layer magnetization and increased damping of the precession in the source layer.

Ferromagnetic resonance (FMR) is a powerful technique by which to observe the spin pumping effect[28]. This technique has the advantage that spin current absorption in layers only a few Ångström thick can be measured as a perturbation of the much larger signal from the source layer. This type of measurement does not require nanofabrication and so finite size magnetostatic effects[230] and activation volume effects[231] do not increase the complexity of the interpretation. However it does not provide a direct measurement of the spin current absorption in the sink layer.

The spin relaxation length in the NM layer has been studied extensively.[232, 233] Recently the penetration of the spin current into the ferromagnetic sink layer has been studied by means of magnetotransport measurements, which have indicated a characteristic length for the absorption of the longitudinal component of spin (i.e. parallel or anti-parallel to **M**) in 3*d* transition metals[58, 234]. Here the dependence on distance from the interface z was found to be exponential with spin current density i.e. $\propto \exp(-z/\lambda_{SD})$, where λ_{SD} is the spin diffusion length. Recently Ghosh *et al.*[235] used spin-pumping to infer that the depth dependence of the transverse component of spin current (i.e. perpendicular to **M**) instead follows a power-law dependence. They found this to be applicable in structurally diverse ferromagnets, with the absorption of the spin current saturating at a FM_2 thickness of 1.2 ± 0.1 nm. This result supports theoretical predictions that the length scales are governed by the transverse spin coherence length λ_J which is proportional to $\pi/|k_f^{\uparrow} - k_f^{\downarrow}|$ to first order where $k_f^{\uparrow(\downarrow)}$ are the majority (minority) spin state Fermi wave vectors[236].

However it is not clear how, for real ultra-thin layers (<1.2 nm), the structure and magnetic state of the sink layer may affect the spin current absorption. As the layer thickness becomes comparable to the atomic radius it is highly unlikely that films form as a smooth layer of only a few atoms thick. As the film's structural parameters have a significant impact on the magnetic order of the sink layer, it is therefore expected to have a significant effect on spin current absorption. While other studies focus purely

on the sink layer, often this layer is part of a larger stack, which adds complexity i.e. it is not immediately clear what effect this surrounding structure may have on spin absorption. Typically a NM with weak spin-orbit coupling is used in the $FM_1/NM/FM_2$ trilayer since, in such materials, the spin flip rate is comparatively small, meaning that if the thickness of the NM is much smaller than the spin-diffusion length, efficient spin transfer is expected from FM_1 to FM_2. For example, in this study the maximum NM (Ag) thickness is 6 nm, which is considerably smaller than the spin diffusion length that is estimated to be 158-170 nm[237, 238]. When other NM layers are present in the layered structure their effect must also be considered, especially if they contain heavy elements with large spin-orbit coupling.

Since the spin current can be eliminated by spin-flip scattering at the FM/NM interfaces and within the NM layers it is critical to directly observe the response of the sink layer, in conjunction with the source, in order to unambiguously conclude that spin absorption within the sink layer is responsible for an increased damping of the source layer. The dynamics of the sink layer have previously been observed by time-resolved magneto-optical Kerr effect studies[239, 237, 240] of epitaxial structures with Ag and Au spacer layers. In spin valves with chemically distinct source and sink layers the element selectivity of x-ray magnetic circular dichroism (XMCD)[241] can be employed to isolate the dynamic response of the source and sink layers and directly measure the magnitude of the spin torque acting on the sink layer.

In this study vector network analyser ferromagnetic resonance (VNA-FMR) is used to determine the dependence of the source layer damping parameter α (which not only has the well established Gilbert damping contribution, but also an additional contribution caused by absorption of the spin current in FM_2) as a function of the sink layer thickness (t_{NiFe}). X-ray detected ferromagnetic resonance (XFMR) is used to make layer selective measurements of the amplitude and phase of precession in the source and sink layers. The torque acting on the sink layer is determined from the experimental data together with a calculated value for the Real part of the spin mixing conductance $\mathrm{Re}(g^{\uparrow\downarrow})$.

10.2 Experimental

Each spin valve structure was grown on a sapphire wafer with a Ta (5 nm)/Cu (100 nm)/Ta (5 nm)/Ru (10 nm) overlayer. A 60 second RF etch was used to remove 3.5 nm of Ru, ensuring a clean surface, before depositing spin valve stacks in the order Ta (5 nm) /Ag (4 nm) /$Ni_{81}Fe_{19}$ (0.3-5.0 nm)/ Ag (6 nm)/ Co_2MnGe (5 nm)/ Ag (2

nm)/ Ta (3 nm). Control samples, one without the $Ni_{81}Fe_{19}$ layer comprising Ta (5 nm)/ Ag (6 nm)/ Co_2MnGe (5 nm)/ Ag (2. nm)/ Ta (3 nm), and a second without the Co_2MnGe layer comprising Ta (5 nm) /Ag (4 nm) /$Ni_{81}Fe_{19}$ (3 nm)/ Ag (6 nm)/Ta (3 nm) were also fabricated. In the as-deposited state, the Co_2MnGe source layer is essentially non-magnetic due to disorder. Field annealing is used to induce the ordered ferromagnetic state (see Fig. 10.4(b)) and induces a small (< 10 Oe) in-plane uniaxial magnetic anisotropy within both layers. VNA-FMR and XFMR measurements were performed on large area 1 x 1 cm^2 films.

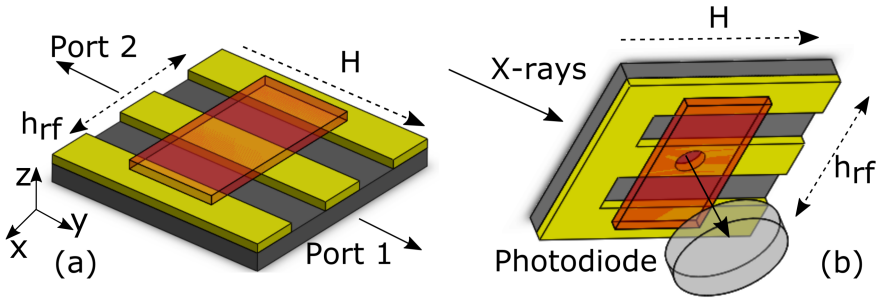

Figure 10.1: (a) Measurement geometries for vector network analyser ferromagnetic resonance (VNA-FMR) and (b) X-ray detected ferromagnetic resonance (XFMR).

VNA-FMR measurements were made by placing samples face down on a 50 Ω coplanar waveguide (CPW) with 500 μm signal track width (Fig. 10.1(a)). A 100 nm layer of photoresist was used to prevent the sample from short circuiting the CPW. The scattering matrix parameters of the composite structure were recorded for frequencies from 0-15 GHz as the bias field was swept between 0.0 and 1.3 kOe[171]. The damping parameter (α) of FM_1 (Co_2MnGe) was extracted from the frequency dependent full width half maximum linewidths $\Delta H(\omega)$ for each FM_2 ($Ni_{81}Fe_{19}$) thickness using the expression[167]

$$\Delta H(\omega) = \Delta H(0) + 2\alpha\omega/\gamma, \tag{10.1}$$

where $\Delta H(0)$ is the contribution due to inhomogeneous broadening.

Phase-resolved XFMR measurements[242, 33, 243] were made upon the same continuous thin films. The sample was placed in contact with a coplanar waveguide fabricated from a printed circuit board. A countersunk hole of 500 μm diameter in the 1 mm wide signal line allowed x-ray access to the sample. Circularly polarized x-rays were used to determine the magnetization along the beam direction using the x-ray magnetic circular dichroism effect. The transmitted x-rays were detected indirectly through x-ray

excited optical luminescence in the sapphire substrate, with the emitted light detected by a photodiode mounted behind the sample (Fig. 10.1(b)). An in vacuum SMA cable was used to deliver a 4 GHz RF current to the CPW, generating an in-plane oscillating magnetic field at the sample surface, exciting precession. A comb generator driven by the 499.65 MHz synchrotron master clock ensured phase coherence of higher harmonics with the x-ray bunches. A static bias field, applied parallel to the CPW signal line, was swept to reveal the ferromagnetic resonance. This transverse geometry allows phase-resolved measurement of the precession by delaying the RF excitation relative to the synchrotron master clock single using a delay line with a resolution of 2 ps. Layer specificity was achieved by tuning the x-ray energy to either the Co L_3 edge in the source (Co_2MnGe) layer or the Fe L_3 edge in the sink ($Ni_{81}Fe_{19}$) layer, allowing direct measurement of the spin dynamics in each layer.

10.3 Results

10.3.1 Vector Network Analyser Ferromagnetic Resonance (VNA-FMR) Measurements

Typical VNA-FMR resonance spectra acquired at a frequency of 8 GHz for different sink layer thicknesses (t_{NiFe}) are shown in Fig. 10.2. For $t_{NiFe} = 1.2$ (b) and 1.8 nm (c) both the Co_2MnGe and $Ni_{81}Fe_{19}$ peaks are distinct and visible allowing observation of the sink layer resonance directly. For $t_{NiFe} \leq 0.9$ nm, as in Fig. 2(a), the $Ni_{81}Fe_{19}$ resonance cannot be identified unambiguously and therefore using this technique, information about the behaviour of the sink layer can only be inferred from the dynamics of the source layer. For the thickest films in this study $t_{NiFe} = 3.0$, Fig. 2(d), and 5.0 nm the Co_2MnGe and $Ni_{81}Fe_{19}$ peaks overlap making it impossible to resolve the behaviour of the individual layers.

For each sample the damping parameter of the source layer has been extracted from the frequency dependent linewidths $\Delta H(\omega)$ (as in Eq. 10.1) obtained by fitting a single Lorentzian function to the absorptive (S_{12}^{Im}) S-parameter. The intrinsic damping has been isolated as in Ref. [167]. Fig. 10.3(b) shows linewidth vs frequency for the two single layer reference samples. Here $\Delta H(0)$ is comparatively large for the Co_2MnGe single layer and small for the $Ni_{81}Fe_{19}$ single layer. In the trilayer stacks, as shown in Fig. 10.3(b) for $t_{NiFe} = 0.3$-1.8 nm, $\Delta H(0)$ gradually decreases with increasing $Ni_{81}Fe_{19}$ thickness. For $t_{NiFe} = 3.0$-5.0 nm, $\Delta H(0)$ is negligible. This effect is shown clearly in Fig. 10.4(a). As $\Delta H(0)$ usually results from structural imperfections[244], and the

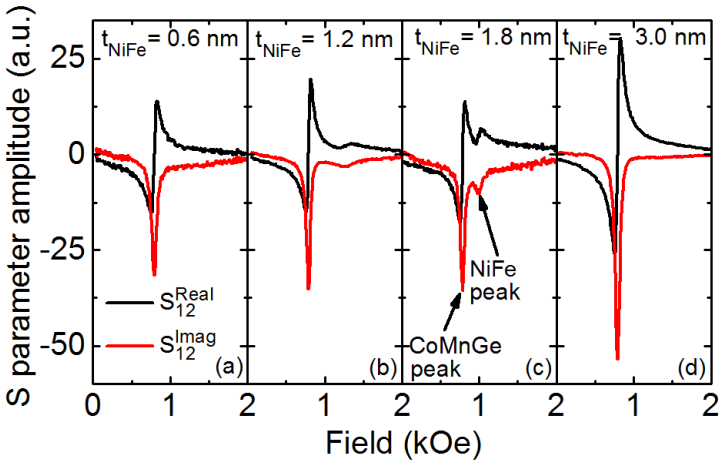

Figure 10.2: Typical experimental VNA-FMR field sweeps at $f = 8$ GHz for sink layer thicknesses of (a) $t_{NiFe} = 0.6$ nm, (b) 1.2 nm, (c) 1.8 nm, and (d) 3.0 nm, showing the S_{12}^{Im} and S_{12}^{Re} scattering matrix components.

Co_2MnGe layer is grown after the $Ni_{81}Fe_{19}$ layer, this result suggests that the increased $Ni_{81}Fe_{19}$ thickness enhances the quality of the Co_2MnGe growth. The insight gained from VNA-FMR about $\Delta H(0)$ is crucial for the fitting and interpretation of the more complex XFMR experiment discussed further below.

Figure 10.4(a) shows α_{CoMnGe} for each $Ni_{81}Fe_{19}$ sink layer thickness. Error bars in this figure represent the statistical error associated with the fit. For $t_{NiFe} \leq 1.8$ nm the variation of α_{CoMnGe} is relatively small. In this region the only samples that show a significantly different value of the damping parameter are $t_{NiFe} = 0.3$ nm and 0.6 nm. At first sight this is surprising since other studies have reported a power law increase in α_{source} with sink layer thickness.[235] The relative insensitivity to t_{NiFe} might lie in the presence of the Ta layer adjacent to the sink. Ta has a high atomic number, and with that large spin-orbit coupling, and therefore scatters injected spins effectively. As a consequence a spin current that passes through the thin $Ni_{81}Fe_{19}$ layer, then also passes across the adjacent Ag layer and is strongly scattered within the Ta.

The increase in damping for the thinnest $Ni_{81}Fe_{19}$ thicknesses, $t_{NiFe} = 0.3$ and 0.6 nm, may be due to the atomic structure of the $Ni_{81}Fe_{19}$ layer. The vibrating sample magnetometer (VSM) data plotted in Fig. 10.4(b) shows that for $t_{NiFe} \leq 0.6$ nm the $Ni_{81}Fe_{19}$ layer does not exhibit ferromagnetic order. Since Fe and Ni are known to be immiscible in Ag[245] intermixing and alloy formation with the adjacent Ag layers can be ruled out. $Ni_{81}Fe_{19}$ films on Ag are found to have a lattice parameter of 0.36 nm[246].

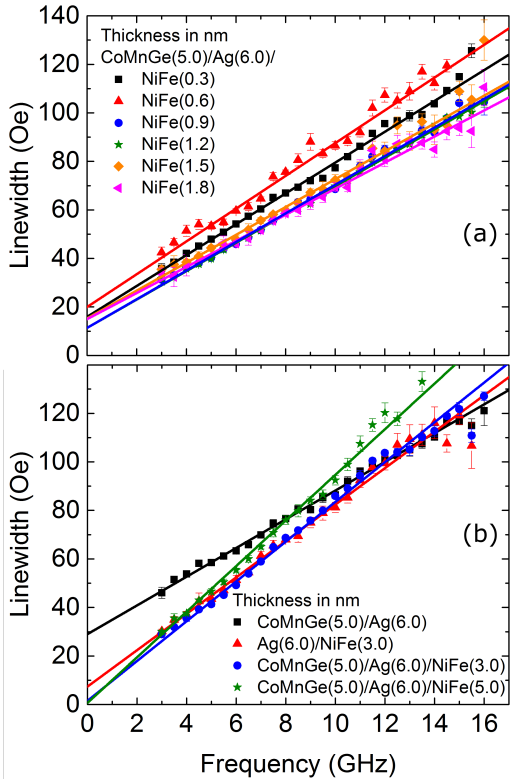

Figure 10.3: VNA-FMR measurements showing frequency dependent linewidths and linear fits to (a) thin sink layer (Co_2MnGe (5 nm)/Ag (6 nm)/$Ni_{81}Fe_{19}$ (0.6-1.8 nm)) trilayers and (b) the thick sink layer (Co_2MnGe (5 nm)/Ag (6 nm)/$Ni_{81}Fe_{19}$ (3.0-5.0 nm)) trilayers, along with single layer reference films without the source layer (Ag (6 nm)/$Ni_{81}Fe_{19}$ (3.0 nm)), and without the sink layer (Co_2MnGe (5 nm)/Ag (6 nm)). These plots are separated for clarity.

When the layer thickness is comparable to the lattice parameter it is highly unlikely that a continuous single layer film is formed. Rather it is likely that these layers are discontinuous, with the grains being superparamagnetic at room temperature, and that the greater structural and magnetic disorder leads to increased spin scattering.

Finally the extracted α_{CoMnGe} values for the thickest $Ni_{81}Fe_{19}$ layers $t_{NiFe} = 3.0$ and $t_{NiFe} = 5.0$ nm appear to rise sharply. However the Co_2MnGe and $Ni_{81}Fe_{19}$ resonances overlap closely in the frequency and field range considered here (Fig. 10.2(d)) to the extent that separate resonances could not be observed in the VNA-FMR experiment. The increase in α could therefore arise from a small but finite difference between the Co_2MnGe and $Ni_{81}Fe_{19}$ resonance fields. Therefore the extracted values provide an upper limit for α_{CoMnGe} and the response of the two ferromagnetic layers needs to be

separated before any further conclusions can be drawn.

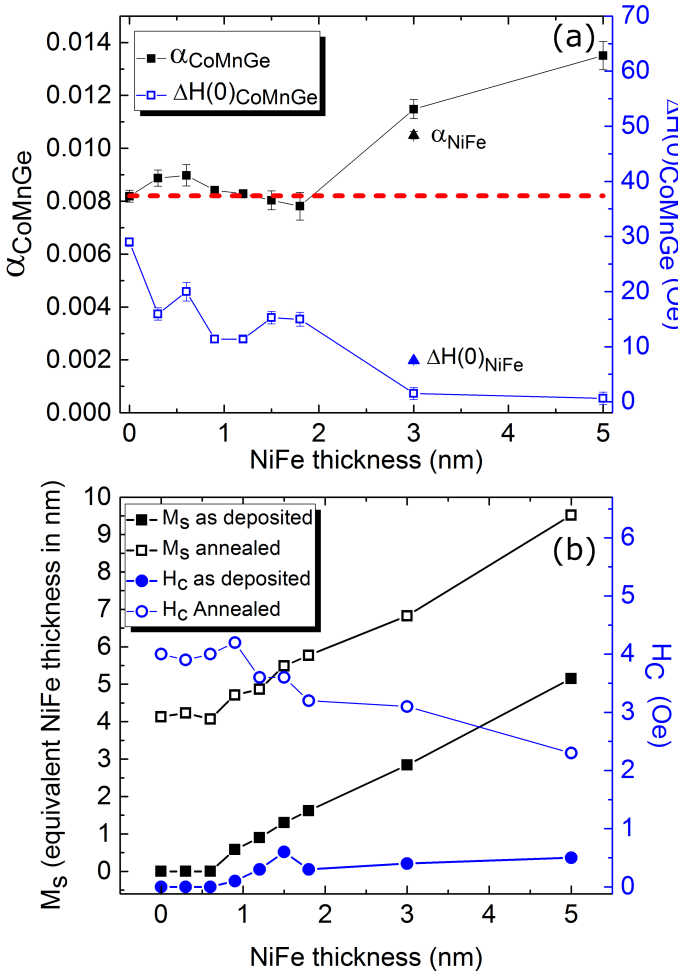

Figure 10.4: (a) Gilbert damping parameter, α, and inhomogeneous broadening $\Delta H(0)$ measured by vector network analyser ferromagnetic resonance (VNA-FMR) (the dashed red line is a guide to the eye) and (b) saturation magnetisation M_s (given in units of equivalent $Ni_{81}Fe_{19}$ thickness, where M_s for $Ni_{81}Fe_{19} \approx 860$ emu/cm^3)[247] and coercive field (H_c) measured by vibrating sample magnetometer (VSM) as a function of $Ni_{81}Fe_{19}$ layer thickness in Co_2MnGe/Ag/$Ni_{81}Fe_{19}$ spin valve structures.

10.3.2 X-ray Ferromagnetic Resonance (XFMR) Measurements

XFMR field scans at $h_{rf} = 4$ GHz are shown in Fig. 10.5. The solid lines are the result of numerical modelling and will be described in the following section. The dispersive (Re) and absorptive (Im) components of the signal are initially mixed due to a phase

delay present within the microwave electronics of the measurement apparatus. These components are recovered by rotating the complex signal in the Argand plane so as to obtain maximum peak height in the Im component at the position of maximum gradient in the Re component, and a flat response on either side of the resonance. For both $t_{\mathrm{NiFe}} = 1.5$ nm (Fig. 10.5(a)) and 1.8 nm (Fig. 10.5(b)) the Co Im and Fe Re data show a clear peak at the Co_2MnGe resonance field $H_{\mathrm{res}} = 204$ Oe, while the Fe Im signal shows a peak at the thickness dependent $Ni_{81}Fe_{19}$ resonance fields of $H_{\mathrm{res}} = 303$ and 258 Oe, respectively. Crucially it is possible to observe the response of the $Ni_{81}Fe_{19}$ sink layer at the Co_2MnGe source layer resonance field. At resonance the Im part of the Co_2MnGe response is unipolar while, at the same field, the Re part of the $Ni_{81}Fe_{19}$ response is bipolar. This behaviour is reversed for the Re part of the Co_2MnGe response. This is a distinct signature of STT due to spin pumping (rather than static dipolar or exchange coupling)[242]. For the thicker $t_{\mathrm{NiFe}} = 3.0$ and 5.0 nm films the resonances of the two magnetic films overlap and the manifestation of spin pumping is an asymmetry of the lineshape. This can be seen most clearly for the $t_{\mathrm{NiFe}} = 5.0$ nm film where the Co_2MnGe lineshape shows a difference in height and shape of the lobes in the Re component and a difference in gradient between the low and high field sloping regions of the Im component. Both effects are predicted and described well by numerical modelling, as described in the following.

The dynamic behavior can be modelled using coupled LLG equations, with additional terms to describe the spin pumping[28, 242]. The precessing magnetization of each layer has two oscillatory (transverse) dynamic components. Since the XMCD arises from the magnetization component parallel to the x-ray wave vector, the x-rays sample the projection of the transverse components along the beam direction. The LLG equations for the response of the i-th layer including the effects of interactions with the j-th layer can be written as

$$\frac{\partial \mathbf{m}_i}{\partial t} = -|\gamma|\mathbf{m}_i \times \left[\mathbf{H}^i_{\mathrm{eff}} + \beta_i \mathbf{M}_j - \frac{\alpha_i^{(0)} + \alpha'_{ii}}{|\gamma_i|}\frac{\partial \mathbf{m}_i}{dt}\right] - \alpha'_{ij}\mathbf{m}_j \times \frac{\partial \mathbf{m}_j}{\partial t}, \quad (10.2)$$

where $\mathbf{m}_i$ and $\mathbf{m}_j$ are unit vectors parallel to the magnetization vectors of the i-th and j-th layers. There are four torque terms represented in Eq. 10.2. The first term gives the torque due to the local effective field $\mathbf{H}^i_{\mathrm{eff}}$ including applied field, crystalline anisotropy and shape anisotropy. The second term gives the torque arising from dipolar or indirect exchange interactions with the other layer. The third term gives the effective Gilbert type damping, including both intrinsic spin-orbit effects and two magnon scattering,

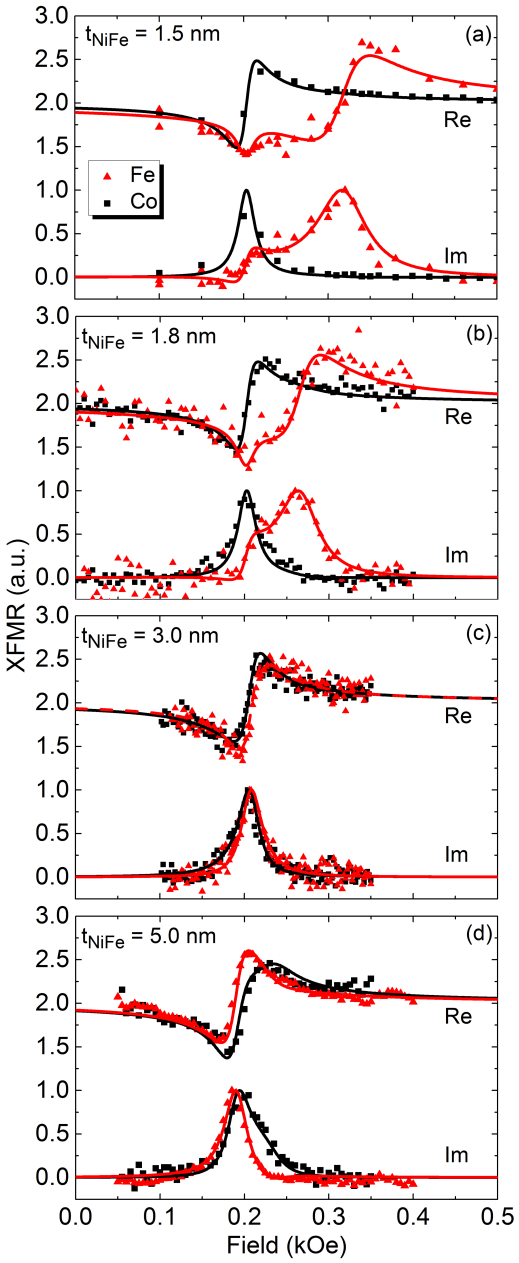

Figure 10.5: The Re and Im components of layer specific XFMR field scans at 4 GHz, for Co_2MnGe (5.0 nm)/Ag (6 nm)/$Ni_{81}Fe_{19}$ (1.5 (a), 1.8 (b), 3.0 (c) and 5.0 (d) nm). The solid lines are the result of numerical simulations of dynamic coupling by STT.

and an extra term with α'_{ii} due to spin pumping with layer i as the source. The final torque term arises due to spin pumping from the other layer j, with layer i as the sink.

For the present samples the second and fourth terms (coupling and spin pumping from other layer) are relatively weak. Therefore, to lowest order, the position of the resonance for a particular layer can be described by the solution of the LLG equation for that layer, when it is isolated from the other. The magnetocrystalline anisotropy field is small and so the in-plane uniaxial anisotropy is neglected. The layer is sufficiently thin that surface anisotropy associated with the interfaces may have a significant effect. This contribution is combined with the shape anisotropy to generate a single perpendicular anisotropy field for each magnetic layer. With these assumptions the relation between field and frequency at resonance can be written as

$$\omega_r^2 = \gamma^2 H_{\rm res}(H_{\rm res} + 4\pi M_{\rm eff}), \tag{10.3}$$

where ω_r is the resonance frequency, $H_{\rm res}$ is the resonance field, $\gamma = \gamma_e g/2$ where $\gamma_e = 2\pi(2.80)$ MHz/Oe, and the spectroscopic splitting factor g is assumed to be 2.11 for $Ni_{81}Fe_{19}$[248] and 2.00 for Co_2MnGe.[249] The effective demagnetising field $4\pi M_{\rm eff} = 4\pi M - 4K_s/Mt$, where K_s is the surface anisotropy constant, which is assumed to have the same value for both surfaces of the layer. For a given film thickness t, the magnetization M is found from the VSM data (Fig. 10.4(b)). The spin pumping contribution to the Gilbert damping coefficient has the form[238]

$$\alpha_{ij}^{'} = \frac{g_i \mu_B {\rm Re}(g_j^{\uparrow\downarrow})}{8\pi M_i t_i}, \tag{10.4}$$

where ${\rm Re}(g^{\uparrow\downarrow})$ is the Real part of the spin mixing conductance (not corrected for the Sharvin conductance[250]). The simplifying approximation that $g_1^{\uparrow\downarrow} = g_2^{\uparrow\downarrow} = g^{\uparrow\downarrow}$ is made so that $\alpha_{11}^{'} = \alpha_{12}^{'} = \alpha_1^{'}$ and $\alpha_{22}^{'} = \alpha_{21}^{'} = \alpha_2^{'}$ with

$$\alpha_1^{'} = \frac{g_1 M_2 t_2}{g_2 M_1 t_1} \alpha_2^{'}. \tag{10.5}$$

The XFMR data was fitted by means of a least squares regression algorithm. In each case the layer magnetisation M_i was set to the value measured by VSM, shown in Fig. 10.4(b). The surface anisotropy constant for Co_2MnGe was constrained to $K_{s1} = -0.090$ erg cm^{-2}. The surface anisotropy constant for $Ni_{81}Fe_{19}$ had the fitted values $K_{s2} = 0.085$ erg cm^{-2}, 0.088 erg cm^{-2}, 0.120 erg cm^{-2} and 0.086 erg cm^{-2} for $t_{\rm NiFe}$ = 1.5 nm, 1.8 nm, 3.0 nm and 5.0 nm respectively. For $t_{\rm NiFe} = 1.5$ and 1.8 nm $\alpha_1^{'}$ and α_1^0 were fixed in the relation $\alpha_1^T = \alpha_1^{'} + \alpha_1^0$ where α_1^T is an effective value that also accounts for the line width offset at zero frequency $\Delta H(0)$, and is derived from the VNA-FMR measured

linewidth at 4 GHz shown in Fig. 10.3(a). This is appropriate for the $t_{NiFe} = 1.5$ and 1.8 nm trilayer films where the Co_2MnGe and $Ni_{81}Fe_{19}$ resonances are distinct and α_1^T can be extracted directly from the VNA-FMR data. However, for the t_{NiFe} =3.0 and 5.0 nm trilayer films the Co_2MnGe and $Ni_{81}Fe_{19}$ resonances are overlapped in the VNA-FMR measurement so direct extraction of α_1^T is not possible. Instead, for t_{NiFe} = 3.0 and 5.0 nm, α_1^0 is fixed using the VNA-FMR measurement of the Co_2MnGe (5.0 nm) reference film (no $Ni_{81}Fe_{19}$ layer) shown in 10.3(b). It can be seen in Fig. 10.3 that growth on $Ni_{81}Fe_{19}$ reduces $\Delta H(0)$. For the $t_{CoMnGe} = 5.0$ nm reference film $\Delta H(0) = 29$ Oe, and for the trilayer films with $t_{NiFe} = 3.0$-5.0 nm, $\Delta H(0)$ is reduced to 0 Oe. This is taken into account in the fits and the α_1^0 parameter, which is fixed in the fitting of trilayer films, is calculated from the reference film linewidth minus $\Delta H(0)$. When fitting the $t_{NiFe} = 3.0$ nm trilayer film α_2^0 was also fixed at the value extracted from VNA-FMR measurements on the $t_{NiFe} = 3.0$ nm reference film (no Co_2MnGe layer). For all films the relative size of $\alpha_1^{'}$ and $\alpha_2^{'}$ is constrained by Eq. 10.5.

The fits are shown in Fig. 10.5 and describe both the source and sink layer resonances well. Inserting the fitted parameter $\alpha_2^{'}$ into Eq. 10.4 then yields $Re(g^{\uparrow\downarrow})$ for each $Ni_{81}Fe_{19}$ thickness. The values of the α parameters and $Re(g^{\uparrow\downarrow})$ are listed in table 10.1. The α_1^0 parameter for the trilayer $t_{NiFe} = 1.5$, 1.8 nm films is seen to agree closely with the α_1^0 of the reference Co_2MnGe film measured by VNA-FMR (used to fit the $t_{NiFe} = 3.0$, 5.0 nm films). The uncertainty in $Re(g^{\uparrow\downarrow})$ is however particularly large for t_{NiFe} = 3.0 nm because the resonance fields of the Co_2MnGe and $Ni_{81}Fe_{19}$ layers are almost identical, as is evident from Fig. 10.5(c). In this case the two magnetizations precess with close to the same phase and so the two spin pumping terms in Eq. (1) almost cancel, as noted previously by Heinrich *et al.*[28], so that the fitting is less sensitive to the magnitude of their prefactors. A particularly large value for $Re(g^{\uparrow\downarrow})$ is observed for the t_{NiFe} = 5.0 nm trilayer, where the spin-pumping effect manifests as a pronounced asymmetry of the Co_2MnGe signal, that is not present for the other t_{NiFe} values. The sensitivity of each fitted curve to the spin-pumping was explored by generating a family of curves around the curve that minimised the sum of the residuals, as shown in the supplementary materials. The confidence intervals for the $Re(g^{\uparrow\downarrow})$ values in Table 10.1 correspond to the curves for which the fit to the data was visibly worse.

The error in the extracted $Re(g^{\uparrow\downarrow})$ values was estimated from lines of 'worst best fit'. All variable parameters from the best linear regression fit were fixed at their optimised values. α_2' was then increased/decreased by a percentage until the lines of 'worst best fit' were visibly worse then the linear regression fits. For sink layer thicknesses t_{NiFe} = 1.5 nm, 1.8 nm variation of α_2' is the variation of a composite parameter which includes

t_{NiFe} (nm)	α_1^0 $\times 10^{-3}$	α_1' $\times 10^{-3}$	α_2^0 $\times 10^{-3}$	α_2' $\times 10^{-3}$	$Re(g^{\uparrow\downarrow})$ $\times 10^{15}$ (cm^{-2})
1.5	8.2	5.2	5.3	19.0	2.52 ± 0.3
1.8	8.4	4.6	7.1	14.3	2.22 ± 0.2
3.0	8.7	9.1	11.0	8.4	2.65 †
5.0	8.7	16.0	9.9	14.0	7.73 ± 2.4

Table 10.1: Damping parameters (α_1^0, α_1', α_2^0 and α_2'), extracted from the fits to XFMR data shown in Fig. 10.5, and $Re(g^{\uparrow\downarrow})$ calculated from Eq. 10.4 for spin valves with increasing sink layer thickness (t_{NiFe}). † an estimation of the uncertainty in $Re(g^{\uparrow\downarrow})$ for t_{NiFe} = 3.0 nm is difficult because the resonance fields of the Co_2MnGe and $Ni_{81}Fe_{19}$ layers are almost identical which leads to a level of degeneracy in the fitting (see supplementary materials).

α_1' as this is fixed in relation to α_2' in accordance with equation 10.5 and also α_1^0 as this is also in a fixed relation with α_2' which is given by $\alpha_1^T = \alpha_1' + \alpha_1^0$ where α_1^T is extracted from VNA-FMR measurements. For sink layer thicknesses t_{NiFe} = 3.0 nm, 5.0 nm variation of α_2' is the variation of a composite parameter which includes α_1' but α_1^0 in this case remains fixed at the reference layer value as discussed previously. The results of these fits are shown in figures 10.6-10.9.

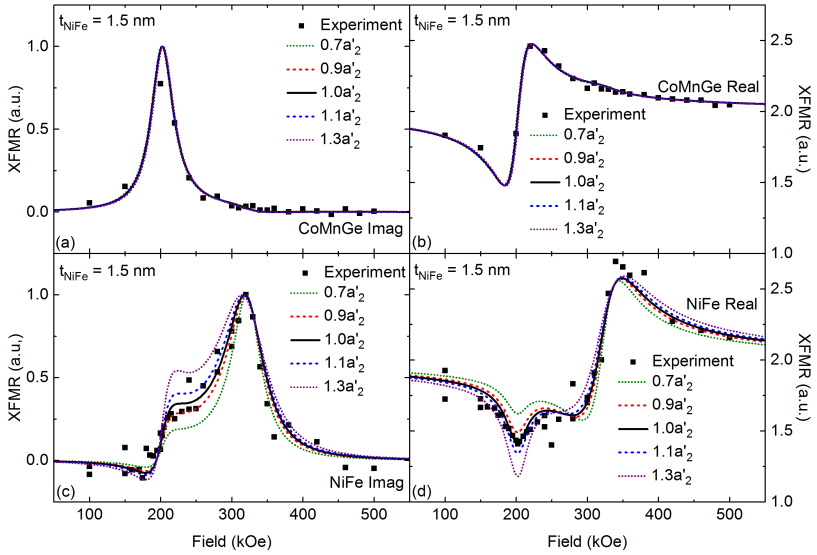

Figure 10.6: Lines of 'worst best fit' to the (a, c) imaginary and (b, d) real components of layer specific XFMR field scans at 4 GHz, for CoMnGe (5.0 nm)/Ag (6 nm)/NiFe (1.5) nm.

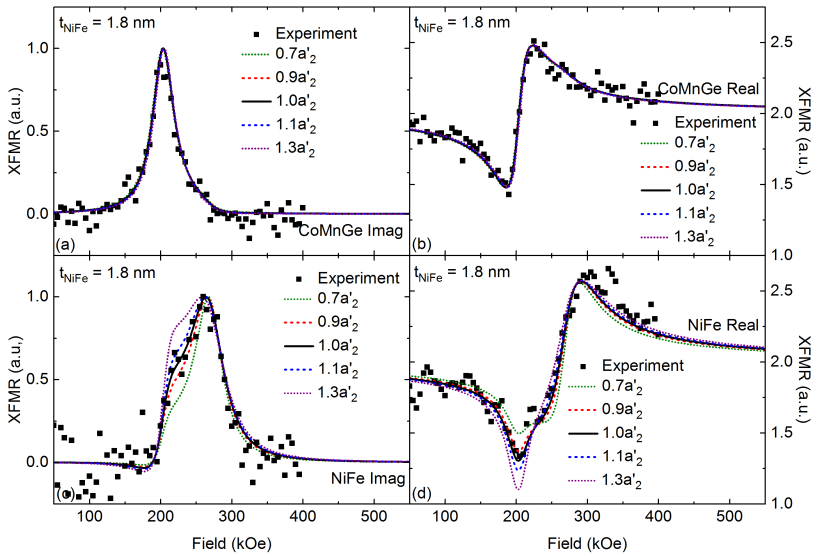

Figure 10.7: Lines of 'worst best fit' to the (a, c) imaginary and (b, d) real components of layer specific XFMR field scans at 4 GHz, for CoMnGe (5.0 nm)/Ag (6 nm)/NiFe (1.8) nm.

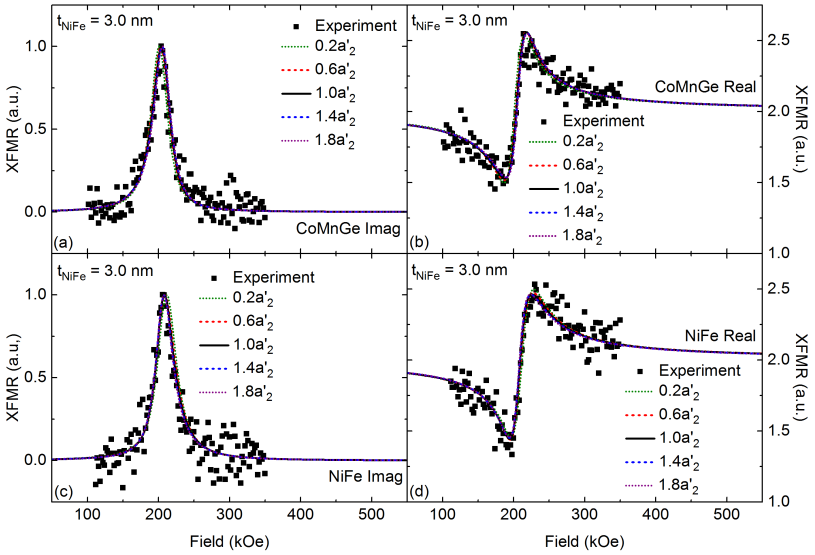

Figure 10.8: Lines of 'worst best fit' to the (a, c) imaginary and (b, d) real components of layer specific XFMR field scans at 4 GHz, for CoMnGe (5.0 nm)/Ag (6 nm)/NiFe (3.0) nm.

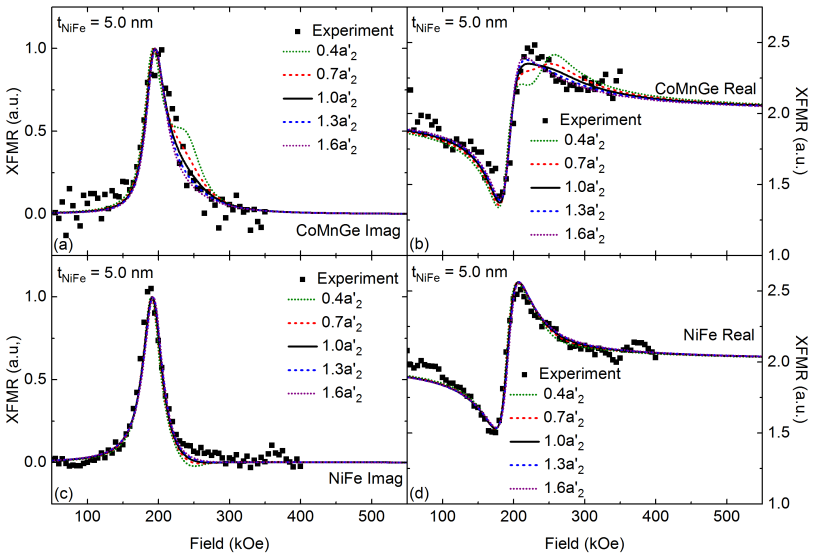

Figure 10.9: Lines of 'worst best fit' to the (a, c) imaginary and (b, d) real components of layer specific XFMR field scans at 4 GHz, for CoMnGe (5.0 nm)/Ag (6 nm)/NiFe (5.0) nm.

The value of $Re(g^{\uparrow\downarrow})$ is a measure of the spin pumping efficiency and is related to the number of conducting channels per spin[250]. An approximate expression for this quantity is given by[238] $Re(g^{\uparrow\downarrow}) \approx 1.2n^{2/3}$, where n is the density of electrons per spin in the NM. For the projected area of a spherical Ag Fermi surface $Re(g^{\uparrow\downarrow}) \approx 1.80 \times 10^{15}$ cm^{-2}. Improved agreement can be expected following correction for the Sharvin conductance[238], however this requires *ab initio* electronic structure calculations. A full description should also include separate values of $g^{\uparrow\downarrow}$ for each interface at which spin scattering can be expected to occur. Therefore the values stated here can be regarded as effective values that describe the two dissimilar interfaces and any internal structure of the spacer layer.

The values of $Re(g^{\uparrow\downarrow})$ shown in Table 1 for t_{NiFe} = 1.5 , 1.8 and 3.0 nm are in reasonable agreement to those expected for a Ag spacer layer with a spherical Fermi surface. The large increase in $Re(g^{\uparrow\downarrow})$ for $t_{NiFe} = 5.0$nm is unexpected in light of the work of Ghosh *et al.*[235]. Given that the $\Delta H(0)$ decreases simultaneously it seems most likely that the increase in $Re(g^{\uparrow\downarrow})$ results from improved interface quality at the upper surface of the $Ni_{81}Fe_{19}$ layers that in turns leads to a smoother Co_2MnGe layer. The rather large value of $Re(g^{\uparrow\downarrow})$ observed for $t_{NiFe} = 5.0$ nm, suggests that either the detailed shape of the Ag Fermi surface needs to be accounted for more carefully, or perhaps that the theoretical description of spin pumping is incomplete for the case of overlapping resonances where spins are pumped from both ferromagnetic layers.

10.4 Summary

Spin pumping has been studied in $Co_2MnGe/Ag/Ni_{81}Fe_{19}$ spin valves with varying sink layer thickness. Using VNA-FMR the transverse spin current absorption in the sink layer was extracted from the source layer damping parameter. Unlike previous studies, which have shown a power-law decay, little variation of the spin current absorption was observed over the 0-1.8 nm thickness range, a behaviour attributed to additional spin scattering in the surrounding stack structure. Small deviations in spin absorption are seen for the thinnest $Ni_{81}Fe_{19}$ layers and are associated with the superparamagnetism of the sink layer for $t_{NiFe} \leq 0.6$ nm. The VNA-FMR experiment highlights the complexities and potential pitfalls of indirect observation of spin-pumping and the need for careful consideration and categorization of each layer in the stack.

Phase resolved XFMR measurements were used to directly measure the torque on the sink layer and revealed a characteristic bipolar phase behaviour of the sink layer at the source layer resonance, a clear fingerprint of spin-current driven precession. The

observed behaviour is reproduced well by a macrospin model that allows the Real part of the spin mixing conductance to be determined. However, when the source and sink layer resonances are coincident, there is a cancellation of the spin currents pumped from the two ferromagnetic layers and the XFMR experiment becomes relatively insensitive to the value of the spin mixing conductance $\mathrm{Re}(g^{\uparrow\downarrow})$. For the samples with the thickest (5 nm) $Ni_{81}Fe_{19}$ layer an increased value of $\mathrm{Re}(g^{\uparrow\downarrow})$ is observed simultaneously with a reduction of $\Delta H(0)$, suggesting that both changes are a consequence of improved interface quality.

In conclusion, we have shown that measurements of the source layer linewidth within a spin valve does not always provide the means to fully determine the spin mixing conductance due to spin current absorption in capping and buffer layers in a multilayer stack. Instead, XFMR can be used to determine the spin mixing conductance $\mathrm{Re}(g^{\uparrow\downarrow})$ from the spin transfer torque exerted upon the sink layer. Our measurements show that the thickness dependent structural quality of the stack has a significant influence upon the extracted $\mathrm{Re}(g^{\uparrow\downarrow})$ values.

Chapter 11

Summary and Future Work

In this thesis the dynamic magnetic and spintronic properties of magnetic thin films fabricated by a variety of methods have been explored using a number of different experimental techniques. TiO_2/CrO_2 and Ta/CoFeB/MgO thin film devices were designed, then fabricated at Brown University utilising primarily, magnetron sputtering deposition, selective area chemical vapour deposition, photolithography, ion-beam etching and thermal annealing. The structural and magnetic properties of these devices were explored at Brown University by vibrating sample magnetometery, X-ray reflection, X-ray diffraction and Hall resistance measurements (also performed in Exeter). The static magnetic and magneto-optical properties were studied by means of the magneto-optical Kerr effect at Exeter University. The dynamic magnetic properties were explored by vector network analyser ferromagnetic resonance, electrical pump-probe time-resolved scanning Kerr microscopy and optical pump-probe scanning Kerr microscopy. The vector network analyser ferromagnetic resonance experiment at Exeter University was developed and a robust algorithm for the programmatic processing of large data sets was developed. Ta/Ag/Co_2MnGe(5 nm)/Ag(6 nm)/$Ni_{81}Fe_{19}$(0-5 nm)/Ag/Ta large area spin valve structures, fabricated by HGST in San Jose California, were studied by vector network analyser ferromagnetic resonance (VNA-FMR), and element-specific phase-resolved x-ray ferromagnetic resonance (XFMR). All of the structures studied in this thesis show promise for use in spintronic devices.

In chapter 5 selective area chemical vapour deposition was demonstrated to be an effective technique for fabricating patterned epitaxial CrO_2 thin films. This technique avoids the typical decomposition to Cr_2O_3 when traditional post-deposition patterning processes are employed. The large uniaxial in plane anisotropy observed in continuous and patterned films, and the dielectric properties of their TiO_2 substrates, make

characterization of their dynamic properties challenging. Nevertheless, by comparing results obtained from complementary dynamical measurement techniques it has been shown that continuous and patterned CrO_2 samples exhibit essentially similar dynamic magnetic properties. If the large anisotropy field can be accommodated this study bodes well for the use of CrO_2 in spintronic devices as its half metallic properties allow the delivery of a highly spin-polarised current. The anisotropy was demonstrated to be sensitive to the thickness of the sample and a treatment of the TiO_2 substrate with hydrofluoric acid. Careful control of these parameters will allow control of the anisotropy magnitude and direction.

Perpendicularly magnetised Ta/CoFeB/MgO layers were studied in chapters 6, 7 and 8. Current induced switching in 140×20 μm Hall bars was studied by simultaneous Kerr microscopy and electrical transport measurements, focusing on currents close to the critical value for switching. For zero applied magnetic field the switching was found to be a stochastic domain wall driven process, the speed of which is strongly dependent upon the value of the applied current. The nucleation of reverse domains appears to begin at one edge of the device, before these domains then grow towards the center of the Hall bar. Modelling the Oersted field through the cross section of the Hall bar reveals that the out of plane component is comparable to the 10 Oe out-of-plane coercive field of the CoFeB, suggesting that the Oersted field may assist the initial domain nucleation on one edge of the Hall bar while opposing reversal on the other edge. With recent interest in utilising Ta/CoFeB/MgO layers in perpendicular MTJs this study highlights the need for careful consideration of the Oersted field when analysing potential contributions to the switching process. Minimisation of the Oersted field contribution, to facilitate study of spin-torques, can be achieved by etching the CoFeB layer at the edge of the device, although it may also be possible to utilise these fields to improve switching efficiency in future technologies.

Spin-transfer torque technology will require the miniaturisation of devices and significant reduction in current duration. These reductions are likely to cause transition from the domain nucleation and propagation regime observed in current-induced switching, to the incoherent and coherent rotation switching regimes. In an effort to move closer to the device dimensions and current durations required for memory technology TRSKM was employed to apply short duration (~70ps) current pulses to Hall bars. The resultant torques are shown to be strongly dependent on the bias field polarity and direction, and pulsed current direction. No significant spatial variance of the torques was observed. The motion of the polar component of the magnetisation was a superposition of two signals acting on different time-scales, a fast

oscillatory component and a slower deflection. This may indicate that the torques in such systems act on different time-scales, Oersted torques are expected to act almost instantaneously while the SOTs rely on electron diffusion processes which may have a longer characteristic time-scale. The relative magnitudes and origins of the SOTs remains an intensely debated subject. In an effort to shed light on this, the symmetries of the torques with respect to the magnetisation and current directions were analysed in terms of parallel and perpendicular spin accumulation. This process was particularly challenging since small signal to noise ratios, due to pulse reflections, meant that a clear signal was obtained only for the polar component of the magnetisation. This highlights the complexity of this task and demonstrates the need for careful design of devices that have minimal effect on the pulse profile.

In a second generation of devices designed specifically for high frequency excitation, several key magnetic parameters such as the coercive field were shown to vary between nominally identical devices fabricated in different sputtering runs. The sensitivity of SOTs to the ferromagnetic and heavy metal structure has been well documented, and so efforts must be made to reduce this variance and carefully control the deposition and patterning procedure if SOT devices are to be used commercially. In the second generation of devices, patterning the CoFeB/MgO layer independently of the Ta under layer allowed patterned element dimensions to be reduced and to be fabricated away from the edge of the Ta under layer, minimising the out-of-plane Oersted field contribution to the torque. The signal line dimensions were also reduced significantly increasing the current density and allowing full vector resolution of the magnetisation dynamics in the TRSKM. The magnetisation dynamics of $1.6 - 10.0$ μm squares were found to be highly sensitive to bias field direction and polarity, and also showed strong spatial variations. Again signals with two distinct time-scales were observed which may be further evidence that different torques in such systems do not have the same characteristic time-scales. Many more interesting questions were raised by this study, in particular why TRSKM images showed a strong bipolar contrast at the edges the square when the magnetisation was saturated in-plane along the direction of current flow. Interpretation of these results is ongoing. However this may be evidence of a spin-accumulation at the lateral edges of the square or evidence of an in-plane spin current generated by the spin Hall effect as charge current flows in the out-of-plane direction into the conducting CoFeB. Another key result in this study was the observation that, for a multi-domain ground state with a small in-plane canting either in or orthogonal to the direction of current flow, the direction of polar rotation was dependent on the direction of canting. A model of the SOTs is currently being developed which, when

applied to these results should allow a qualitative determination of the dominant SOTs in this structure.

This study demonstrates the efficacy of the TRSKM technique for exploring SOTs and lays the groundwork for further studies. A wide range of devices was fabricated to explore the effects of device size (to explore switching regimes), shape anisotropy (to aid deterministic zero field switching), element separation (to explore stray field interaction distances), position (to explore the effects of Oersted fields) and notched designs (to trap domains). Time constraints only allowed time-resolved study of a limited number of devices. However this experiment has since been taken up by colleagues who have this large parameter space to explore. A key future development of this work is the application of a lower frequency, large bipolar pulsed current. The bipolar current will allow imaging of the current-induced switching between the perpendicular magnetic states providing this occurs in less than the 1 μs time delay between picked laser pulses. This experiment is currently being set up and shows promising results. The device dimensions in this study stretched the limits of the photolithography patterning procedure. In order to reduce to the nano-scale another patterning technique such as e-beam lithography will need to be utilised.

In chapter 10 spin-pumping was studied in Co_2MnGe layer/Ag/$Ni_{81}Fe_{19}$ spin valves with varying sink layer thickness. It was shown that measurements of the source layer linewidth are not necessarily a reliable means of determining the spin mixing conductance for a multilayer stack due to spin absorption by layers outside the spin valve. Instead XFMR was used to determine an effective spin mixing conductance from the spin transfer torque acting upon the sink layer. Using VNA-FMR the transverse spin current absorption in the sink layer was extracted from the source layer damping parameter. Unlike previous studies, which have shown a power-law decay, little variation of the spin current absorption was observed over the 0-1.8 nm thickness range, a behaviour attributed to additional spin scattering in the surrounding stack structure. Small deviations in spin absorption are seen for the thinnest $Ni_{81}Fe_{19}$ layers and are associated with the superparamagnetism of the sink layer for $t_{NiFe} \leq 0.6$ nm. The VNA-FMR experiment highlights the complexities and potential pitfalls of indirect observation of spin-pumping and the need for careful consideration and categorization of each layer in the stack.

Phase resolved XFMR measurements were used to directly measure the torque on the sink layer and revealed a characteristic bipolar phase behaviour of the sink layer at the source layer resonance, a clear fingerprint of spin-current driven precession. The observed behaviour is reproduced well by a macrospin model that allows the real part

of the spin mixing conductance to be determined. However when the source and sink layer resonances are coincident, there is a cancellation of the spin currents pumped from the two ferromagnetic layers and the XFMR experiment becomes relatively insensitive to the value of the spin mixing conductance $Re(g^{\uparrow\downarrow})$. For the samples with the thicket (5 nm) $Ni_{81}Fe_{19}$ layer an increased value of $Re(g^{\uparrow\downarrow})$ is observed simultaneously with a reduction of $\Delta H(0)$, suggesting that both changes are a consequence of improved interface quality.

We have demonstrated that measurements of the source layer linewidth within a spin valve are not necessarily a reliable means of determining the spin mixing conductance due to spin current absorption in the outer layers of the multilayer stack. Instead, XFMR can be used to determine the spin mixing conductance $Re(g^{\uparrow\downarrow})$ from the spin transfer torque exerted upon the sink layer. Our measurements show that the thickness dependent structural quality of the stack has a significant influence upon the extracted $Re(g^{\uparrow\downarrow})$ values. A obvious progression of this work in an exploration of how improvements of the interface quality will impact $Re(g^{\uparrow\downarrow})$. Several simple methods such as annealing, additional layers or chemical pretreatment all have the potential to improve interface quality and may lead to further increases in $Re(g^{\uparrow\downarrow})$.

Bibliography

[1] M. N. Baibich, J. M. Broto, A. Fert, F. N. Van Dau, F. Petroff, P. Eitenne, G. Creuzet, A. Friederich, and J. Chazelas, *Phys. Rev. B*, **61**, 2472 (1988).

[2] M. Julliere, *Phys. Lett. A*, **54**, 225 (1975).

[3] W. Pickett and J. Moodera, *Phys. Today*, **54**, 83 (2001).

[4] G. Ju, A. Vertikov, A. V. Nurmikko, C. Canady, G. Xiao, R. F. C. Farrow, and A. Cebollada, *Phys. Rev. B*, **57**, R700 (1998).

[5] Y. Ji, G. J. Strijkers, F. Y. Yang, C. L. Chien, J. M. Byers, A. Anguelouch, G. Xiao, and A. Gupta, *Phys. Rev. B*, **86**, 5585 (2001).

[6] C. König, M. Fonin, M. Laufenberg, A. Biehler, W. Bührer, M. Kläui, U. Rüdiger, and G. Güntherodt, *Phys. Rev. B*, **75**, 144428 (2007).

[7] Q. Zhang, Y. Li, A. V. Nurmikko, G. X. Miao, G. Xiao, and A. Gupta, *J. Appl. Phys.*, **96**, 7527 (2004).

[8] L. Yuan, Y. Ovchenkov, A. Sokolov, C.-S. Yang, B. Doudin, and S. H. Liou, *J. Appl. Phys.*, **93**, 6850 (2003).

[9] K. Ando, S. Fujita, J. Ito, S. Yuasa, Y. Suzuki, Y. Nakatani, T. Miyazaki, and H. Yoda, *J. Appl. Phys.*, **115**, 172607 (2014).

[10] J. Slonczewski, *J. Magn, Magn. Mater.*, **159**, L1 (1996).

[11] L. Berger, *Phys. Rev. B*, **54**, 9353 (1996).

[12] A. Driskill-Smith, D. Apalkov, V. Nikitin, X. Tang, S. Watts, D. Lottis, K. Moon, A. Khvalkovskiy, R. Kawakami, X. Luo, A. Ong, E. Chen, and M. Krounbi, in *2011 3rd IEEE International Memory Workshop (IMW)*, (IEEE2011), 1–3, (2011).

[13] L. Liu, O. J. Lee, T. J. Gudmundsen, D. C. Ralph, and R. A. Buhrman, *Phys. Rev. B*, **109**, 096602 (2012).

[14] G. Yu, P. Upadhyaya, Y. Fan, J. G. Alzate, W. Jiang, K. L. Wong, S. Takei, S. A. Bender, L.-T. Chang, Y. Jiang, M. Lang, J. Tang, Y. Wang, Y. Tserkovnyak, P. K. Amiri, and K. L. Wang, *Nat. Nanotechnol.*, **9**, 548 (2014).

[15] L. Liu, C.-F. Pai, Y. Li, H. W. Tseng, D. C. Ralph, and R. A. Buhrman, *Science*, **336**, 555 (2012).

[16] J. Kim, J. Sinha, M. Hayashi, M. Yamanouchi, S. Fukami, T. Suzuki, S. Mitani, and H. Ohno, *Nat. Mater.*, **12**, 240 (2013).

[17] J. Torrejon, F. Garcia-Sanchez, T. Taniguchi, J. Sinha, S. Mitani, J.-V. Kim, and M. Hayashi, *Phys. Rev. B*, **91**, 214434 (2015).

[18] X. Qiu, P. Deorani, K. Narayanapillai, K.-S. Lee, K.-J. Lee, H.-W. Lee, and H. Yang, *Sci. Rep.*, **4**, 4491 (2014).

[19] X. Qiu, K. Narayanapillai, Y. Wu, P. Deorani, X. Yin, A. Rusydi, K.-J. Lee, H.-W. Lee, and H. Yang, *Nat. Nanotechnol.*, **10**, 333 (2013).

[20] A. Manchon, *arXiv*, 1204.4869 (2012).

[21] K. Garello, C. O. Avci, I. M. Miron, M. Baumgartner, A. Ghosh, S. Auffret, O. Boulle, G. Gaudin, and P. Gambardella, *Appl. Phys. Lett.*, **105**, 212402 (2014).

[22] C. Zhang, M. Yamanouchi, H. Sato, S. Fukami, S. Ikeda, F. Matsukura, and H. Ohno, *J. Appl. Phys.*, **115**, 17C714 (2014).

[23] C. Bi, L. Huang, S. Long, Q. Liu, Z. Yao, L. Li, Z. Huo, L. Pan, and M. Liu, *Appl. Phys. Lett.*, **105**, 022407 (2014).

[24] L. Liu, R. A. Buhrman, and D. C. Ralph, *arXiv*, 1111.3702 (2011).

[25] C. Zhang, S. Fukami, H. Sato, F. Matsukura, and H. Ohno, *Appl. Phys. Lett.*, **107**, 012401 (2016).

[26] I. Zutić and H. Dery, *Nat. Mater.*, **10**, 647 (2011).

[27] T. Yang, T. Kimura, and Y. Otani, *Nat. Phys.*, **4**, 851 (2008).

[28] B. Heinrich, Y. Tserkovnyak, G. Woltersdorf, A. Brataas, R. Urban, and G. E. W. Bauer, *Phys. Rev. B*, **90**, 187601 (2003).

[29] S. I. Kiselev, J. C. Sankey, I. N. Krivorotov, N. C. Emley, R. J. Schoelkopf, R. A. Buhrman, and D. C. Ralph, *Nature*, **425**, 380 (2003).

[30] M. V. Costache, M. Sladkov, S. M. Watts, C. H. van der Wal, and B. J. van Wees, *Phys. Rev. B*, **97**, 216603 (2006).

[31] T. Kimura, Y. Otani, T. Sato, S. Takahashi, and S. Maekawa, *Phys. Rev. Lett.*, **98**, 156601 (2007).

[32] E. Saitoh, M. Ueda, H. Miyajima, and G. Tatara, *Appl. Phys. Lett.*, **88**, 182509 (2006).

[33] J. Li, L. R. Shelford, P. Shafer, A. Tan, J. X. Deng, P. S. Keatley, C. Hwang, E. Arenholz, G. Van Der Laan, R. J. Hicken, and Z. Q. Qiu, *Phys. Rev. Lett.*, **117**, 076602 (2016).

[34] B. D. Cullity and C. D. Graham, *Introduction to magnetic materials*, (Wiley-IEEE Press, Hoboken, 2009).

[35] P. Weiss, *Comptes Rendus*, **143**, 1136 (1906).

[36] A. H. Morrish, *The Physical Principles of Magnetism*, (Wiley-IEEE Press, 1965).

[37] E. C. Stoner, *P. Roy. Soc. Lond. A Mat.*, **165**, 372 (1938).

[38] J. Stöhr and H. C. Siegmann, *Magnetism: From fundamentals to nanoscale dynamics*, (Springer, Berlin, 2006).

[39] E. C. Stoner, *P. Roy. Soc. Lond. A Mat.*, **169**, 339 (1939).

[40] W. Brown, *Micromagnetics*, (Wiley, New York, 1963).

[41] C. P. Enz, in *Original Scientific Papers*, (Springer, Berlin, 1985).

[42] H. Young, R. Freedman, and A. Ford, *University Physics with Modern Physics*, (Pearson, London, 2003).

[43] C. Kittel, *Introduction to Solid State Physics*, (Wiley, New York, 2004).

[44] W. Pauli, *Z. Phys.*, **31**, 765 (1925).

[45] S. Blundell, *Magnetism in Condensed Matter*, (Oxford University Press, Oxford, 2001).

[46] J. C. Slater, *Phys. Rev.*, **35**, 509 (1930).

[47] A. L. Kholmetskii, O. V. Missevitch, and T. Yarman, *Am. J. Phys.*, **78**, 428 (2010).

[48] Y. Tserkovnyak, A. Brataas, G. E. W. Bauer, and B. I. Halperin, *Rev. Mod. Phys.*, **77**, 1375 (2005).

[49] H. L. Wang, C. H. Du, Y. Pu, R. Adur, P. C. Hammel, and F. Y. Yang, *Phys. Rev. B*, **112**, 197201 (2014).

[50] G. H. O. Daalderop, P. J. Kelly, and M. F. H. Schuurmans, *Phys. Rev. B*, **41**, 11919 (1990).

[51] GITAM Institute of Technology, *Domain theory of Ferromagnetism*, (http://eresources.gitam.edu/Engg_Phys/semester_2/magnetic/domain.htm. accessed 10/01/2017).

[52] H. W. F. Sung and C. Rudowicz, *arXiv*, 0210657 (2002).

[53] T. Gilbert, *Phys. Rev.*, **100**, 1243 (1955).

[54] J. Kuneš and V. Kamberský, *Phys. Rev. B*, **65**, 212411 (2002).

[55] O. Yalçin, *Ferromagnetic Resonance - Theory and Applicaitons*, (InTech, Rejika, 2013).

[56] B. Kochelaev and Y. Yablokov, *The Beginning of Paramagnetic Resonance*, (World Scientific Publishing, Singapore, 1995).

[57] R. S. Macomber, *A Complete Introduction To Modern NMR Spectroscopy*, (Wiley, New York, 1998).

[58] J. Bass and W. P. Pratt, *J. Phys. Condens. Matter*, **19**, 183201 (2007).

[59] E. Y. Tsymbal and D. G. Pettifor, *Solid State Phys.*, **56**, 113 (2001).

[60] T. Valet and A. Fert, *Phys. Rev. B*, **48**, 7099 (1993).

[61] N. F. Mott and H. Massey, *The Theory of Atomic Collisions*, (Clarendon, Oxford, 1949).

[62] M. Johnson, *Phys. Rev. B*, **70**, 2142 (1993).

[63] R. E. Camley and J. Barna, *Phys. Rev. B*, **63**, 664 (1989).

[64] P. M. Levy, S. Zhang, and A. Fert, *Phys. Rev. B*, **65**, 1643 (1990).

[65] J.-G. J. Zhu and C. Park, *Mater. Today*, **9**, 36 (2006).

[66] J. Mathon, *Phase Transit.*, **76**, 491 (2003).

[67] D. C. Ralph and M. D. Stiles, *J. Magn. Magn. Mater.*, **320**, 1190 (2008).

[68] M. Tsoi, A. Jansen, J. Bass, W.-C. Chiang, M. Seck, V. Tsoi, and P. Wyder, *Phys. Rev. B*, **80**, 4281 (1998).

[69] J. Katine, F. Albert, R. Buhrman, E. Myers, and D. Ralph, *Phys. Rev. Lett.*, **84**, 3149 (2000).

[70] I. M. Miron, G. Gaudin, S. Auffret, B. Rodmacq, A. Schuhl, S. Pizzini, J. Vogel, and P. Gambardella, *Nat. Mater.*, **9**, 230 (2010).

[71] D. Fang, H. Kurebayashi, J. Wunderlich, K. Výborný, L. P. Zârbo, R. P. Campion, A. Casiraghi, B. L. Gallagher, T. Jungwirth, and A. J. Ferguson, *Nat. Nanotechnol.*, **6**, 413 (2011).

[72] A. Chernyshov, M. Overby, X. Liu, J. K. Furdyna, Y. Lyanda-Geller, and L. P. Rokhinson, *Nat. Phys.*, **5**, 10 (2008).

[73] T. Suzuki, S. Fukami, N. Ishiwata, M. Yamanouchi, S. Ikeda, N. Kasai, and H. Ohno, *Appl. Phys. Lett.*, **98**, 142505 (2011).

[74] I. M. Miron, K. Garello, G. Gaudin, P.-J. Zermatten, M. V. Costache, S. Auffret, S. Bandiera, B. Rodmacq, A. Schuhl, and P. Gambardella, *Nature*, **476**, 189 (2011).

[75] H. Kurebayashi, O. Dzyapko, V. E. Demidov, D. Fang, A. J. Ferguson, and S. O. Demokritov, *Nat. Mater.*, **10**, 660 (2011).

[76] K. Obata and G. Tatara, *Phys. Rev. B*, **77**, 214429 (2008).

[77] A. Manchon and S. Zhang, *Phys. Rev. B*, **78**, 212405 (2008).

[78] X. Wang and A. Manchon, *Phys. Rev. B*, **108**, 117201 (2012).

[79] A. Vedyayev, N. Strelkov, M. Chshiev, N. Ryzhanova, and B. Dieny, *arXiv*, 1108.2589 (2011).

[80] A. Manchon, *arXiv*, 1204.4869 (2012).

[81] S. Zhang, P. M. Levy, and A. Fert, *Phys. Rev. B*, **88**, 236601 (2002).

[82] E. H. Hall, *Am. J. Math.*, **2**, 287 (1879).

[83] M. I. Dyakonov, *arXiv*, 1210.3200 (2012).

[84] Y. K. Kato, R. C. Myers, A. C. Gossard, and D. D. Awschalom, *Science*, **306**, 1910 (2004).

[85] J. Wunderlich, B. Kaestner, J. Sinova, and T. Jungwirth, *Phys. Rev. Lett.*, **94**, 047204 (2005).

[86] S. O. Valenzuela and M. Tinkham, *Nature*, **442**, 176 (2006).

[87] Q. Hao and G. Xiao, *Phys. Rev. Appl.*, **3**, 034009 (2015).

[88] Y. Kajiwara, K. Harii, S. Takahashi, J. Ohe, K. Uchida, M. Mizuguchi, H. Umezawa, H. Kawai, K. Ando, K. Takanashi, S. Maekawa, and E. Saitoh, *Nature*, **464**, 262 (2010).

[89] Y. K. Kato, R. C. Myers, A. C. Gossard, and D. D. Awschalom, *Science*, **306**, 1910 (2004).

[90] J. Inoue and H. Ohno, *Science*, **309**, 2004 (2005).

[91] R. Karplus and J. Luttinger, *Phys. Rev.*, **95**, 1154 (1954).

[92] N. F. Mott, *P. Roy. Soc. Lond. A Mat.*, **153**, 699 (1936).

[93] N. Nagaosa, J. Sinova, S. Onoda, A. H. MacDonald, and N. P. Ong, *Rev. Mod. Phys.*, **82**, 1539 (2010).

[94] I. M. Miron, G. Gaudin, S. Auffret, B. Rodmacq, A. Schuhl, S. Pizzini, J. Vogel, and P. Gambardella, *Nat. Mater.*, **9**, 230 (2010).

[95] E. Rashba and I. Boiko, *Sov. Phys. Solid State*, **2**, 1109 (1960).

[96] G. Dresselhaus, *Phys. Rev.*, **100**, 580 (1955).

[97] A. Manchon, H. C. Koo, J. Nitta, S. M. Frolov, and R. A. Duine, *Nat. Mater.*, **14**, 871 (2015).

[98] H. Nakamura, T. Koga, and T. Kimura, *Phys. Rev. B*, **108**, 206601 (2012).

[99] X. Wang and A. Manchon, *Phys. Rev. B*, **108**, 117201 (2012).

[100] X. Wang, C. O. Pauyac, and A. Manchon, *arXiv*, 1206.6726 (2012).

[101] L. Liu, T. Moriyama, D. C. Ralph, and R. A. Buhrman, *Phys. Rev. Lett.*, **106**, 036601 (2011).

[102] S. Zhang and Z. Li, *Phys. Rev. B*, **93**, 127204 (2004).

[103] C. O. Avci, K. Garello, C. Nistor, S. Godey, B. Ballesteros, A. Mugarza, A. Barla, M. Valvidares, E. Pellegrin, A. Ghosh, I. M. Miron, O. Boulle, S. Auffret, G. Gaudin, and P. Gambardella, *Phys. Rev. B*, **89**, 214419 (2014).

[104] K. Garello, I. M. Miron, C. O. Avci, F. Freimuth, Y. Mokrousov, S. Blügel, S. Auffret, O. Boulle, G. Gaudin, and P. Gambardella, *Nat. Nanotechnol.*, **8**, 587 (2013).

[105] C. Onur Avci, K. Garello, I. Mihai Miron, G. Gaudin, S. Auffret, O. Boulle, and P. Gambardella, *Appl. Phys. Lett.*, **100**, 212404 (2012).

[106] X. Fan, J. Wu, Y. Chen, M. J. Jerry, H. Zhang, and J. Q. Xiao, *Nat. Commun.*, **4**, 1799 (2013).

[107] T. D. Skinner, M. Wang, A. T. Hindmarch, A. W. Rushforth, A. C. Irvine, D. Heiss, H. Kurebayashi, and A. J. Ferguson, *Appl. Phys. Lett.*, **104**, 062401 (2014).

[108] H. Pierson, *Handbook of Chemical Vapour Deposition*, (Noyes Publications, New York, 1992).

[109] M. Ohring, *The materials science of thin films I*, (Academic Press, Cambridge, 1992).

[110] K. Choy, *Prog. Mater. Sci.*, **48**, 57 (2003).

[111] G. Miao, G. Xiao, and A. Gupta, *Phys. Rev. B*, **71**, 094418 (2005).

[112] X. W. Li, A. Gupta, and G. Xiao, *Appl. Phys. Lett.*, **75**, 713 (1999).

[113] AutoCAD (computer program), AUTODESK (2015).

[114] Photomasking company, Advance Reprocuctions Corp (ARC) (http://advancerepro.com/ accessed 10/01/2017).

[115] R. A. Parker, *Phys. Rev.*, **124**, 1719 (1961).

[116] Crystec, *TiO2 datasheet*, (http://www.crystec.de/daten/tio2.pdf accessed 10/01/2017).

[117] B. Rameev, F. Yildiz, S. Kazan, B. Aktas, A. Gupta, L. R. Tagirov, D. Rata, D. Buergler, P. Gruenberg, C. M. Schneider, S. Kämmerer, G. Reiss, and A. Hütten, *Phys. Status Solidi A*, **203**, 1503 (2006).

[118] B. Rameev, A. Gupta, F. Yıldız, L. Tagirov, and B. Aktaş, *J. Magn. Magn. Mater.*, **300**, e526 (2006).

[119] B. Rameev, A. Gupta, A. Anguelouch, G. Xiao, F. Yıldız, L. Tagirov, and B. Aktaş, *J. Magn, Magn. Mater.*, **272**, 1167 (2004).

[120] B. Z. Rameev, A. Gupta, G. X. Miao, G. Xiao, F. Yildiz, L. R. Tagirov, and B. Akta, *Phys. Status Solidi A*, **201**, 3350 (2004).

[121] G.-X. Miao, G. Xiao, and A. Gupta, *Phys. Status Solidi A*, **203**, 1513 (2006).

[122] S. Lab, *Material Safety Data Sheet, Chromium Trioxide MSDS*, (https://www.sciencelab.com/page/S/PVAR/SLC2068 accessed 01/02/2015).

[123] M. S. Anwar and F. d. W. en Natuurwetenschappen, *Spin triplet supercurrents in thin films of ferromagnetic CrO_2*, Ph.D. thesis (2011).

[124] Transene Inc, *Etchants List*, (http://transene.com/etchants/ accessed 03/04/2015).

[125] Q. Hao, *Giant Spin Hall Effect and Anomalous Hall Effect in Solids with Strong Spin-Orbit Coupling*, Ph.D. thesis, Brown University (2015).

[126] Q. Hao and G. Xiao, *Phys. Rev. B*, **91**, 224413 (2015).

[127] R. Shimabukuro, K. Nakamura, T. Akiyama, and T. Ito, *Physica E*, **42**, 1014 (2010).

[128] A. Manchon, C. Ducruet, L. Lombard, S. Auffret, B. Rodmacq, B. Dieny, S. Pizzini, J. Vogel, V. Uhlíř, M. Hochstrasser, and G. Panaccione, *J. Appl. Phys.*, **104**, 043914 (2008).

[129] S. Monso, B. Rodmacq, S. Auffret, G. Casali, F. Fettar, B. Gilles, B. Dieny, and P. Boyer, *Appl. Phys. Lett.*, **80**, 4157 (2002).

[130] S. Foner, *Rev. Sci. Instrum.*, **27**, 261 (1956).

[131] S. Foner, *Rev. Sci. Instrum.*, **30**, 548 (1959).

[132] L. Spinu, B. Dodrill, and C. Radu, Mangetometry Measurements in *Magnetics Technology International* (2013).

[133] A. Zieba, *Rev. Sci. Instrum.*, **53**, 1344 (1982).

[134] V. Holy, J. Kubena, I. Ohlidal, K. Lischka, and W. Plotz, *Phys. Rev. B*, **47**, 15896 (1993).

[135] E. Bontempi, *X-Ray Reflectivity for the characterization of thin films*, (Transworld Research Network, 2004).

[136] M. Yasaka, *Rigaku J.*, **26**, 1, (2010).

[137] A. I. Lvovsky, *Encyclopedia of Optical Engineering*, (CRC Press, Boca Raton, 2003).

[138] K. Charles, *Introduction to Solid State Physics*, (Wiley, New York, 2004).

[139] B. Cullity, *Elements of X-ray Diffraction*, (Addison-Wesley, Boston, 1959).

[140] M. Faraday, *Trans. Roy. Soc. Lond.*, **136**, 1 (1846).

[141] A. Kundt, *Philos. Mag.*, **18**, 308 (1884).

[142] J. Kerr, *Philos. Mag*, **3**, 321 (1877).

[143] J. Kerr, *Philos. Mag*, **5**, 161 (1878).

[144] P. Weinberger, *Philos. Mag. Lett.*, **88**, 897 (2008).

[145] Z. Q. Qiu and S. D. Bader, *Rev. Sci. Instrum.*, **71**, 1243 (2000).

[146] S. B. Z. Q. Qiu, (K. Bennemann (editor)) in *Nonlinear Optics in Metals*, (Clarendon Press, Oxford, 1998).

[147] K. Zvezdin, Anatoly, *Modern magneto-optics and magneto-optical materials: Studies in Condensed Matter*, (Taylor & Francis, Oxford, 1997).

[148] G. Metzger, P. Pluvinag, and R. Torguet, *Ann. Phys.*, **10**, 5 (1965).

[149] J. Wu, J. R. Moore, and R. J. Hicken, *J. Magn. Magn. Mater.*, **222**, 189 (2000).

[150] Z. Qui and S. Badar, (K. Bennemann (editor)) in *Nonlinear Optics in Metals*, (Clarendon Press, Oxford, 1998).

[151] P. Weiss, *J. Phys. Theor.*, **6**, 661 (1907).

[152] J. N. Lalena, D. A. Cleary, *Principles of inorganic materials design*, (Wiley, New York, 2005).

[153] W. Heisenberg, *Zeitschrift for Physik*, **38**, 411 (1926).

[154] I. Tamm, *Fundamentals of the Theory of Electricity*, (Mir, Moscow, 1979).

[155] H. R. Hulme, *Proc. R. Soc. London, Ser. A.*, **135**, 237 (1932).

[156] P. N. Argyres and E. N. Adams, *Phys. Rev.*, **104**, 900 (1956).

[157] H. S. Bennett and E. A. Stern, *Phys. Rev.*, **137**, A448 (1965).

[158] R. Hicken, N. Hughes, J. Moore, D. Schmool, R. Wilks, and J. Wu, *J. Magn. Magn. Mater.*, **242**, 559 (2002).

[159] P. Keatley, *Time-Resolved Magneto-Optical Investigations of Picosecond Magnetisation Dynamics in Arrays of Non-Ellipsoidal Ferromagnetic Nano-Elements*, Ph.D. thesis, University of Exeter (2008).

[160] J. H. Scofield, *Am. J. Phys.*, **62**, 129 (1994).

[161] P. K. Dixon and L. Wu, *Rev. Sci. Instrum.*, **60**, 3329 (1989).

[162] N. Subrahmanyam, B. Lal, and M. Avandhanulu, *A Text Book of Optics*, (S. Chand & Co Ltd, Lucknow, 2006).

[163] P. Gray and C. Searle, *Principles Physics, Models, and Circuits*, (Wiley, New York, 1969).

[164] Agilent, *Network Analyzer Basics*, (http://cp.literature.agilent.com/litweb/pdf/5965-7917E.pdf accessed 11/12/2016),

[165] J. Ericsson, *Design of a Vector Network Analyzer Ferromagnetic Resonance set up and measurements on multilayer Heusler samples*, Ph.D. thesis, Uppsala University (2010).

[166] N. Ingo, *Magnetization Dynamics of Confined Ferromagnetic Systems*, Ph.D. thesis, Regensburg University (2006).

[167] R. Urban, G. Woltersdorf, and B. Heinrich, *Phys. Rev. B*, **87**, 217204 (2001).

[168] G. A. Kouzaev, *Applications of Advanced Electromagnetics: Components and Systems*, (Springer, New York ,2013).

[169] F. Giesen, *Magnetization Dynamics of Nanostructured Ferromagnetic Rings and Rectangular Elements*, Ph.D. thesis, Hamburg University (2005).

[170] NTT Plala, *Co-planar waveguide calculator*, (http://www17.plala.or.jp/i-lab/tool/cpw_e.htm accessed 05/06/2016).

[171] C. J. Durrant, M. Jokubaitis, W. Yu, H. Mohamad, L. R. Shelford, P. S. Keatley, G. Xiao, and R. J. Hicken, *J. Appl. Phys.*, **117**, 17B707 (2015).

[172] X. Zou and G. Xiao, *Phys. Rev. B*, **77**, 054417 (2008).

[173] X. Zou, G. Xiao, S. Huang, T. Chen, and C.-L. Chien, *J. Appl. Phys.*, **103**, 07D710 (2008).

[174] X. Zou and G. Xiao, *Appl. Phys. Lett.*, **91**, 113512 (2007).

[175] X. Zou and G. Xiao, *J. Appl. Phys.*, **103**, 07D701 (2008).

[176] B. Z. Rameev, A. Gupta, G. X. Miao, G. Xiao, F. Yildiz, L. Tagirov, and B. Akta, *Tech. Phys. Lett.*, **31**, 802 (2005).

[177] G. M. Müller, M. Münzenberg, G.-X. Miao, and A. Gupta, *Phys. Rev. B*, **77**, 020412 (2008).

[178] Q. Zhang, A. V. Nurmikko, G. X. Miao, G. Xiao, and A. Gupta, *Phys. Rev. B*, **74**, 064414 (2006).

[179] G. Miao, G. Xiao, and A. Gupta, *Phys. Rev. B*, **71**, 094418 (2005).

[180] D. S. Rodbell, *J. Phys. Soc. Jap.*, **21**, 1224 (1966).

[181] G. X. Miao, A. Gupta, G. Xiao, and A. Anguelouch, *Thin Solid Films*, **478**, 159 (2005).

[182] A. Wypych, I. Bobowska, M. Tracz, A. Opasinska, S. Kadlubowski, A. Krzywania-Kaliszewska, J. Grobelny, and P. Wojciechowski, *J. Nanomater.*, **2014**, 1 (2014).

[183] M. Ben Omar and A. Matoussi, in *Annual Report on Conference on Electrical Insulation and Dielectric Phenomena, CEIDP*, 467 (2012).

[184] S. Takata, A. Hachiya, and Y. Matsumoto, *J. Ceram. Soc. Jap.*, **2**, 366 (2012).

[185] B. Prasai, B. Cai, M. K. Underwood, J. P. Lewis, and D. A. Drabold, *J. Mater. Sci.*, **47**, 7515 (2012).

[186] H. Nagata, T. Shinriki, K. Shima, M. Tamai, and E. Min Haga, *J. Vac. Sci. Technol. A*, **17**, 1018 (1999).

[187] J. Gerkema and A. R. Miedema, *Surf. Sci.*, **124**, 351 (1983).

[188] P. Keatley, V. Kruglyak, R. Hicken, J. Childress, and J. Katine, *J. Magn. Magn. Mater.*, **306**, 298 (2006).

[189] Y. Liu, L. R. Shelford, V. V. Kruglyak, R. J. Hicken, Y. Sakuraba, M. Oogane, Y. Ando, and T. Miyazaki, *J. Appl. Phys.*, **101**, 09C106 (2007).

[190] S. Choudhary and R. Goyal, *J. Supercond. Nov. Magn.*, **29**, 139 (2016).

[191] S. Choudhary and M. Varshney, *J. Supercond. Nov. Magn.*, **28**, 3141 (2015).

[192] S. Choudhary and S. Jalu, *Phys. Lett. A*, **379**, 1661 (2015).

[193] C. J. Durrant, R. J. Hicken, Q. Hao, and G. Xiao, *Phys. Rev. B*, **93**, 014414 (2016).

[194] Z. Z. Bandic and R. H. Victora, *Proceedings of the IEEE*, **96**, 1749 (2008).

[195] M. Julliere, *Phys. Lett. A*, **54**, 225 (1975).

[196] C. O. Avci, K. Garello, C. Nistor, S. Godey, B. Ballesteros, A. Mugarza, A. Barla, M. Valvidares, E. Pellegrin, A. Ghosh, I. M. Miron, O. Boulle, S. Auffret, G. Gaudin, and P. Gambardella, *Phys. Rev. B*, **89**, 214419 (2014).

[197] K. Garello, I. M. Miron, C. O. Avci, F. Freimuth, Y. Mokrousov, S. Blügel, S. Auffret, O. Boulle, G. Gaudin, and P. Gambardella, *Nat. Nanotechnol.*, **8**, 587 (2013).

[198] J. Kim, J. Sinha, M. Hayashi, M. Yamanouchi, S. Fukami, T. Suzuki, S. Mitani, and H. Ohno, *Nat. Mater.*, **12**, 240 (2013).

[199] G. Yu, P. Upadhyaya, K. L. Wong, W. Jiang, J. G. Alzate, J. Tang, P. K. Amiri, and K. L. Wang, *Phys. Rev. B*, **89**, 104421 (2014).

[200] E. Kultursay, M. Kandemir, A. Sivasubramaniam, and O. Mutlu, in *2013 IEEE International Symposium on Performance Analysis of Systems and Software (ISPASS)*, 256 (2013).

[201] J. Carter and K. Rajamani, *Computer*, **43**, 76 (2010).

[202] U. Hoelzle and L. A. Barroso, *Synthes. Lect. Comp. Arch.*, **8**, 1 (2013).

[203] J. Hayakawa, S. Ikeda, Y. M. Lee, F. Matsukura, and H. Ohno, *Appl. Phys. Lett.*, **89**, 232510 (2006).

[204] S. Ikeda, J. Hayakawa, Y. Ashizawa, Y. M. Lee, K. Miura, H. Hasegawa, M. Tsunoda, F. Matsukura, and H. Ohno, *Appl. Phys. Lett.*, **93**, 082508 (2008).

[205] S. Ikeda, K. Miura, H. Yamamoto, K. Mizunuma, H. D. Gan, M. Endo, S. Kanai, J. Hayakawa, F. Matsukura, and H. Ohno, *Nat. Mater.*, **9**, 721 (2010).

[206] H. Almasi, D. R. Hickey, T. Newhouse-Illige, M. Xu, M. R. Rosales, S. Nahar, J. T. Held, K. A. Mkhoyan, and W. G. Wang, *Appl. Phys. Lett.*, **106**, 182406 (2015).

[207] S. Ikeda, J. Hayakawa, Y. M. Lee, F. Matsukura, Y. Ohno, T. Hanyu, and H. Ohno, *IEEE Transactions on Electron Devices*, **54**, 991 (2007).

[208] D. C. Worledge, G. Hu, D. W. Abraham, J. Z. Sun, P. L. Trouilloud, J. Nowak, S. Brown, M. C. Gaidis, E. J. O'Sullivan, and R. P. Robertazzi, *Appl. Phys. Lett.*, **98**, 022501 (2011).

[209] Y. Huai, F. Albert, P. Nguyen, M. Pakala, and T. Valet, *Appl. Phys. Lett.*, **84**, 3118 (2004).

[210] Y. Wang, P. Deorani, X. Qiu, J. H. Kwon, and H. Yang, *Appl. Phys. Lett.*, **105**, 152412 (2014).

[211] O. J. Lee, L. Q. Liu, C. F. Pai, Y. Li, H. W. Tseng, P. G. Gowtham, J. P. Park, D. C. Ralph, and R. A. Buhrman, *Phys. Rev. B*, **89**, 024418 (2014).

[212] A. Ganguly, K. Kondou, H. Sukegawa, S. Mitani, S. Kasai, Y. Niimi, Y. Otani, and A. Barman, *Appl. Phys. Lett.*, **104**, 072405 (2014).

[213] C.-F. Pai, L. Liu, Y. Li, H. W. Tseng, D. C. Ralph, and R. A. Buhrman, *Appl. Phys. Lett.*, **101**, 122404 (2012).

[214] D. Lacour, J. A. Katine, N. Smith, M. J. Carey, and J. R. Childress, *Appl. Phys. Lett.*, **85**, 4681 (2004).

[215] P. S. Keatley, V. V. Kruglyak, A. Neudert, E. A. Galaktionov, R. J. Hicken, J. R. Childress, and J. A. Katine, *Phys. Rev. B*, **78**, 214412 (2008).

[216] I. M. Miron, K. Garello, G. Gaudin, P.-J. Zermatten, M. V. Costache, S. Auffret, S. Bandiera, B. Rodmacq, A. Schuhl, and P. Gambardella, *Nature*, **476**, 189 (2011).

[217] J. C. Sankey, Y.-T. Cui, J. Z. Sun, J. C. Slonczewski, R. A. Buhrman, and D. C. Ralph, *Nat. Phys.*, **4**, 67 (2007).

[218] I. D. Mayergoyz, *Mathematical Models of Hysteresis and Their Applications*, (Elsevier, Amsterdam, 2003).

[219] K. S. Lee, D. Go, A. Manchon, P. M. Haney, M. D. Stiles, H. W. Lee, and K. J. Lee, *Phys. Rev. B*, **91**, 144401 (2015).

[220] P. S. Keatley, A. Aziz, M. Ali, B. J. Hickey, M. G. Blamire, and R. J. Hicken, *Phys. Rev. B*, **89**, 094421 (2014).

[221] K. Garello, C. O. Avci, I. M. Miron, M. Baumgartner, A. Ghosh, S. Auffret, O. Boulle, G. Gaudin, and P. Gambardella, *Appl. Phys. Lett.*, **105**, 212402 (2014).

[222] K. Yagami, A. A. Tulapurkar, A. Fukushima, and Y. Suzuki, *Appl. Phys. Lett.*, **85**, 5634 (2004).

[223] L. You, O. Lee, D. Bhowmik, D. Labanowski, and J. Hong, *Proc. Natl. Acad. Sci. U.S.A.*, **112**, 10310 (2014).

[224] M. Heibel, *Vector Network Analyzer (VNA) Calibration: The Basics*, (https://cas.web.cern.ch/cas/Denmark-2010/Caspers/ (5911487) accessed 12/12/2016).

[225] P. Varshney and H. Agrawal, Spintronics Technology: A Review, in *National conference on advances in technology and applied sciences, Jodpur* (2014).

[226] J. Sinova, S. O. Valenzuela, J. Wunderlich, C. Back, and T. Jungwirth, *Rev. Mod. Phys.*, **87**, 1213 (2015).

[227] Y. K. Kato, R. C. Myers, A. C. Gossard, and D. D. Awschalom, *Science*, **306**, 1910 (2004).

[228] Y. Tserkovnyak, A. Brataas, and G. E. W. Bauer, *Phys. Rev. B*, **88**, 117601 (2002).

[229] D. Wei, M. Obstbaum, M. Ribow, C. H. Back, and G. Woltersdorf, *Nat. Commun.*, **5**, 3768 (2014).

[230] R. D. McMichael and M. D. Stiles, *J. Appl. Phys.*, **97**, 10J901 (2005).

[231] P. Krone, D. Makarov, M. Albrecht, T. Schrefl, and D. Suess, *J. Magn. Magn. Mater.*, **322**, 3771 (2010).

[232] T. Gerrits, M. L. Schneider, and T. J. Silva, *J. Appl. Phys.*, **99**, 023901 (2006).

[233] X. Lou, C. Adelmann, S. A. Crooker, E. S. Garlid, J. Zhang, K. S. M. Reddy, S. D. Flexner, C. J. Palmstrøm, and P. A. Crowell, *Nat. Phys.*, **3**, 197 (2007).

[234] Q. Yang, P. Holody, S.-F. Lee, L. L. Henry, R. Loloee, P. A. Schroeder, W. P. Pratt, and J. Bass, *Phys. Rev. B*, **72**, 3274 (1994).

[235] A. Ghosh, S. Auffret, U. Ebels, and W. E. Bailey, *Phys. Rev. Lett.*, **109**, 127202 (2012).

[236] J. Zhang, P. M. Levy, S. Zhang, and V. Antropov, *Phys. Rev. Lett.*, **93**, 256602 (2004).

[237] B. Kardasz, O. Mosendz, B. Heinrich, Z. Liu, and M. Freeman, *J. Appl. Phys.*, **103**, 07C509 (2008).

[238] B. Kardasz and B. Heinrich, *Phys. Rev. B*, **81**, 094409 (2010).

[239] O. Mosendz, G. Woltersdorf, B. Kardasz, B. Heinrich, and C. H. Back, *Phys. Rev. B*, **79**, 224412 (2009).

[240] G. Woltersdorf, O. Mosendz, B. Heinrich, and C. H. Back, *Phys. Rev. Lett.*, **99**, 246603 (2007).

[241] G. van der Laan and A. I. Figueroa, *Coord. Chem. Rev.* **277**, 95 (2014).

[242] M. K. Marcham, L. R. Shelford, S. A. Cavill, P. S. Keatley, W. Yu, P. Shafer, A. Neudert, J. R. Childress, J. A. Katine, E. Arenholz, N. D. Telling, G. van der Laan, and R. J. Hicken, *Phys. Rev. B*, **87**, 180403 (2013).

[243] M. K. Marcham, P. S. Keatley, A. Neudert, R. J. Hicken, S. A. Cavill, L. R. Shelford, G. van der Laan, N. D. Telling, J. R. Childress, J. A. Katine, P. Shafer, and E. Arenholz, *J. Appl. Phys.*, **109**, 07D353 (2011).

[244] B. Heinrich and J. F. Cochran, *Adv. Phys.*, **42**, 523 (1993).

[245] K. Nomura, S. Kikuchi, M. Yasuda, K. Tokumitsu, and Y. Ujihira, *Hyperfine Interact*, **148**, 307 (2003).

[246] J. O. Bockris, B. Conway, and R. E. White, *Modern Aspects of Electrochemisty No. 22*, (Springer, New York ,1992).

[247] H. D. Arnold and G. W. Elmen, *Bell Syst. Tech. J.*, **2**, 101 (1923).

[248] J. M. Shaw, H. T. Nembach, T. J. Silva, and C. T. Boone, *J. Appl. Phys.*, **114**, 243906 (2013).

[249] H. T. Nembach, T. J. Silva, J. M. Shaw, M. L. Schneider, M. J. Carey, S. Maat, and J. R. Childress, *Phys. Rev. B*, **84**, 054424 (2011).

[250] Y. Tserkovnyak, A. Brataas, G. E. W. Bauer, and B. I. Halperin, *Rev. Mod. Phys.*, **77**, 1375 (2005).